

FULL FIELD RECONSTRUCTION AND UNCERTAINTY QUANTIFICATION OF
PARTICLE IMAGE VELOCIMETRY MEASUREMENTS IN A 5×5 ROD BUNDLE WITH
MIXING VANE SPACER GRIDS

A Dissertation

by

MASON PAUL CHILDS

Submitted to the Office of Graduate and Professional Studies of
Texas A&M University
in partial fulfillment of the requirements for the degree of
DOCTOR OF PHILOSOPHY

Chair of Committee, Yassin Hassan
Committee Members, Maria King
William Marlow
Rodolfo Vaghetto
Head of Department, John Hurtado

May 2019

Major Subject: Nuclear Engineering

Copyright 2019 Mason Paul Childs

ABSTRACT

One of the most commonly used methods for quantifying fluid velocity profiles is particle image velocimetry (PIV). This non-invasive measurement technique employs seeding particles in a transparent simulant fluid flowing through a geometry of interest at Reynolds number (Re) in the regime of what is expected during operation. A laser sheet is projected through the fluid to illuminate the particles, and two subsequent photographs of the particle-seeded fluid are taken with a Δt recorded between the two images. Displacement of the particles from one image to the other, δ_i , which is calculated using a generalized cross correlation, along with the known Δt , are used to determine a velocity of a fluid element in the laser plane. Efforts to expand this planar two-dimension two-component (2D2C) method to a volumetric three-dimension three-component (3D3C) PIV have been pursued, which require large computational resources for processing. This study aimed to quantify a 3D3C velocity measurement in a prototypical pressurized water reactor (PWR) geometry of rods with a mixing vane spacer grid.

A new matched-index-of-refraction (MIR) facility for rod bundle and spacer grid testing was developed and constructed within the Thermal-Hydraulics Laboratory of the Nuclear Engineering Department at Texas A&M University (TAMU). The facility was designed to overcome the challenge of producing high fidelity and low uncertainty data, especially near the mixing vanes, where data is sparsely available. This investigation explores an innovation in MIR fluid and presents results for a full field 3D3C velocity measurement at $Re=27,390$. The full field measurements are constructed via trilinear interpolation from multiple 2D2C PIV measurements. These 3D3C ensemble-averaged velocity, root-mean-square (RMS) fluctuating velocity, Reynolds stresses, and vorticity fields are presented downstream of a prototypical PWR spacer grid in a 5×5 rod bundle. A full field uncertainty quantification (UQ) of the results is also provided. Profiles taken at different subchannel positions having similar geometrical features are compared to demonstrate coherence of the results and quality of the MIR for improved PIV. New data of the complex flow near and within the mixing vanes region of the spacer grid could be measured with the new methodology.

ACKNOWLEDGMENTS

The author would like to express appreciation to their supervisors, Professor Yassin Hassan, Professor Rodolfo Vaghetto, and Professor Thien Duy Nguyen for their guidance, which was instrumental in the completion of this work.

The author would also like to expressly thank Professor André Campagnole dos Santos for his constant help during his time at Texas A&M while on loan from the Center for the Development of Nuclear Technology in Brazil.

The author also acknowledges and thanks the many students surrounding him who assisted in the work. Thanks to Nolan Goth, Philip Jones, William Headley, and Nicolas Quintanar, who all would have but were not required to risk life and limb in the completion of construction of the flow loop utilized.

The author also thanks his parents, Lane and Paula Childs, and his in-laws, Walter and Nancy Cowie, who have all encouraged him to do his best and stay in school, and who never let him forget that they are proud of him. Finally, the author would like to express their most sincere loving gratitude to his wife, Paige, who is infinitely patient with and supports him in everything he does.

CONTRIBUTORS AND FUNDING SOURCES

Contributors

This work was supported by a dissertation committee chaired by Professor Yassin Hassan of the Departments of Nuclear Engineering and Mechanical Engineering, consisting of Professors William Marlow, and Rodolfo Vaghetto of the Department of Nuclear Engineering and Professor Maria King of the Departments of Mechanical Engineering and Biological & Agricultural Engineering.

Data collection was performed by the student and assisted in part by Professor André Campagnole dos Santos of the Center for the Development of Nuclear Technology. Professor dos Santos aided in preliminary analyses depicted in Chapter 4, which were also assisted in part by Professors Yassin Hassan and Thien Nguyen of the Department of Nuclear Engineering. These preliminary results depicted in Sections 5.1 and 5.2 were published 2019 in an article listed in the Journal of Experimental Thermal and Fluid Science.

All other work conducted for the dissertation was completed by the student independently.

Funding Sources

Graduate study was supported by a research assistantship from the Department of Nuclear Engineering at Texas A&M University. Partial support for facility construction was provided by the U.S. Department of Energy (DOE) Consortium for Advanced Simulation of Light Water Reactors (CASL).

NOMENCLATURE

A cross sectional flow area

C_{12} cross correlation between images 1 and 2 in a frame

D_H hydraulic diameter

$Eval$ PRANA vectory validation variable

I measured intensity of tracer particle reflectance

L characteristic length

M magnification factor

P kinematic pressure

P_w wetted perimeter

$R_{\bar{\phi}}$ statistical residual for an arbitrary variable's mean, $\bar{\phi}$

Re Reynolds number

T temperature

X_i digital position coordinate

δ_i component-wise displacement between a image pair

λ wavelength of electromagnetic radiation

$\mathcal{F}\{\phi\}$ Fourier transform of an arbitrary variable, ϕ

μ fluid viscosity

ν kinematic viscosity

ρ fluid density

σ_{ϕ} statistical standard deviation for an arbitraty variable, ϕ

n refractive index

n_D refractive index at the Fraunhofer "D" sodium emmission near 589 nm wavelength

p rod pitch length

t_L largest scale eddy turnover time

t_p response time of a particle in fluid flow

u, v, w velocity vector

u_i shorthand velocity vector

x, y, z Cartesian coordinates

x_i shorthand Cartesian coordinates

2D2C two-dimension two-component

2D3C two-dimension three-component

3D2C three-dimension two-component

3D3C three-dimension three-component

CASL Consortium for Advanced Simulation of Light Water Reactors

CCD charge-coupled device

CFD computational fluid dynamics

CW clockwise

DAS data acquisition system

DNS direct numerical simulation

DOE U.S. Department of Energy

DWO Discrete Window Offset

EPDM ethylene propylene diene terpolymer

FEP fluorinated ethylene propylene

FOV field of view

KAERI Korea Atomic Energy Research Institute

LDV laser Doppler velocimetry

LES large-eddy simulation

MIR matched-index-of-refraction

NIST the National Institute of Standards and Technology

NPSH net positive suction head

NPT national pipe thread

NS Navier-Stokes

OD outer diameter
PIV particle image velocimetry
PMMA poly(methyl methacrylate)
PVC polyvinyl chloride
PWR pressurized water reactor
RANS Reynolds-averaged Navier-Stokes
RMS root-mean-square
ROI region of interest
RPC robust phase correlation
RTD resistance temperature detector
SPIV stereoscopic particle image velocimetry
SS stainless steel
TAMU Texas A&M University
UOD universal outlier detection
UQ uncertainty quantification
V&V verification and validation
VFD variable frequency drive

TABLE OF CONTENTS

	Page
ABSTRACT	ii
ACKNOWLEDGMENTS	iii
CONTRIBUTORS AND FUNDING SOURCES	iv
NOMENCLATURE	v
TABLE OF CONTENTS	viii
LIST OF FIGURES	x
LIST OF TABLES.....	xviii
1. INTRODUCTION.....	1
1.1 Motivation, Verification, and Validation	2
1.2 Theory and Governing Equations	2
1.3 Previous Work & Literature Review	5
2. PROJECT SCOPE.....	9
2.1 Objectives	9
2.2 Requirements & Specifications	9
3. FACILITY DESCRIPTION	11
3.1 Matched Index of Refraction Materials	11
3.2 Fluid Considerations	14
3.3 Visualization Test Section	17
3.4 Plena	19
3.5 Flow Loop and Instrumentation	20
3.6 Flow Conditions for $Re=27,390$	21
4. PARTICLE IMAGE VELOCIMETRY METHODOLOGY	23
4.1 Two Dimension Two Component Image Collection.....	23
4.1.1 Particle Image Velocimetry Cross Correlation & Image Processing	30
4.2 Two Dimension Two Component Calibration	33
4.3 Particle Image Velocimetry Uncertainty Quantification.....	35
4.3.1 Calibration & Digital Displacement Uncertainty	35

4.3.2	Uncertainty as Convergence Residual	36
4.3.3	Statistical Uncertainty Propagation	40
4.3.4	Coordinates uncertainty	41
4.4	Full Field Three Dimension Two Component, and Three Dimension Three Component Reconstruction	42
4.4.1	Three Dimension Three Component Reconstruction via Trilinear Interpolation	43
5.	RESULTS	46
5.1	Two Dimension Two Component Particle Image Velocimetry Results	46
5.1.1	Mean Velocity	46
5.1.2	Fluctuating Root Mean Square & Shear Stress	50
5.1.3	Vorticity	55
5.2	Two Dimension Two Component Particle Image Velocimetry Uncertainty Results ...	56
5.2.1	Calibration & Digital Displacement Uncertainty Results	56
5.2.2	Convergence Residual Results	57
5.2.3	Propagated Statistical Uncertainty	61
5.2.4	Combined Uncertainty Results	64
5.3	Combined Two Dimension Two Component Particle Image Velocimetry Results	67
5.3.1	Mean Velocity	67
5.3.2	Fluctuating Root Mean Square & Shear Stress	70
5.3.3	Vorticity	73
5.4	Interpolated Three Dimension Three Component Particle Image Velocimetry Results	76
5.4.1	Mean Velocity	77
5.4.2	Vorticity	81
6.	CONCLUSIONS & FUTURE WORK	84
	REFERENCES	86
	APPENDIX A. TEST SECTION DRAWINGS	92
	APPENDIX B. PLENA DRAWINGS	96
	APPENDIX C. CALIBRATION DATA	122
	APPENDIX D. TWO DIMENSION TWO COMPONENT RESULTS	124

LIST OF FIGURES

FIGURE	Page
1.1 Computer rendering of 5×5 spacer grid.....	1
1.2 two-dimension two-component (2D2C) particle image velocimetry (PIV) results for an fluorinated ethylene propylene (FEP) matched-index-of-refraction (MIR) constructed 5×5 rod bundle performed at Texas A&M University (TAMU) [1, 2]. Reprinted with permission from Conner et al [2].	5
1.3 Mean velocity component results using stereoscopic particle image velocimetry (SPIV) for an FEP MIR constructed 5×5 rod bundle performed at TAMU [3, 4]. Reprinted from Childs et al [4].	6
1.4 Transverse velocity results from PIV studies on prototypical rod bundles using axial cross section laser planes [5, 6]. Reprinted with permission from Conner et al [2].....	7
1.5 Korea Atomic Energy Research Institute (KAERI) benchmark - high fidelity data within 2.6× oversized subchannels [7, 8]. Reprinted with permission from Chang et al [7].	8
3.1 Borosilicate glass tube submerged in a non-mixed combination of D-limonene and water. Lack of light ray refraction can be observed via the horizontal lines on the glass container, which are partially behind the submerged tube.	12
3.2 Refractive index of D-limonene as a function of transmitted light wavelength of electromagnetic radiation (λ) and fluid temperature (T).	13
3.3 Refractive index of borosilicate glass as a function of transmitted light λ and medium T	14
3.4 Difference of refractive indexes of borosilicate glass and D-limonene as a function of transmitted light λ and medium T	15
3.5 Photo of glass tube rod bundle construction prior to insertion in test section. The region of interest (ROI) is highlighted.....	17
3.6 Photo of test section installed in the facility before D-limonene filling. The ROI is highlighted.	18

3.7	Positioning of glass tube bundle in the polycarbonate test section. Set screws were used from two adjacent walls (3.7a) to fix the spacer grids in a corner edge of against two walls (3.7b).	19
3.8	Plena used for connection of experimental test section with flow loop.	20
3.9	Facility flow loop layout sketch.	21
4.1	Image of the PIV setup.	24
4.2	Laser plane alignment and camera orientation for first test, consisting of measurements of u and w . The origin corner is highlighted in red.	26
4.3	Image focus and alignment relative to the rods and grid at the first and fifth rod row. Camera positioning for the first test is also shown, and the origin corner is highlighted in red.	27
4.4	Pixel displacement relative to the average position of the center of the rods between planes taken at the center of the rods.	28
4.5	Laser plane alignment and camera position for second test, consisting of measurements of v and w . The origin corner is highlighted in red.	29
4.6	Background subtracted images of a measurement plane R as indicated from Figure 4.2. Image B has saturated brightness and highlights that the spacer grid vanes are still visible; however, rods are not, even though that in this image there are two rows of rods in front of the plane.	31
4.7	Average of PRANA's PRANA vectory validation variable ($Eval$) in all preliminary planes.	32
4.8	Calibration plate image at plane B used in determination of magnification factor (M) for the first test. Similar images were collected for the second test.	34
4.9	Convergence of \bar{u} velocity component and $\overline{u'w'}$ Reynolds stress.	38
4.10	Convergence of measured and derived quantities for all preliminary planes at the final set, where 2000 velocity fields are used.	39
4.11	Depiction of data used for trilinear interpolation of data in the highly discretized spatial mesh.	44
5.1	Mean axial velocity, $\overline{w_1}$, for plane II at $y=51.75$ mm.	47
5.2	Mean axial velocity, $\overline{w_2}$, for plane III at $x=14.75$ mm.	48
5.3	Mean transverse velocity, \bar{u} , for plane II at $y=51.75$ mm.	49

5.4	Mean transverse velocity, \bar{v} , for plane III at $x=14.75$ mm.....	49
5.5	root-mean-square (RMS) velocity, $w'_{1,RMS}$, for plane II at $y=51.75$ mm.	50
5.6	RMS velocity, $w'_{2,RMS}$, for plane III at $x=14.75$ mm.....	51
5.7	RMS velocity, u'_{RMS} , for plane II at $y=51.75$ mm.	52
5.8	RMS velocity, v'_{RMS} , for plane III at $x=14.75$ mm.....	52
5.9	Mean Reynolds shear stress, $\overline{u'w'_1}$, for plane II at $y=51.75$ mm.....	53
5.10	Mean Reynolds shear stress, $\overline{v'w'_2}$, for plane III at $x=14.75$ mm.....	54
5.11	Mean vorticity, $\overline{\omega_y}$, for plane II at $y=51.75$ mm.....	55
5.12	Mean vorticity, $\overline{\omega_x}$, for plane III at $x=14.75$ mm.....	56
5.13	Physical and magnification uncertainty for plane II at $y=51.75$ mm.....	57
5.14	Physical and magnification uncertainty for plane III at $x=14.75$ mm.....	58
5.15	Residual uncertainty for mean transverse velocity of plane II at $y=51.75$ mm.....	59
5.16	Residual uncertainty for mean transverse velocity of plane III at $x=14.75$ mm.....	59
5.17	Residual uncertainty for transverse RMS velocity of plane II at $y=51.75$ mm.....	60
5.18	Residual uncertainty for transverse RMS velocity of plane III at $x=14.75$ mm.....	60
5.19	Statistical uncertainty for mean transverse velocity of plane II at $y=51.75$ mm.....	61
5.20	Statistical uncertainty for mean transverse velocity of plane III at $x=14.75$ mm.....	62
5.21	Statistical uncertainty for transverse RMS velocity of plane II at $y=51.75$ mm.....	63
5.22	Statistical uncertainty for transverse RMS velocity of plane III at $x=14.75$ mm.....	63
5.23	Combined uncertainty for mean transverse velocity of plane II at $y=51.75$ mm.....	64
5.24	Combined uncertainty for mean transverse velocity of plane III at $x=14.75$ mm.....	65
5.25	Combined uncertainty for transverse RMS velocity of plane II at $y=51.75$ mm.....	66
5.26	Combined uncertainty for transverse RMS velocity of plane III at $x=14.75$ mm.....	66
5.27	Mean axial velocity components $\overline{w_1}$, and $\overline{w_2}$ for test 1 (left) and test 2 (right), respectively. Slices at $z=6.03$ mm (5.27a) and $z=36.87$ mm (5.27b).	68

5.28	Mean transverse velocity components \bar{u} , and \bar{v} for test 1 (left) and test 2 (right), respectively. Slices at $z=6.03$ mm (5.28a) and $z=36.87$ mm (5.28b).	69
5.29	Axial RMS velocity components $w'_{1,RMS}$, and $w'_{2,RMS}$ for test 1 (left) and test 2 (right), respectively. Slices at $z=6.03$ mm (5.29a) and $z=36.87$ mm (5.29b).	71
5.30	Transverse RMS velocity components u'_{RMS} , and v'_{RMS} for test 1 (left) and test 2 (right), respectively. Slices at $z=6.03$ mm (5.30a) and $z=36.87$ mm (5.30b).	72
5.31	Mean Reynolds shear stress $\overline{u'w'_1}$, and $\overline{v'w'_2}$ for test 1 (left) and test 2 (right), respectively. Slices at $z=6.03$ mm (5.31a) and $z=36.87$ mm (5.31b).	74
5.32	Mean transverse vorticity components $\overline{\omega_y}$, and $\overline{\omega_x}$ for test 1 (left) and test 2 (right), respectively. Slices at $z=6.03$ mm (5.32a) and $z=36.87$ mm (5.32b).	75
5.33	Length of mixing vane downstream of spacer grid used in determination of z_{vane}	76
5.34	Cross section of mixing vane spacer grid region used in presentation of center four subchannel analysis.	77
5.35	Mean axial velocity for center four subchannels at $z^+=0.0$ hydraulic diameter (D_H) ($z=6.03$ mm).	78
5.36	Mean axial velocity for center four subchannels at $z^+=3.0D_H$ ($z=36.84$ mm).	79
5.37	Mean transverse velocity for center four subchannels at $z^+=0.0D_H$ ($z=6.03$ mm).	79
5.38	Mean transverse velocity for center four subchannels at $z^+=3.0D_H$ ($z=36.84$ mm).	80
5.39	Mean velocity magnitude, $ \overline{u_i} $, with transverse direction indicated by 1/3 sampled arrows for center four subchannels at $z^+=0.0D_H$ (5.39a) and $z^+=3.0D_H$ (5.39b).	81
5.40	Mean transverse vorticity contours interpolated for center four subchannels at $z^+=0.0D_H$ ($z=6.03$ mm).	82
5.41	Mean transverse vorticity contours where $\overline{\omega_i}t_L=\pm 1$ for center four subchannels at $z^+=0.0D_H$ ($z=6.03$ mm).	83
5.42	Mean transverse vorticity contours where $\overline{\omega_i}t_L=\pm 2$ for center four subchannels at $z^+=0.0D_H$ ($z=6.03$ mm).	83
D.1	\bar{w} , $y = 2.25$ mm.	125
D.2	\bar{w} , $y = 14.25$ mm.	125
D.3	\bar{w} , $y = 26.25$ mm.	125
D.4	\bar{w} , $y = 39.75$ mm.	125

D.5	$\bar{w}, y = 51.75\text{mm}.$	125
D.6	$\bar{w}, y = 63.75\text{mm}.$	125
D.7	$\bar{w}, x = 2.75\text{mm}.$	126
D.8	$\bar{w}, x = 14.75\text{mm}.$	126
D.9	$\bar{w}, x = 26.75\text{mm}.$	126
D.10	$\bar{w}, x = 40.25\text{mm}.$	126
D.11	$\bar{w}, x = 52.25\text{mm}.$	126
D.12	$\bar{w}, x = 64.25\text{mm}.$	126
D.13	$\bar{u}, y = 2.25\text{mm}.$	127
D.14	$\bar{u}, y = 14.25\text{mm}.$	127
D.15	$\bar{u}, y = 26.25\text{mm}.$	127
D.16	$\bar{u}, y = 39.75\text{mm}.$	127
D.17	$\bar{u}, y = 51.75\text{mm}.$	127
D.18	$\bar{u}, y = 63.75\text{mm}.$	127
D.19	$\bar{v}, x = 2.75\text{mm}.$	128
D.20	$\bar{v}, x = 14.75\text{mm}.$	128
D.21	$\bar{v}, x = 26.75\text{mm}.$	128
D.22	$\bar{v}, x = 40.25\text{mm}.$	128
D.23	$\bar{v}, x = 52.25\text{mm}.$	128
D.24	$\bar{v}, x = 64.25\text{mm}.$	128
D.25	$\bar{\omega}_y, y = 2.25\text{mm}.$	129
D.26	$\bar{\omega}_y, y = 14.25\text{mm}.$	129
D.27	$\bar{\omega}_y, y = 26.25\text{mm}.$	129
D.28	$\bar{\omega}_y, y = 39.75\text{mm}.$	129
D.29	$\bar{\omega}_y, y = 51.75\text{mm}.$	129

D.30 $\overline{\omega}_y, y = 63.75\text{mm}$.	129
D.31 $\overline{\omega}_x, x = 2.75\text{mm}$.	130
D.32 $\overline{\omega}_x, x = 14.75\text{mm}$.	130
D.33 $\overline{\omega}_x, x = 26.75\text{mm}$.	130
D.34 $\overline{\omega}_x, x = 40.25\text{mm}$.	130
D.35 $\overline{\omega}_x, x = 52.25\text{mm}$.	130
D.36 $\overline{\omega}_x, x = 64.25\text{mm}$.	130
D.37 $\sqrt{\overline{w'w'}}$, $y = 2.25\text{mm}$.	131
D.38 $\sqrt{\overline{w'w'}}$, $y = 14.25\text{mm}$.	131
D.39 $\sqrt{\overline{w'w'}}$, $y = 26.25\text{mm}$.	131
D.40 $\sqrt{\overline{w'w'}}$, $y = 39.75\text{mm}$.	131
D.41 $\sqrt{\overline{w'w'}}$, $y = 51.75\text{mm}$.	131
D.42 $\sqrt{\overline{w'w'}}$, $y = 63.75\text{mm}$.	131
D.43 $\sqrt{\overline{w'w'}}$, $x = 2.75\text{mm}$.	132
D.44 $\sqrt{\overline{w'w'}}$, $x = 14.75\text{mm}$.	132
D.45 $\sqrt{\overline{w'w'}}$, $x = 26.75\text{mm}$.	132
D.46 $\sqrt{\overline{w'w'}}$, $x = 40.25\text{mm}$.	132
D.47 $\sqrt{\overline{w'w'}}$, $x = 52.25\text{mm}$.	132
D.48 $\sqrt{\overline{w'w'}}$, $x = 64.25\text{mm}$.	132
D.49 $\sqrt{\overline{u'u'}}$, $y = 2.25\text{mm}$.	133
D.50 $\sqrt{\overline{u'u'}}$, $y = 14.25\text{mm}$.	133
D.51 $\sqrt{\overline{u'u'}}$, $y = 26.25\text{mm}$.	133
D.52 $\sqrt{\overline{u'u'}}$, $y = 39.75\text{mm}$.	133
D.53 $\sqrt{\overline{u'u'}}$, $y = 51.75\text{mm}$.	133

D.54 $\sqrt{u'u'}$, $y = 63.75\text{mm}$.	133
D.55 $\sqrt{v'v'}$, $x = 2.75\text{mm}$.	134
D.56 $\sqrt{v'v'}$, $x = 14.75\text{mm}$.	134
D.57 $\sqrt{v'v'}$, $x = 26.75\text{mm}$.	134
D.58 $\sqrt{v'v'}$, $x = 40.25\text{mm}$.	134
D.59 $\sqrt{v'v'}$, $x = 52.25\text{mm}$.	134
D.60 $\sqrt{v'v'}$, $x = 64.25\text{mm}$.	134
D.61 $\overline{u'w'}$, $y = 2.25\text{mm}$.	135
D.62 $\overline{u'w'}$, $y = 14.25\text{mm}$.	135
D.63 $\overline{u'w'}$, $y = 26.25\text{mm}$.	135
D.64 $\overline{u'w'}$, $y = 39.75\text{mm}$.	135
D.65 $\overline{u'w'}$, $y = 51.75\text{mm}$.	135
D.66 $\overline{u'w'}$, $y = 63.75\text{mm}$.	135
D.67 $\overline{v'w'}$, $x = 2.75\text{mm}$.	136
D.68 $\overline{v'w'}$, $x = 14.75\text{mm}$.	136
D.69 $\overline{v'w'}$, $x = 26.75\text{mm}$.	136
D.70 $\overline{v'w'}$, $x = 40.25\text{mm}$.	136
D.71 $\overline{v'w'}$, $x = 52.25\text{mm}$.	136
D.72 $\overline{v'w'}$, $x = 64.25\text{mm}$.	136
D.73 \overline{Eval} , $y = 2.25\text{mm}$.	137
D.74 \overline{Eval} , $y = 14.25\text{mm}$.	137
D.75 \overline{Eval} , $y = 26.25\text{mm}$.	137
D.76 \overline{Eval} , $y = 39.75\text{mm}$.	137
D.77 \overline{Eval} , $y = 51.75\text{mm}$.	137
D.78 \overline{Eval} , $y = 63.75\text{mm}$.	137

D.79 \overline{Eval} , $x = 2.75\text{mm}$	138
D.80 \overline{Eval} , $x = 14.75\text{mm}$	138
D.81 \overline{Eval} , $x = 26.75\text{mm}$	138
D.82 \overline{Eval} , $x = 40.25\text{mm}$	138
D.83 \overline{Eval} , $x = 52.25\text{mm}$	138
D.84 \overline{Eval} , $x = 64.25\text{mm}$	138

LIST OF TABLES

TABLE	Page
2.1 Requirements and Specifications for the MIR, isothermal flow loop.	10
3.1 Summary of fluids and potential rod materials at 22.2°C.	12
3.2 Experimental fluid flow conditions.	22
4.1 Relative uncertainty values.....	37
4.2 Set sizes for residual convergence calculation.	37
4.3 Vector positioning uncertainty values.	42
C.1 Magnification factor calculations for measurements of u and w_1 . Depth of planes, y , indicates nominal center position of the 1.5 mm thick sheet.	122
C.2 Magnification factor calculations for measurements of v and w_2 . Depth of planes, x , indicates nominal center position of the 1.5 mm thick sheet.	123
D.1 Plane positions for select full subchannel planes.	124

1. INTRODUCTION

Nuclear reactors are commonly used in commercial electrical power generation stations. One of the most prevalent electricity generating nuclear reactors is the pressurized water reactor (PWR). Within a PWR core, fission is used to generate heat in fuel rods, which is transferred to high pressure water in the primary coolant loop. This high pressure coolant is then used as the heat source in a steam generator to boil water in the secondary loop, which is used to spin a turbine connected to an electric generator. Spacer grids, like the one shown in Figure 1.1, are an important part of fuel rod assemblies in PWRs. They improve mechanical strength, reduce vibration, and ensure rod pitch length (p) spacing. Mixing vanes, which can be clearly seen extending from the top of a grid in Figure 1.1, are added to the downstream end of spacer grids in order to increase turbulent mixing within subchannels. This mixing improves thermal hydraulic performance of fuel rod assemblies and increases the convective heat transfer to the primary coolant. For these reasons, spacers grids with mixing vanes have been studied extensively using numerical, mostly computational fluid dynamics (CFD), and experimental methodologies [7, 9, 1, 10, 11, 12, 13].

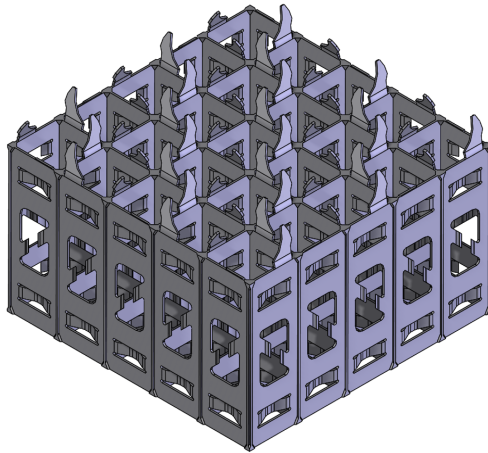


Figure 1.1: Computer rendering of 5×5 spacer grid.

1.1 Motivation, Verification, and Validation

With the fast increase of computational power over the past decade, CFD studies have shifted to more advanced models of turbulent flow characteristics such as large-eddy simulation (LES) and even direct numerical simulation (DNS), that has led to the possibility of in-depth understanding of small scale localized phenomena [14].

These highly spatially resolved numerical data sets need to go through a process of verification and validation (V&V) [15] to be confidently used in a decision making process. For the validation process, equally resolved experimental data that provide high level of information is required [16, 17]. A well quantified and low relative uncertainty is also crucial for proper interpretation of V&V results, as it might hinder the ability to assess the quality of the selected model [18]. Proper information on spatial position of the measurements and its uncertainty is also crucial as this is a problematic aspect in comparisons of numerical and experimental data sets [17].

One of the leading experimental techniques for obtaining detailed measurement of the flow field with theoretically low uncertainty in rod bundles is the use of non invasive PIV in a MIR flow loop [1, 3, 19, 20, 21]. These laser-based techniques present some notable advantages over previously used experimental methods for velocity measurement such as hot-wire anemometry. Specifically, changes to geometry and disturbances to flow characteristics can be avoided, so long as suitable seeding particles are used.

1.2 Theory and Governing Equations

For notational convenience purposes in this dissertation, Cartesian coordinates (x, y, z) are written as x_i , and the velocity vector (u, v, w) is rewritten as u_i .

For homogeneous incompressible flows where fluid density (ρ) is constant, the mass conservation equation is used to describe the flow of a fluid element in x_i space. Often called the continuity equation [22], it can be written as

$$\frac{\partial u_i}{\partial x_i} = 0. \tag{1.1}$$

Assuming no external forces, the Navier-Stokes (NS) equation for all x_i , which describes the conservation of momentum, are given as

$$\frac{\partial u_i}{\partial t} + u_j \frac{\partial u_i}{\partial x_j} = -\frac{\partial P}{\partial x_i} + \nu \frac{\partial^2 u_i}{\partial x_j^2}, \quad (1.2)$$

where ρ and fluid viscosity (μ) are combined as μ/ρ which is kinematic viscosity (ν). Absolute fluid pressure is similarly combined with ρ as kinematic pressure (P). Equations 1.1 and 1.2 define a closed problem with four unknowns: u, v, w , and P .

In increasingly turbulent systems, the fluctuating component of velocity increases, increasing computational demand. To simplify the problem, the spatial velocity vector, u_i , is split into its mean component and temporal fluctuation, which is called Reynolds decomposition, given by

$$u_i(x_i, t) = \overline{u_i}(x_i) + u'_i(x_i, t). \quad (1.3)$$

Where $\overline{u_i}(x_i)$ is the average of each velocity component over a sufficient time period to ensure statistically stationary flow as

$$\overline{u_i}(x_i) = \lim_{T \rightarrow \infty} \frac{1}{T} \int_{t_0}^{t_0+T} u_i(x_i, t) dt. \quad (1.4)$$

One important property of this averaging is that the mean of the fluctuating quantity is equal to zero ($\overline{u'_i} = 0$). Applying this time averaging to the continuity equation (1.1), results in

$$\frac{\partial \overline{u_i}}{\partial x_i} = 0, \quad (1.5)$$

and applied to the NS equation (1.2) gives

$$\overline{u_j} \frac{\partial \overline{u_i}}{\partial x_j} + \frac{\partial \overline{u'_i u'_j}}{\partial x_j} = -\frac{\partial \overline{P}}{\partial x_i} + \nu \frac{\partial^2 \overline{u_i}}{\partial x_j^2}, \quad (1.6)$$

in which the time derivative has been averaged to zero and a new variable has been introduced

which must either be calculated, or modeled. This term, $\overline{u'_i u'_j}$, is the Reynolds stress and is highly dependent on the type of flow being characterized. This additional term presents an issue in closing the system of equations defined by Equations 1.5 and 1.6. There are 6 additional variables to be determined, and each individually fluctuating component cannot be simply calculated. To mitigate this, closure models are often implemented, in which each individual component of $\overline{u'_i u'_j}$ is determined algebraically or empirically. Further description of Reynolds-averaged Navier-Stokes (RANS) closure models is beyond the scope of this dissertation, and the reader is directed to works such as Pope [22] for further information.

Due to properties of the Reynolds average, the fluctuating component cannot simply be measured repeatedly and averaged, as would be done for the mean velocity components. This requires the RMS of the velocity component to be used in it's stead, which is defined as

$$u_{i,\text{RMS}} = \sqrt{\frac{1}{N} \sum_{n=1}^N (u_{i,n} - \bar{u}_i)^2}. \quad (1.7)$$

This amounts to the standard deviation of the velocity measurements, and provides a meaningful measure of the fluctuating component, as well as velocity error.

Lastly, for eddy scale analysis which can aid in ultra-high-resolution CFD filter size quantification, vorticity of the velocity field should be quantified. This pseudovector quantity describes local spinning motion of fluid via the following relationship:

$$\omega_i = \nabla \times u_i = \left(\frac{\partial}{\partial x}, \quad \frac{\partial}{\partial y}, \quad \frac{\partial}{\partial z} \right) \times (u, \quad v, \quad w) \quad (1.8)$$

$$= \left(\frac{\partial w}{\partial y} - \frac{\partial v}{\partial z}, \quad \frac{\partial u}{\partial z} - \frac{\partial w}{\partial x}, \quad \frac{\partial v}{\partial x} - \frac{\partial u}{\partial y} \right). \quad (1.9)$$

Because this quantity is not explicitly transported in current CFD, an evolution equation for ω_i is not required. This pseudovector does not represent a physical quantity which can be directly measured, but provides a convenient and elegant manner for displaying results. Further reading can again be found in Pope [22], as well as Majda & Bertozzi [23].

1.3 Previous Work & Literature Review

As stated, a number of previous studies on prototypical PWR mixing vane spacer grids have been conducted. At the Thermal-Hydraulics Laboratory of the Nuclear Engineering Department at TAMU, a 5×5 rod bundle was previously constructed using FEP tubes filled with water. A study of 2D2C PIV was conducted by Dominguez and Hassan [1] with good results which are summarized in Figure 1.2. This experiment demonstrated the usefulness of 2D2C measurements in an axial orientation for forced flow in the presented geometry.

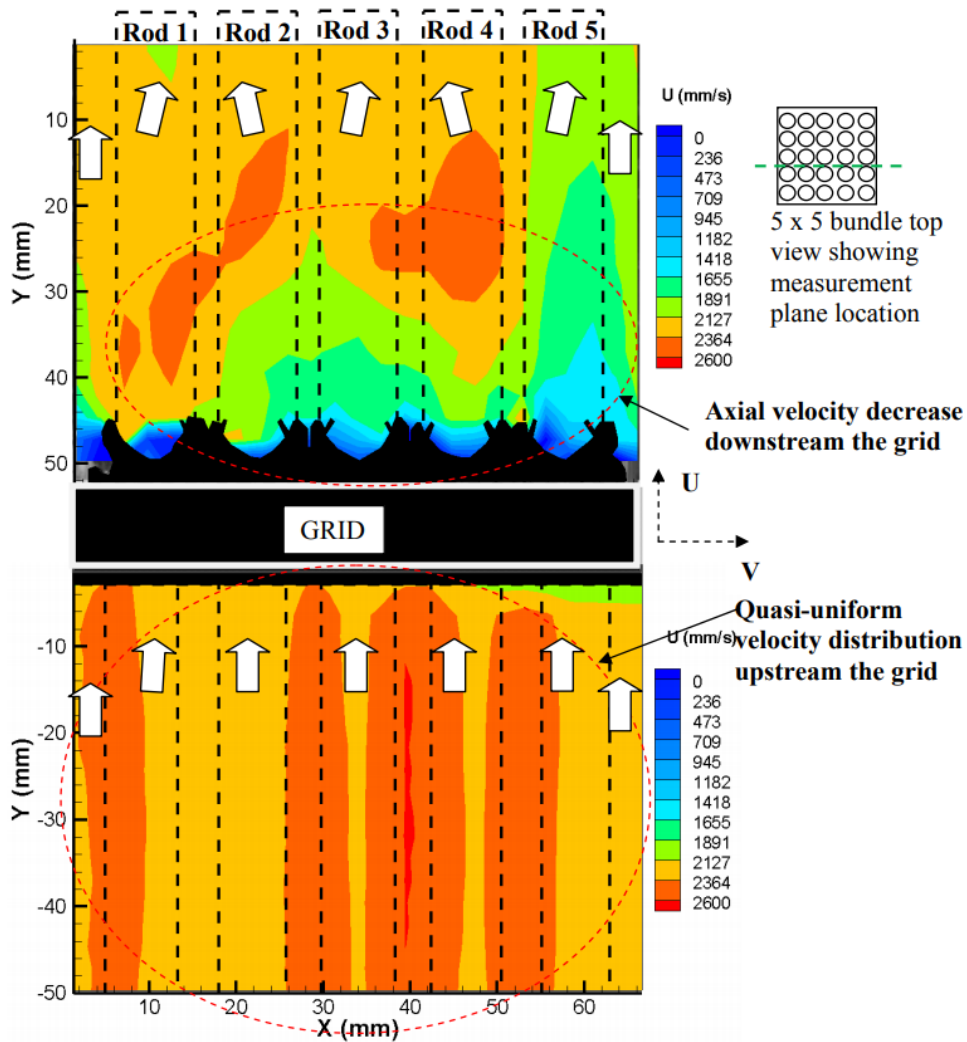


Figure 1.2: 2D2C PIV results for an FEP MIR constructed 5×5 rod bundle performed at TAMU [1, 2]. Reprinted with permission from Conner et al [2].

A two-dimension three-component (2D3C) study was later conducted within the same test section at TAMU [3, 4] as is shown in Figure 1.3. Quantitative analysis of this data was extensive, however images and data close to the mixing vane were difficult to collect, due to construction and materials limitations presented by the mock fuel bundle. As well, use of FEP tubes presented an unnecessary contributor to uncertainty, as the rod geometry was relatively soft and experienced a tendency to move with flow induced vibrations. Image collection through multiple layers of rods was also difficult to achieve, as light transmission through the rod walls was relatively low when compared to the working fluid.

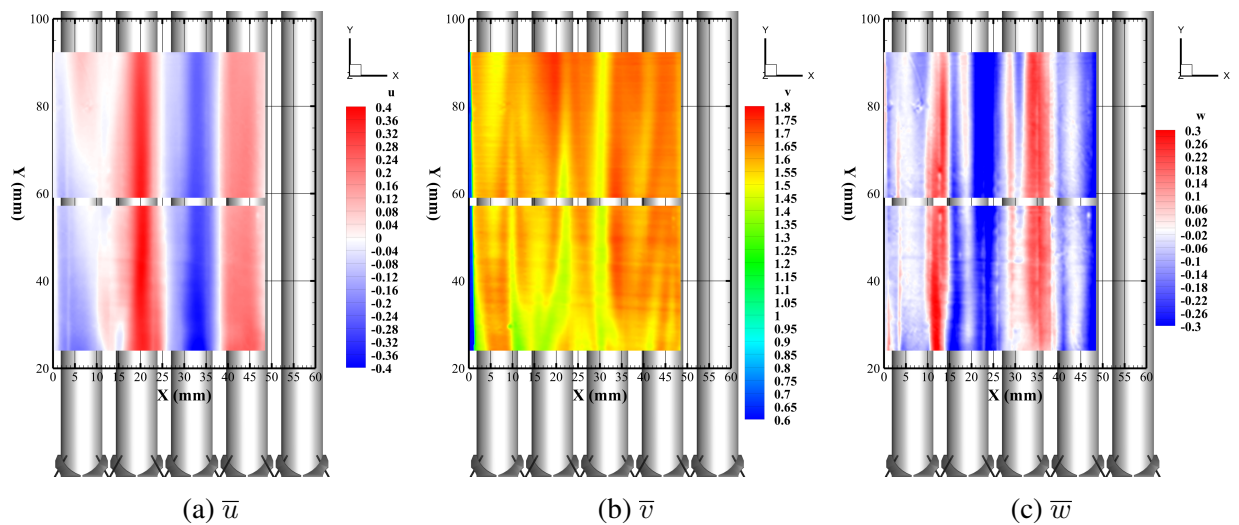


Figure 1.3: Mean velocity component results using SPIV for an FEP MIR constructed 5×5 rod bundle performed at TAMU [3, 4]. Reprinted from Childs et al [4].

In order to make measurements on prototypical PWR rod bundles, a number of PIV studies was performed by Holloway, McClusky, and others within the Department of Mechanical Engineering at Clemson University [5, 6, 10]. This rod bundle was constructed without the use of MIR materials. This was a novel measurement which made use of photon interactions properties in the fact that refracted light was kept in plane by only making measurements with axial-slicing planes. A velocity field from one of these measurements is portrayed in Figure 1.4.

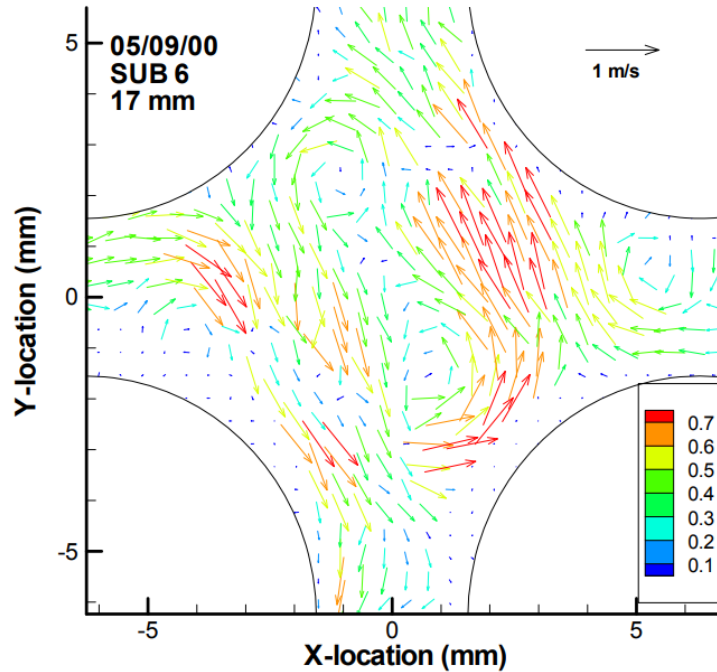


Figure 1.4: Transverse velocity results from PIV studies on prototypical rod bundles using axial cross section laser planes [5, 6]. Reprinted with permission from Conner et al [2].

The PIV measurements made at Clemson were limited to single subchannels due to use of a borescope. This required numerous measurements to be taken in order to quantify flow throughout the full geometry. As such, measurements were made out to maximum of $4.2D_H$ downstream of the mixing vane. These measurements were used largely for calculations in heat transfer alterations, and were not specifically for velocity quantification. As such, they were effective for their purpose, but were not the highest resolution data which has been presented in a 5×5 rod geometry.

One of the current highest resolution datasets which exists for a 5×5 rod bundle is included in the benchmark test for CFD [8]. This data, which is shown in part in Figure 1.5, was collected using laser Doppler velocimetry (LDV) on a $2.6 \times$ scaled rod geometry.

Due to the measurement type selected, velocity vectors were collected at a minimum of $1.0D_H$ from tips of mixing vanes. This presents a volume of data within the ROI of the mixing vane's effects, which was yet not studied. As well, the $2.6 \times$ scaling of the geometry permitted for fairly large subchannels which may not represent relative scales for vorticity and turbulent structures that

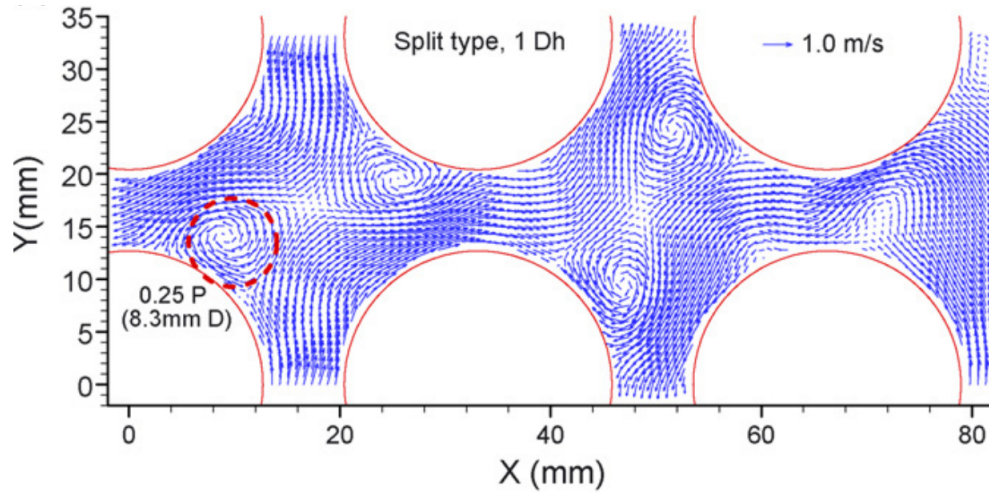


Figure 1.5: KAERI benchmark - high fidelity data within $2.6\times$ oversized subchannels [7, 8]. Reprinted with permission from Chang et al [7].

exist in a prototypical PWR. geometry.

In order to study this near-vane region in a prototypical geometry, a new rod bundle and flow loop construction was proposed for the use of a new MIR combination. This new construction, which has been extensively studied and is partly described in this dissertation, permits high resolution, and high fidelity data near and even within the mixing vane region. An improved MIR combination and relatively high test section optical clarity may permit recognized planar 2D2C and 2D3C measurements in any x -, y -, or z -normal direction. A detailed uncertainty quantification of each planar measurement may reveal areas for improvement of the measurement in the particular geometry. It has been proposed that a number of measurement planes also presents a method for combining multiple PIV planes in order to generate a three-dimension three-component (3D3C) full field velocity measurement.

2. PROJECT SCOPE

Research project requirements and specifications were outlined based on previous works' literature review. Test specifications were constrained by a turbulent flow condition regime, and full field velocity measurements. Objectives are provided in the following section, along with their associated requirements, and specifications.

2.1 Objectives

Primary objectives of the research described in this dissertation were three fold:

1. Determine a new MIR combination for PIV measurements to improve on limitations of current state-of-the-art materials.
2. Design, procure, and construct a generalized-test section, isothermal experimental flow loop facility making use of the new MIR combination.
3. Collect full field velocity measurements to characterize fluid flow in a experimental 5×5 -mock fuel assembly with prototypical mixing vane spacer grids in a fully turbulent flow regime.

2.2 Requirements & Specifications

Requirements for the project were defined as what the experimental flow loop must do. Specifications were defined as how the requirements would be met. Table 2.1 provides the primary requirements of the experimental facility, which were comparable to previous flow loops as had been constructed at the Thermal-Hydraulics Laboratory of the Nuclear Engineering Department at TAMU.

Table 2.1: Requirements and Specifications for the MIR, isothermal flow loop.

Requirement	Specification
Velocity measurements in edge, corner, and interior subchannels shall be possible in order to facilitate a full field reconstruction.	Edge, corner, and interior subchannel measurements will be made possible via MIR materials selection and a fully transparent, minimum intrusion test section.
The Reynolds number shall constitute a fully turbulent flow regime.	The selection of full-port valves, large piping and hosing, low fluid viscosity, and appropriate pump sizing with sufficient net positive suction head (NPSH) will ensure Reynolds number (Re) of at least 14,000 and beyond 30,000.
Fluid flow shall be volumetrically rate measured and controlled.	Flow rate will be driven with a centrifugal pump controlled by a variable frequency drive (VFD), and measured via a high precision flow meter.
The flow loop shall be temperature measured and controlled to ensure isothermal operation.	Temperature will be measured with a digital sensor, and controlled by a secondary water loop scaled to the selected pump.
Flow-induced vibrations shall be minimized in the fuel assembly and support structure.	Rubber isolation pads, flexible hosing, and metal framing will be utilized where appropriate to dampen vibrations in the test section and instrumentation.
The flow loop shall be protected from over-pressurization to prevent test section, or piping failure.	Overpressure protection will be provided via a semi-closed loop construction, which shall always be open to atmospheric pressure.
All temperature, pressure, and flow rate measurements shall be made such repeatability is possible.	A data acquisition system (DAS) will be used to record simultaneous measurements of temperature, pressure, and flow rate.
Sufficient length shall be provided to ensure fully developed flow, and quantify inlet conditions for the ROI in the test section.	A fully transparent channel will be utilized for the test section to ensure measurement capability upstream of the ROI, which is to be no less than prototypical distance for PWR spacer grids.

3. FACILITY DESCRIPTION

Prior to construction of the experimental facility, a detailed design of the visualization test section, as well as the flow loop required to achieve the desired experimental conditions was conducted. The following sections describe the selection process of materials for MIR, as well as construction of the flow loop.

3.1 Matched Index of Refraction Materials

Several MIR facilities have been build over the past years to study rod bundles [3, 20, 24, 25]. Many material combinations of MIR fluids and rods have been studied with each combination exhibiting strengths and weaknesses in different experimental parameters. In order to provide better PIV measurements in a PWR prototypical 5×5 rod bundle, an extensive study of new MIR combinations was conducted and a new pair has been determined to provide better light transmission and closer MIR. Table 3.1 presents a list of common MIR combinations used for rod bundles along with their refractive indexes and known limitations. The last row of the table presents the new combination of materials used in experiments for the presented research dissertation.

The used fluid is the organic solvent D-limonene and for the transparent rods, borosilicate glass. As shown in Table 3.1 the refractive index at the Fraunhofer “D” sodium emission near 589 nm wavelength (n_D) of the materials match to the fourth decimal at ambient temperature. This new combination shares the rigidity of quartz rods without the trade-off of a fluid with high viscosity. In fact, D-limonene has both density (1.18 ratio) and viscosity (1.05 ratio) comparable to water, which makes working with the fluid and obtaining data at considerably high Re simpler. These characteristics make the new material combination one of the most promising for MIR experiments in rod bundles yet. An example of the MIR combination can be seen in Figure 3.1.

The observed MIR as shown in the Figure 3.1 represents a good qualitative example of the use of D-limonene with borosilicate glass. To determine a best working condition for the fluid and rod MIR, a short study of the refractive index (n) of the MIR materials was conducted. From the

Table 3.1: Summary of fluids and potential rod materials at 22.2°C.

Fluid	Rod material	Fluid / Rod (n_D)	Limitations
Water	FEP [3, 24]	1.333 / 1.350 ($\Delta n_D = 0.017$) [26, 27]	FEP tubes are flexible and easily deformed. Relatively low transmission of light.
Mineral oil	Quartz [20]	1.4585 / 1.4584 ($\Delta n_D = 0.0001$) [28, 29]	Oil has a high viscosity compared to water. Quartz is difficult to machine.
<i>p</i> -Cymene	PMMA [25]	1.4908 / 1.4912 ($\Delta n_D = 0.0004$) [30]	PMMA index of refraction changes under stress and heat. Porosity leads to decay of transparency and stress crazing under degradation from <i>p</i> -Cymene.
D-Limonene	Borosilicate glass	1.4726 / 1.4727 ($\Delta n_D = 0.0001$) [31, 32]	Difficult to machine glass.



Figure 3.1: Borosilicate glass tube submerged in a non-mixed combination of D-limonene and water. Lack of light ray refraction can be observed via the horizontal lines on the glass container, which are partially behind the submerged tube.

National Institute of Standards and Technology (NIST), a functional form of the refractive index of the working fluid, D-limonene, as a function of T and transmitted λ was determined. The resulting values for n are shown in Figure 3.2. The frequently cited measurement for n_D , is highlighted.

A difference of n can be seen from this wavelength and that of the laser used in experimentation, which is highlighted by the green line at 532 nm.

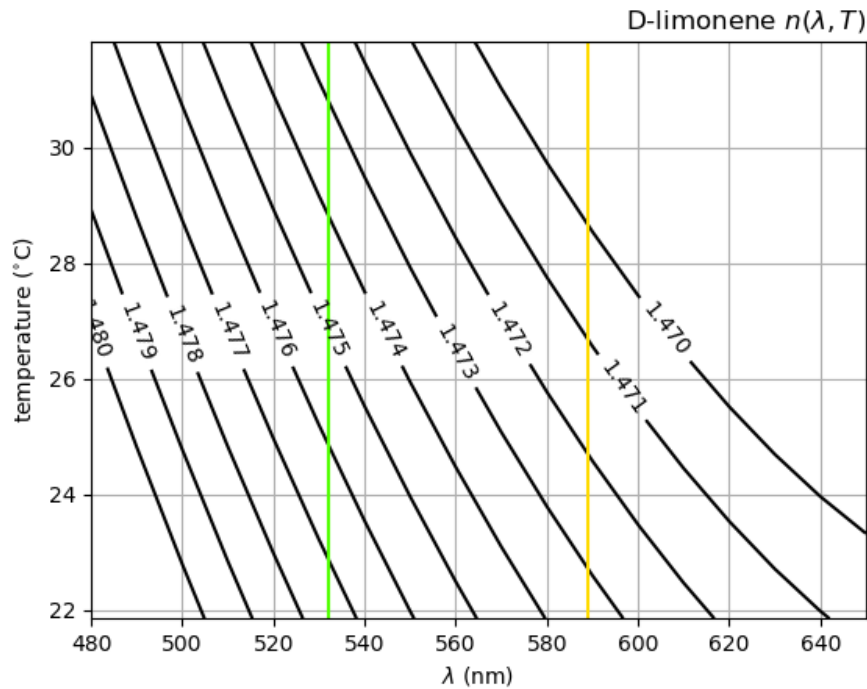


Figure 3.2: Refractive index of D-limonene as a function of transmitted light λ and fluid T .

Using data from Corning Inc., the approximate refractive index for borosilicate glass was calculated over the same combined domain of transmitted light wavelength and temperature (λ, T). Resultant values for refractive index as shown in Figure 3.3. Due to the nature of borosilicate glass, the refractive index is much less sensitive to temperature than it is to photon λ . The 532 nm wavelength of the laser used in experimentation is once again highlighted.

Differences in n of the two materials was then calculated over the $T\lambda$ domain. Resulting differences is shown in Figure 3.4. To maintain a minimum difference of refractive index, the fluid working temperature was determined to be somewhere in the range of 22–26°C. Unfortunately, the data for borosilicate glass refractive index is fairly sparse, and exact content-formulas of glass con-

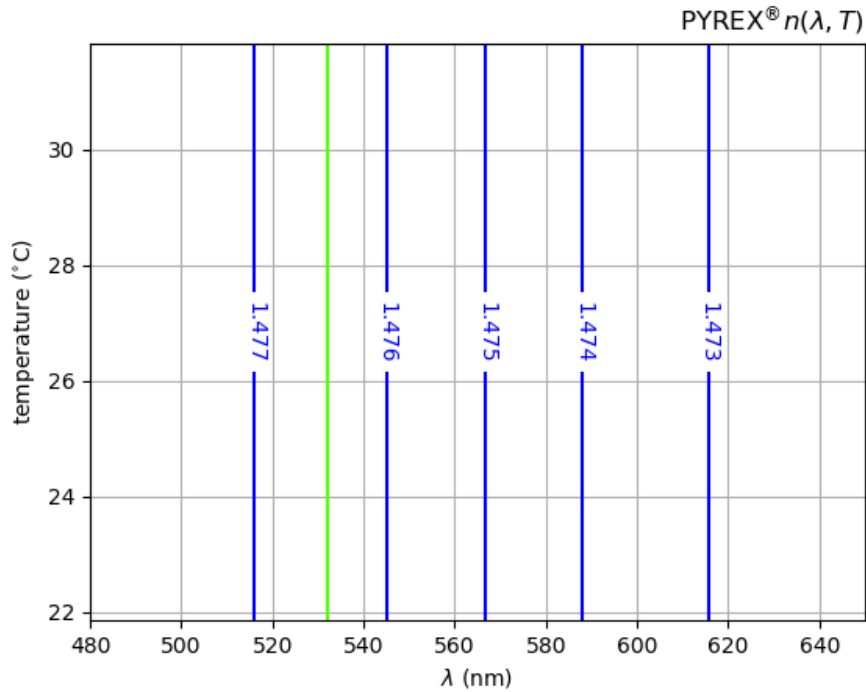


Figure 3.3: Refractive index of borosilicate glass as a function of transmitted light λ and medium T .

stituent materials is not well published, so this range was only an estimate, and exact temperatures had to be determined qualitatively during experimentation.

3.2 Fluid Considerations

Due to the use of the new fluid for MIR studies, a number of compatibility tests were required to ensure wetted materials' longevity and functionality while immersed in D-limonene. These test were similar in nature, although significantly less extensive, to a number of chemical consideration tests which were made during the study of PMMA-constructed wire-wrapped rod bundles immersed in *p*-cymene, which was also conducted at the Thermal-Hydraulics Laboratory of the Nuclear Engineering Department at TAMU [33]. As was observed during the procurement of test quantities of D-limonene, plastic is commonly used for packaging. Plastics, however, experience adverse reactions when exposed to D-limonene for extended periods of time. Occasionally, D-limonene may permeate the walls of plastic packaging bottles and cause labeling to fall off, as it is

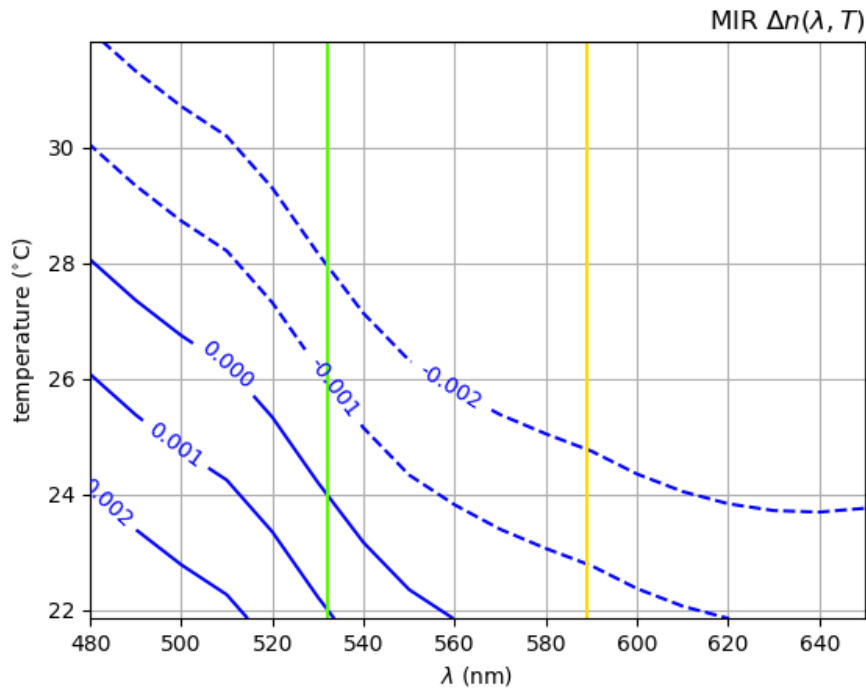


Figure 3.4: Difference of refractive indexes of borosilicate glass and D-limonene as a function of transmitted light λ and medium T .

an effective solvent for most adhesive compounds.

To determine suitability of experimental facility materials, chemical compatibility of D-limonene was performed with borosilicate glass and glued polycarbonate in order to examine the behavior of test section materials (Section 3.3) in the presence of the simulant fluid. Chemical immersion testing was also performed with polyvinyl chloride (PVC), as well as buna-N, which were the selected materials for the flow loop construction (Section 3.5).

Affects of D-limonene to the surfaces of borosilicate glass were observed to be negligible. No change to the matching of refractive index of the fluid and borosilicate glass tubes was quantifiable, even after multiple days of immersion. Similar results were observed with small sections of glued polycarbonate sheets. As well, the methyl acrylate adhesive for the polycarbonate test pieces appeared to maintain strength if the suggested curing time was observed. As such, the test section materials were determined to be sufficiently compatible with the simulant fluid.

PVC and buna-N, which were selected for loop construction and joint sealing, respectively, are listed as “fair” in the context of chemical compatibility with D-limonene. With this in mind, the materials were immersed in D-limonene for a number of days to determine their resistance to chemical degradation. After the test, no difference was observed from the samples, and the materials were deemed sufficiently compatible for use in construction of the flow loop.

Unfortunately, many of the PVC valves and tank fittings which were used in the construction of the loop were improperly determined to have buna-N seals, and were instead fitted with ethylene propylene diene terpolymer (EPDM). This material was not tested for chemical compatibility, and is *not* recommended for use in D-limonene applications. As such, a large volume of D-limonene was lost due to the failure of a tank fitting seal after being immersed in the fluid for a number of days following filling of the flow loop.

After completion of the facility operation which provided the data for the presented investigation, a redesign of the flow loop was completed using only stainless steel (SS) piping with viton and nylon seals. These materials are all well documented as compatible with D-limonene, as well as other organic solvents. Retrofitting of the experimental facility has led to a marked improvement in the operation of the flow loop and collection of data from the test section. Further analysis of the improved test loop is beyond the scope of this study, however, and is expected to be described in later work.

3.3 Visualization Test Section

To assemble a rod bundle as similar as possible to a PWR fuel rod geometry, borosilicate glass tubes were used to construct a 5×5 rod bundle. Glass tubes with outer diameter (OD) equal to 9.59 mm were selected. These tubes were the closest to a PWR fuel rod OD which were readily commercially available. Each tube was filled with D-limonene and capped at both ends. To quantify the uncertainty of the OD, each tube was individually measured along its length and displayed a total expanded uncertainty of ± 0.11 mm. Expanded uncertainty of the OD included tolerances from the tube manufacturer and the standard deviation of OD measurements. The bundle was constructed with three prototypical spacer grids which exhibit dimensions similar to a PWR 17×17 fuel bundle. The grids were positioned 51.0 cm apart as is typical for a PWR. Figure 3.5 shows the mock fuel rod bundle during construction prior to installment in a transparent test section. The center spacer grid was selected as the ROI to ensure a fully developed flow profile, as might be seen in an average selection of 5×5 rods in a PWR.

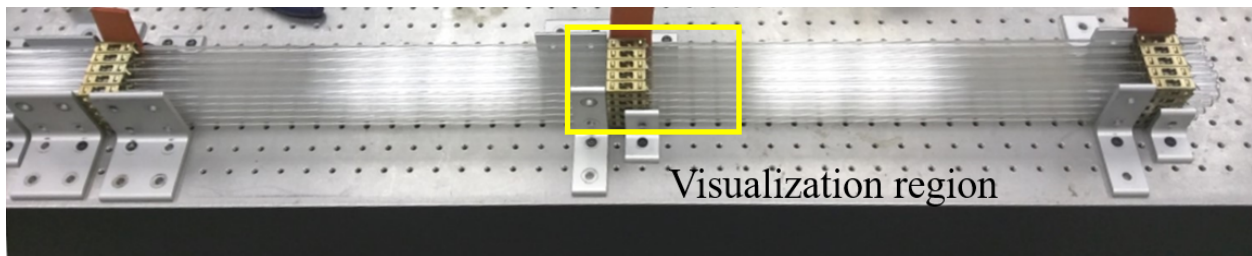


Figure 3.5: Photo of glass tube rod bundle construction prior to insertion in test section. The ROI is highlighted.

The visualization region consisted of a high quality square cross section polycarbonate channel with dimensions of $66.5 \times 66.5 \times 1524$ mm ($\pm 0.3 \times 0.3 \times 5$ mm). The test section used in the presented experiments is shown in Figure 3.6. Drawings of the test section are contained in Appendix A.

The bundle was positioned in the test section by pressing the grids against two of the walls

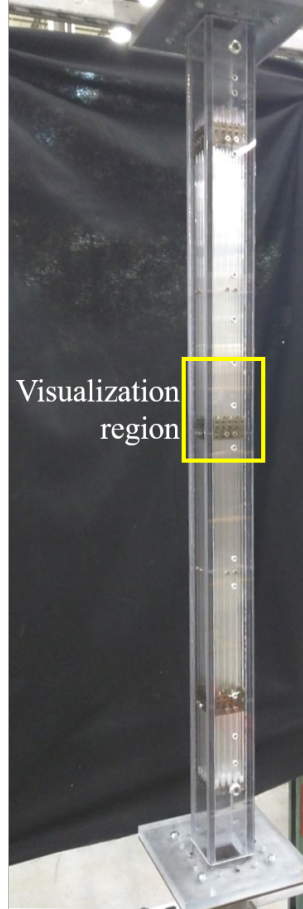
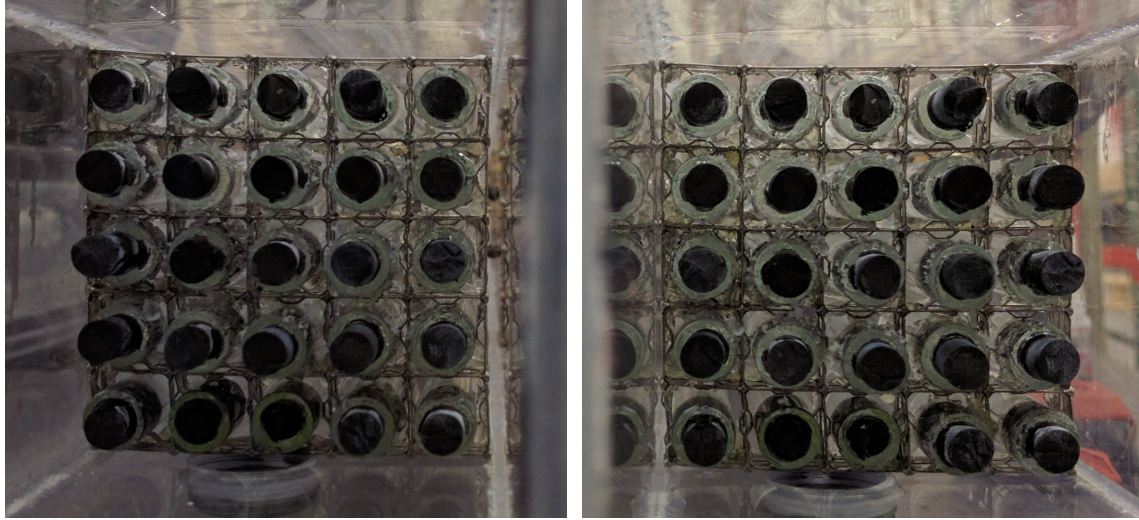


Figure 3.6: Photo of test section installed in the facility before D-limonene filling. The ROI is highlighted.

using set screws on the test section wall at specific heights which can be seen in Figure 3.7. By positioning the grids in one corner, relative angle between the test section wall and spacer grid was eliminated. Flow induced movement of the grid relative to the test section wall was also greatly reduced. This allowed for observation of the impact on bulk flow of a non-symmetric gap between the bundle and test section walls.

For quantitative analysis, some length measurements within the presented dissertation have been normalized with hydraulic diameter (D_H). This is calculated as in Equation 3.1, and is equal to 10.27 mm for the presented test section.

$$D_H = \frac{4A}{P_w}, \quad (3.1)$$



(a) Far wall

(b) Close wall

Figure 3.7: Positioning of glass tube bundle in the polycarbonate test section. Set screws were used from two adjacent walls (3.7a) to fix the spacer grids in a corner edge of against two walls (3.7b).

Equation 3.1 makes use of the cross sectional flow area (A) inside the $66.5 \text{ mm} \times 66.5 \text{ mm}$ square test section and between the 25 rods of diameter 9.59 mm , approximately 26.3 cm^2 , and wetted perimeter (P_w) of the test section and rods, approximately 1.02 m .

3.4 Plena

Inlet and outlet plena for the visualization test section, shown in Figure 3.8, were fabricated from SS plate. A $66.8 \times 66.8 \text{ mm}$ square cross section channel was welded to a square flange with holes that matched the pattern on the test section's connection flanges. The other end of the square channel was welded to a sealed mixing box with dimensions $241 \times 241 \times 102 \text{ mm}$. Two opposite walls of the mixing box were fitted with a 2" national pipe thread (NPT) through hole. The lower plenum, shown in Figure 3.8a, was also fit with a 1" NPT through hole in the bottom for instrumentation and draining, however was not used for the purposes of this study.

The upper plenum was fit with a removable top plate as can be seen in Figure 3.8b. This permits for the use of a transparent top plate for later PIV measurements to be performed from the top of the test section, however is beyond the scope of this investigation. Detailed drawings used

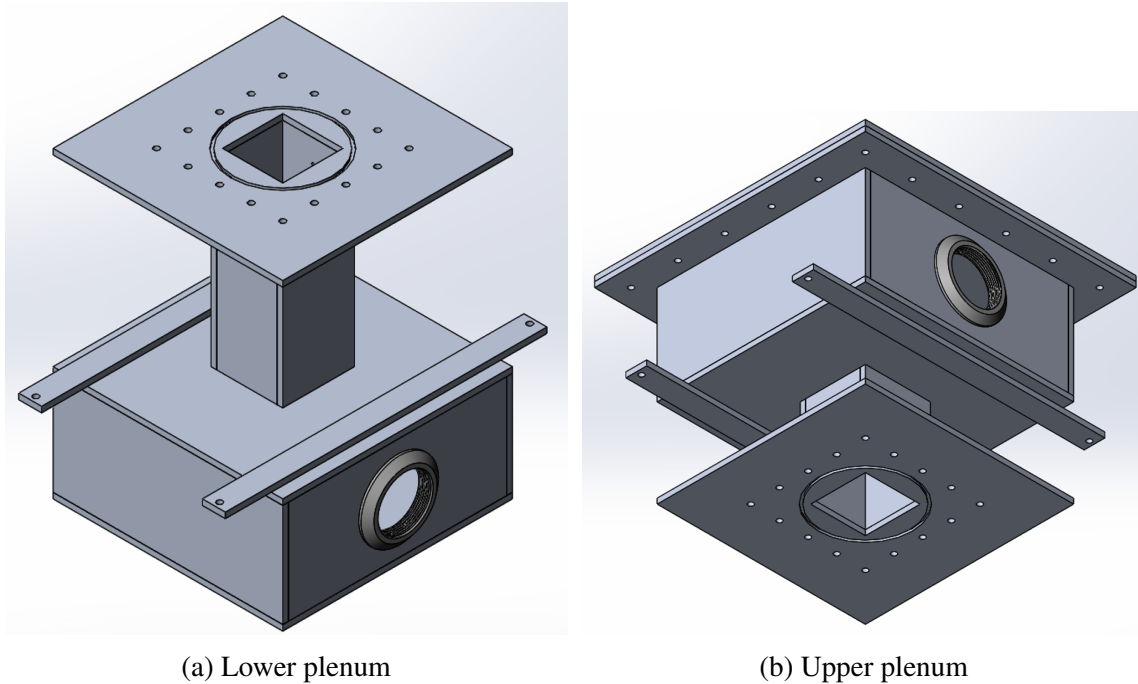


Figure 3.8: Plena used for connection of experimental test section with flow loop.

for fabrication of the plena are contained in Appendix B.

3.5 Flow Loop and Instrumentation

A sketch of the facility's layout is presented in Figure 3.9. The facility was designed to isolate the test section from the vibration induced by the flow and the pump of the main circuit while allowing flexibility to adapt different test sections. Dimensions of the test section region can be easily varied, allowing flexibility and re-usability of the flow loop with different MIR test sections.

The 15 Hp pump is capable of flow rates greater than 20 l/s, which allows experiments to be performed at high Re . The flow rate is controlled using a VFD connected to the pump. A 400 l tank provides the working fluid to the system. A secondary water cooling loop is built into the tank to maintain an isothermal fluid state during operation. This is particularly important for MIR experiments as the refractive index is seen to vary with fluid temperature as described in Section 3.1.

The circuit is instrumented with a high precision Sierra InnovaMass vortex shedding volumet-

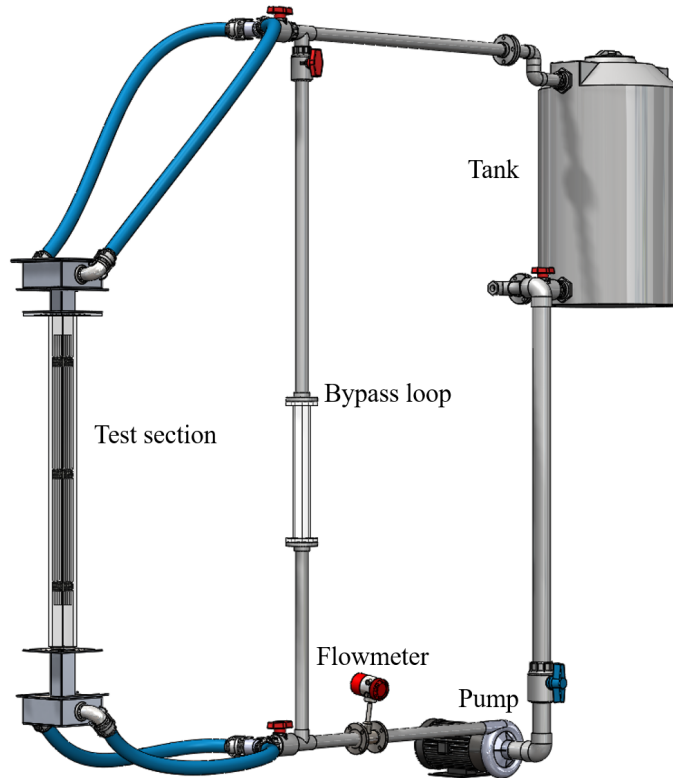


Figure 3.9: Facility flow loop layout sketch.

ric flow rate meter (0.7 % of reading accuracy). This flow meter includes an integrated absolute pressure sensor (± 3.5 kPa accuracy), and temperature measurements ($\pm 1^\circ\text{C}$ accuracy) via a resistance temperature detector (RTD).

3.6 Flow Conditions for $Re=27,390$

The experiments were performed under the flow conditions shown in Table 3.2. Combined uncertainty for temperature, pressure, and flowrate was calculated using the above referenced accuracy for the loop flow meter, along with the standard deviation of each measurement taken over the course of each experimental run.

Uncertainty for the density of D-limonene was calculated using the Tait equation for liquids, as found from NIST, using the maximum deviation from nominal values of temperature and pressure as input parameters [34]. A similar approach was used for the viscosity of D-limonene using the equation of state for fluid viscosity laid out by Andrade [35, 36], making use again of maximum

deviations from nominal temperature.

Table 3.2: Experimental fluid flow conditions.

Parameter	Value	Uncertainty	Units
Temperature	22.2	2.1	°C
Pressure	195.4	7.3	kPa
Density	841.9	3.6	kg/m ³
Viscosity	907	54	μPa.s
Flow rate	7.51	0.13	l/s
<i>Re</i>	27390	480	-

4. PARTICLE IMAGE VELOCIMETRY METHODOLOGY*

The following chapter details the collecting of images for multiple measurement planes of 2D2C velocity fields. These measurements were collected in a manner to provide all components necessary to reconstruct a full 3D3C velocity field. For each plane, a detailed uncertainty quantification (UQ) was performed and is outlined. A full field uncertainty was also constructed from the multiple planes similar to the 3D3C velocity field.

4.1 Two Dimension Two Component Image Collection

A 2D2C PIV setup was assembled to perform measurements of the velocity field in the 5×5 rod bundle downstream of the middle spacer grid in the test section. A total of 45 velocity fields parallel to the x and z axes were measured across the full test section width. Figure 4.1 shows the PIV setup of the six planes between and outside the five rows of rods used which were used for preliminary analysis, as well as the defined axes origin for both directions of collection. Even though in the picture there are rods and fluid in the test section, due to MIR, they can't be seen.

Figure 4.1 shows the positions of the xz measured planes relative to the rod bundle. Planes J-AA and R-II were each positioned two pitches ($2p$) away from each other at geometrically symmetric positions relative to the spacer grid. These planes were selected for preliminary analysis as they were expected to show symmetrically coherent velocity profiles with small differences attributed to the distance to the walls of the test section.

To determine frame separation time, as well as appropriate particle seeding size for the presented Re , the largest scale eddy turnover time (t_L) defined by Equation 4.1 was calculated to be on the order of 10^{-3} s. Where the diagonal distance between two non-adjacent rods surrounding a sub channel is considered the characteristic length (L), which is 8.23 mm; the spatiotemporal

*Sections 4.1–4.3 are reprinted, in part and with modifications, with permission from A. A. C. dos Santos, M. Childs, T. D. Nguyen, and Y. Hassan, “Convergence study and uncertainty quantification of average and statistical PIV measurements in a matched refractive index 5×5 rod bundle with mixing vane spacer grid,” *Experimental Thermal and Fluid Science*, vol. 102, pp. 215–231, 2019.

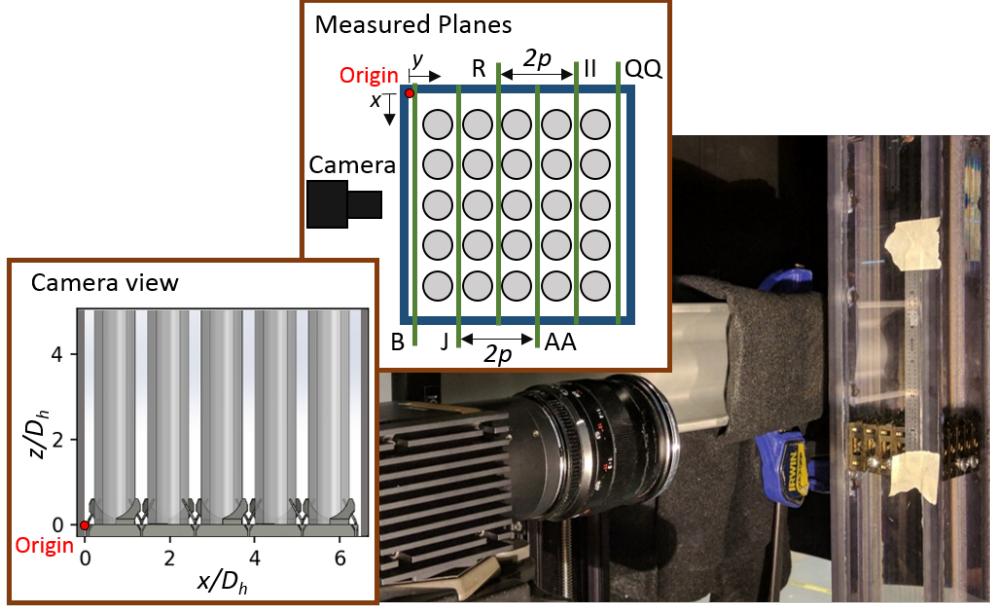


Figure 4.1: Image of the PIV setup.

average axial bulk velocity, $\langle \bar{w} \rangle$, is the characteristic velocity.

$$t_L = \frac{L}{\langle \bar{w} \rangle} \quad (4.1)$$

The fluid was seeded by silver-coated hollow glass spheres with a mean diameter, d_p , of $13 \mu\text{m}$ and density, ρ_p , of 1.6 g/cc . These particle parameters were used to calculate the response time of a particle in fluid flow (t_p) defined by Equation 4.2 [38], which was on the order of 10^{-5} s .

$$t_p = \frac{d_p^2 \rho_p}{18\mu} \quad (4.2)$$

The Stokes number, defined as the ratio of the time of a particle to the characteristic time of the flow, was determined to be much less than one, ensuring the tracer particles follow the flow closely [39].

A pass-through time of 0.019 s , defined as the mean time taken for all the particles present in a image to move out of the field of view (FOV), was calculated. As such, a 0.1 s time delay between

image pairs was sufficiently large to ensure statistical independence of the subsequent image pairs. An intra-pair time delay of $100 \mu\text{s}$ was small enough to ensure a maximum particle displacement of 14.98 pixels. These characteristics allow for good statistical convergence of PIV since each pair is significantly spaced in time relative to the flow, however limiting the ability to capture time resolved flows.

To illuminate the tracer particles, a 532 nm 200 mJ double head pulse laser was used to generate two 1.5 mm ($0.146D_H$) thick sheets of light $100 \mu\text{s}$ apart every 0.1 s. A double exposure IMPERX Bobcat 2.0 four megapixel charge-coupled device (CCD) camera with 50 mm focal length, f , lens with $f/2$ aperture was used to capture the flow field in the entire width of the test section from $0-5D_H$ downstream of the spacer grid. The camera was synchronized to the laser using a signal board connected to a DAS so that image pairs of the flow field were obtained at the correct moment with Δt between laser pulses. The captured images had 2352×1768 pixels of resolution and 12 bit of depth. The double exposure camera allows two high resolution images to be captured in quick succession. At each measurement plane a total of 2000 image pairs were collected over the course of 200 s. This number was determined sufficient to perform a convergence analysis while still keeping the total number of images low enough for timely analysis.

The camera was mounted to a computer-controlled traverse system, as was the laser optics that project the light sheets. The BiSlide[®] traverse system enabled a movement step of $63.67 \mu\text{m}$ ($0.0062D_H$) with high precision of both the camera (y_{cam}) and laser sheet (y_{lsr}). The laser plane was swept through the entire depth of the test section as shown in Figure 4.2. Focus of a single laser sheet was achieved using the lens adjustments, after which the camera and lens settings were maintained and the camera only moved by the traverse system. To maintain focus on the plane at different laser sheet positions the camera was moved a distance proportional to laser step by a factor of the inverse of the refractive index of D-limonene based on the Snell's law as shown in Equation 4.3.

$$\frac{\Delta y_{\text{lsr}}}{\Delta y_{\text{cam}}} = \frac{n_{\text{air}}}{n_{\text{lim}}}. \quad (4.3)$$

This technique allowed all planes measured with the same camera setup and field of view. This

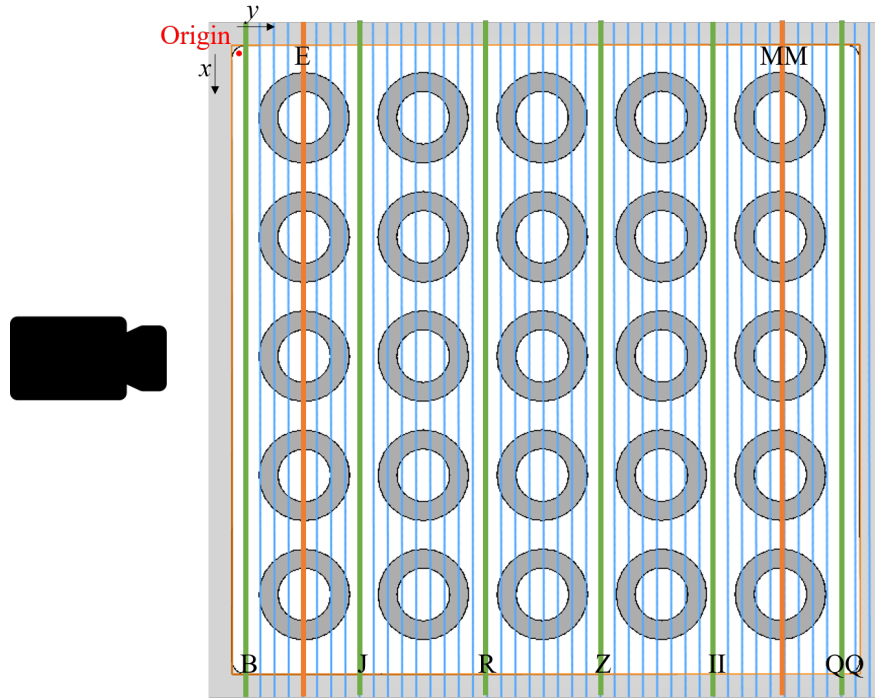


Figure 4.2: Laser plane alignment and camera orientation for first test, consisting of measurements of u and w . The origin corner is highlighted in red.

can be demonstrated in Figure 4.3 that shows planes taken at the center of the rods of the first and fifth row of rods from the camera. In the figure both rods and spacer grid in view are highlighted to demonstrate the effectiveness of the traversing method.

The camera was aligned with the face of the test section and the laser sheets were aligned by visual assessments against physical references and using images obtained by the camera. For example, the diameter of the rods was measured in the image as the laser plane was rotated slightly about an x -parallel axis until the relative difference in measurable diameter from top to bottom of the image was less than the physical tolerance of the rod diameter from caliper measurements. This correlated to a rod diameter measurement of 339 ± 3 pixels. Angular alignment was also evaluated in the image assessing rod rotation and possible pitch and yaw of the plane. This was performed evaluating the dimensions of rods from the images taken at their center at the bottom to top and left to right. The results were a rotation angle no greater than $-0.28 \pm 0.27^\circ$, pitch of $\pm 0.12^\circ$ and yaw $\pm 0.16^\circ$ considering clockwise (CW) positive rotation relative to the images collected. The small

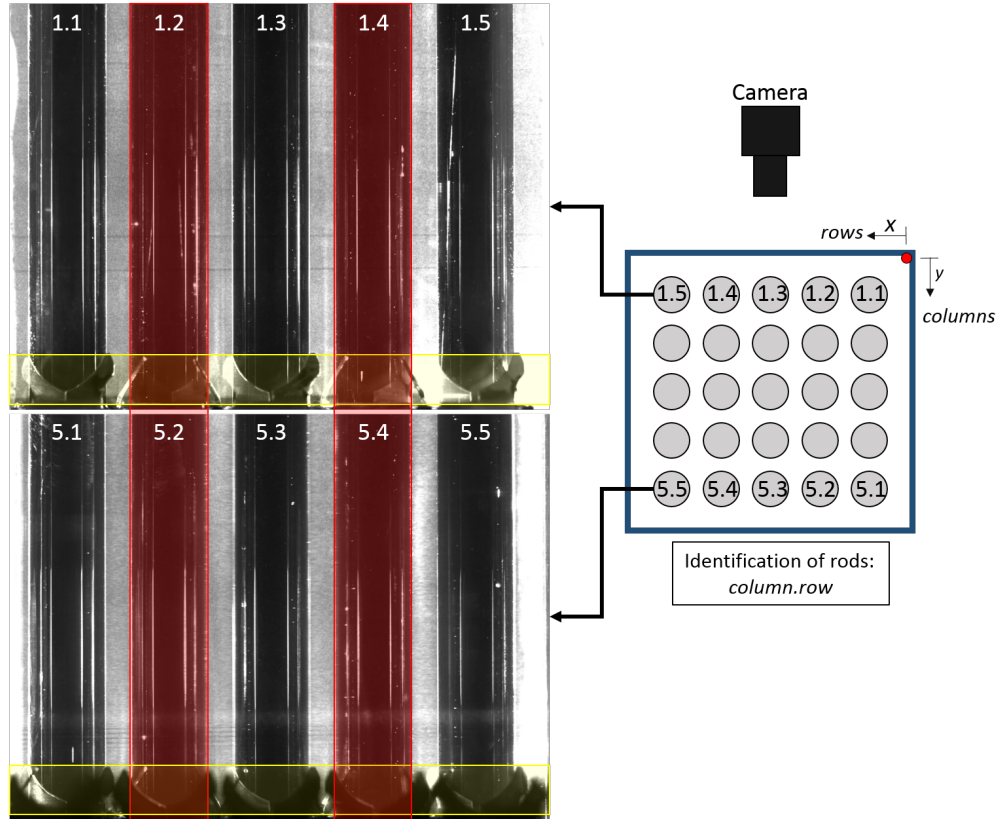


Figure 4.3: Image focus and alignment relative to the rods and grid at the first and fifth rod row. Camera positioning for the first test is also shown, and the origin corner is highlighted in red.

observed rotation angle was corrected in the results to avoid bias error.

To evaluate and verify rod positions in the test section, images were taken with the laser plane projected through the center of each row of rods as shown in Figure 4.3. An assessment of x displacement relative to the average columnar-center of each rod was performed and is presented in Figure 4.4. Based on this evaluation using ImageJ [40], the total maximum error of positioning of the measured rod centers for each row was of 5 pixels, and appeared independent of position of the rod within the test section, indicated by a discontinuous color gradient in Figure 4.4. Depth positioning, y , of the laser was obtained by finding the PIV measurable limits in the depth of the test section, ie the total distance the laser could be traversed while still being projected through the test section open channel. It was found that the entire test section channel was measurable and that the depth uncertainty was of $0.073D_H$. This uncertainty is attributed to glue on the inside corners

of the test section, which prevented laser sheet projection at the minimum and maximum depth of laser sheet placement, and did not greatly affect measurements in the bulk of the test section. More on this is discussed in laser sections.

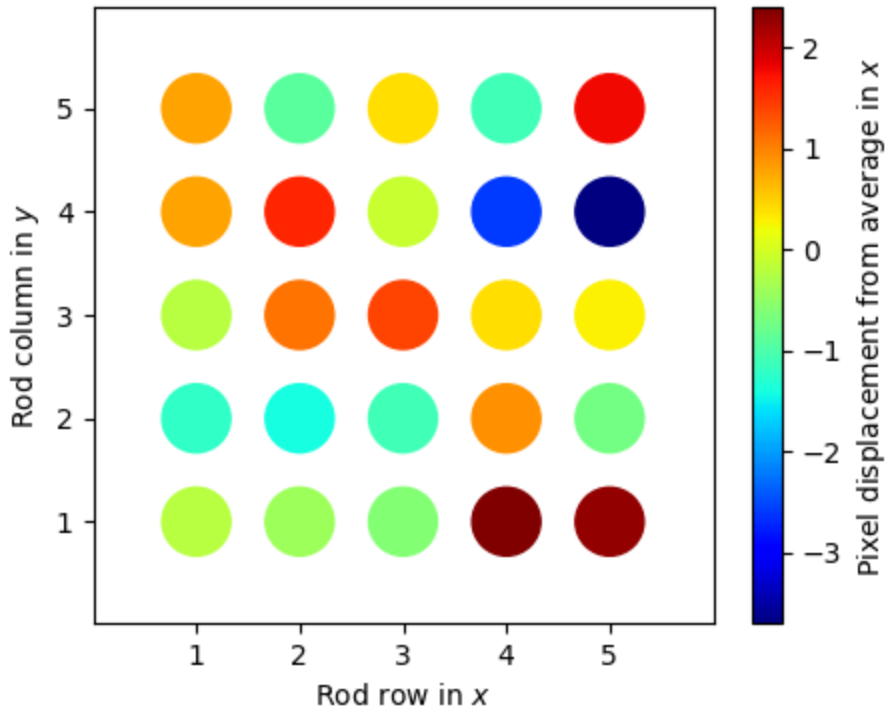


Figure 4.4: Pixel displacement relative to the average position of the center of the rods between planes taken at the center of the rods.

A double exposure four mega pixel CCD camera was used to capture the flow field in the entire width of the test section from $-0.1D_H$ – $5D_H$ downstream the spacer grid. The captured images had 2352×1768 pixels of resolution and 12 bit of depth. The double exposure CCD camera allows two high resolution images to be captured in quick succession. The same image resolution and capture rate were used for all image collection during the experimentation.

Images were first collected at all measurement planes parallel to the xz -plane as a first test for quantification of velocities u and w . This required the scanning of the laser plane throughout

the test section in y as described by the Equation 4.3. The test section was then rotated 90° CW about the z axis when viewed from above. Within the ROI, this correlates to an axes mapping of $x \rightarrow y$, and $y \rightarrow -x$, with no change in the z axis. Rotation of the test section permitted velocity components v and w to then be measured without adjustment of the camera and laser setup. Image collection for the second test proceeded the same as described for the first test, with scanning of the laser and camera in the x coordinate following the same pattern as described for y in test 1, which was governed by Equation 4.3 and is illustrated in Figure 4.5.

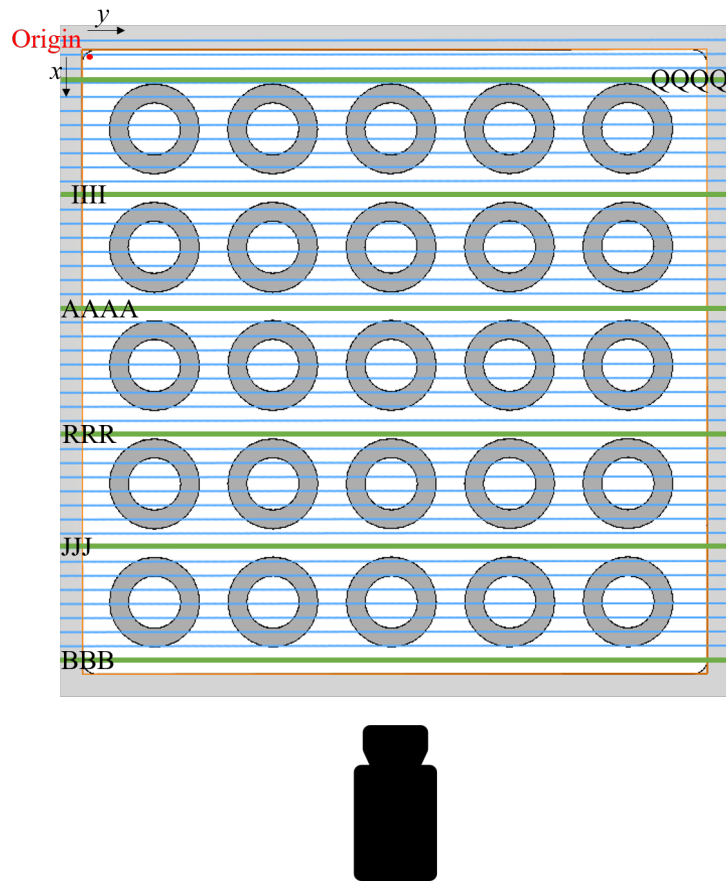


Figure 4.5: Laser plane alignment and camera position for second test, consisting of measurements of v and w . The origin corner is highlighted in red.

4.1.1 Particle Image Velocimetry Cross Correlation & Image Processing

In order to measure fluid velocity between collected images in both photos of each frame, the measured intensity of tracer particle reflectance (I) within the digital position coordinate (X_i) is compared between two images. This is accomplished by calculating a cross correlation between images 1 and 2 in a frame (C_{12}), which is given as Equation 4.4 [41, 42]:

$$C_{12}(\delta_i) = E \{I_1(X_i) I_2(X_i + \delta_i)\} \quad (4.4)$$

$$\simeq \mathcal{F}^{-1} \{ \mathcal{F} \{I_2(X_i)\} \cdot \mathcal{F} \{I_1(X_i)\}^* \}, \quad (4.5)$$

where δ_i is a digital displacement which is determined by the window sizing in PIV, and is calculated for every point within the Discrete Window Offset (DWO). The Fourier-based correlation approximation, $\mathcal{F} \{ \phi \}$ in Equation 4.5, is employed to increase computational efficiency in PRANA [43]. This algorithm generates a X_i space function of C_{12} , with peaks each correlating to an offset defined by τ . Each of these peaks define a possible displacement within the processed window based on particle pattern recognition.

Before cross correlation was applied to the image set, a background subtraction preprocessing of the captured images was performed by subtracting from every image the sum of all images divided by the number of collected images. This removes most of the bright areas present in the images due to reflections from the spacer grids. Figure 4.6 shows an example image obtained after the background subtraction operation. In the figure a saturated contrast image is shown that indicates not all of the brightness from the mixing vanes was removed with the background subtraction process due to changing reflection intensity on the vanes between images. This fact was used to an advantage in data processing, as is explained below.

The PIV images were processed using the PRANA PIV code [43]. Advanced multi-pass, multi-grid PIV processing using DWO and robust phase correlation (RPC) algorithms were used as described in Equation 4.5. Three interrogation window passes were performed. The first pass was of 64×64 pixel with 50% overlap to respect the 1/4 window rule for maximum displacement of

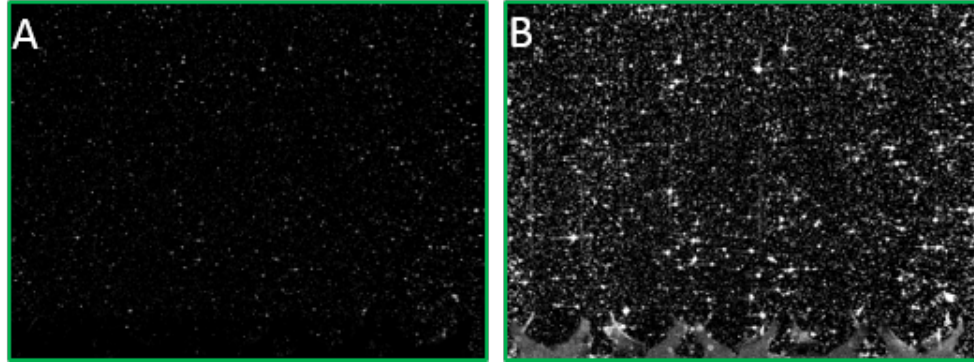


Figure 4.6: Background subtracted images of a measurement plane R as indicated from Figure 4.2. Image B has saturated brightness and highlights that the spacer grid vanes are still visible; however, rods are not, even though that in this image there are two rows of rods in front of the plane.

the first PIV grid mesh [44, 42]. The final pass of 32×32 pixels with 75% overlap yielded a mesh of 294×221 displacement vectors.

The universal outlier detection (UOD) method [45] with checks for additional peaks and vector replacement was used to validate the velocity field. If a vector is outside of validation criteria when compared to its 8 neighbors in a 3×3 vector space, it is replaced by the vector obtained by the second- and third-largest peaks calculated in cross-correlation, successively. If the vector fails these validation tests, it is replaced by the median of the 8 neighboring vectors. When the last happens, a 1 is written to *Eval* saved within the results file; if the vector passes the validation, *Eval* is set to 0.

It is expected that validation will fail in sporadic locations of the vector field due to random effects [46, 47, 48]. Regions with large illumination noise, such as a reflection on the vanes, and low particle sampling areas, such as in shades produced by the spacer grid, are expected to show a consistent failure in validation. With the knowledge of this fact, points with systematic failure to validate within a large data set could be eliminated from the vector field, as they are probably non-physical vectors in regions that can't be measured due to shading or surface reflections. Based on this, PRANA's *Eval* parameter was used to eliminate bad vectors from the field.

The averaged evaluation parameter for each of the preliminary measurement planes is presented

in Figure 4.7. A mask was applied only to the bottom and sides of the image that were consistently dark. As can be seen in the Figure 4.7, high (> 0.4) average evaluation parameter (\overline{Eval}) can be seen in the region where the vanes are located and near the edges of the image. At these regions, relatively large fractions of the displacement vector in the 2000 vector fields data set was replaced due to validation failure. Using this data, a threshold was established, removing any vector with a $\overline{Eval} > 0.4$. At the spacer grid region a stricter $Eval$ threshold of 0.3 was defined eliminating more vectors that could be influenced by errors propagated from the bright areas.

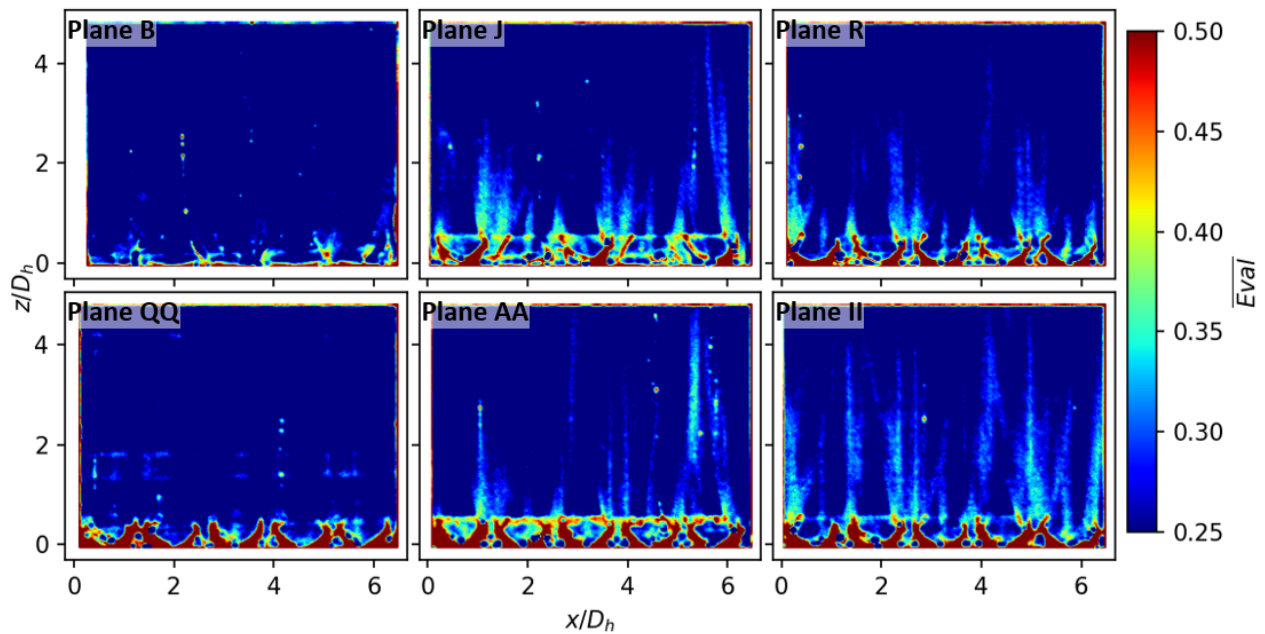


Figure 4.7: Average of PRANA's $Eval$ in all preliminary planes.

It is interesting to note in Figure 4.7 that the edges of the field all contain poor validation vectors. This occurs due to lack of surrounding information for validation, and is present immediately adjacent to any masked region. This is one of the justifications for this approach of vector elimination instead of traditional masking. Masking also influences the flow field measurements in its near vicinity, due to the small number of neighbor vectors which are used in UOD comparison [49]. Manually masking complex geometries is unreliable and time consuming and could gener-

ate over and under masked regions. Automated masking and machine learning PIV processing is being developed and shows potential, however still have limitations in reflection regions and non-stable images [49] or rely on very strong, well defined reflective regions and some manual positioning [50]. This method moves towards automation in an attempt to reduce qualitative masking approach.

Figure 4.7 also shows that rod reflections, though small, were present. These reflections, however, were a function of the position of the laser sheet relative to the mixing vanes, and not a problem with the MIR. This can be seen in comparison of Planes B and QQ, which show similar \overline{Eval} in the bulk of the flow even though they are at the near-wall extremes of the test section. Looking at the \overline{Eval} averaged over the entire field of each plane yields similar results within $\pm 5\%$ with no tendency in function of depth.

4.2 Two Dimension Two Component Calibration

Images of a calibration plate placed inside a parallel, identical size, test section were taken to convert pixel displacement as collected from the CCD camera to length units via the M . This is required due to the change of media of the reflected laser light from the D-limonene and polycarbonate of the test section ROI construction, and the air in which the camera resides. Because the camera was moved a different length than the laser in order to accommodate for the different n the two objects were moving in, the total distance from object plane to lens (Z_0 in Raffel et al [38]) was changing, while length from the lens to the image collection plane (z_0 [38]) remains fixed. A unit-less M cannot be determined as is the standard for optical measurements [38].

The calibration plate used was a LaVision 058-5-DSDP plate; it was moved using a micrometer traverse system for calibration of M . The plate contains 132 reference dots spaced 5 mm (± 0.02 mm) apart in two perpendicular directions. An example calibration image is shown in Figure 4.8. ImageJ [40] was used to find the centroid of every point on the analyzed images. The pixel-wise hypotenuse between each point was then determined, and a ratio of mm/pixel was calculated using the known distance between points.

As can be seen in the calibration image in Figure 4.8, some of the calibration plate extended



Figure 4.8: Calibration plate image at plane B used in determination of M for the first test. Similar images were collected for the second test.

out of the camera's FOV. This is due to the use of two cameras stacked in the z direction in order to collect a larger total FOV. Additional processing of these images is reserved for future work, and is beyond the scope of this dissertation. Even with the use of a fraction of the calibration plate in the image, a relative uncertainty of the calculated M for each image plane, as well as between image planes, was sufficiently small to assume a constant M for each test. This made for a streamlining of image post processing, and was the goal of the camera laser movement as described in Section 4.1.

For the first test, which consisted of measurements of u and w_1 , sixteen plane positions were used to define the magnification factor. Fifteen planes were used for the second test, which consisted measurements of v and w_2 . The calculated M was 2.8446×10^{-2} mm/pixel ($\pm 2.0926 \times 10^{-4}$ mm/pixel) for the u and w_1 measurements. M was calculated as 2.8484×10^{-2} mm/pixel ($\pm 2.6666 \times 10^{-4}$ mm/pixel) for measurements of v and w_2 . Data for calculating each test's M are contained in Appendix C. Calculated uncertainty for each test M included machining tolerance of the calibration plate as described above, and $2x$ the standard deviation (σ_ϕ) of the magnification ratio calculated in each image. Further uncertainty is described in Section 4.3. After calibration was complete, the test specific M was used along with the PIV Δt to scale each pixel-wise dis-

placement field to a velocity field measurement using Equation 4.6.

4.3 Particle Image Velocimetry Uncertainty Quantification

A detailed uncertainty quantification (UQ) was performed for each of the 2000 velocity fields calculated at each of the 45 planes for both tests. Positioning uncertainty of vector fields within the test section geometry was also quantified. This work was described in detail for six preliminary analysis planes in dos Santos et al [37], and is reproduced here.

To calculate uncertainty, first the instantaneous velocity must be defined. The instantaneous velocity components are obtained as a function of M in mm/pixel, component-wise displacement between a image pair (δ_i) in pixels, and the intra-pair time delay, Δt , in seconds. The relation for u_i is defined in Equation 4.6:

$$u_i = M \frac{\delta_i}{\Delta t} \quad (4.6)$$

The combined and expanded component-wise velocity uncertainty, U_{u_i} , can be defined as the quadrature sum of each individual variable uncertainty contribution as shown in Equation 4.7 multiplied by the coverage factor of 2 for a 95% uncertainty band.

$$\left(\frac{U_{u_i}}{u_i}\right)^2 = \left(2\frac{U_M}{M}\right)^2 + \left(2\frac{U_{\delta_i}}{\delta_i}\right)^2 + \left(2\frac{U_{\Delta t}}{\Delta t}\right)^2 \quad (4.7)$$

4.3.1 Calibration & Digital Displacement Uncertainty

Similar to described as in Section 4.2, uncertainty of the magnification factor, U_M , was calculated as shown in Equation 4.8.

$$(U_M)^2 = (U_{cal})^2 + (U_{dev})^2 + (U_{dist})^2 + (U_{\alpha})^2 \quad (4.8)$$

In Equation 4.8, U_{cal} is the uncertainty of dot position and size due to physical manufacturing limits of the calibration plate, U_{dev} is the plane positioning uncertainty, defined as the maximum difference between M values obtained in the evaluated planes, U_{dist} is the distortion of the image

due to lens and camera detector, defined as the maximum standard deviation of the magnification factor (σ_M) calculated on a calibration image, and U_α is the angle of the calibration plate relative to the camera plane, calculated assuming the largest angle of 0.5° based on image angle assessment of the calibration plate.

Uncertainty of coordinate-wise pixel displacement, U_{δ_i} , was calculated as Equation 4.9.

$$(U_{\delta_i})^2 = (U_{subpixel})^2 + (U_\beta)^2 \quad (4.9)$$

This uncertainty is attributed to $U_{subpixel}$, the sub pixel resolution limit of the DWO method used in PRANA [51, 52], as well as the laser measurement plane angle relative to the “true” velocity plane, U_β , estimated assuming the largest possible angular deviation based on angles assessed with the calibration images as previously discussed.

The time delay uncertainty $U_{\Delta t}$ can be estimated as the sum of all possible delays that can occur. As all of the processes are electronically controlled this value is very small and estimated as $U_{\Delta t} = 20\text{ns}$ which is orders of magnitude lower than the value of Δt .

Table 4.1 presents the values for each uncertainty sources accounted. Displacement uncertainty due to the angle U_β has different values for each velocity component. It is one of the major components and has heavy implications for the lateral velocity components uncertainty, U_u and U_v .

4.3.2 Uncertainty as Convergence Residual

A statistical convergence analysis was performed to assess the mean velocity fields. A variable residual (R_ϕ) was calculated using Equation 4.10.

$$R_\phi = \phi_s - \phi_{s-1} \quad (4.10)$$

In Equation 4.10 ϕ indicates an arbitrary measured variable, such as \bar{u} , and s indicates the set-number, which determines the number of frames used in the calculation, as in Table 4.2. Each image set contains a number of image pairs 20% greater than the previous to assess the rate of

Table 4.1: Relative uncertainty values.

Parameters	Value
$\left(\frac{U_{cal}}{M}\right)$	0.00400
$\left(\frac{U_{dev}}{M}\right)$	0.00080
$\left(\frac{U_{dist}}{M}\right)$	0.00341
$\left(\frac{U_{\alpha}}{M}\right)$	0.00669
$\left(\frac{U_M}{M}\right)$	0.01165
$\left(\frac{U_{subpixel}}{\delta_i}\right)$	$0.03/\delta_i$
$\left(\frac{U_{\beta}}{\delta_x}\right)_u$	$0.04838/\delta_x$
$\left(\frac{U_{\beta}}{\delta_y}\right)_v$	$0.04843/\delta_y$
$\left(\frac{U_{\beta}}{\delta_z}\right)_w$	$0.00746/\delta_z$

convergence. By using a constant increase rate of frames, convergence is not weighted and over-estimated as the size of step grows [47].

Table 4.2: Set sizes for residual convergence calculation.

s	N
1	156
2	187
3	224
4	269
5	323
6	388
7	465
8	558
9	670
10	804
11	965
12	1157
13	1389
14	1667
15	2000

Figure 4.9 exemplifies the convergence study results presenting the average residual for data

taken along a horizontal line for various axial positions. The lateral velocity component \bar{u} and the shear Reynolds stress ($R_{\bar{u}'\bar{w}'}$) are presented.

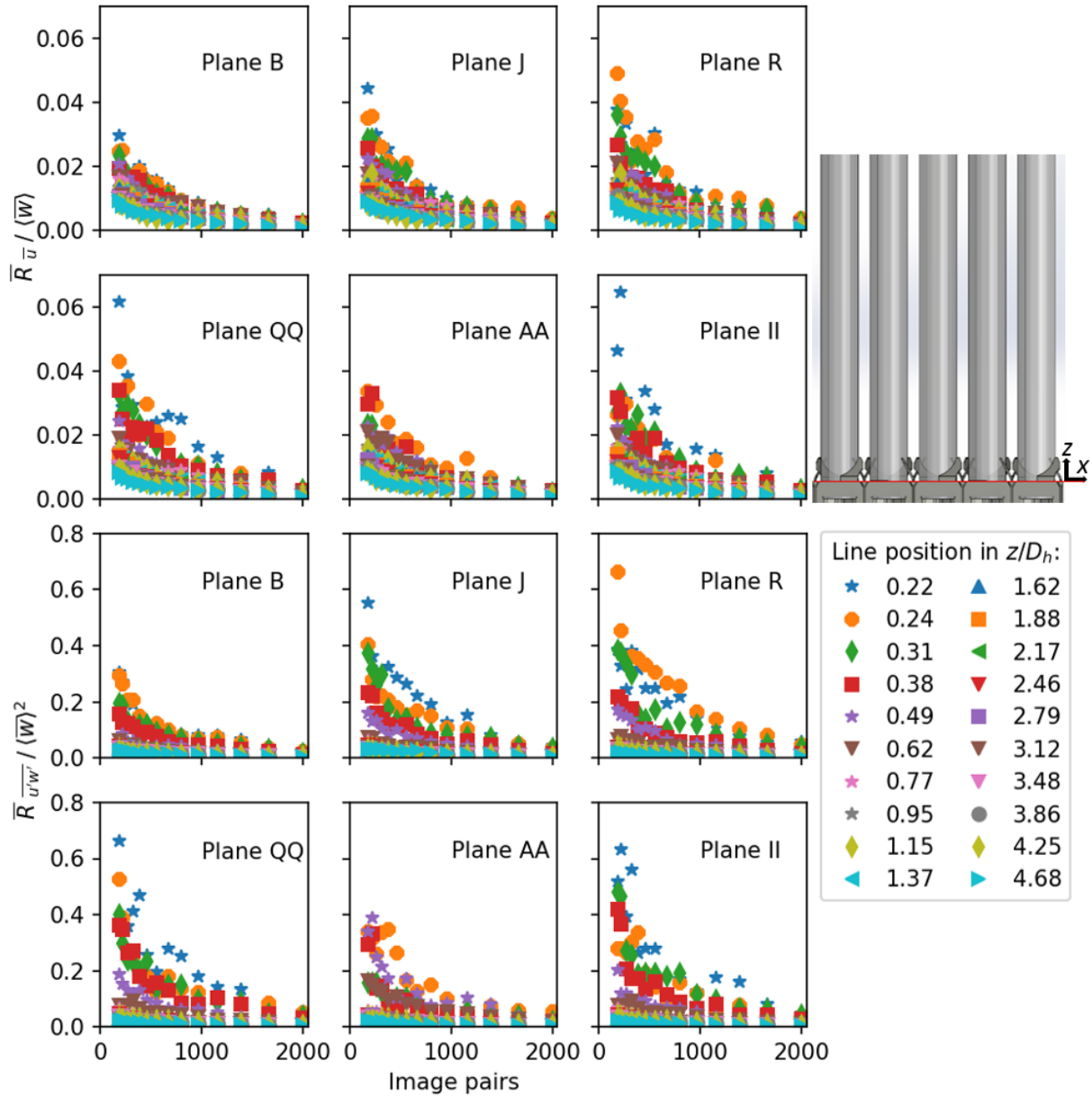


Figure 4.9: Convergence of \bar{u} velocity component and $\bar{u}'\bar{w}'$ Reynolds stress.

Convergence behavior was similar for all planes and in all positions along the axial direction, which are shown in Figure 4.9, even in the region within the spacer grid ($z/D_h < 0.6$). This

behavior was present for all variables. The exponentially convergent behavior observed matches expected theoretical convergence of statistically independent PIV data based on studies performed with synthetic images [47]]. These findings evidence that a high MIR quality was obtained and also that the results are consistent and well converged at the last set.

Figure 4.10 shows the final residual value for the full data set with 2000 velocity field frames at all planes, for all variables. Residual results are averages along lines crossing the width of the test section in x at various heights z . It can be observed that all planes converged to similar residual values in every section of the flow field for each evaluated variable. This is another indication that a the MIR combination used provides high quality images, even at relatively deep regions of measurement. Higher residuals, which are expected, can be observed at the spacer grid vane regions, and close to the maximum z coordinate of the velocity field due to poor sampling in this region. Lower sampling, however, is due to the elimination of vectors based on larger \overline{Eval} . As well, these higher residuals are still within experimental error and are accounted for in the UQ propagation.

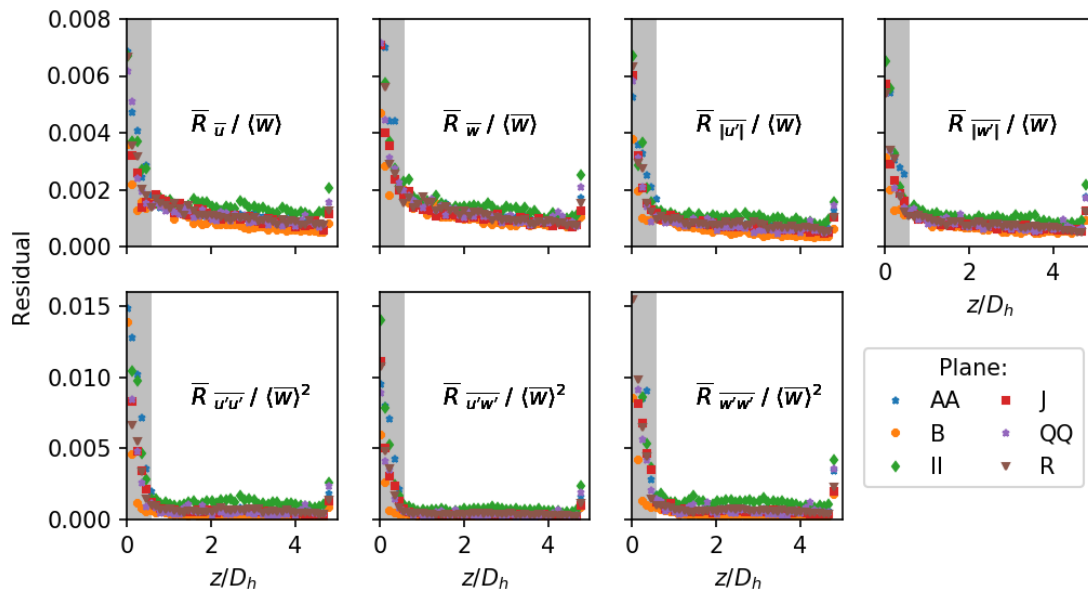


Figure 4.10: Convergence of measured and derived quantities for all preliminary planes at the final set, where 2000 velocity fields are used.

4.3.3 Statistical Uncertainty Propagation

Propagation of uncertainty for the averaged velocity can be considered as the sum of the mean of U_{u_i} , $\overline{U_{u_i}}$, the convergence residual, R_{u_i} , and the standard deviation of the instantaneous velocity (σ_{u_i}) divided by the square root of the effective number of image pairs [47], N , as shown in Equation 4.11. Convergence of the variables (Figure 4.10) showed exponentially approaching zero behavior for the variables, assuming this behavior true for an increasing data set, the value for R_{u_i} was taken as the residual of the full set.

$$(U_{\overline{u_i}})^2 = (\overline{U_{u_i}})^2 + (2R_{\overline{u_i}})^2 + \left(2\frac{\sigma_{u_i}}{\sqrt{N}}\right)^2. \quad (4.11)$$

It is important to note that the effective number of pairs for each plane in this dissertation is the total number of pairs, $N=2000$, since each pair is statistically independent to each other. This is guaranteed due to the large relative time step between pair measurements, equal to 4 full flow passings and $>40t_L$. Making use of the large number of statistically independent instantaneous flow fields to calculate average velocity, the fluctuating component, u'_i , can be determined using Equation 4.12.

$$u'_i = \overline{u_i} - u_i. \quad (4.12)$$

The combined and expanded uncertainty of this derived variable is, in turn, calculated from both contributing variables as shown in Equation 4.13.

$$(U_{u'_i})^2 = (U_{\overline{u_i}})^2 + (U_{u_i})^2. \quad (4.13)$$

Similarly to the velocity components, uncertainty for the fluctuating velocity, as RMS, was propagated as shown in Equation 4.14.

$$\left(U_{\overline{u'_i}}\right)^2 = \left(\overline{U_{u'_i}}\right)^2 + \left(2R_{\overline{u'_i}}\right)^2 + \left(2\frac{\sigma_{u'_i}}{\sqrt{N}}\right)^2. \quad (4.14)$$

In which it is important to note that even though the mean of the fluctuating component is 0, the uncertainty of that measurement about a mathematical mean can still be quantified (ie $\overline{u'_i} = 0 \not\Rightarrow U_{u'_i} = 0$). This could provide an overestimate of fluctuating uncertainty, however, as the RMS of the measurements is equal, but only shifted by one mean, as indicated in Equation 4.12. Further understanding of this UQ should be investigated. Making use of the Equation 4.13, Reynolds stress, $u'_i u'_j$, combined and expanded uncertainties can be calculated using Equation 4.15.

$$\left(U_{u'_i u'_j}\right)^2 = \left(u'_j U_{u'_i}\right)^2 + \left(u'_i U_{u'_j}\right)^2. \quad (4.15)$$

The propagated uncertainty for the average Reynolds stress based on the same assumptions can be calculated as shown in Equation 4.16.

$$\left(U_{\overline{u'_i u'_j}}\right)^2 = \left(\overline{U_{u'_i u'_j}}\right)^2 + \left(2R_{\overline{u'_i u'_j}}\right)^2 + \left(2\overline{u'_j} \frac{\sigma_{u'_i}}{\sqrt{N}}\right)^2 + \left(2\overline{u'_i} \frac{\sigma_{u'_j}}{\sqrt{N}}\right)^2 \quad (4.16)$$

Uncertainty for the Reynolds stresses could be underestimated using the presented method due to the finite spatial resolution of the PIV algorithm that does not allow the detection of fluctuations of length scales smaller than the interrogation window [47]. A detailed analysis of the PIV algorithm response of a known flow and the computed uncertainty would be necessary to assess this uncertainty component and is beyond the scope of this dissertation.

4.3.4 Coordinates uncertainty

Positioning uncertainty is one of the most crucial quantities for validation of highly resolved CFD results [17]. V&V efforts are frequently troubled by profiles that would match if only they were in a slightly different position within the flow geometry. However, the lack of proper information on position uncertainty prevents certain conclusions of spatial profile positioning be made and good validation achieved. Position expanded uncertainty can be calculated according to Equation 4.17.

$$\left(U_{x_i}\right)^2 = \left(2U_M\right)^2 + \left(2U_{pos}\right)^2 + \left(2U_{PIV}\right)^2 + \left(2U_{angle}\right)^2, \quad (4.17)$$

which is attributed to the magnification factor uncertainty, U_M , uncertainty of measurement plane angles relative to the “true” coordinates of the expected flow components, U_{angle} , uncertainty of PIV vector mesh spacing, U_{PIV} , and uncertainty of reference geometry position in the field U_{pos} .

For the in-plane transverse coordinates, x in test 1 and y in test 2, angle uncertainty is progressive relative to a reference point. Considering the maximum deviation due to estimated angle based on the image-central reference point, gives a maximum value of 5.75 pixels for U_{angle} . For U_{pos} there is a 2 pixels uncertainty based on imageJ [40] assessment. Finally, U_{PIV} was considered 4 pixels, equal to half the most resolved PIV mesh size. Depth uncertainty of an arbitrary measurement plane was due to the traverse and reference positioning uncertainty. Absolute uncertainty for each vector coordinate is described in Table 4.3

Table 4.3: Vector positioning uncertainty values.

Test No.	Coord.	U_{x_i} (mm)
1	x	0.411
	y	0.267
	z	0.411
2	x	0.285
	y	0.409
	z	0.409

4.4 Full Field Three Dimension Two Component, and Three Dimension Three Component Reconstruction

In order to analyze the full axial cross section of the visualization region, the test section depth was discretized into 45 y -normal planar measurements as shown in Figure 4.2. The Δy between measurement planes was determined using the estimated laser sheet thickness. This set of 45 planes results in a near full field measurement of two components of time-averaged velocity, specifically \bar{u} and \bar{w}_1 . This combination of data sets was called a three-dimension two-component (3D2C) measurement.

To generate the data set, each vector quantity in every plane was linearized into a single row. Every row was then assigned a third coordinate value based on its corresponding plane's depth in the test section. For example, every point in plane E was assigned a $y=6.75$. The planar data was then concatenated and sorted based on the full x_i assigned from PRANA and the described concatenation process.

A similar discretization was achieved for measurements of v and w_2 , as described above. The Δx was once again determined by laser sheet thickness, and in order to maintain a similar number of laser sheets across the test section depth. These planes were also assigned depth, x , positions according to plane identification. The full vector data was then concatenated as rows into a 3D2C measurement and sorted based on x_i .

With the concatenated 3D2C measurements, a horizontal (z -normal) slice of the now-volumetric data was made, which was perpendicular to the plane of data collection. Positions in z were selected as similar as possible between the two datasets. This permitted for comparison of multiple profiles along geometrically symmetric profile lines as shown in Section 5.4.

4.4.1 Three Dimension Three Component Reconstruction via Trilinear Interpolation

In order to present high resolution data for each variable of interest measured, as well as derived quantities such as RMS components, shear stress, and vorticity, a highly discretized spatial mesh was desired. Generation of the spatial mesh was accomplished using the high resolution of vector spacing from 2D2C planes for both tests 1 and 2. For example, the 45 planar discretization of the y coordinate in test 1 was combined with the 294 displacement vector discretization in y from test 2's 2D2C planes, as described in Section 4.1.1. Due to the z offset of images between the two tests, this resulted in a doubling of vector resolution in the axial direction.

To calculate values at the new, highly discretized mesh, a trilinear interpolation method was used, as described by Kang [53], and summarized here. To calculate an arbitrary variable, ϕ , at a point of interest in the new mesh x, y, z the eight closest neighboring data points ($\phi_{000}, \dots, \phi_{111}$) were selected as shown in Figure 4.11.

With the nearest neighbors of existing data determined, a coordinate-wise distance from each

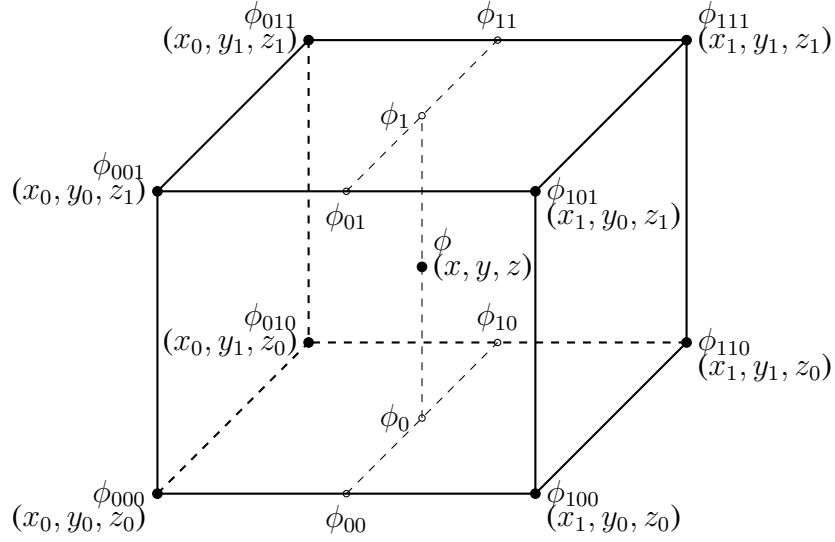


Figure 4.11: Depiction of data used for trilinear interpolation of data in the highly discretized spatial mesh.

point is determined as

$$x_d = \frac{x - x_0}{x_1 - x_0} \quad (4.18)$$

$$y_d = \frac{y - y_0}{y_1 - y_0} \quad (4.19)$$

$$z_d = \frac{z - z_0}{z_1 - z_0} \quad (4.20)$$

Interpolation along the first axis, shown as x here, is accomplished to generate four intermediate values along axis parallel lines between the existing data points:

$$\phi_{00} = \phi_{000}(1 - x_d) + \phi_{100}(x_d) \quad (4.21)$$

$$\phi_{01} = \phi_{001}(1 - x_d) + \phi_{101}(x_d) \quad (4.22)$$

$$\phi_{10} = \phi_{010}(1 - x_d) + \phi_{110}(x_d) \quad (4.23)$$

$$\phi_{11} = \phi_{011}(1 - x_d) + \phi_{111}(x_d) \quad (4.24)$$

These can then be used to calculate interpolated values on planes which are parallel to the first two

axes, x and y , as

$$\phi_0 = \phi_{00}(1 - y_d) + \phi_{10}(y_d) \quad (4.25)$$

$$\phi_1 = \phi_{01}(1 - y_d) + \phi_{11}(y_d) \quad (4.26)$$

Finally, the third coordinate is interpolated along in order to calculate the predicted value of ϕ at (x, y, z) .

$$\phi = \phi_0(1 - z_d) + \phi_1(z_d) \quad (4.27)$$

This simple algorithm gives a weighted value of ϕ which is inversely proportional to its distance from all nearest neighbors. It is important to note that further interpolation, such as cubic or quintic, could be used to incorporate further data points than just the eight closest neighbors. Due to the smoothing which is achieved in PIV, however, this may lead to false approximations of values, especially near walls or masked regions. As such, only the described 3D trilinear interpolation method was used. Further study on approximations of values near walls and masked regions may provide insight to the fluid mechanics scales which are resolved in PIV, however are beyond the scope of this dissertation.

5. RESULTS

The following chapter illustrates results for the 2D2C planar measurements for both tests 1 (y -normal) and 2 (x -normal), quantified uncertainty for these planes, and the planar slices (z -normal) from combined 3D3C data. The last contains a number of highly-resolved spatially interpolated results for the 4 center subchannels, which exhibit highly symmetric flow structures.

5.1 Two Dimension Two Component Particle Image Velocimetry Results

The following section illustrates results from a mathematical mean for a number of vertical planes which were measured during both test 1, and test 2; in which 2000 statistically independent, discrete measurements of u and w_1 , and v and w_2 , respectively were collected. From these measurements, the fluctuating component of velocity was calculated as the RMS and is presented. Reynolds shear stress was also calculated and is illustrated for the planes. Vorticity fields were concurrently calculated during the velocity averaging process, and each mean component of vorticity was subsequently calculated. Mean vorticity fields for the planes are also presented.

In the following sections, plane II at $y = 51.75$ mm is used to illustrate the plane which had the most rods between it and the CCD camera for measurement while still residing fully within the spacer grid xy profile, and exhibiting flow forcing from the vanes. Plane III at $x = 14.75$ mm is illustrated for test 2, which was also measured with the most rods between camera and plane while still residing in the full spacer grid profile and exhibiting mixing vane effects. These planes show similar velocity profiles, despite having a non-identical spacer grid and mixing vane pattern which drives the flow. This illustrates an interesting phenomenon, which may warrant further investigation into the full effect of vane placement and shape.

5.1.1 Mean Velocity

After processing of images and calibration of the pixel-wise calculated displacement, the mean velocity fields were calculated for each plane. For brevity, planes II and III are presented here with full results for each plane contained in Appendix D. For comparison of velocities, Figure 5.1

which contains a measure of \overline{w}_1 from plane II is compared to \overline{w}_2 , which is from plane III and contained in Figure 5.2.

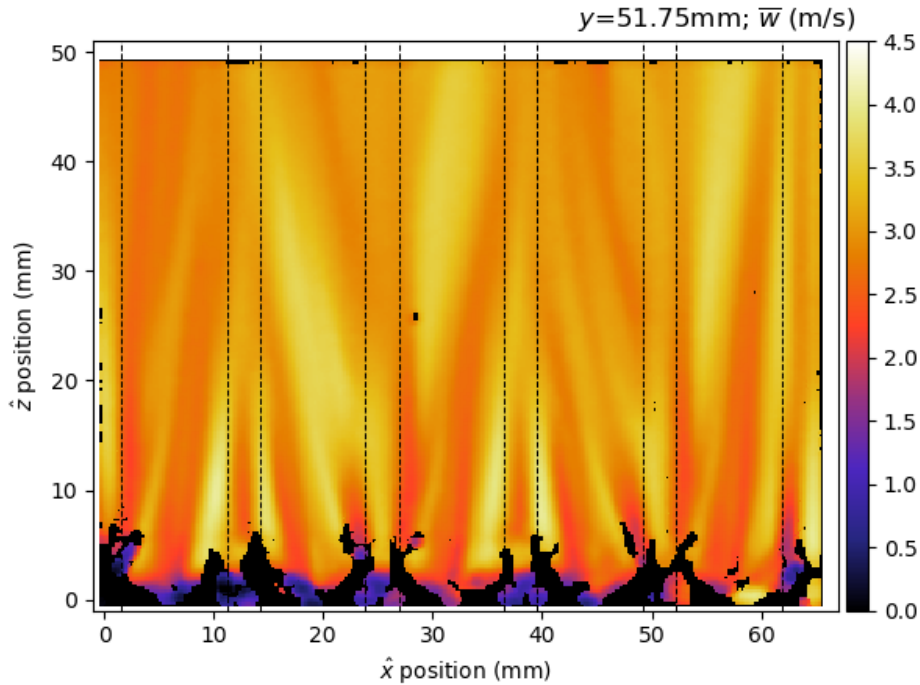


Figure 5.1: Mean axial velocity, \overline{w}_1 , for plane II at $y=51.75$ mm.

Axial velocity, which is the dominant component is clearly affected immediately downstream of the mixing vane tips, which can be seen in the velocity fields due to the vector elimination described in Section 4.3. These points of lower axial velocity correspond to a greater transverse component of velocity. Field measurements of \overline{u} for plane II from test 1 are presented in Figure 5.3. These can be compared to \overline{v} for plane III from test 2, which are presented in Figure 5.4. Similarities can be seen between the presented planes due to the near-symmetry of the mixing vane upstream of the velocity fields. Converging velocities can be seen in alternating subchannels along the horizontal coordinate for both tests.

Of interest is the secondary peaks in transverse velocity near $z=30$ mm, which are clearly

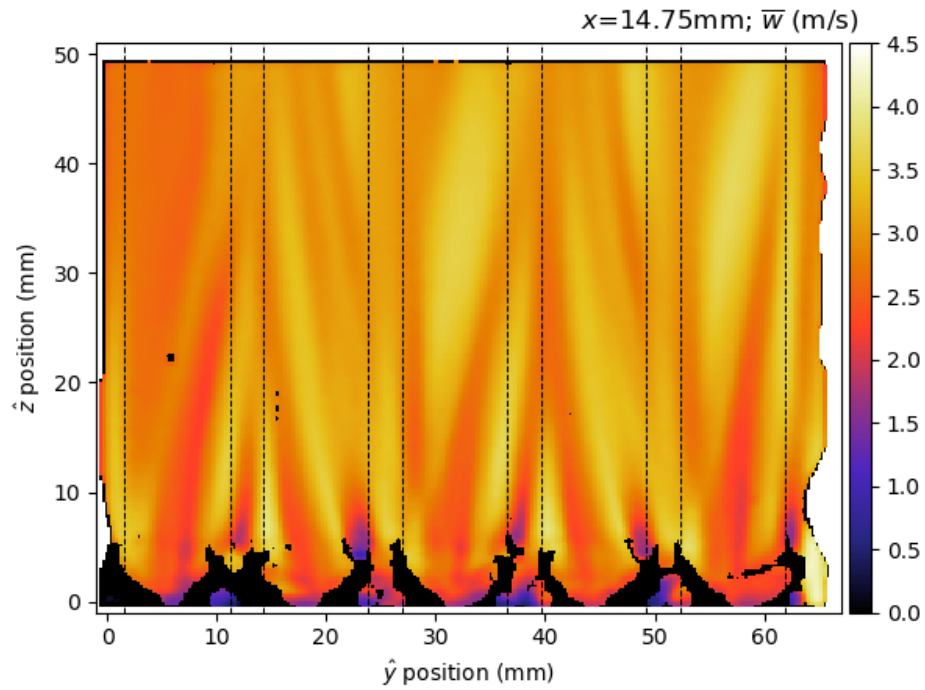


Figure 5.2: Mean axial velocity, \bar{w}_2 , for plane III at $x=14.75$ mm.

resolved in both test results. These increases in non-axial flow stem from upstream peaks in out-of-plane velocity, which cannot be measured with the 2D2C PIV. These present interest and need for a full 3D3C reconstruction and are further illustrated in Section 5.4.

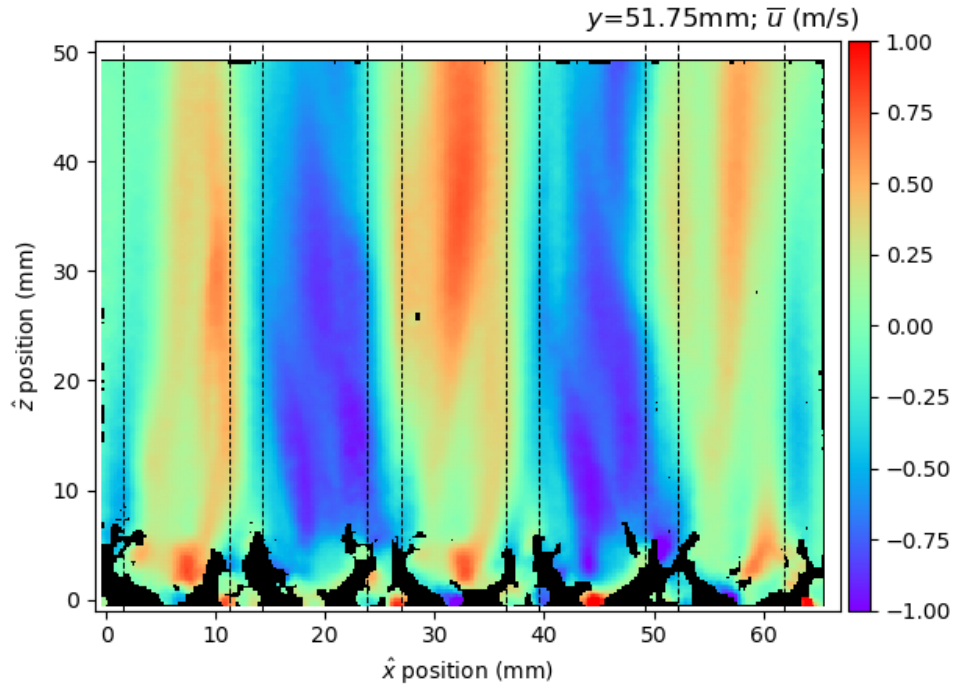


Figure 5.3: Mean transverse velocity, \bar{u} , for plane II at $y=51.75$ mm.

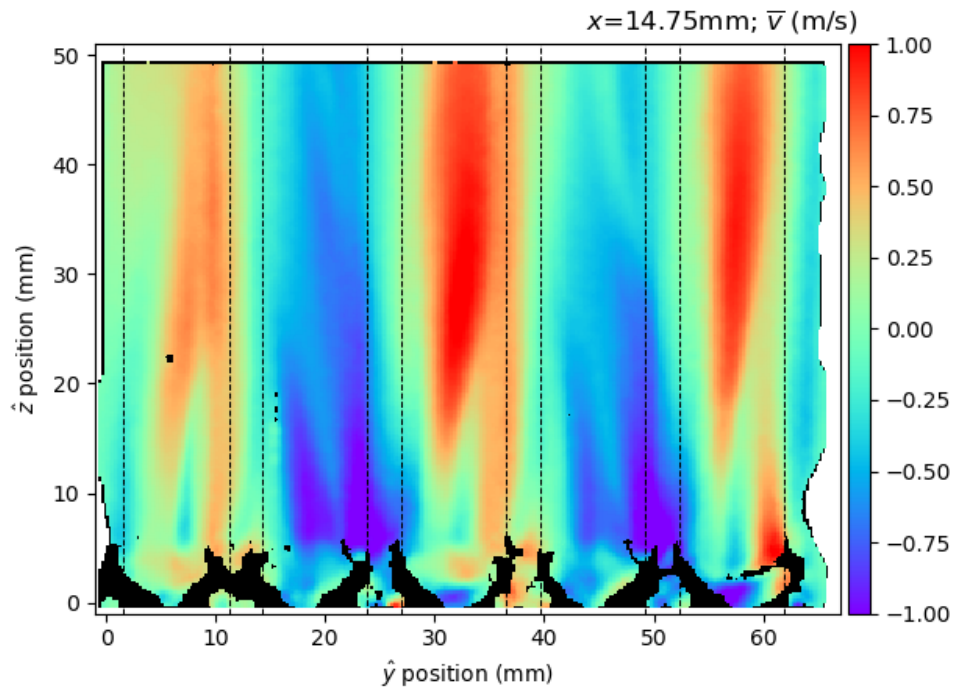


Figure 5.4: Mean transverse velocity, \bar{v} , for plane III at $x=14.75$ mm.

5.1.2 Fluctuating Root Mean Square & Shear Stress

For each of the 2000 measurements made for the final set, the instantaneous velocity components were subtracted from the means in order to calculate the fluctuating components. These were used for calculating the vertical RMS components, presented in Figures 5.5 and 5.6. RMS for the transverse velocity components are contained in Figures 5.7 and 5.8. Strong turbulence can be observed near the mixing vanes, which are again illustrated by the vector elimination process. These regions are expected to have the greatest turbulence, as they exhibit strong effects from the spacer grid geometry upstream of the mixing vanes, which have a more regular forcing pattern. This region's large number of irregular walls create many competing turbulent boundary layers which appear to predominantly straighten within the $z < 20$ mm domain, as is most clearly seen in the $w'_{1,RMS}$ and $w'_{2,RMS}$ plots.

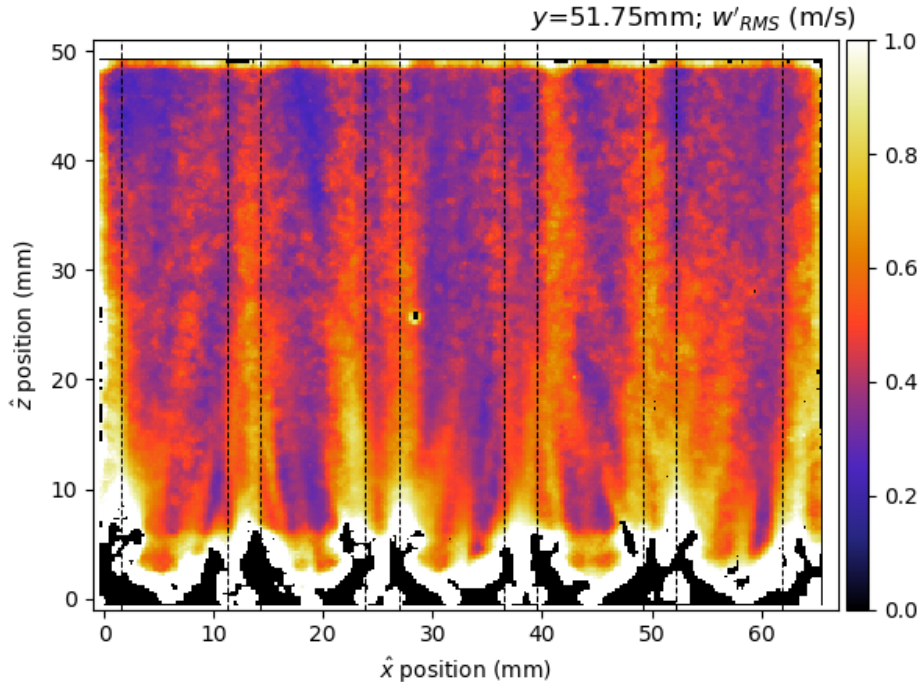


Figure 5.5: RMS velocity, $w'_{1,RMS}$, for plane II at $y=51.75$ mm.

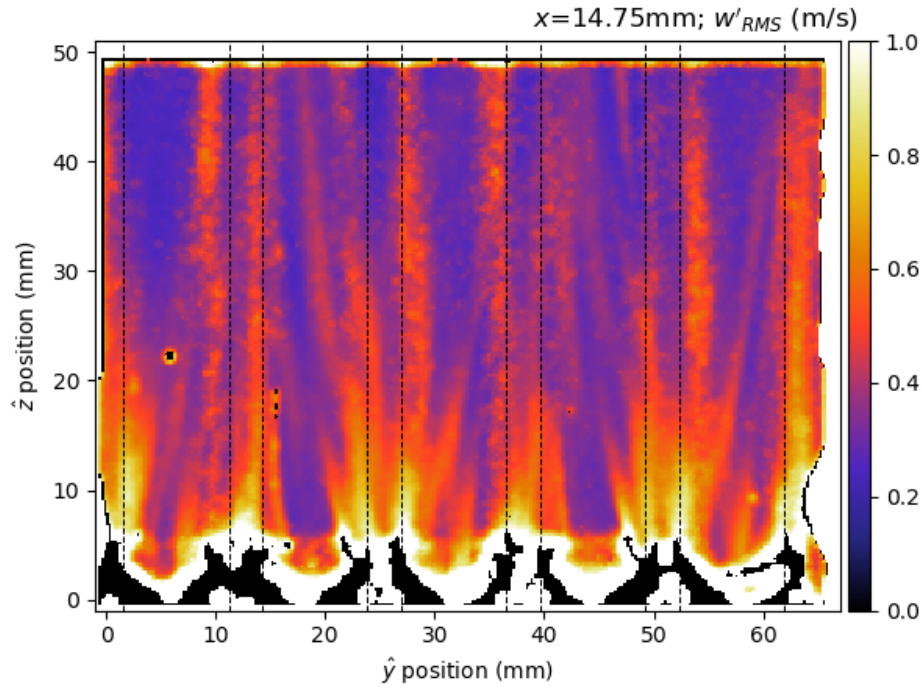


Figure 5.6: RMS velocity, $w'_{2,RMS}$, for plane III at $x=14.75$ mm.

The RMS exhibit a random variance throughout the coordinate domain. This can be attributed to statistical sampling, and is further emphasized by the convergence residual, which is discussed in Section 5.2. Also of note is the increases in perceived RMS near the masked regions and the edges of the FOV for the camera. These regions are artificially high, and would not be included in a full result which includes measurements further downstream of the mixing vane. Processing and analysis of this collected image data, however, is beyond the scope of this dissertation.

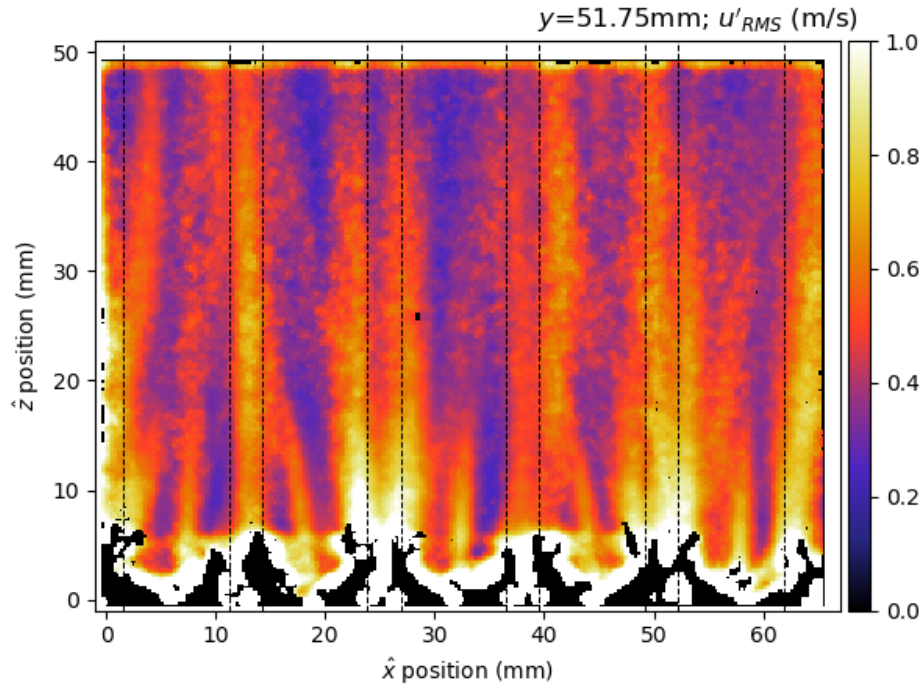


Figure 5.7: RMS velocity, u'_{RMS} , for plane II at $y=51.75$ mm.

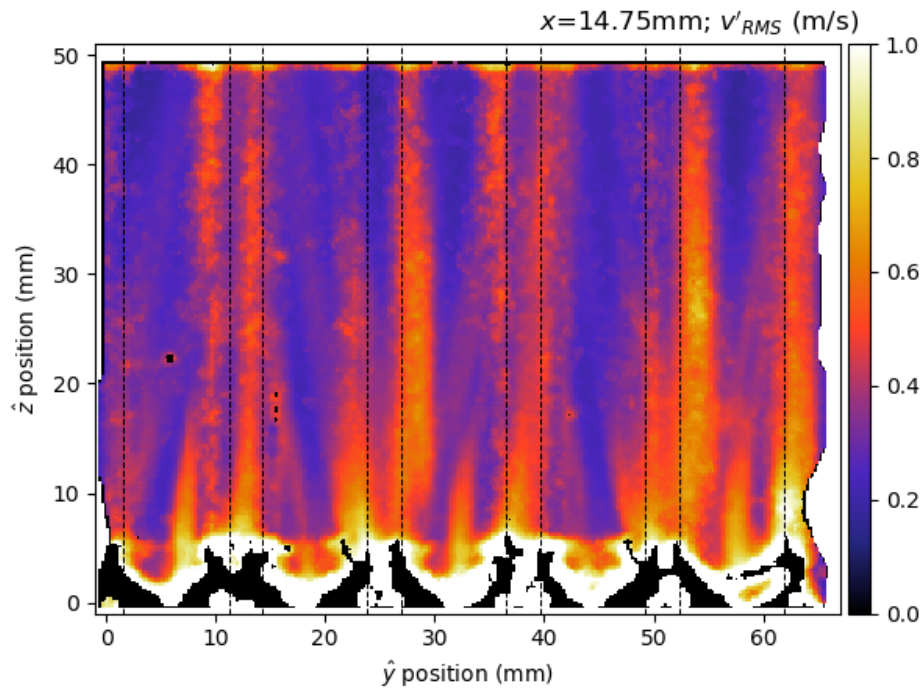


Figure 5.8: RMS velocity, v'_{RMS} , for plane III at $x=14.75$ mm.

Reynolds shear stress was also calculated using the fluctuating velocity components. Due to the nature of a 2D2C measurement, only 2 of the three components derived from Reynolds shear stress were able to be measured with the vertical planes. Test 1 presented results for $\overline{u'w'_1}$ as in Figure 5.9, and test 2 resulted in a measurement of $\overline{v'w'_2}$, which is contained in Figure 5.10.

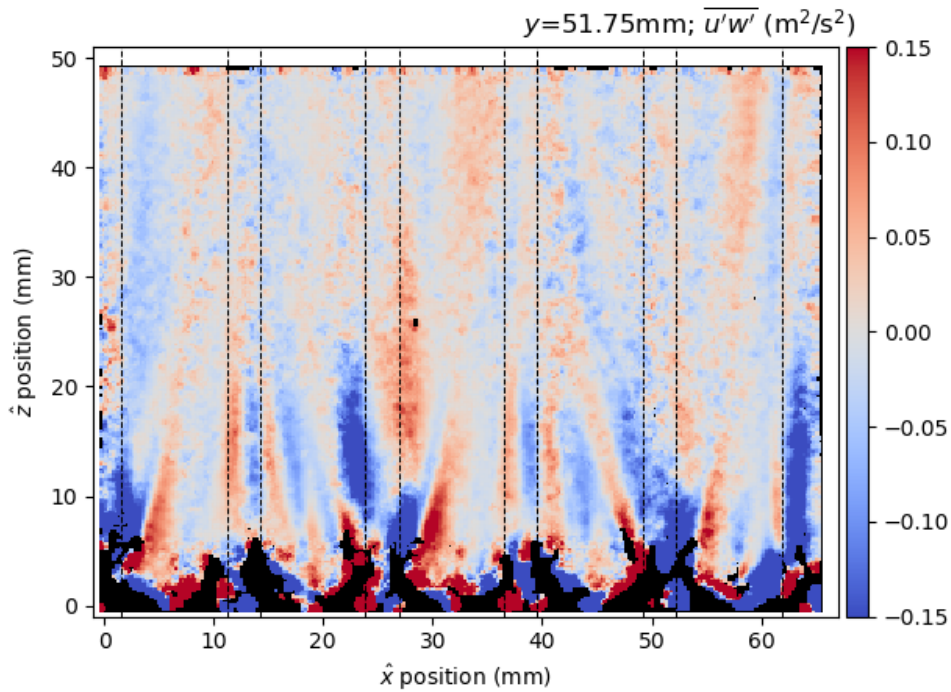


Figure 5.9: Mean Reynolds shear stress, $\overline{u'w'_1}$, for plane II at $y=51.75$ mm.

Differences in convergence and PIV quality become more evident when shear stress is analyzed. As the fluctuating component and secondary statistics take more measurements to converge, the combination of two results in a larger uncertainty, which correlates to less coherent average measurements. Test 1, which presents results for u and w_1 has higher overall values for the shear stress, which indicates that the statistical convergence for this test was not as good as test 2. Reasons for this are difficult to identify, although it could be attributed to a slight change in the flow loop between the two test. A sparging line was added within the fluid storage tank,

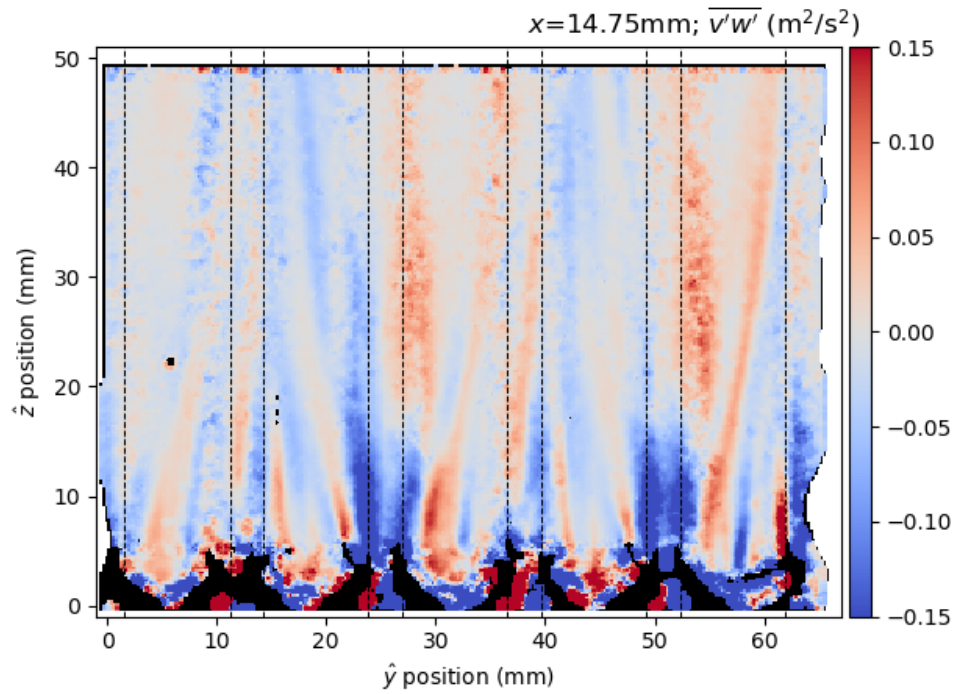


Figure 5.10: Mean Reynolds shear stress, $\overline{v'w'}$, for plane III at $x=14.75$ mm.

which reduced vibration, and minimized bubble appearance in the images collected by the CCD cameras. Additional information is contained in Section 5.2, which highlights various uncertainty components for the presented planes.

5.1.3 Vorticity

For each velocity field measured, the associated vorticity component was calculated as in Equation 1.8. For test 1, ω_y was calculated and is presented for plane II in Figure 5.11. Similarly, ω_x was calculated for the planes measured in test 2 and plane III is illustrated in Figure 5.12. These vorticity fields show highly coherent and symmetric flow patterns.

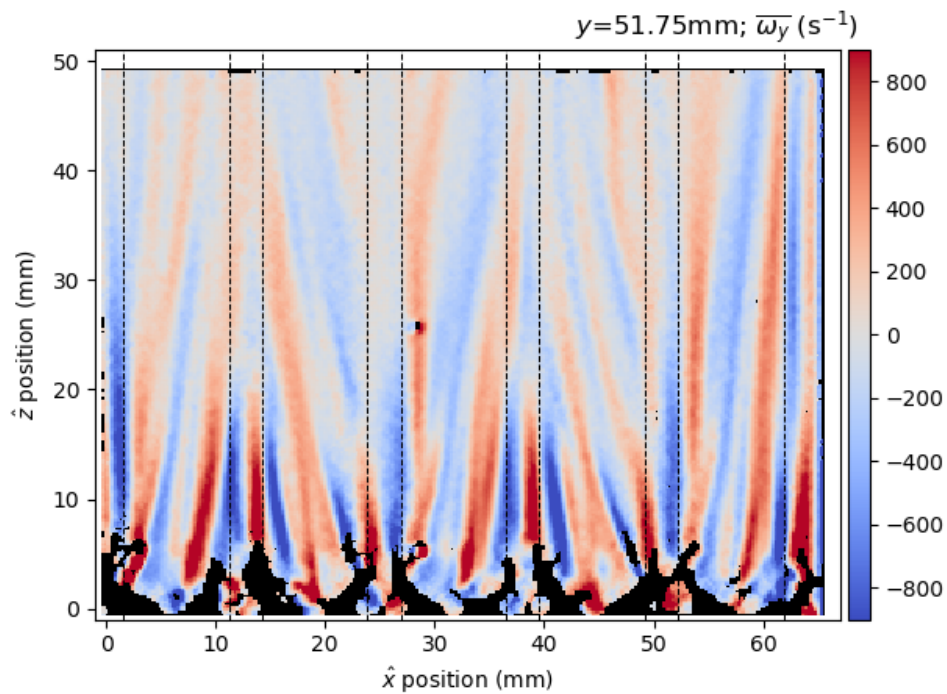


Figure 5.11: Mean vorticity, $\overline{\omega}_y$, for plane II at $y=51.75$ mm.

Sizes of the vorticity structures, which can be clearly seen in the ω_i color contours can be used for determination of mesh size, similar to characteristic length measurements, in high resolution CFD calculations. These are useful for bridging gaps in resolution between DNS and LES or filtered RANS. Further determination and use of these vorticity structures an illustration of possible filter size is described later in Section 5.4.

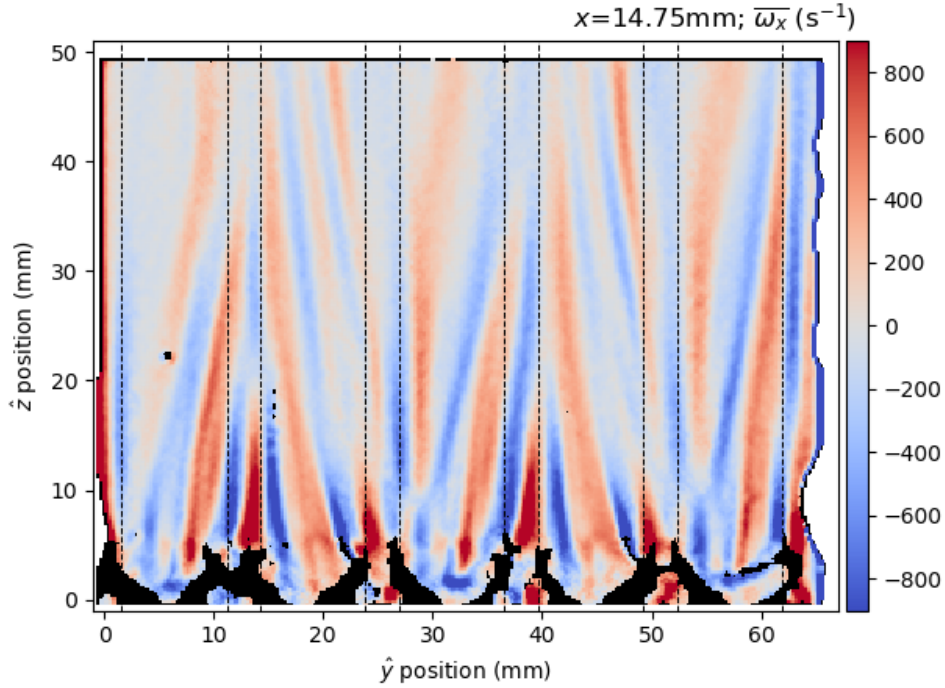


Figure 5.12: Mean vorticity, $\overline{\omega_x}$, for plane III at $x=14.75$ mm.

5.2 Two Dimension Two Component Particle Image Velocimetry Uncertainty Results

5.2.1 Calibration & Digital Displacement Uncertainty Results

Uncertainty of magnification and digital displacement account for planes II and III, which were the furthest away from the camera position while still exhibiting strong mixing vane influence is shown in Figure 5.13 and 5.14, respectively. This component of is one of the largest contributors to the total uncertainty for velocity. Vector elimination based on *Eval* can also clearly be seen at the mixing vanes, where vector validation is poor, as well as the outside edge of the vector field, where vector sampling is decreased.

This component of uncertainty represents the largest component of uncertainty for the first-order statistical mean velocities. This component could be reduced with higher resolution cameras, as well as higher quality glass rods. Due to the commercial availability of the tubes used, a minimum achievable physical uncertainty component would dwarf the other parts which are discussed

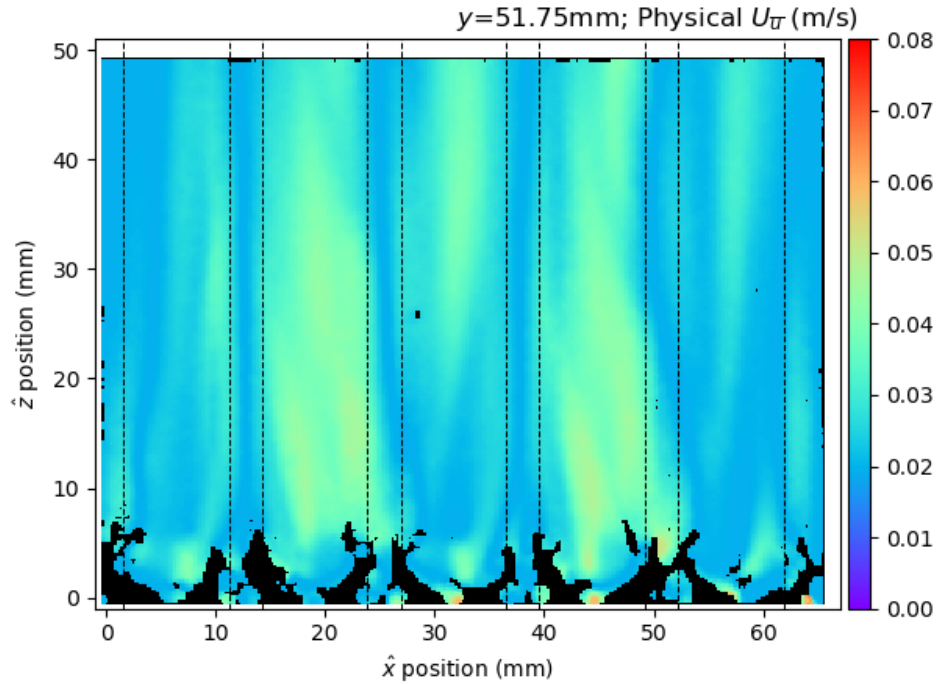


Figure 5.13: Physical and magnification uncertainty for plane II at $y=51.75$ mm.

below. This was understood during quantification of the physical tolerances of the tubes and construction of the rod bundle. Proof of concept for the combined measurement technique was the primarily goal of this study, and was attained with the presented hardware setup.

5.2.2 Convergence Residual Results

Uncertainty due to residual convergence for planes II and III are shown as an example in Figures 5.15 and 5.16, respectively. This uncertainty is calculated as described in Equation 4.10. The random nature of this uncertainty component can be clearly seen in the apparent bright spots, which have no well-defined pattern, unlike the physical calibration uncertainty. This uncertainty component is fairly small when compared to the physical and magnification uncertainty, especially at the last set when $N=2000$. This uncertainty is expected to trend toward zero as $N \rightarrow \infty$.

The convergence residual is even more emphasized for the fluctuating velocity RMS components, which are presented in Figures 5.17 and 5.18 for planes II and III, respectively. It is

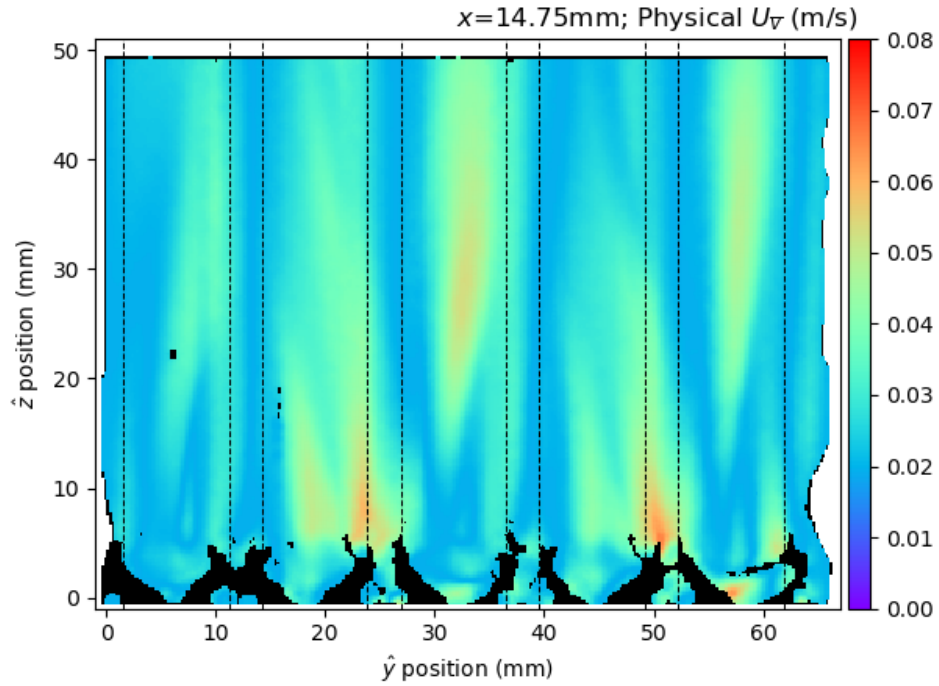


Figure 5.14: Physical and magnification uncertainty for plane III at $x=14.75$ mm.

interesting to note the larger residuals near the subchannels, in particular nearest the edges of the rods, which are indicated by the dotted lines. This is to be expected, as the curvature of the rods along the line drawn from the point of reflection off the particle to the camera sensor would have the largest number of interfaces to pass through with the most oblique angles possible. Additional measurements are expected to decrease this uncertainty.

Results from the first test for u'_{RMS} exhibit larger values of uncertainty overall when compared to v'_{RMS} . This may be attributed to the small improvements made to operation of the test loop throughout the two tests, which reduced vibration in the mechanical structure as well as bubble appearance which was discussed above.

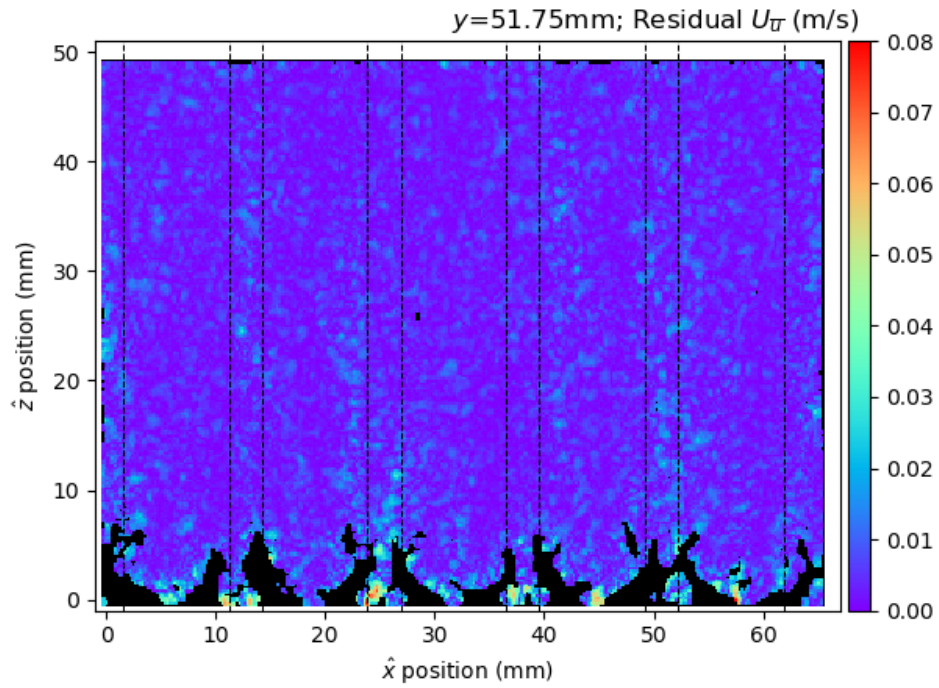


Figure 5.15: Residual uncertainty for mean transverse velocity of plane II at $y=51.75$ mm.

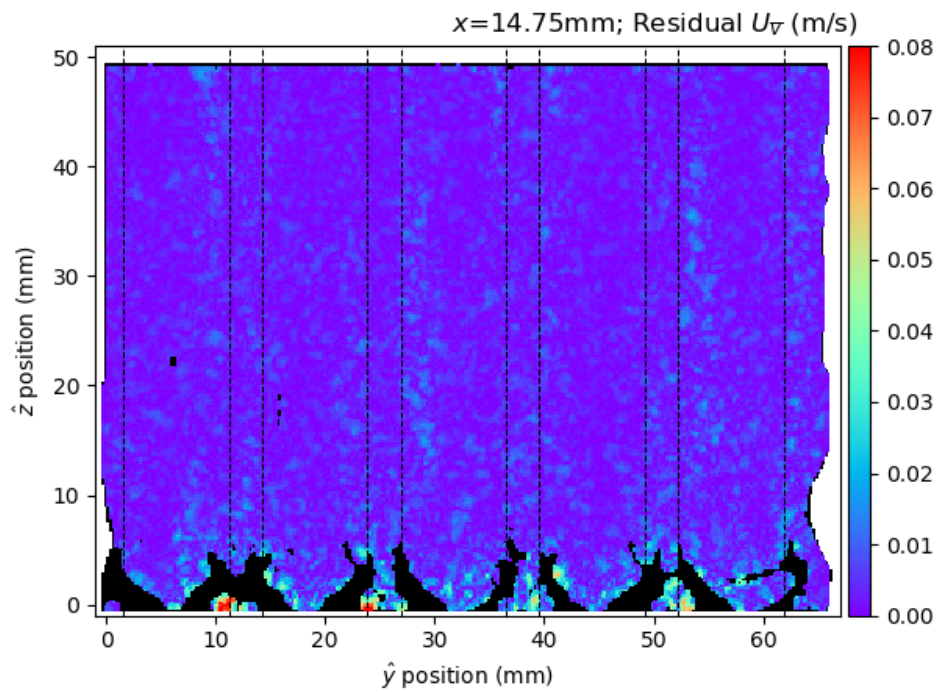


Figure 5.16: Residual uncertainty for mean transverse velocity of plane III at $x=14.75$ mm.

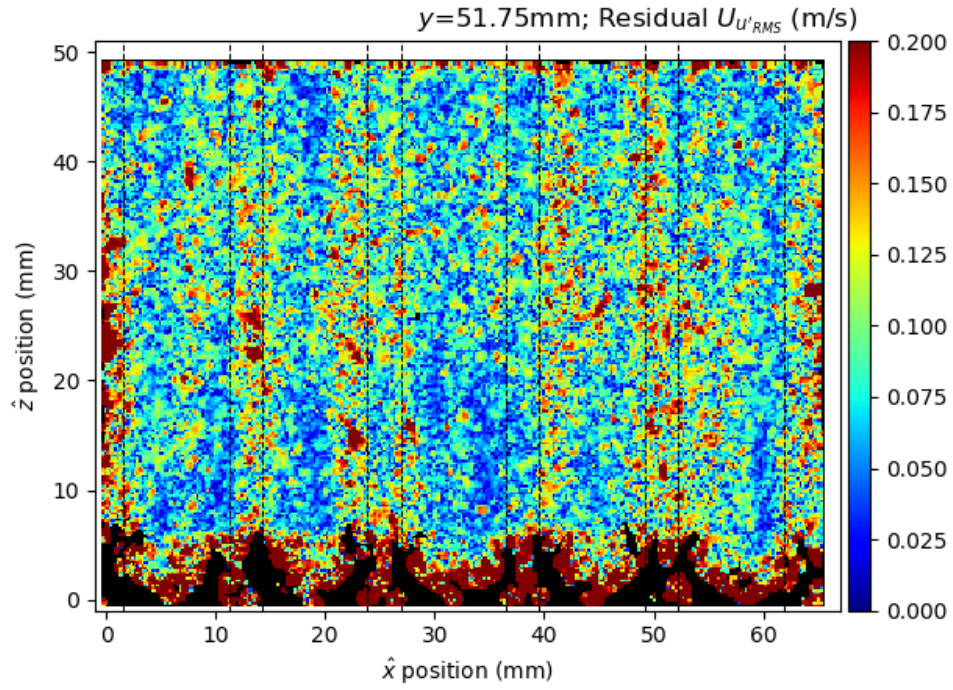


Figure 5.17: Residual uncertainty for transverse RMS velocity of plane II at $y=51.75$ mm.

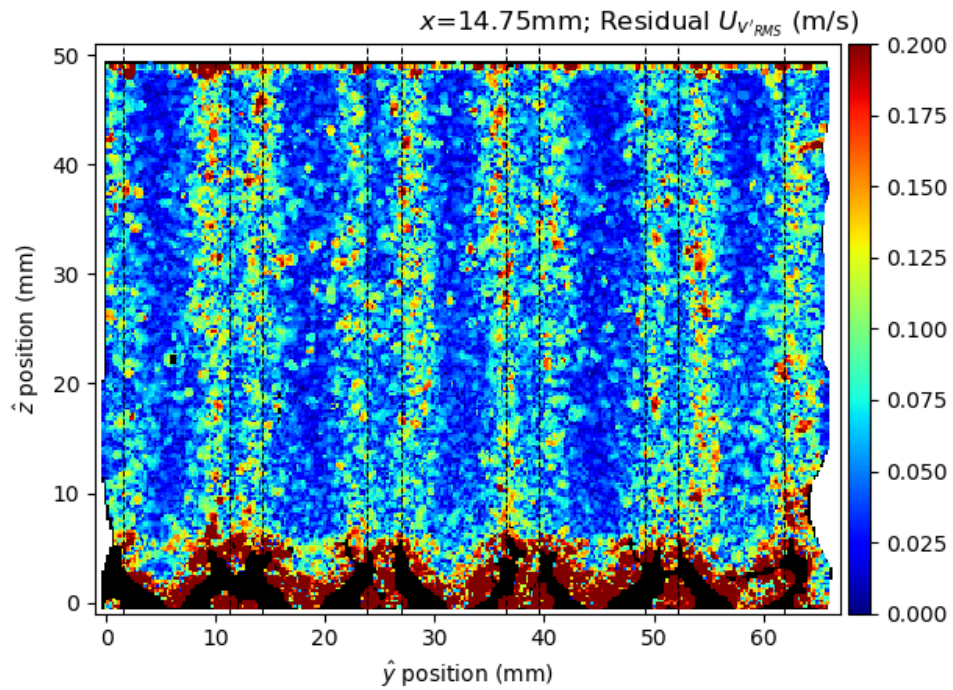


Figure 5.18: Residual uncertainty for transverse RMS velocity of plane III at $x=14.75$ mm.

5.2.3 Propagated Statistical Uncertainty

An example of statistical uncertainty for planes II and III are shown in Figures 5.19 and 5.20, respectively. This component of uncertainty is also relatively small when compared to magnification. Although this component is expected to go to zero as $N \rightarrow \infty$ for some components, it does not trend as quickly as the residual for mean components which are first order statistics.

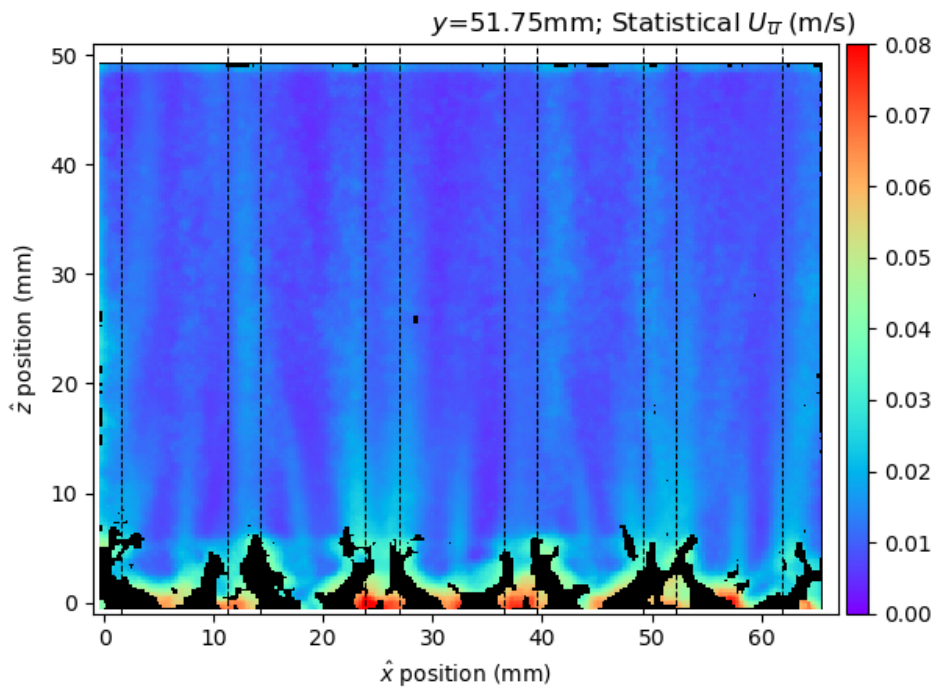


Figure 5.19: Statistical uncertainty for mean transverse velocity of plane II at $y=51.75$ mm.

The random nature of this statistical uncertainty is somewhat visible in the minor tertiary peaks which are exhibited in the bulk flow, especially in the middle of rods which are the larger gaps between the dotted vertical lines. Although this is not as pronounced as is seen in the residual uncertainty, it indicates the value of a large sample size to draw from. As $N \rightarrow \infty$, This uncertainty can be further reduced.

Statistical uncertainty components for the transverse RMS velocity components are portrayed

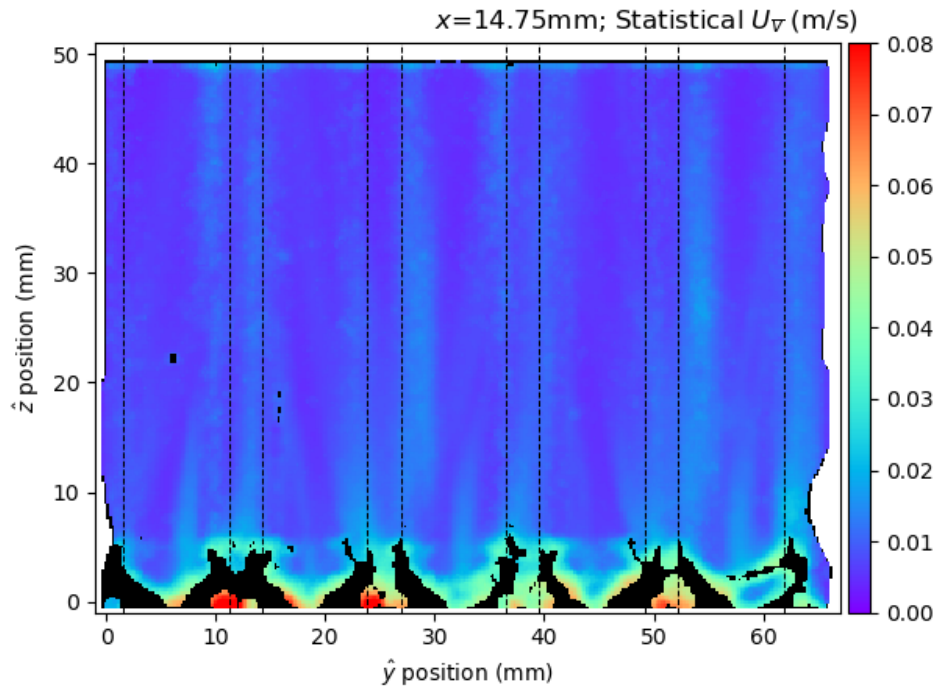


Figure 5.20: Statistical uncertainty for mean transverse velocity of plane IIII at $x=14.75$ mm.

in Figures 5.21 and 5.22. These show a greater uncertainty than the first order statistical uncertainty for the means discussed above. This correlates to a shift in dominant uncertainty, as these second order statistics are of the same magnitude as the residuals, which is not the case for mean velocity uncertainties. Additional measurements would aid in decreasing these values, which is the case for all statistical uncertainty.

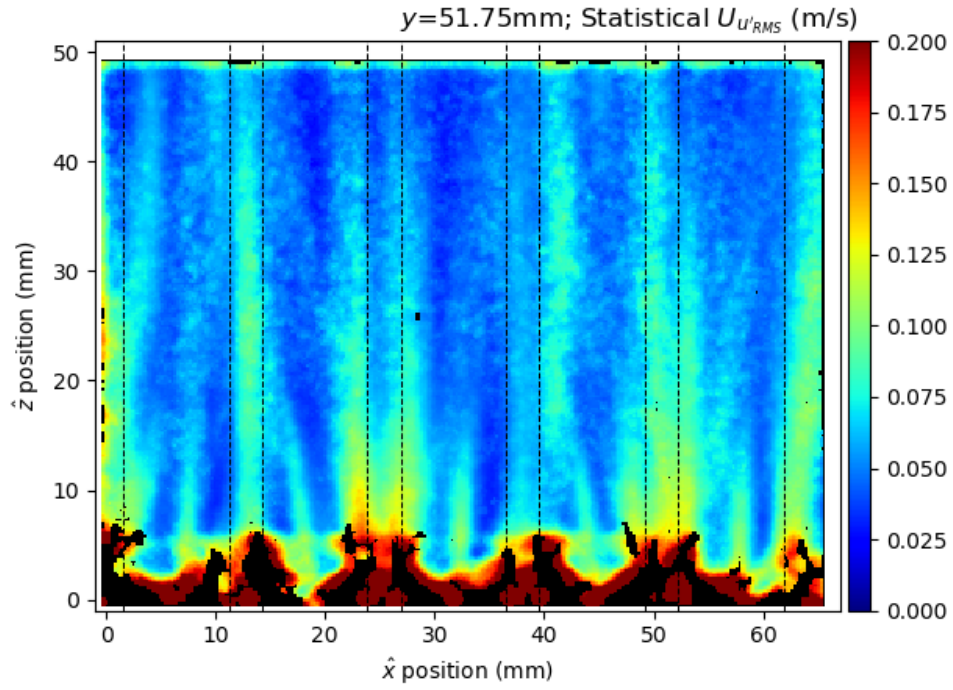


Figure 5.21: Statistical uncertainty for transverse RMS velocity of plane II at $y=51.75$ mm.

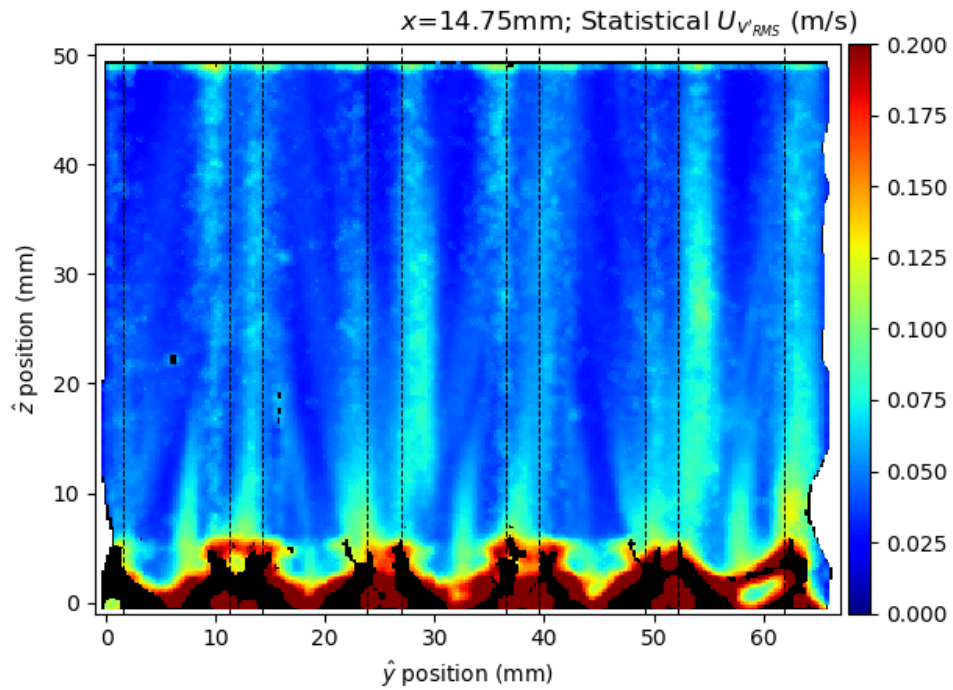


Figure 5.22: Statistical uncertainty for transverse RMS velocity of plane III at $x=14.75$ mm.

5.2.4 Combined Uncertainty Results

For each measured and derived velocity component, each of the above illustrated uncertainties were combined in quadrature as described in Equations 4.11. The combined uncertainty for mean transverse velocity of planes II and III are presented in Figures 5.23 and 5.24, respectively.

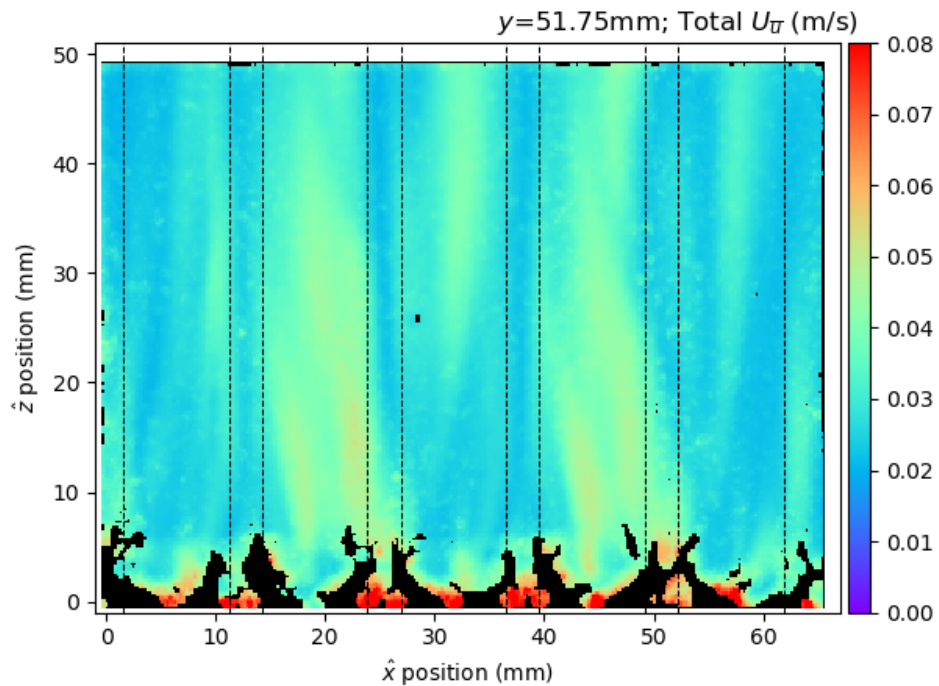


Figure 5.23: Combined uncertainty for mean transverse velocity of plane II at $y=51.75$ mm.

Combined uncertainty for the first order statistical means can be seen to be dominated by the physical calibration uncertainty. This uncertainty, while the largest source, was still well within acceptable experimental error for the presented measurements, and approximately equal to tolerances of hardware used in loop and bundle construction. Improved manufacturing processes and higher quality test section and rod materials may lead to a reduction in this uncertainty in future experiments.

The combined uncertainty for RMS transverse velocity of planes II and III are presented in

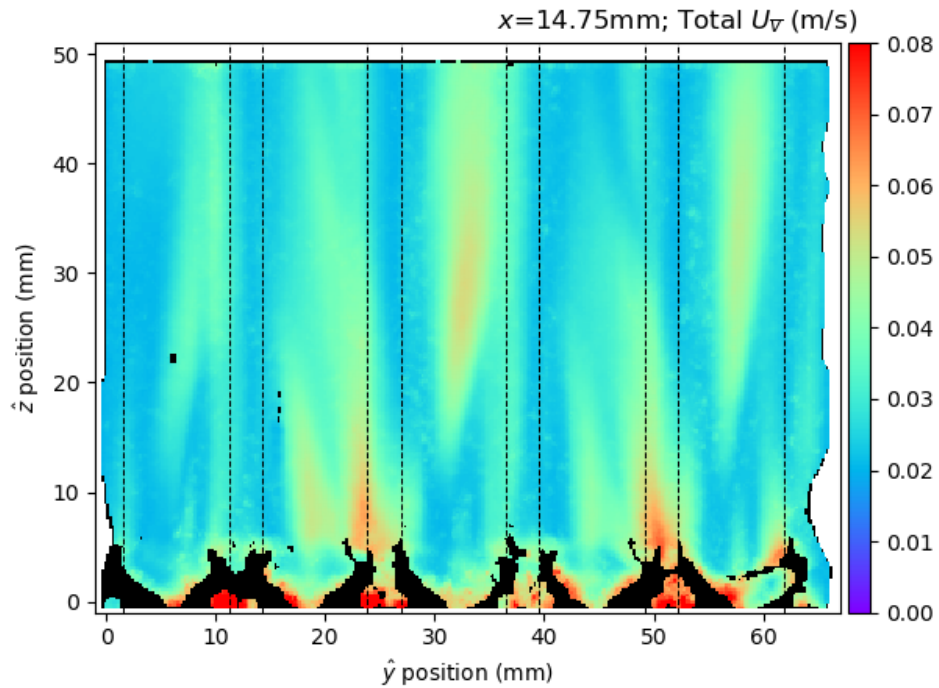


Figure 5.24: Combined uncertainty for mean transverse velocity of plane III at $x=14.75$ mm.

Figures 5.25 and 5.26, respectively. This uncertainty is seen to be random in nature, which is to be expected for uncertainties of statistical components of a value measured in a statistically random sampling manner, as was accomplished for this dissertation. More measurements are the only way to greatly reduce this uncertainty, which was within acceptable experimental error for the data set presented.

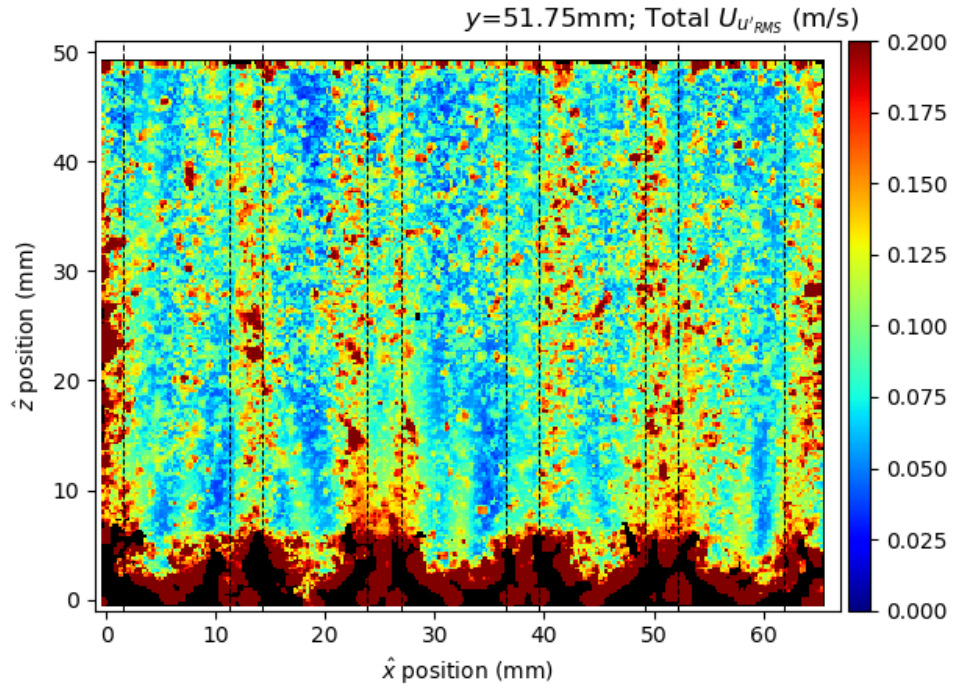


Figure 5.25: Combined uncertainty for transverse RMS velocity of plane II at $y=51.75$ mm.

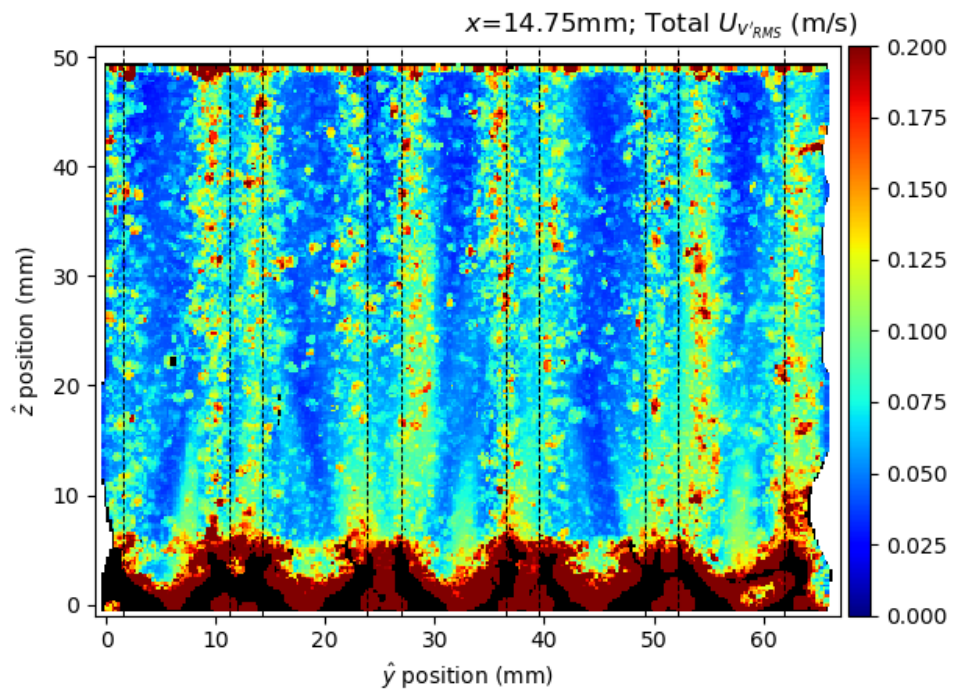


Figure 5.26: Combined uncertainty for transverse RMS velocity of plane III at $x=14.75$ mm.

5.3 Combined Two Dimension Two Component Particle Image Velocimetry Results

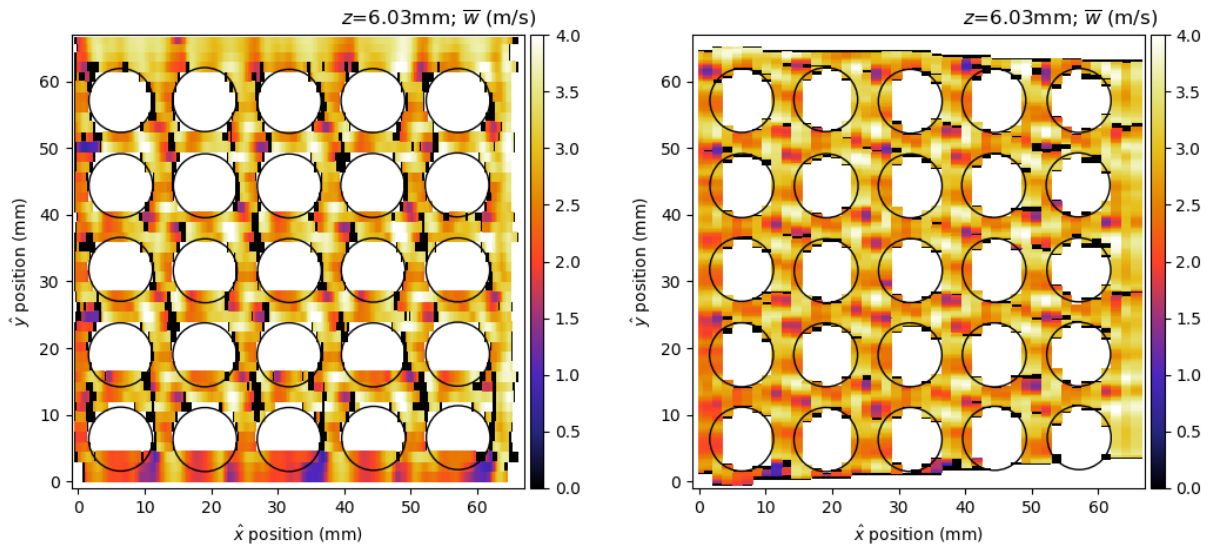
As described in Section 4.4, each of the planes mean data was concatenated into a single dataset. For each test 1 and 2, this resulted in two 3D2C data sets each with 2.9×10^6 vector points. Many of the planes, which exhibited large x - or y -normal cross sections of rods, were useful in quantifying subchannel velocity profiles, although they contained largely empty vector data within the rods. The 3D2C measurements were sliced in a z -normal plane, and plotted for various axial positions.

5.3.1 Mean Velocity

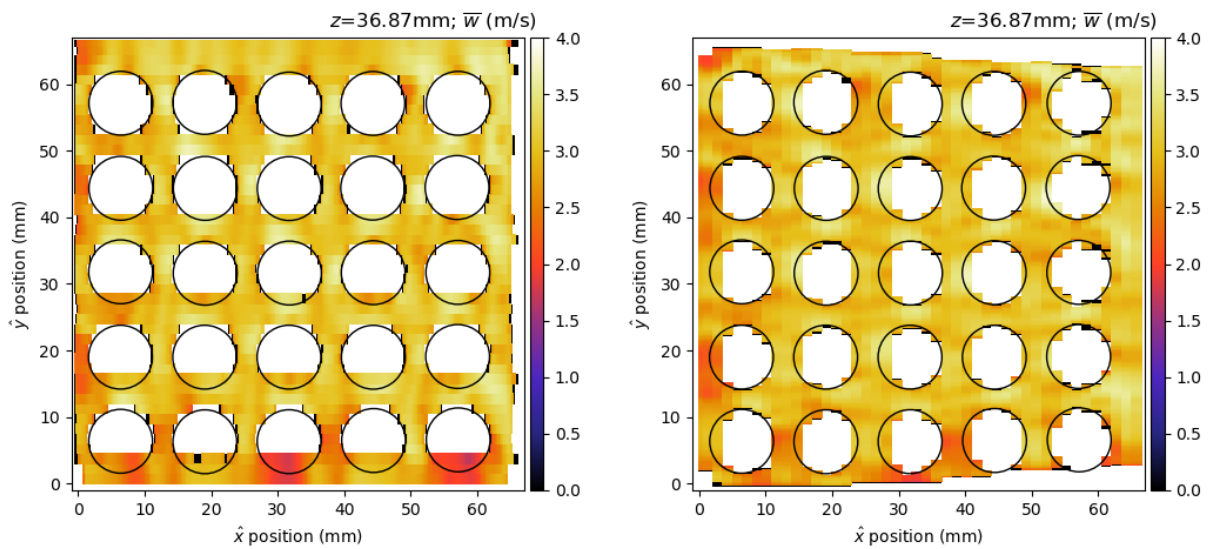
To compare the axial velocity measurements made in tests 1 and 2, w_1 and w_2 were plotted side by side at a z plane nearest to the mixing vane tips, which are presented in Figure 5.27a. These redundant measurements were qualitatively compared to one another to determine the effectiveness of concatenating planes which have a relatively thick Δx_i when compared to the vector spacing along a plane's height or width. The axial velocity peaks can be somewhat distinguished in the subchannels to be at opposing positions approximately 30° or 60° off an x -parallel line drawn through each subchannel, as is exhibited in the measurements made in the KAERI benchmark [8]. Data presented in Holloway et al and others [5, 6, 10] show similar shapes, but at a 90° rotation. This is highlighted further in the interpolated results in Section 5.4.

The flattening of the axial velocity profile downstream of the mixing vane can be observed in comparison between the slices at $z=6.03$ and 36.87 mm. This flattening of velocity profile correlates to a spatial average of 2.84 m/s which is calculated from desired Re near $28,000$. This profile flattening is one of the primary reasons for use of mixing vanes in PWRs, as a flattened velocity profile does not exhibit the high levels of mixing as required for effective thermal transfer in a coolant.

The mean transverse velocity components were also plotted side by side for comparison at a number of axial heights and are portrayed in Figure 5.28. The velocity profiles are plotted with the same color gradient to more clearly portray the differences in velocity near and far downstream of



(a) $z=6.03$ mm

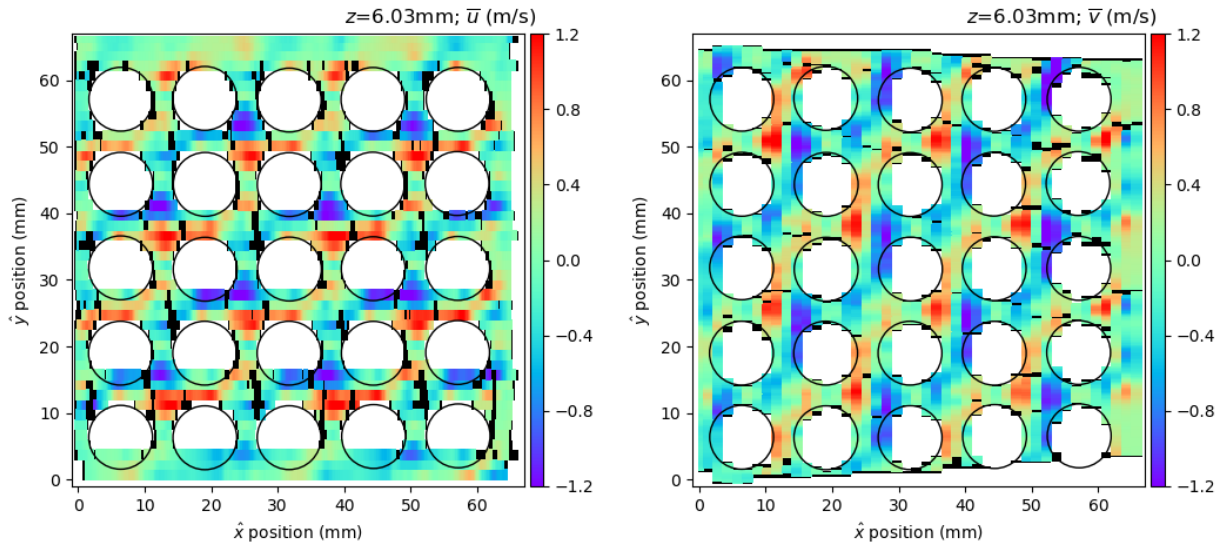


(b) $z=36.87$ mm

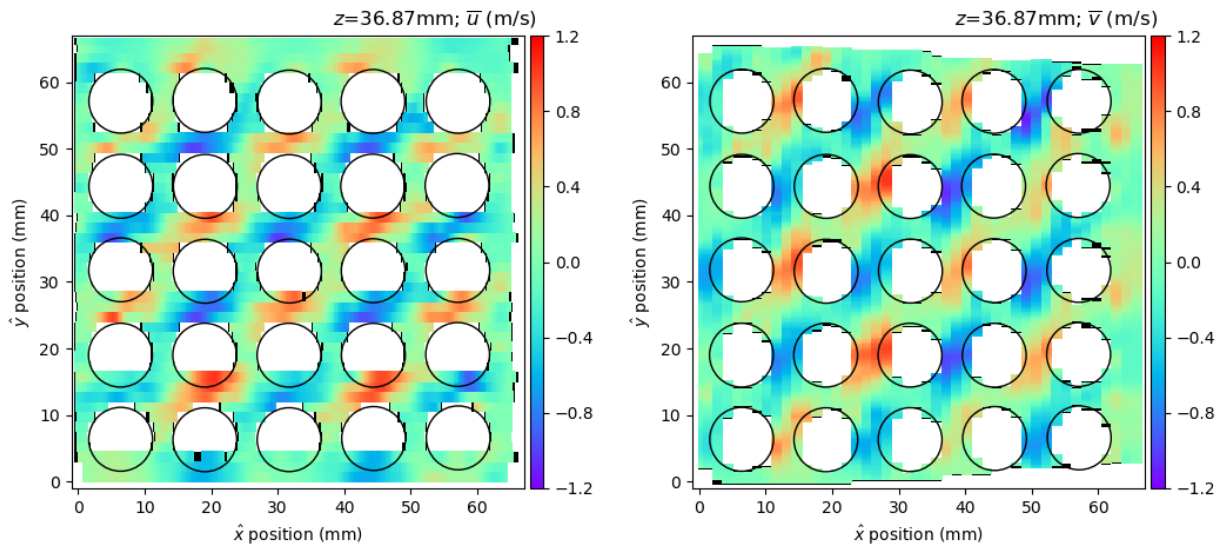
Figure 5.27: Mean axial velocity components \overline{w}_1 , and \overline{w}_2 for test 1 (left) and test 2 (right), respectively. Slices at $z=6.03$ mm (5.27a) and $z=36.87$ mm (5.27b).

the mixing vane. At the lower $z=6.03$ mm, the alterations to transverse velocity can be seen to be highly local with large gradients. Each of the subchannels appears to have two large competing velocity trends. Further from the mixing vane ($z=36.87$ mm), these strong transverse velocity peaks appear to exist more in the narrow space between adjacent rods, which alternate direction

with each p . Subchannels still exhibit crosscurrent flow, which shows a symmetry about any $2p$ shift, although it is not as strong as very near to the vanes. This is to be expected for any viscous fluid, which tends to smooth velocity profiles as is shown with the axial components of the fluid velocity.



(a) $z=6.03$ mm



(b) $z=36.87$ mm

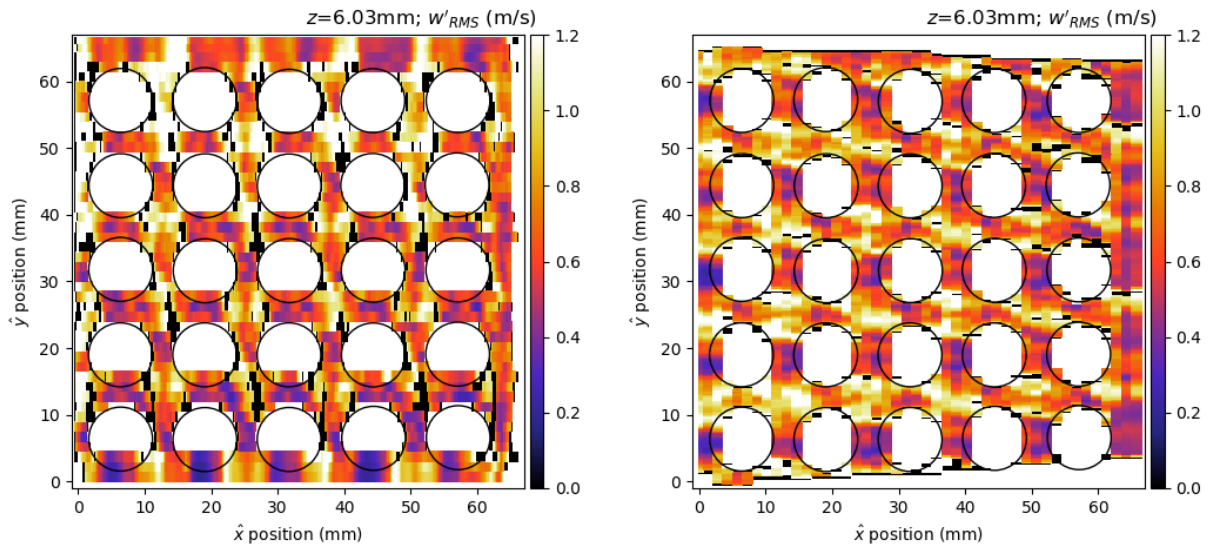
Figure 5.28: Mean transverse velocity components \bar{u} , and \bar{v} for test 1 (left) and test 2 (right), respectively. Slices at $z=6.03$ mm (5.28a) and $z=36.87$ mm (5.28b).

5.3.2 Fluctuating Root Mean Square & Shear Stress

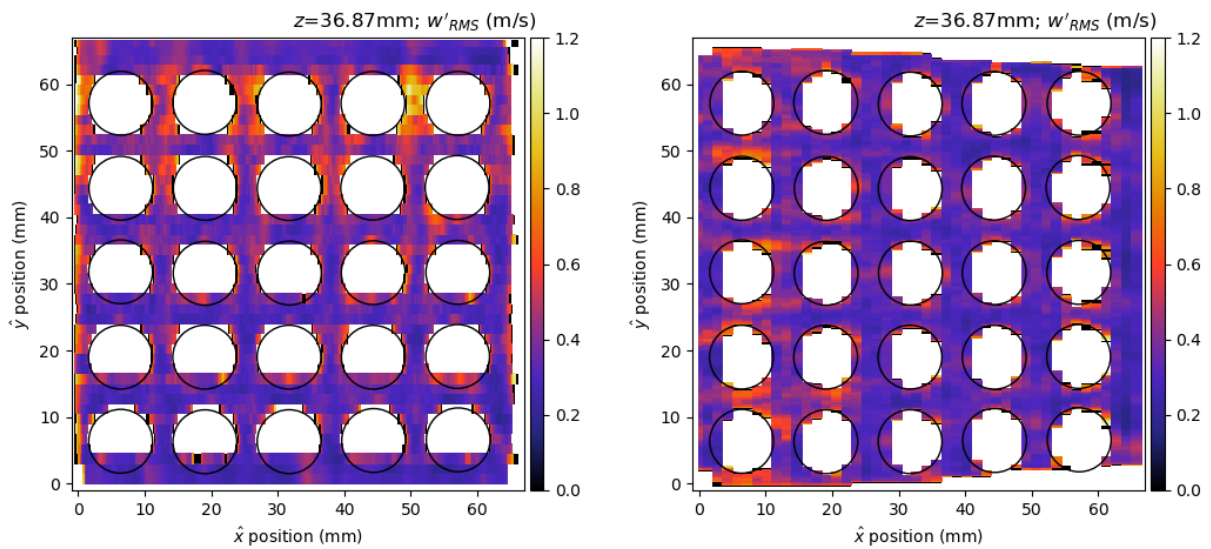
The RMS was calculated for each velocity component measured in both tests, as illustrated in Section 5.1. Similarly as was done with the mean components, the redundant axial velocity RMS components were plotted side by side to qualitatively determine an effectiveness of the scanning PIV method. Results for the RMS slices are contained in Figure 5.29. This plot begins to show the possible weakness of the scanning method, as patterns become much more difficult to discern, and symmetry is less coherent between the two tests. Still, good symmetry can be seen within a single tests concatenated results from a $2p$ shift. This can be similarly observed in the RMS of the horizontal velocity components which are contained in Figure 5.30.

Moving further from the mixing vane, as in Figures 5.29b and 5.30b, the decay of turbulence can be observed. A greater than 80% decrease in relative turbulent intensity can be observed just within the FOV for the single camera which was utilized for ROI analysis. Of interest in the further downstream plots is the perceived increase in RMS velocity components near the y maximum coordinate in test 1 and near the x minimum coordinate in test 2. These correlate to the maximum distance between the particle illuminating laser plane and the CCD camera, which acts as a qualitative indicator in the effect of the MIR in image collection. As discussed in Section 5.1, positions which are “behind” relatively large number of rod/fluid interfaces experience greater refraction of the particle-reflected light. This refraction of light throughout the test section before it is able to reach the camera adds some uncertainty to each measurement. This leads to an increase in statistical uncertainty, which is difficult to quantify. Ways to reduce this uncertainty may include using a camera at each side of the test section, when possible, to minimize the material through which the illumination plane is observed; or the collection of more image pairs, which will always lead to a decrease in statistical uncertainty.

For each frame, the two fluctuating components were combined in a simple product termed the Reynolds shear stress, which is the difficult term in Equation 1.6. The concatenated shear stress datasets were sliced at the same z planes 6.03 mm and 36.87 mm for analysis which are shown in Figure 5.31.



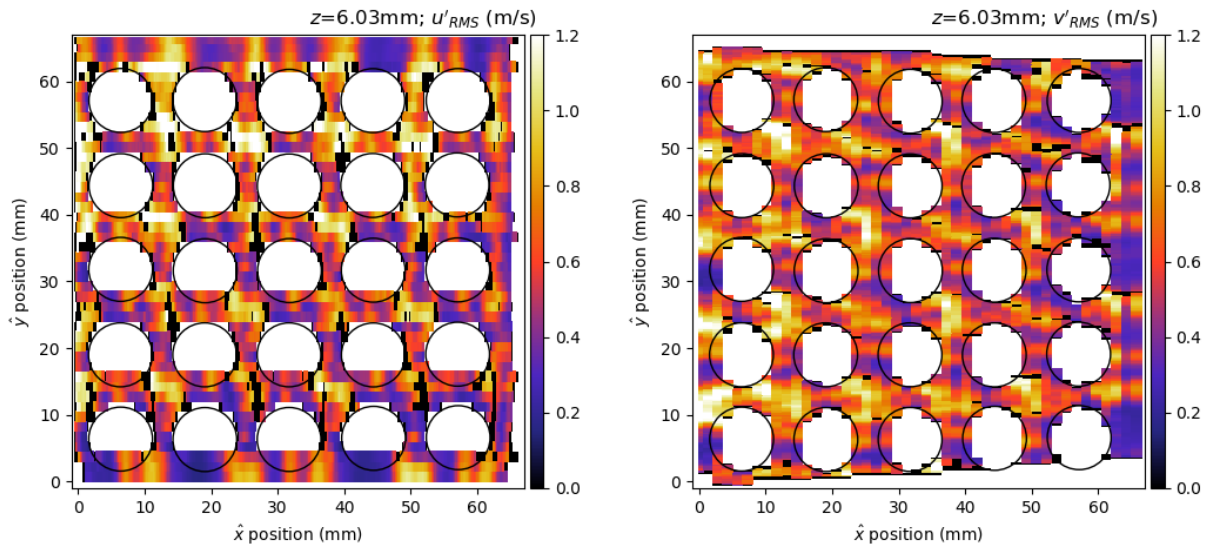
(a) $z=6.03$ mm



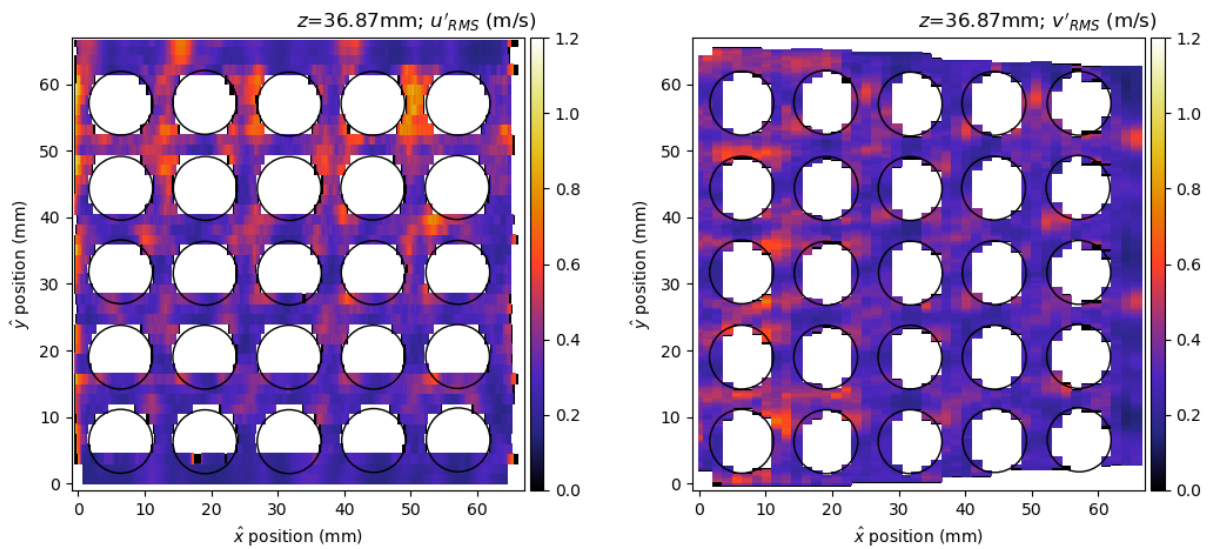
(b) $z=36.87$ mm

Figure 5.29: Axial RMS velocity components $w'_{1,RMS}$, and $w'_{2,RMS}$ for test 1 (left) and test 2 (right), respectively. Slices at $z=6.03$ mm (5.29a) and $z=36.87$ mm (5.29b).

As it is for calculation in any CFD effort, shear stress is one of the most difficult derived quantities to measure. This is demonstrated in the irregular patterns and overall incoherent nature of shear stress plots. Interior subchannels exhibit some symmetry among $2p$ shifts, which is expected for the mixing vane geometry, and also seen in the previous plots. These patterns are much more



(a) $z=6.03$ mm



(b) $z=36.87$ mm

Figure 5.30: Transverse RMS velocity components u'_{RMS} , and v'_{RMS} for test 1 (left) and test 2 (right), respectively. Slices at $z=6.03$ mm (5.30a) and $z=36.87$ mm (5.30b).

difficult to discern in the exterior and near wall subchannels. This is especially difficult to combat, as only one component of shear stress can be measured in a 2D2C PIV measurement plane, which means that there is no redundancy between the two tests for comparison. While large areas of increased Reynolds shear stress can be seen in every other main subchannel, very little can be de-

terminated other than large gradients exists near the mixing vane tips. Additional study of these same planes with 2D3C SPIV may be able to determine more of the shape of the shear stress profiles, and should be pursued further.

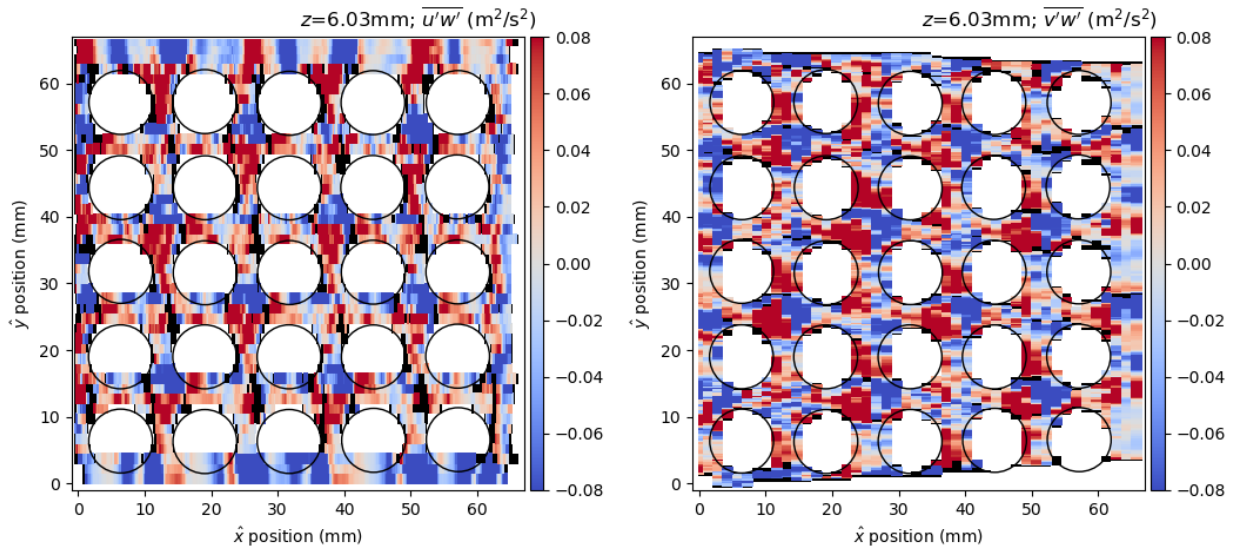
As seen in the velocity RMS plots, a rapid decay of turbulence and therefore shear stress, is observable between the slice near the mixing vane and further downstream, Figures 5.31a and 5.31b, respectively. This is to be expected within the rod bundle, which acts as an effective flow straightener without a mixing vane to disturb the fluid streamlines.

Further work to quantify Reynolds shear stress profiles would be beneficial for the presented geometry, especially in a z -normal plane, which would be able to measure the third component of shear stress, $\overline{u'v'}$, which could not be quantified with the current PIV setup. Otherwise, with the current dataset, better resolution is desired to speak quantitatively about shear stress profiles within the PWR geometry. An attempt to improve this resolution is undertaken in Section 5.4.

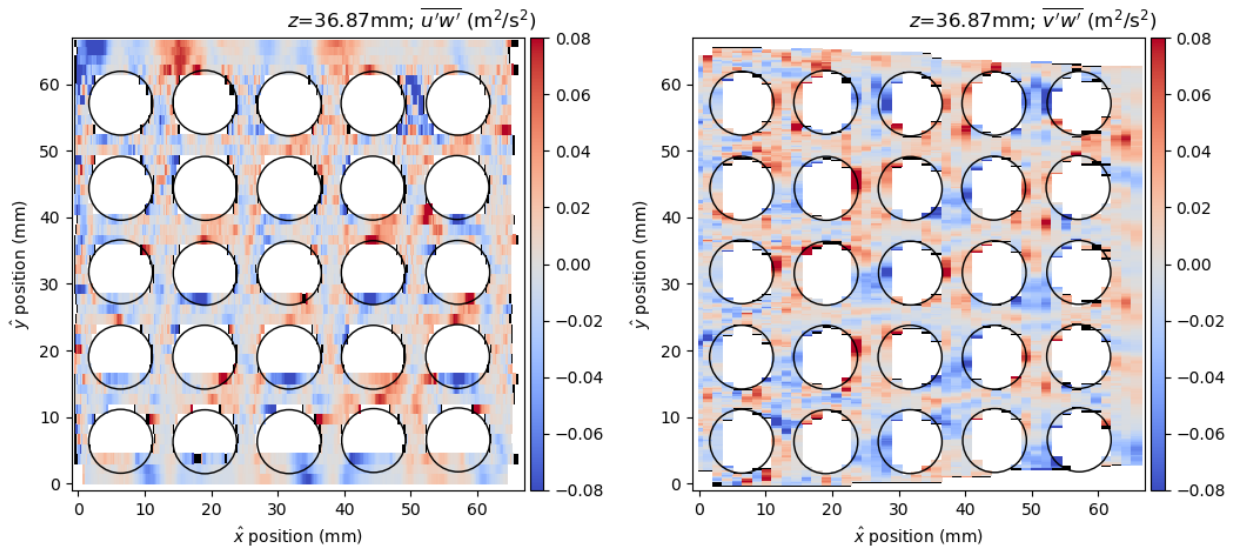
5.3.3 Vorticity

Vorticity, as described by Equation 1.8, was calculated for each of the measurements taken in both tests. The mean quantity of vorticity was similarly concatenated along with the velocity, RMS, and shear stress components as shown in Section 5.1. The mean transverse vorticity components, $\overline{\omega_y}$, and $\overline{\omega_x}$, were plotted at the same z slices in Figure 5.32.

Because vorticity is a calculation based on first order statistics, ie mean velocity, it shows much better coherent structures than those seen in the velocity RMS or shear stress profiles. Within a single test slice, good symmetry can be seen between subchannels separated by $2p$. As well, similar vortical structures can be seen between the two test slices, which is similarly observed in the velocity profiles. At $z=6.03$ mm (Figure 5.32a), vector elimination can be clearly seen in a regular pattern where the vanes protrude up into the dataset slice, which is the same vector elimination as exhibited in the other measured variables and derived quantities. More pronounced peaks and patterns in the vorticity can be seen downstream of the mixing vanes (Figure 5.32b), than when compared to the second order statistical quantities, which exhibit rather chaotic behavior far from the driving force of the mixing vane.



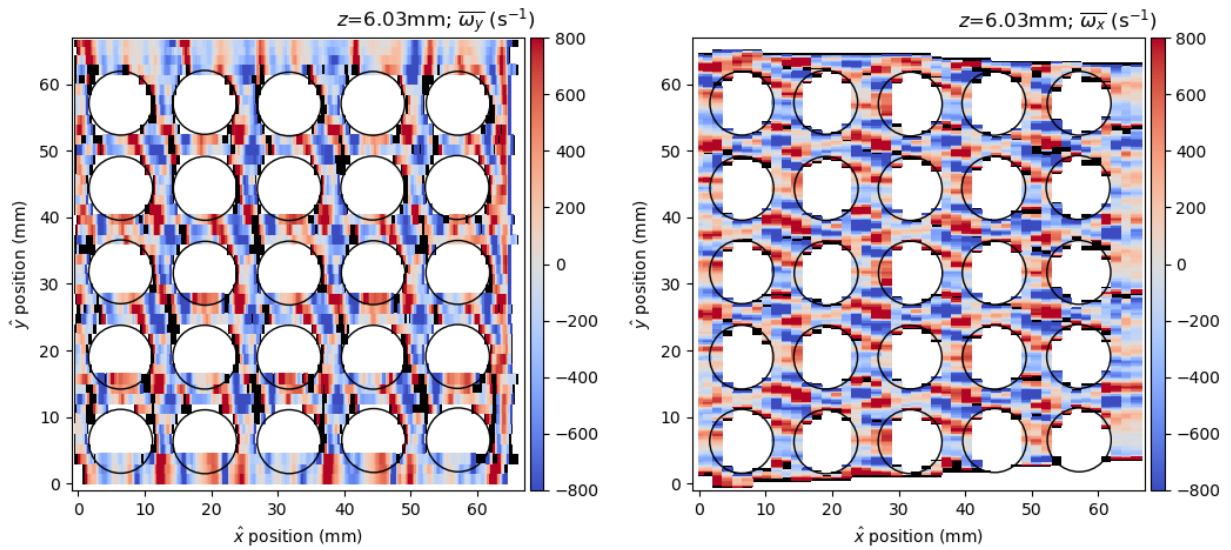
(a) $z=6.03$ mm



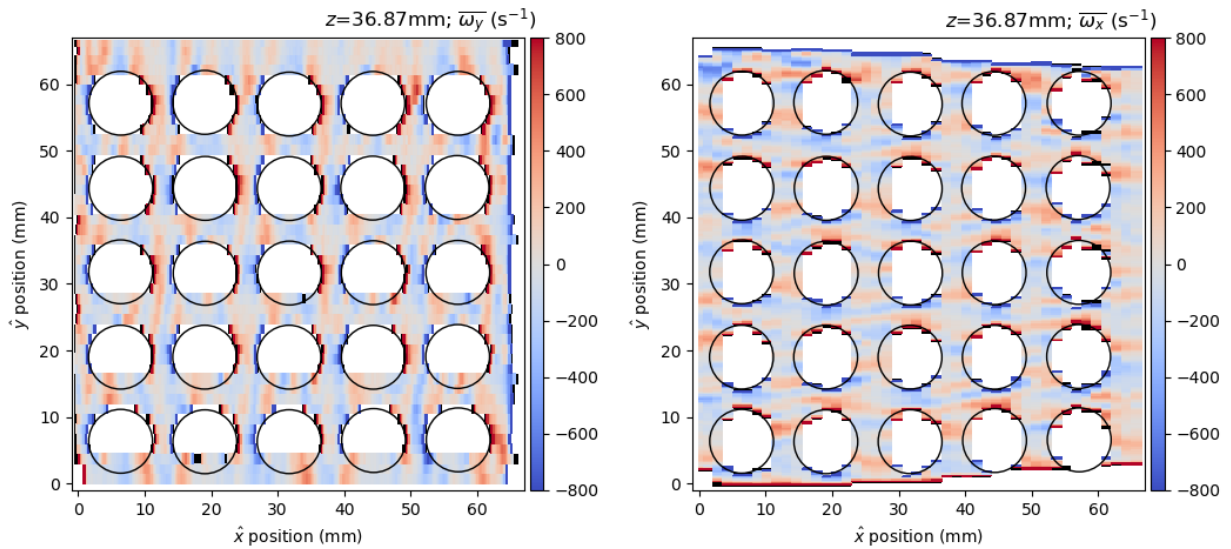
(b) $z=36.87$ mm

Figure 5.31: Mean Reynolds shear stress $\overline{u'w'_1}$, and $\overline{v'w'_2}$ for test 1 (left) and test 2 (right), respectively. Slices at $z=6.03$ mm (5.31a) and $z=36.87$ mm (5.31b).

Because of the apparent size of the vortical structures, it appears they may be good candidates for resolution improvement via interpolation, as presented in Section 5.4.



(a) $\overline{\omega}_i$ $z=6.03$ mm



(b) $\overline{\omega}_i$ $z=36.87$ mm

Figure 5.32: Mean transverse vorticity components $\overline{\omega}_y$, and $\overline{\omega}_x$ for test 1 (left) and test 2 (right), respectively. Slices at $z=6.03$ mm (5.32a) and $z=36.87$ mm (5.32b).

5.4 Interpolated Three Dimension Three Component Particle Image Velocimetry Results

Following observation of the sliced data, an attempt to improve resolution for the data, as well as a uniform grid mapping for 1:1 variable comparison, was achieved via the trilinear interpolation described in Section 4.4. For an arbitrary selected (x, y, z) in the ROI, interpolation occurred between all eight adjacent datapoints which were inversely weighted based on distance from the point of interest. Interpolated results are plotted on a simply modified z^+ axis which is defined as in Equation 5.1.

$$z^+ = z - z_{\text{vane}}, \quad (5.1)$$

where z_{vane} is the length of the mixing vane tip away from the edge of the straps on the spacer grid, approximately 6.06 mm as indicated in Figure 5.33. Due to the size of an average pixel in the vertical 2D2C planar measurements, the spatially averaged position of the first vector placed above the mixing vane's tips does extend slightly into the vanes, however, this effect is very small, as it is less than two pixels (<0.06 mm).

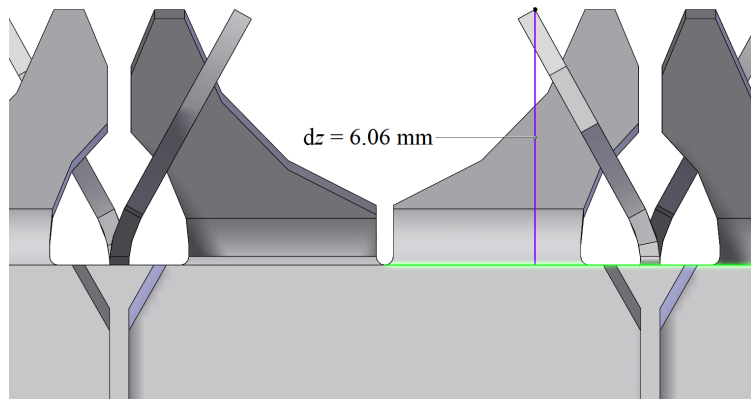


Figure 5.33: Length of mixing vane downstream of spacer grid used in determination of z_{vane} .

To better observe the high discretized interpolated data the four center subchannels, oriented as shown in Figure 5.34, were selected for data presentation. These subchannels represent the least

affected by no slip behavior due to the test section polycarbonate walls. As such, these four center subchannels are the closest to what may be seen in an average subchannel in a prototypical PWR.

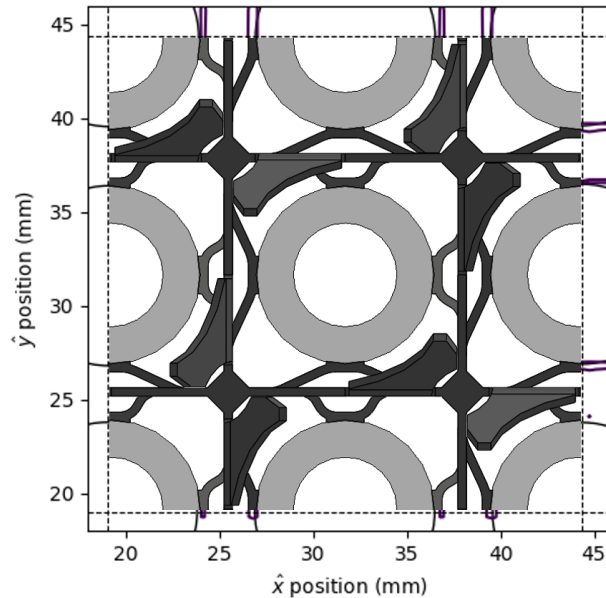


Figure 5.34: Cross section of mixing vane spacer grid region used in presentation of center four subchannel analysis.

5.4.1 Mean Velocity

To assess the trilinear interpolation results, and to compare velocity measurements made between the two tests, w_1 and w_2 were plotted side by side at a plane nearest to the tips of the mixing vane in Figure 5.35. As in Section 5.3, these redundant measurements results provide a qualitative assessment of the ability of the 45 plane coarse discretization to capture the same flow characteristics which are seen in the >290 vector fine discretization of the same spatial domain.

The axial velocity component clearly shows the dual peak pattern in the center four subchannels. These velocity peaks at approximate 30° or 60° lines off of x have been seen in studies such as Holloway et al and others [5, 6, 10], as well as the KAERI benchmark [8]. The peaks are in the open corners of the subchannels which are visible in Figure 5.34, while residing closer to the following flat surface of the adjacent mixing vane. Peaks appear to be independent of the spring or

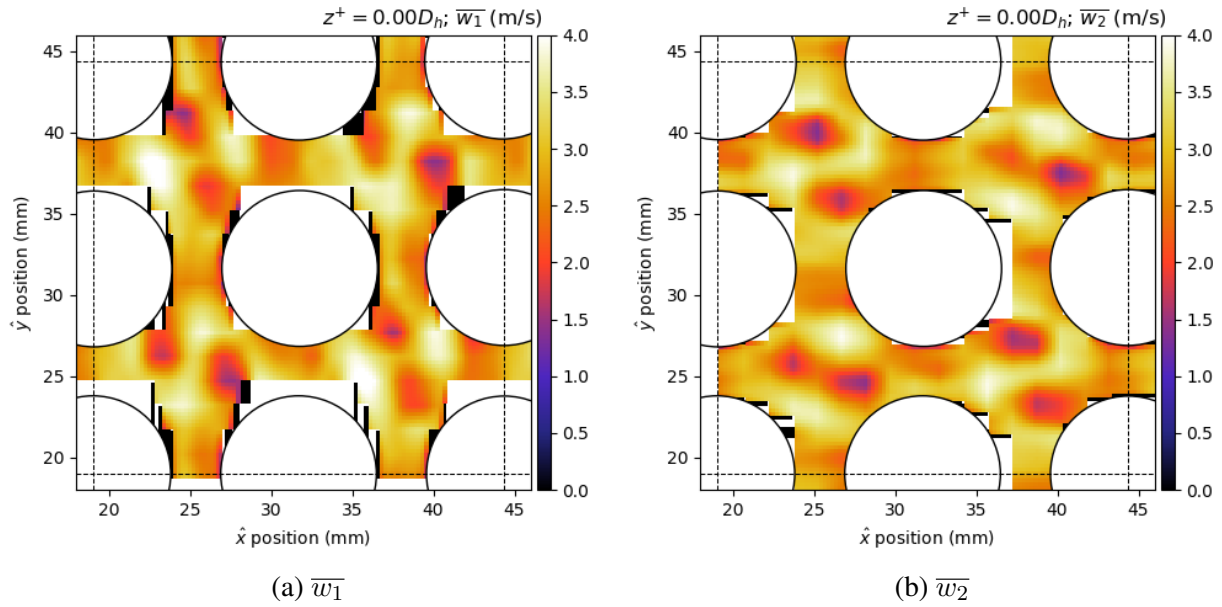


Figure 5.35: Mean axial velocity for center four subchannels at $z^+=0.0D_H$ ($z=6.03$ mm).

dimple shape below, which is likely due to the extremely small scale velocity disturbances these features generate. The symmetric peaks can be distinguished in both tests' results, and show good coherence in most regions which were not masked. Over masking in some of the regions near the rods can be seen to have eliminated a number of vectors, which prevented interpolation of data close to some of the rods.

Flattening of the velocity axial profile was again observed downstream of the mixing vane, as the profiles were plotted at $z^+=3.0D_H$ in Figure 5.36. This velocity approaches the expected average from the determination of Re , which is equal to 2.84 ± 0.05 m/s.

Profiles for the mean transverse velocity components were also interpolated and plotted for various heights downstream of the mixing vane. The profiles for both \overline{u} and \overline{v} at the mixing vane tips are shown in Figure 5.37. Good symmetry of the dominant transverse velocity peaks can be observed between the nonadjacent subchannels, as is expected for the presented geometry. As well, the swirl pattern of non-dominant velocity components has been clearly resolved, even though it was mostly indistinguishable in the combined profile slices without interpolation. This is

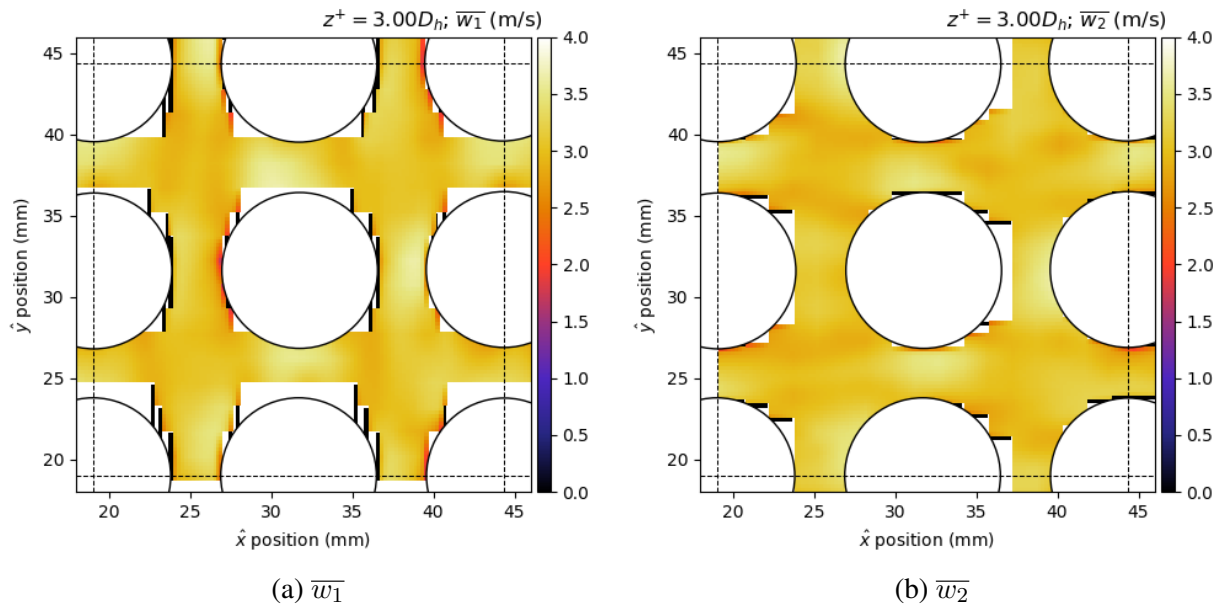


Figure 5.36: Mean axial velocity for center four subchannels at $z^+=3.0D_H$ ($z=36.84$ mm).

a good indicator that most, if not all, velocity scales have been resolved with the presented planar discretization.

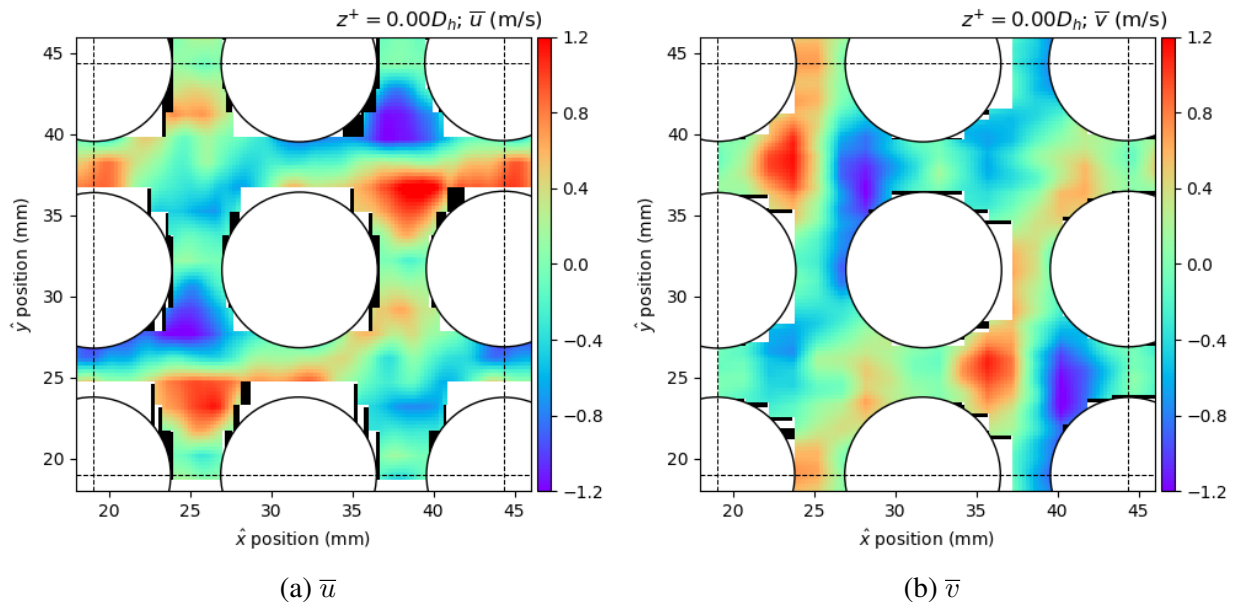


Figure 5.37: Mean transverse velocity for center four subchannels at $z^+=0.0D_H$ ($z=6.03$ mm).

Transverse velocity profiles further downstream of the mixing vane were plotted side by side. The downstream profiles, in Figure 5.38, show the movement of the transverse velocity peaks into the narrow space between rods, rather than the interior subchannel peaks which are seen in the profiles immediately downstream of the vanes. The same expected symmetry of nonadjacent subchannels can again be observed.

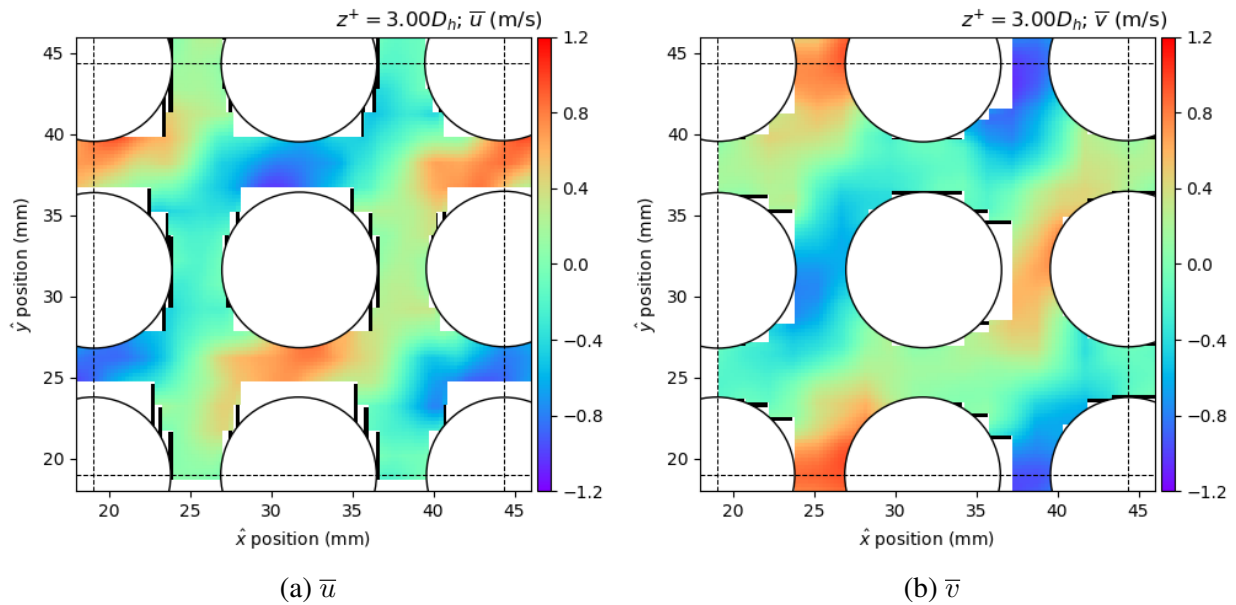


Figure 5.38: Mean transverse velocity for center four subchannels at $z^+ = 3.0D_H$ ($z = 36.84$ mm).

With a 1:1 mapping of u, v, w , the vector components were then combined into a single velocity vector magnitude, and plotted on the same slices in z . In-plane direction of the vectors was indicated with magnitude arrows in Figure 5.39. Vectors were sample at $1/3$ for clarity in visualization. These plots show most clearly the previously seen axial-slice profiles as shown in the studies by Holloway et al and others [5, 6, 10], as well as the KAERI benchmark [8].

Decay of the highly swirling velocity profile can be seen between the two axial slice profiles at $z^+ = 0.0D_H$ ($z = 6.03$ mm) and $z^+ = 3.0D_H$ ($z = 36.84$ mm). The velocity approaches a two-directional shear flow profile, with shear boundary layers existing along diagonal lines where $x = y$, which are

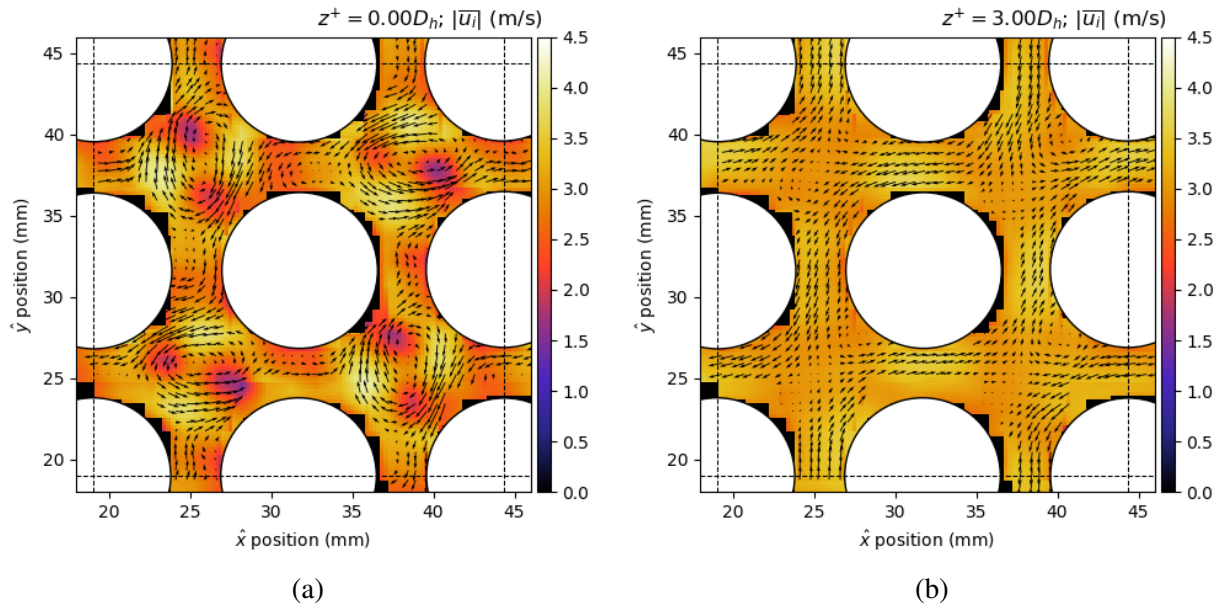


Figure 5.39: Mean velocity magnitude, $|\bar{u}_i|$, with transverse direction indicated by 1/3 sampled arrows for center four subchannels at $z^+=0.0D_H$ (5.39a) and $z^+=3.0D_H$ (5.39b).

parallel in each subchannel. Also of note is the clearly visible symmetry at the most narrow point between rods at the edges of the interior four subchannel domain. This repeatedly observed two-subchannel symmetry may be useful for system codes or subchannel calculations. Unfortunately, due to the coarse discretization of the direction normal to the most narrow width of the subchannel between adjacent rods, additional information about highly discretized momentum flux between subchannels cannot be determined.

5.4.2 Vorticity

From the mean fields presented in Section 5.3, a highly discretized vorticity field was generated from the interpolation described in Section 4.4. The absolute vorticity fields at the mixing vane tips are presented in Figure 5.40. The alternate subchannels again show good symmetry, even with the interpolation occurring from datasets which were not collected on the same domain. This is a good indicator that the number of planes used to discretize the ROI in the test section was sufficient to capture most of the scales of velocity. Additional planes may be able to better resolve the smaller

scale velocity components, however this may also require an improved laser optics setup, which was not readily available.

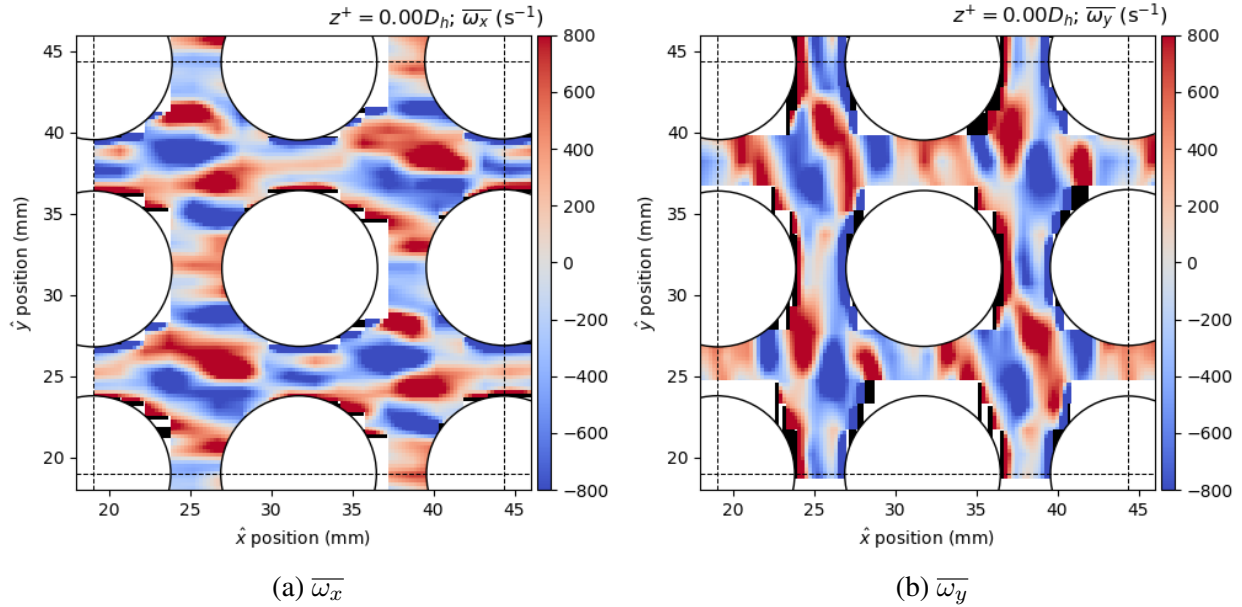


Figure 5.40: Mean transverse vorticity contours interpolated for center four subchannels at $z^+=0.0D_H$ ($z=6.03$ mm).

To quantify a characteristic vortical structure, the absolute vorticity field was nondimensionalized using the characteristic timescale, which is the largest eddy turnover time as described by Equation 4.1. With the vorticity nondimensionalized, contour lines where $\overline{\omega}_i t_L = \pm 1$ were presented in Figure 5.41, and where $\overline{\omega}_i t_L = \pm 2$ presented in Figure 5.42 for the axial slice immediately downstream of the mixing vanes ($z^+=0.0D_H$).

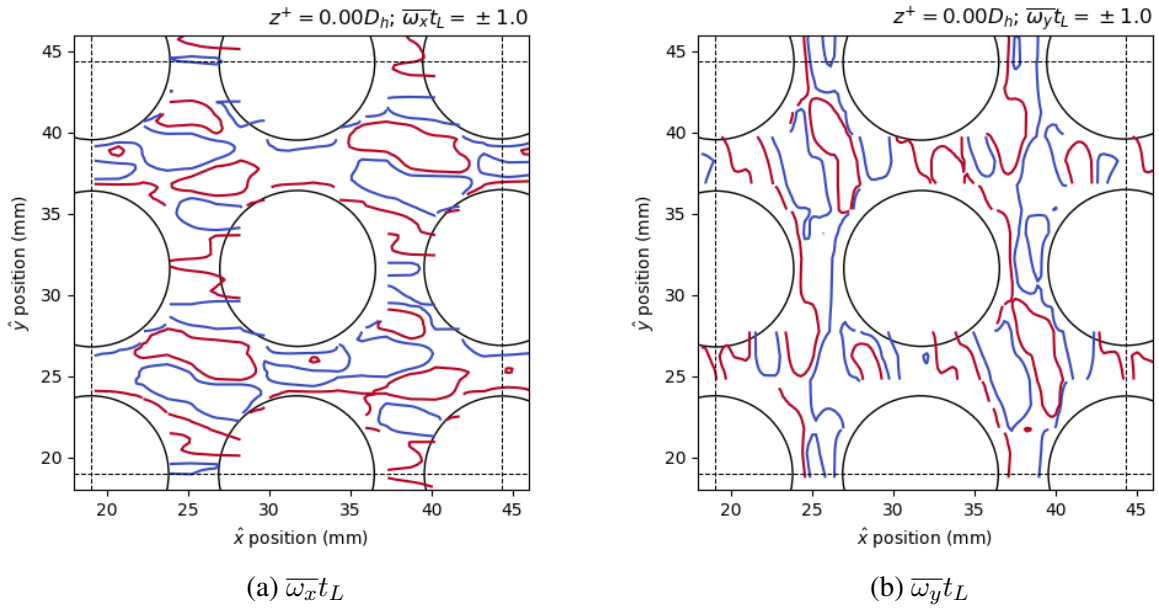


Figure 5.41: Mean transverse vorticity contours where $\overline{\omega_i}t_L = \pm 1$ for center four subchannels at $z^+ = 0.0D_H$ ($z = 6.03$ mm).

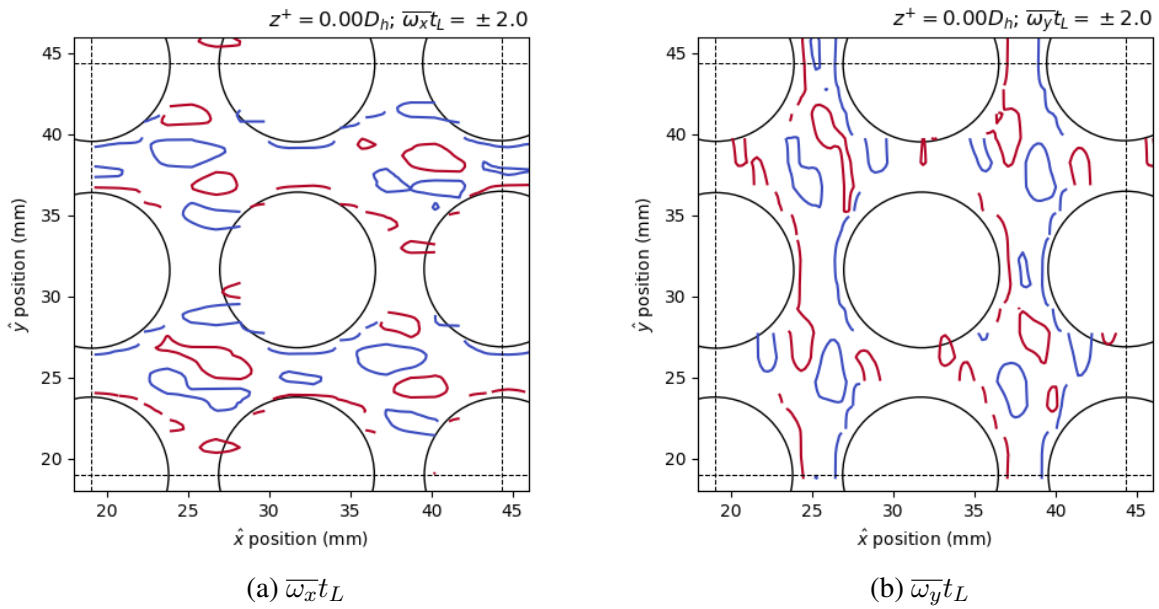


Figure 5.42: Mean transverse vorticity contours where $\overline{\omega_i}t_L = \pm 2$ for center four subchannels at $z^+ = 0.0D_H$ ($z = 6.03$ mm).

6. CONCLUSIONS & FUTURE WORK

The objective of the presented research was to produce full field velocity data in a 5×5 square-lattice rod bundle with PWR prototypical mixing vane spacer grids. Specifically, the experimental data was intended to quantify uncertainty of vector measurement and positioning within the ROI, as well as the first to measure velocity near, and even below, the tips of the mixing vanes. The methodology to meet this objective was the utilization of an MIR test section and mock fuel rod bundle. To this end, a new experimental flow facility with laser-based optical measurement techniques such as 2D2C PIV and 2D3C SPIV was constructed.

Images were collected in each of forty five, 1.5 mm thick, planes in both a y -normal, and x -normal orientation. The images were used in generation of a statistical significant number of velocity measurements of u, w , and v, w , respectively. First- and second-order statistics were calculated for each of the 90 measurement sets, as well as derived quantities such as Reynolds shear stress and vorticity. The ensemble averaged datasets were concatenated based on laser sheet placement within the mixing vane test section ROI. Slices of the datasets were then quantified at various z -normal planes which were axially downstream of the mixing vane.

A detailed UQ was performed on the two datasets, which employed a number of recognized methods for determining statistical uncertainty, as well as a novel UQ of the physical calibration, and a statistical residual calculation for generation of a combined expanded uncertainty for each quantity presented.

From the two combined datasets, a highly resolved full 3D3C velocity vector field was generated using a simple trilinear interpolation algorithm for the center four subchannels, which most closely represent an average subchannel far from wall effects in a prototypical PWR geometry. The interpolated data revealed a number of recognized characteristics which have been observed by earlier studies of similar geometry. As well, redundant data showed good comparison after interpolation, indicating a verification of the scanning PIV method employed. Derived components from the dataset showed good symmetry, as expected from physical phenomena.

Presented experimental work may be used to further the understanding of in-core coolant behavior in prototypical PWR geometry to facilitate possible uprates, as well as license extension efforts. The data may be used for improvements in system and subchannel codes which are commonly used in efforts to meet regulatory needs. Further, the highly resolved data presented may be used for V&V of CFD turbulence models, which demand detailed vetting before use in generalized design efforts.

Further work includes a large number of images which were collected, and are available for use in expansion of the current 3D3C dataset. These images were collected concurrent with the presented data source, and provide similarly detailed data beyond the presented $4.8D_H$ ROI. This data may also provide a further understanding of the length of a mixing vane's effects within the rod bundle.

An additional image set was also collected with both cameras simultaneously as z -normal planes for use in 3D2C SPIV analysis. This image set would be useful in a similar concatenation manner for generation of another 3D3C velocity field to be compared to the current presented data set. As well, images were collected upstream of the mixing vane which may be used for boundary condition determination in CFD analysis efforts.

REFERENCES

- [1] E. E. Dominguez-Ontiveros and Y. A. Hassan, “Non-intrusive experimental investigation of flow behavior inside a 5×5 rod bundle with spacer grids using piv and mir,” *Nuclear Engineering and Design*, vol. 239, no. 5, pp. 888–898, 2009.
- [2] M. E. Conner, Y. A. Hassan, and E. E. Dominguez-Ontiveros, “Hydraulic benchmark data for pwr mixing vane grid,” *Nuclear Engineering and Design*, vol. 264, pp. 97–102, 2013.
- [3] T. Nguyen and Y. Hassan, “Stereoscopic particle image velocimetry measurements of flow in a rod bundle with a spacer grid and mixing vanes at a low reynolds number,” *International Journal of Heat and Fluid Flow*, vol. 67, pp. 202–219, 2017.
- [4] M. Childs, M. Marciniak, D. T. Nguyen, and Y. Hassan, “Stereoscopic PIV experimental investigation of flow behavior in a 5x5 spacer grid with mixing vane,” in *American Nuclear Society Annual Meeting*, 2017.
- [5] H. L. McClusky, M. V. Holloway, D. E. Beasley, and M. E. Conner, “Development of swirling flow in a rod bundle subchannel,” *Journal of Fluids Engineering*, vol. 124, no. 3, pp. 747–755, 2002.
- [6] H. L. McClusky, M. V. Holloway, T. A. Conover, D. E. Beasley, M. E. Conner, and L. D. Smith, “Mapping of the lateral flow field in typical subchannels of a support grid with vanes,” *Journal of fluids engineering*, vol. 125, no. 6, pp. 987–996, 2003.
- [7] S. K. Chang, S. K. Moon, W. P. Baek, and Y. D. Choi, “Phenomenological investigations on the turbulent flow structures in a rod bundle array with mixing devices,” *Nuclear Engineering and Design*, vol. 238, no. 3, pp. 600–609, 2008.
- [8] S.-K. Chang, S. Kim, and C.-H. Song, “Turbulent mixing in a rod bundle with vaned spacer grids: Oecd/nea–kaeri cfd benchmark exercise test,” *Nuclear Engineering and Design*, vol. 279, pp. 19–36, 2014.

- [9] M. E. Conner, E. Baglietto, and A. M. Elmahdi, “CFD methodology and validation for single-phase flow in PWR fuel assemblies,” *Nuclear Engineering and Design*, vol. 240, no. 9, pp. 2088–2095, 2010.
- [10] M. V. Holloway, H. L. McClusky, D. E. Beasley, and M. E. Conner, “The effect of support grid features on local, single-phase heat transfer measurements in rod bundles,” in *ASME 2003 Heat Transfer Summer Conference*, pp. 547–560, American Society of Mechanical Engineers, 2003.
- [11] S. K. Yang and M. K. Chung, “Turbulent flow through spacer grids in rod bundles,” *Journal of Fluids Engineering*, vol. 120, no. 4, pp. 786–791, 1998.
- [12] S. K. Kang and Y. A. Hassan, “Computational fluid dynamics (CFD) round robin benchmark for a pressurized water reactor (PWR) rod bundle,” *Nuclear Engineering and Design*, vol. 301, pp. 204–231, 2016.
- [13] H. Castro, V. Silva, A. A. C. dos Santos, and M. Veloso, “5x5 rod bundle flow field measurements downstream a PWR spacer grid,” in *Proceedings of 2017 International Nuclear Atlantic Conference - INAC 2017, Belo Horizonte, Brazil*, 2017.
- [14] S. Benhamadouche, “On the use of (U)RANS and LES approaches for turbulent incompressible single phase flows in nuclear engineering applications,” *Nuclear Engineering and Design*, vol. 312, pp. 2 – 11, 2017. 16th International Topical Meeting on Nuclear Reactor Thermal Hydraulics.
- [15] V. . Committee *et al.*, “Standard for verification and validation in computational fluid dynamics and heat transfer,” *American Society of Mechanical Engineers, New York*, 2009.
- [16] W. L. Oberkampf and B. L. Smith, “Assessment criteria for computational fluid dynamics model validation experiments,” *Journal of Verification, Validation and Uncertainty Quantification*, vol. 2, no. 3, p. 031002, 2017.
- [17] B. L. Smith, “The difference between traditional experiments and cfd validation benchmark experiments,” *Nuclear Engineering and Design*, vol. 312, pp. 42–47, 2017.

- [18] P. J. Roache, “Interpretation of validation results following asme v&v20-2009,” *Journal of Verification, Validation and Uncertainty Quantification*, vol. 2, no. 2, p. 024501, 2017.
- [19] S. Hosokawa, T. Yamamoto, J. Okajima, and A. Tomiyama, “Measurements of turbulent flows in a 2×2 rod bundle,” *Nuclear Engineering and Design*, vol. 249, pp. 2–13, 2012.
- [20] G. E. McCreery, H. M. McIlroy, K. D. Hamman, and H. Zhang, “Design of wire-wrapped rod bundle matched index-of-refraction experiments,” in *16th International Conference on Nuclear Engineering*, pp. 595–605, American Society of Mechanical Engineers, 2008.
- [21] Z. Zhang, K. Suzuki, S. Hosokawa, and A. Tomiyama, “Motion of small bubbles near a grid spacer in a two by three rod bundle,” in *16th International Conference on Nuclear Engineering*, pp. 449–457, American Society of Mechanical Engineers, 2008.
- [22] S. B. Pope, *Turbulent flows*. IOP Publishing, 2001.
- [23] A. J. Majda and A. L. Bertozzi, *Vorticity and incompressible flow*, vol. 27. Cambridge University Press, 2002.
- [24] X. Li, Z. Mi, S. Tan, R. Wang, and X. Wang, “PIV study of velocity distribution and turbulence statistics in a rod bundle,” *Annals of Nuclear Energy*, vol. 117, pp. 305 – 317, 2018.
- [25] T. Nguyen, N. Goth, P. Jones, R. Vaghetto, and Y. Hassan, “Stereoscopic PIV measurements of near-wall flow in a tightly packed rod bundle with wire spacers,” *Experimental Thermal and Fluid Science*, vol. 92, pp. 420 – 435, 2018.
- [26] A. N. Bashkatov and E. A. Genina, “Water refractive index in dependence on temperature and wavelength: a simple approximation,” in *Saratov Fall Meeting 2002: Optical Technologies in Biophysics and Medicine IV*, vol. 5068, pp. 393–396, International Society for Optics and Photonics, 2003.
- [27] R. French, J. Rodríguez-Parada, M. Yang, R. Derryberry, and N. Pfeiffenberger, “Optical properties of polymeric materials for concentrator photovoltaic systems,” *Solar Energy Materials and Solar Cells*, vol. 95, no. 8, pp. 2077–2086, 2011.

- [28] C. Stoots, S. Becker, K. Condie, F. Durst, and D. McEligot, “A large-scale matched index of refraction flow facility for lida studies around complex geometries,” *Experiments in fluids*, vol. 30, no. 4, pp. 391–398, 2001.
- [29] N. Amini and Y. A. Hassan, “An investigation of matched index of refraction technique and its application in optical measurements of fluid flow,” *Experiments in fluids*, vol. 53, no. 6, pp. 2011–2020, 2012.
- [30] P. M. Bardet, C. D. Fu, C. E. Sickel, and N. A. Weichselbaum, “Refractive index and solubility control of para-cymene solutions,” in *2014 International Symposium on Applications of Laser Techniques to Fluid Mechanics, Instituto Superior Tecnico, Lisbon, Portugal*, 2014.
- [31] A. Arce, A. Marchiaro, O. Rodriguez, and A. Soto, “Liquid–liquid equilibria of limonene+linalool+ diethylene glycol system at different temperatures,” *Chemical Engineering Journal*, vol. 89, no. 1-3, pp. 223–227, 2002.
- [32] C. G. Works, “Pyrex glass code 7740 - material properties,” tech. rep., Corning Glass Works, New York, ID (United States), 1987.
- [33] N. E. Goth, *Design and PIV Measurements on a Wire-Wrapped 61-Rod Hexagonal Fuel Assembly Experimental Facility*. MS thesis, Texas A&M University, 2017.
- [34] J. H. Dymond and R. Malhotra, “The tait equation: 100 years on,” *International Journal of Thermophysics*, vol. 9, pp. 941–951, Nov 1988.
- [35] E. d. C. Andrade, “The viscosity of liquids,” 1930.
- [36] E. d. C. Andrade, “LVIII. a theory of the viscosity of liquids.–part II,” *The London, Edinburgh, and Dublin Philosophical Magazine and Journal of Science*, vol. 17, no. 113, pp. 698–732, 1934.
- [37] A. A. C. dos Santos, M. Childs, T. D. Nguyen, and Y. Hassan, “Convergence study and uncertainty quantification of average and statistical PIV measurements in a matched refractive index 5×5 rod bundle with mixing vane spacer grid,” *Experimental Thermal and Fluid Science*, vol. 102, pp. 215–231, 2019.

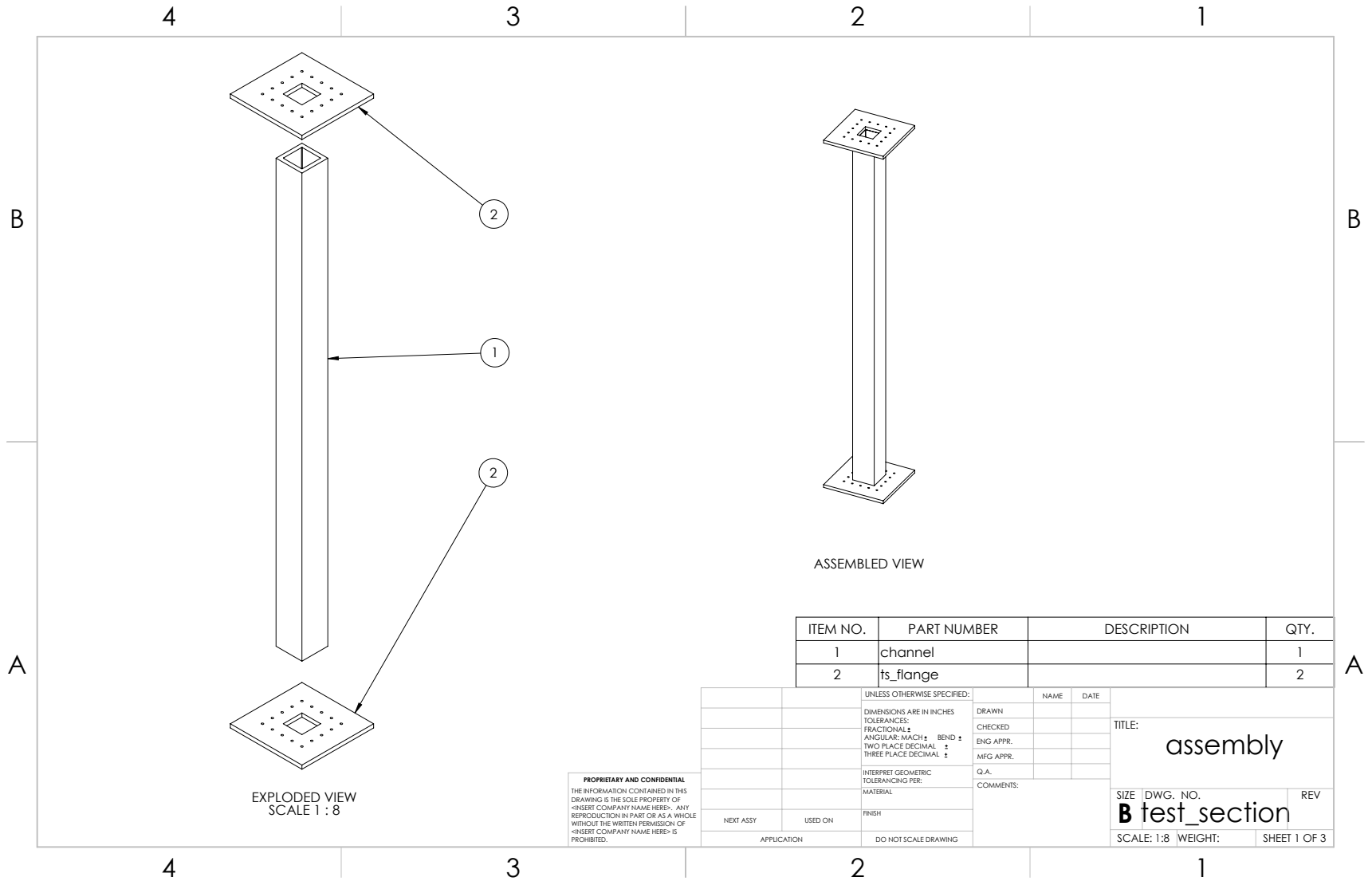
- [38] M. Raffel, C. E. Willert, J. Kompenhans, *et al.*, *Particle image velocimetry: a practical guide*. Springer Science & Business Media, 2007.
- [39] C. Tropea and A. L. Yarin, *Springer handbook of experimental fluid mechanics*, vol. 1. Springer Science & Business Media, 2007.
- [40] C. T. Rueden, J. Schindelin, M. C. Hiner, B. E. DeZonia, A. E. Walter, E. T. Arena, and K. W. Eliceiri, “Imagej2: Imagej for the next generation of scientific image data,” *BMC Bioinformatics*, vol. 18, p. 529, Nov 2017.
- [41] A. Eckstein and P. Vlachos, “A robust phase correlation DPIV processing algorithm for time resolved measurements,” in *Proceedings of the Seventh International PIV Symposium*, 2007.
- [42] A. Eckstein and P. P. Vlachos, “Assessment of advanced windowing techniques for digital particle image velocimetry (DPIV),” *Measurement Science and Technology*, vol. 20, no. 7, p. 075402, 2009.
- [43] A. Eckstein and P. P. Vlachos, “Digital particle image velocimetry (DPIV) robust phase correlation,” *Measurement Science and Technology*, vol. 20, no. 5, p. 055401, 2009.
- [44] T. Persoons and T. S. O’Donovan, “High dynamic velocity range particle image velocimetry using multiple pulse separation imaging,” *Sensors*, vol. 11, no. 1, pp. 1–18, 2010.
- [45] J. Westerweel and F. Scarano, “Universal outlier detection for PIV data,” *Experiments in fluids*, vol. 39, no. 6, pp. 1096–1100, 2005.
- [46] R. Mejia-Alvarez and K. Christensen, “Robust suppression of background reflections in piv images,” *Measurement Science and Technology*, vol. 24, no. 2, p. 027003, 2013.
- [47] A. Sciacchitano and B. Wieneke, “PIV uncertainty propagation,” *Measurement Science and Technology*, vol. 27, no. 8, p. 084006, 2016.
- [48] L. Lu and V. Sick, “High-speed particle image velocimetry near surfaces,” *Journal of visualized experiments: JoVE*, no. 76, 2013.

- [49] A. Masullo and R. Theunissen, “Automated mask generation for PIV image analysis based on pixel intensity statistics,” *Experiments in Fluids*, vol. 58, no. 6, p. 70, 2017.
- [50] D. Dussol, P. Druault, B. Mallat, S. Delacroix, and G. Germain, “Automatic dynamic mask extraction for PIV images containing an unsteady interface, bubbles, and a moving structure,” *Comptes Rendus Mécanique*, vol. 344, no. 7, pp. 464–478, 2016.
- [51] P. Sabharwall, R. Skifton, C. Stoots, E. S. Kim, and T. Conder, “PIV uncertainty methodologies for CFD code validation at the MIR facility,” tech. rep., Idaho National Lab.(INL), Idaho Falls, ID (United States), 2013.
- [52] S. Nishio, “Uncertainty analysis and example for PIV measurements,” in *Proceedings of 25th International Towing Tank Conference (ITTC), Fukuoka, Japan, September*, pp. 14–20, 2008.
- [53] H. R. Kang, *Computational color technology*. Spie Press Bellingham, 2006.

APPENDIX A

TEST SECTION DRAWINGS

Drawings used in the fabrication of the test section were unavailable at the time of loop design and construction. The following drawings were used in the approximations of as-built assembly of the rod bundle and test section. All units are presented in inches.

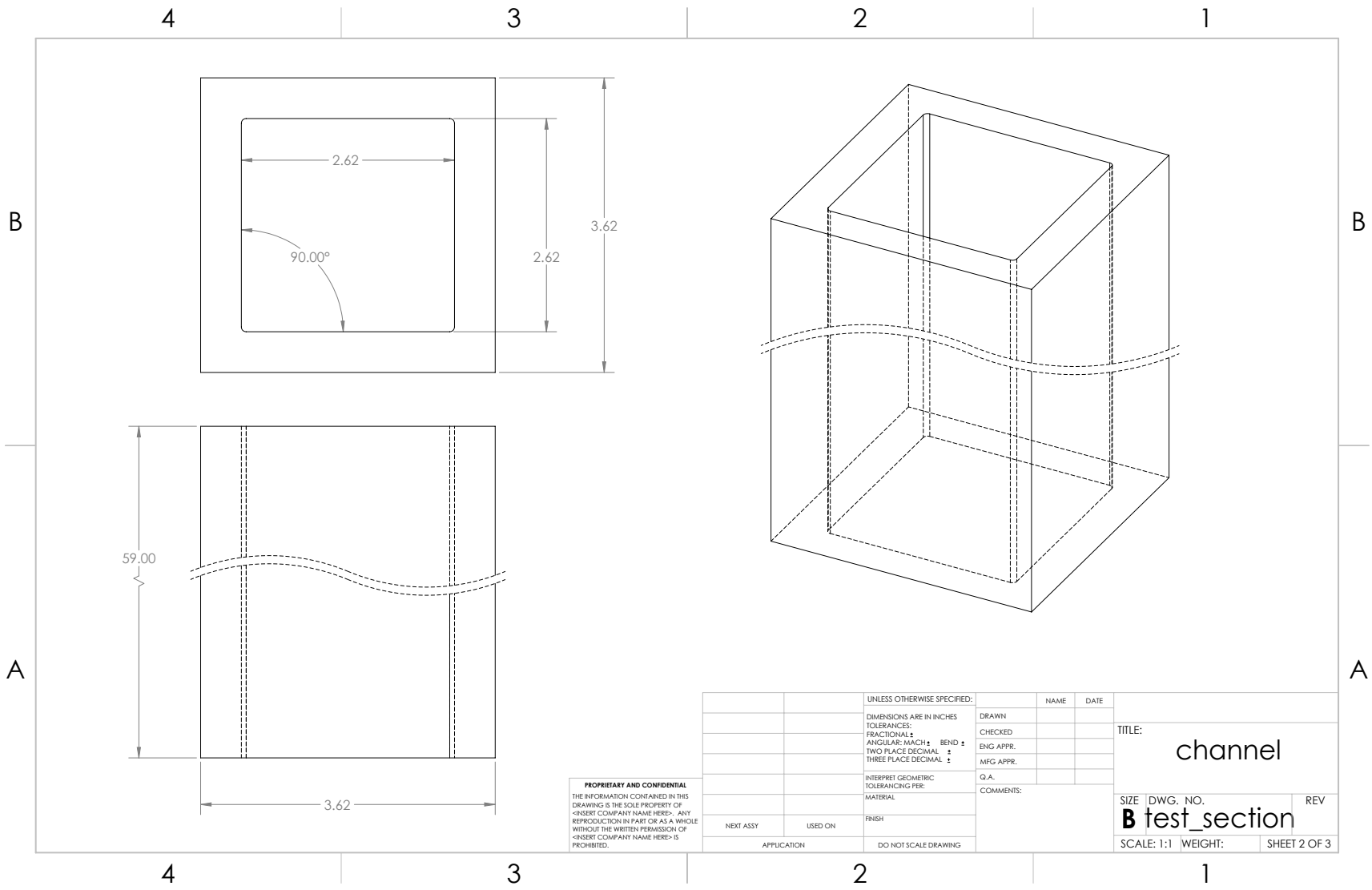


ITEM NO.	PART NUMBER	DESCRIPTION	QTY.
1	channel		1
2	ts_flange		2

UNLESS OTHERWISE SPECIFIED:		NAME	DATE	TITLE: assembly SIZE DWG. NO. REV B test_section SCALE: 1:8 WEIGHT: SHEET 1 OF 3
DIMENSIONS ARE IN INCHES		DRAWN		
TOLERANCES:		CHECKED		
FRACTIONAL ±		ENG APPR.		
ANGULAR: MACH ± BEND ±		MFG APPR.		
TWO PLACE DECIMAL ±		Q.A.		
THREE PLACE DECIMAL ±		COMMENTS:		
NEXT ASSY	USED ON	FINISH		
APPLICATION	DO NOT SCALE DRAWING			

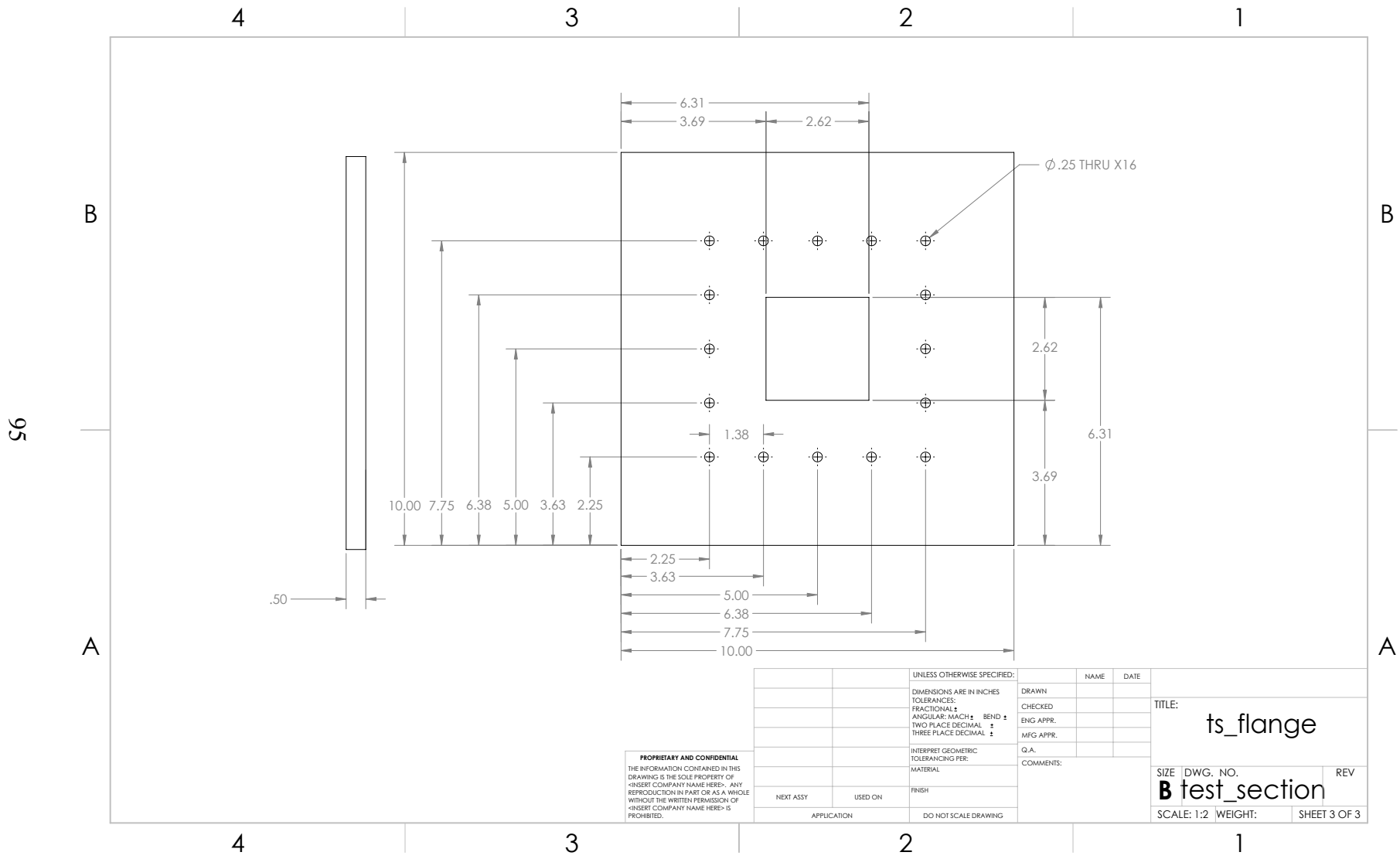
PROPRIETARY AND CONFIDENTIAL
 THE INFORMATION CONTAINED IN THIS DRAWING IS THE SOLE PROPERTY OF <INSERT COMPANY NAME HERE>. ANY REPRODUCTION IN PART OR AS A WHOLE WITHOUT THE WRITTEN PERMISSION OF <INSERT COMPANY NAME HERE> IS PROHIBITED.

94



PROPRIETARY AND CONFIDENTIAL
 THE INFORMATION CONTAINED IN THIS DRAWING IS THE SOLE PROPERTY OF <INSERT COMPANY NAME HERE>. ANY REPRODUCTION IN PART OR AS A WHOLE WITHOUT THE WRITTEN PERMISSION OF <INSERT COMPANY NAME HERE> IS PROHIBITED.

		UNLESS OTHERWISE SPECIFIED:		NAME	DATE
		DIMENSIONS ARE IN INCHES		DRAWN	
		TOLERANCES:		CHECKED	
		FRACTIONAL: ±		ENG APPR.	
		ANGULAR: MACH ± BEND ±		MFG APPR.	
		TWO PLACE DECIMAL ±		Q.A.	
		THREE PLACE DECIMAL ±		COMMENTS:	
		INTERPRET GEOMETRIC TOLERANCING PER:			
		MATERIAL:			
NEXT ASSY	USED ON	FINISH			
APPLICATION		DO NOT SCALE DRAWING			
			TITLE: channel		
			SIZE DWG. NO.	REV	
			B test_section		
			SCALE: 1:1	WEIGHT:	SHEET 2 OF 3



PROPRIETARY AND CONFIDENTIAL
 THE INFORMATION CONTAINED IN THIS DRAWING IS THE SOLE PROPERTY OF <INSERT COMPANY NAME HERE>. ANY REPRODUCTION IN PART OR AS A WHOLE WITHOUT THE WRITTEN PERMISSION OF <INSERT COMPANY NAME HERE> IS PROHIBITED.

		UNLESS OTHERWISE SPECIFIED:		NAME	DATE
		DIMENSIONS ARE IN INCHES		DRAWN	
		TOLERANCES:		CHECKED	
		FRACTIONAL ±		ENG APPR.	
		ANGULAR: MACH ±		MFG APPR.	
		BEND ±		Q.A.	
		TWO PLACE DECIMAL ±		COMMENTS:	
		THREE PLACE DECIMAL ±			
		INTERPRET GEOMETRIC TOLERANCING PER:			
		MATERIAL			
NEXT ASSY	USED ON	FINISH			
APPLICATION		DO NOT SCALE DRAWING			
			TITLE: ts_flange		
			SIZE DWG. NO.		REV
			B test_section		
			SCALE: 1:2 WEIGHT:		SHEET 3 OF 3

APPENDIX B

PLENA DRAWINGS

The following drawings were used in the fabrication of the plena which joined the test section with the constructed flow loop. All units are presented in inches.

4

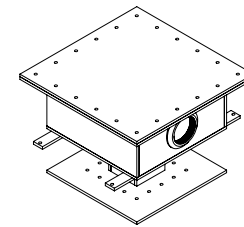
3

2

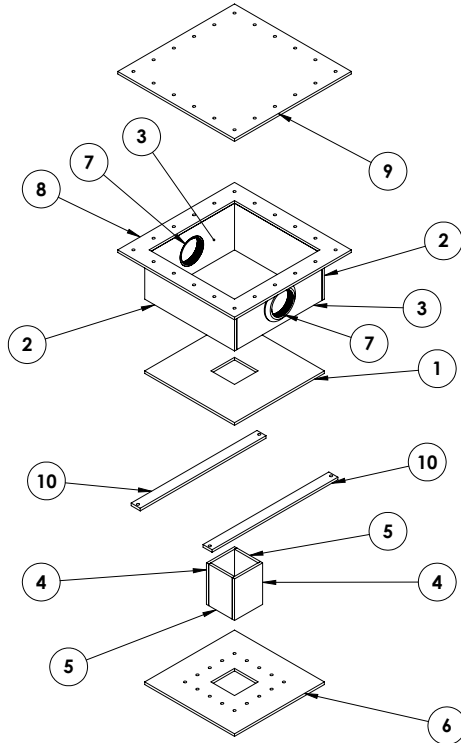
1

REVISIONS

ZONE	REV.	DESCRIPTION	DATE	APPROVED
------	------	-------------	------	----------



ASSEMBLED VIEW



EXPLODED VIEW

ITEM NO.	PART NUMBER	DESCRIPTION	QTY.
1	Box Side A		1
2	Box Side C		2
3	Box Side D		2
4	Column Side A (Top)		2
5	Column Side B (Top)		2
6	Flange		1
7	8694T49		2
8	Top Flange		1
9	Top Flange	Top End Cap	1
10	Mounting Bracket		2

UNLESS OTHERWISE SPECIFIED:		NAME	DATE
DIMENSIONS ARE IN INCHES			
TOLERANCES:			
FRACTIONAL ±	DRAWN		
ANGULAR: MACH ± BEND ±	CHECKED		
TWO PLACE DECIMAL ±	ENG APPR.		
THREE PLACE DECIMAL ±	MFG APPR.		
INTERPRET GEOMETRIC TOLERANCING PER:	Q.A.		
MATERIAL	COMMENTS:		
FINISH			
DO NOT SCALE DRAWING			

TITLE:		
Assembly		
SIZE DWG. NO.	REV	
B Top Box		
SCALE: 1:8 WEIGHT:	SHEET 1 OF 11	

SOLIDWORKS Educational Product. For Instructional Use Only

97

B

B

A

A

4

3

2

1

4 3 2 1

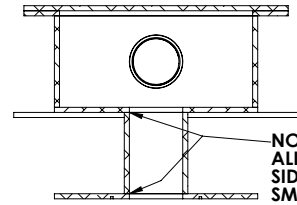
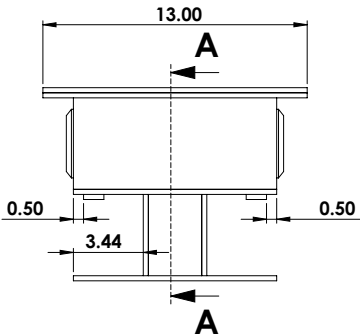
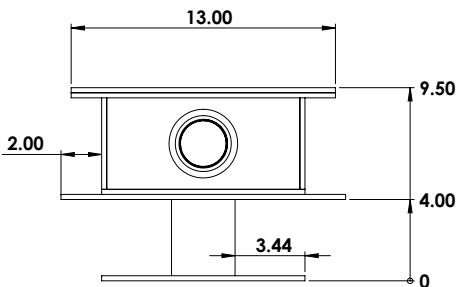
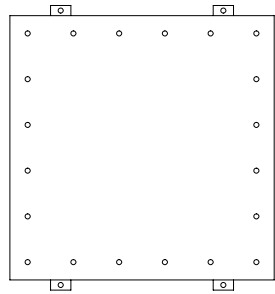
B

B

A

A

REVISIONS				
ZONE	REV.	DESCRIPTION	DATE	APPROVED



SECTION A-A

SOLIDWORKS Educational Product. For Instructional Use Only

4 3 2 1

UNLESS OTHERWISE SPECIFIED:	NAME	DATE	
DIMENSIONS ARE IN INCHES	DRAWN		
TOLERANCES:	CHECKED		
FRACTIONAL: ±	ENG APPR.		
ANGULAR: MACH ± BEND ±	MFG APPR.		
TWO PLACE DECIMAL ±	Q.A.		
THREE PLACE DECIMAL ±	COMMENTS:		
INTERPRET GEOMETRIC TOLERANCING PER:			
MATERIAL			
FINISH			
DO NOT SCALE DRAWING			

TITLE:
Assembly

SIZE DWG. NO. REV
B Top Box
SCALE: 1:5 WEIGHT: SHEET 2 OF 11

66

4 3 2 1

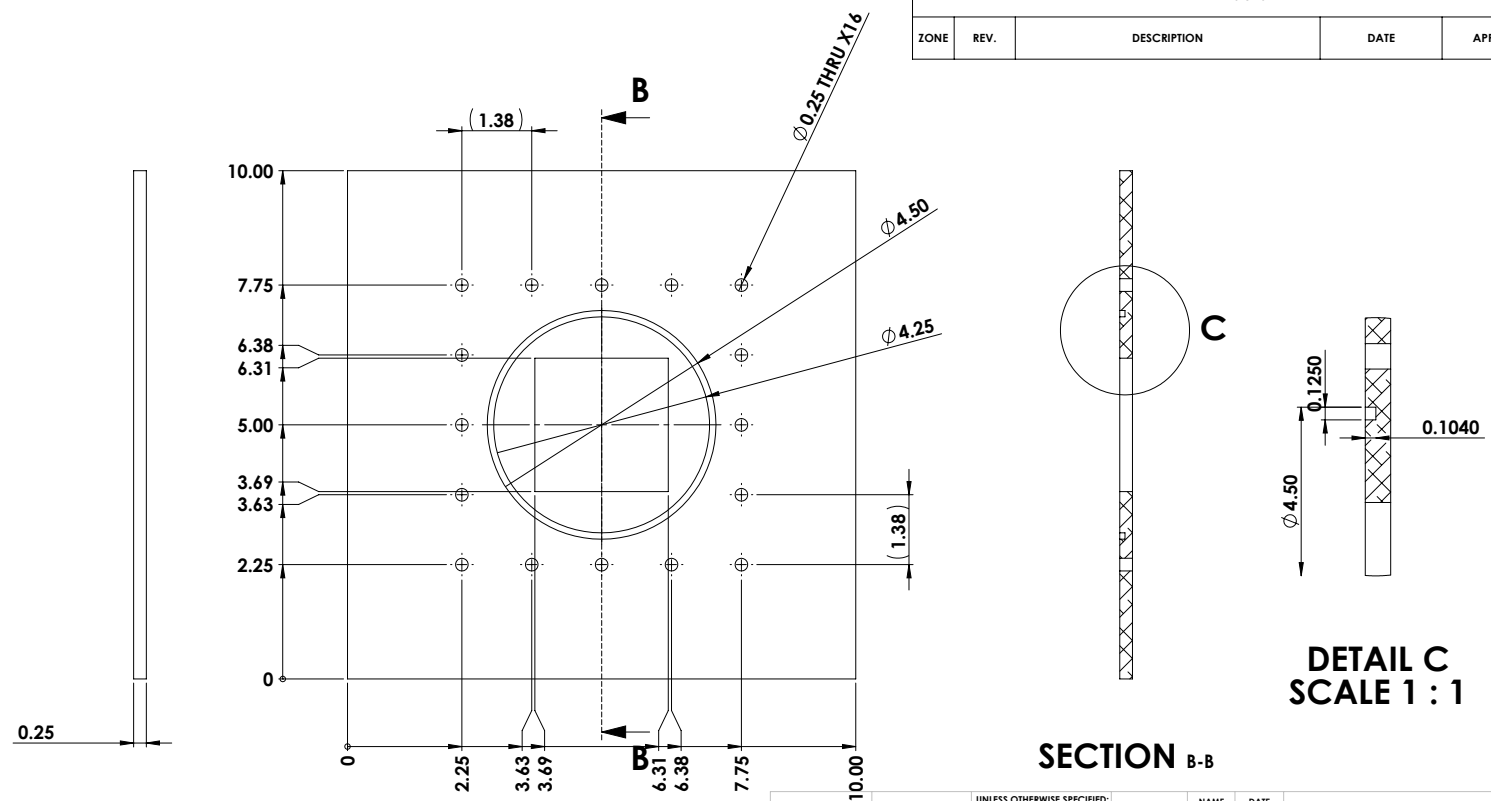
B

B

A

A

REVISIONS				
ZONE	REV.	DESCRIPTION	DATE	APPROVED



DETAIL C
SCALE 1 : 1

SECTION B-B

SOLIDWORKS Educational Product. For Instructional Use Only

PROPRIETARY AND CONFIDENTIAL
THE INFORMATION CONTAINED IN THIS
DRAWING IS THE SOLE PROPERTY OF
<INSERT COMPANY NAME HERE>. ANY
REPRODUCTION IN PART OR AS A WHOLE
WITHOUT THE WRITTEN PERMISSION OF
<INSERT COMPANY NAME HERE> IS
PROHIBITED.

UNLESS OTHERWISE SPECIFIED:		NAME	DATE	TITLE: Flange
DIMENSIONS ARE IN INCHES		DRAWN		
TOLERANCES:		CHECKED		
FRACTIONAL ±		ENG APPR.		
ANGULAR: MACH ± BEND ±		MFG APPR.		SIZE DWG. NO. REV B Top Box
TWO PLACE DECIMAL ±				
THREE PLACE DECIMAL ±		Q.A.		SCALE: 1:2 WEIGHT: SHEET 3 OF 11
INTERPRET GEOMETRIC TOLERANCING PER:		COMMENTS:		
NEXT ASSY	USED ON	MATERIAL	FINISH	
APPLICATION	DO NOT SCALE DRAWING			

4 3 2 1

100

B

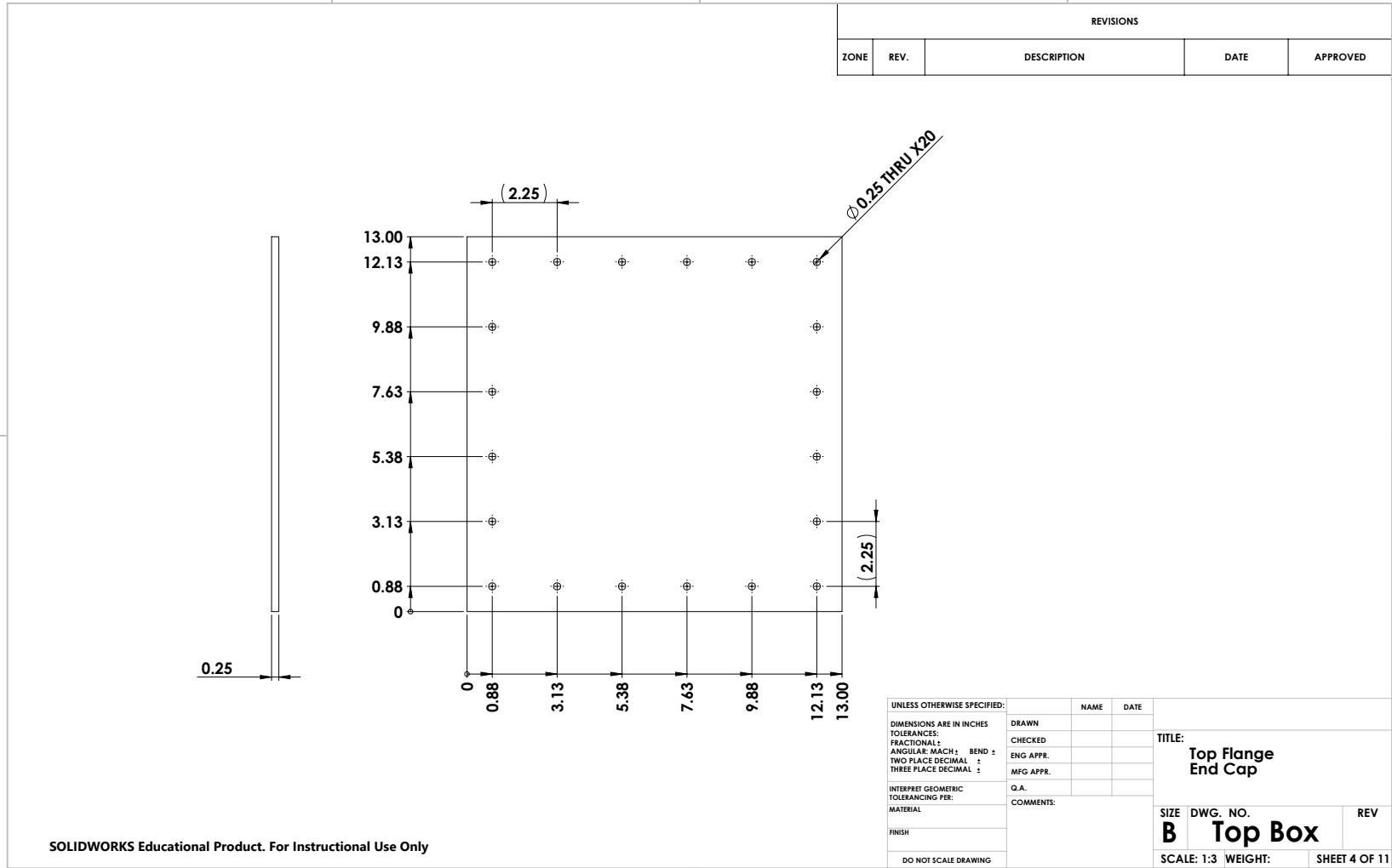
A

4

3

2

1



REVISIONS				
ZONE	REV.	DESCRIPTION	DATE	APPROVED

SOLIDWORKS Educational Product. For Instructional Use Only

4

3

2

1

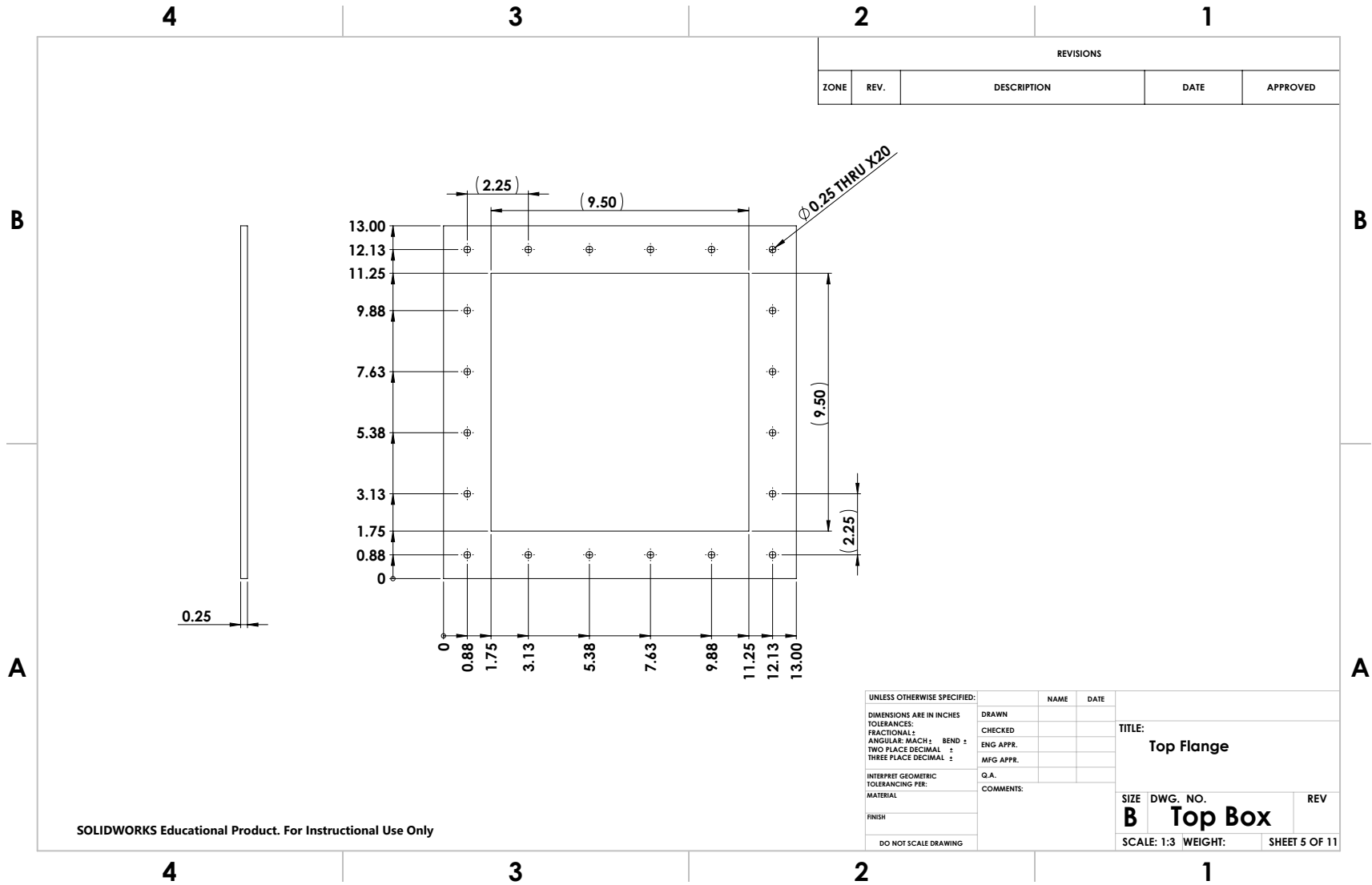
B

A

UNLESS OTHERWISE SPECIFIED:	NAME	DATE	
DIMENSIONS ARE IN INCHES	DRAWN		
TOLERANCES:	CHECKED		
FRACTIONAL: ±	ENG APPR.		
ANGULAR: MACH ± BEND ±	MFG APPR.		
TWO PLACE DECIMAL ±			
THREE PLACE DECIMAL ±			
INTERPRET GEOMETRIC TOLERANCING PER:	Q.A.		
MATERIAL	COMMENTS:		
FINISH			
DO NOT SCALE DRAWING			

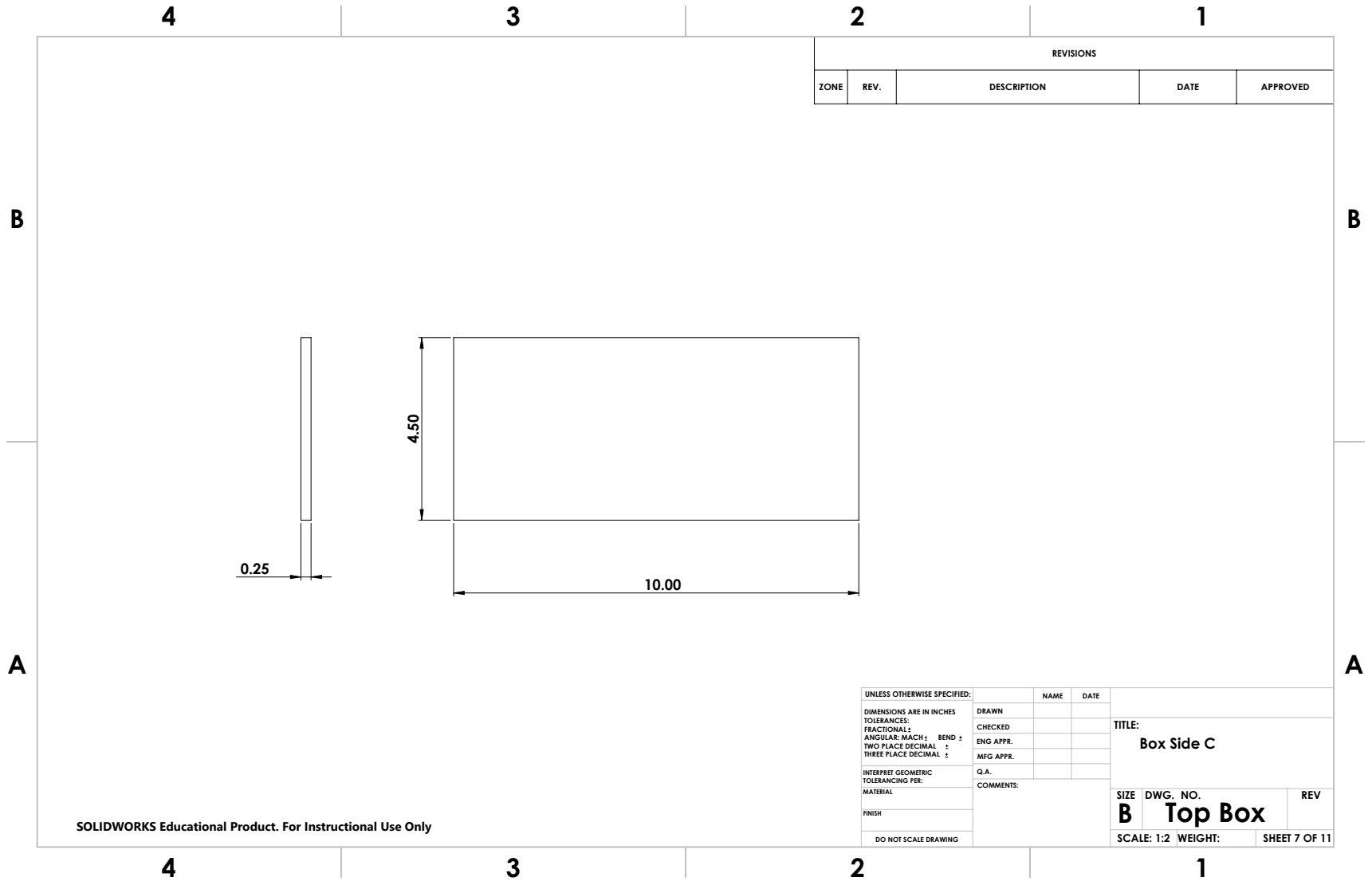
TITLE:		
Top Flange End Cap		
SIZE	DWG. NO.	REV
B	Top Box	
SCALE: 1:3	WEIGHT:	SHEET 4 OF 11

101



SOLIDWORKS Educational Product. For Instructional Use Only

103



SOLIDWORKS Educational Product. For Instructional Use Only

REVISIONS				
ZONE	REV.	DESCRIPTION	DATE	APPROVED

UNLESS OTHERWISE SPECIFIED:	NAME	DATE	
DIMENSIONS ARE IN INCHES	DRAWN		
TOLERANCES:	CHECKED		
FRACTIONAL: ±	ENG APPR.		
ANGULAR: MACH ± BEND ±	MFG APPR.		
TWO PLACE DECIMAL ±			
THREE PLACE DECIMAL ±			
INTERPRET GEOMETRIC TOLERANCING PER:	Q.A.		
MATERIAL	COMMENTS:		
FINISH			
DO NOT SCALE DRAWING			
TITLE: Box Side C			REV
SIZE	DWG. NO.	B Top Box	
SCALE: 1:2 WEIGHT:		SHEET 7 OF 11	

104

B

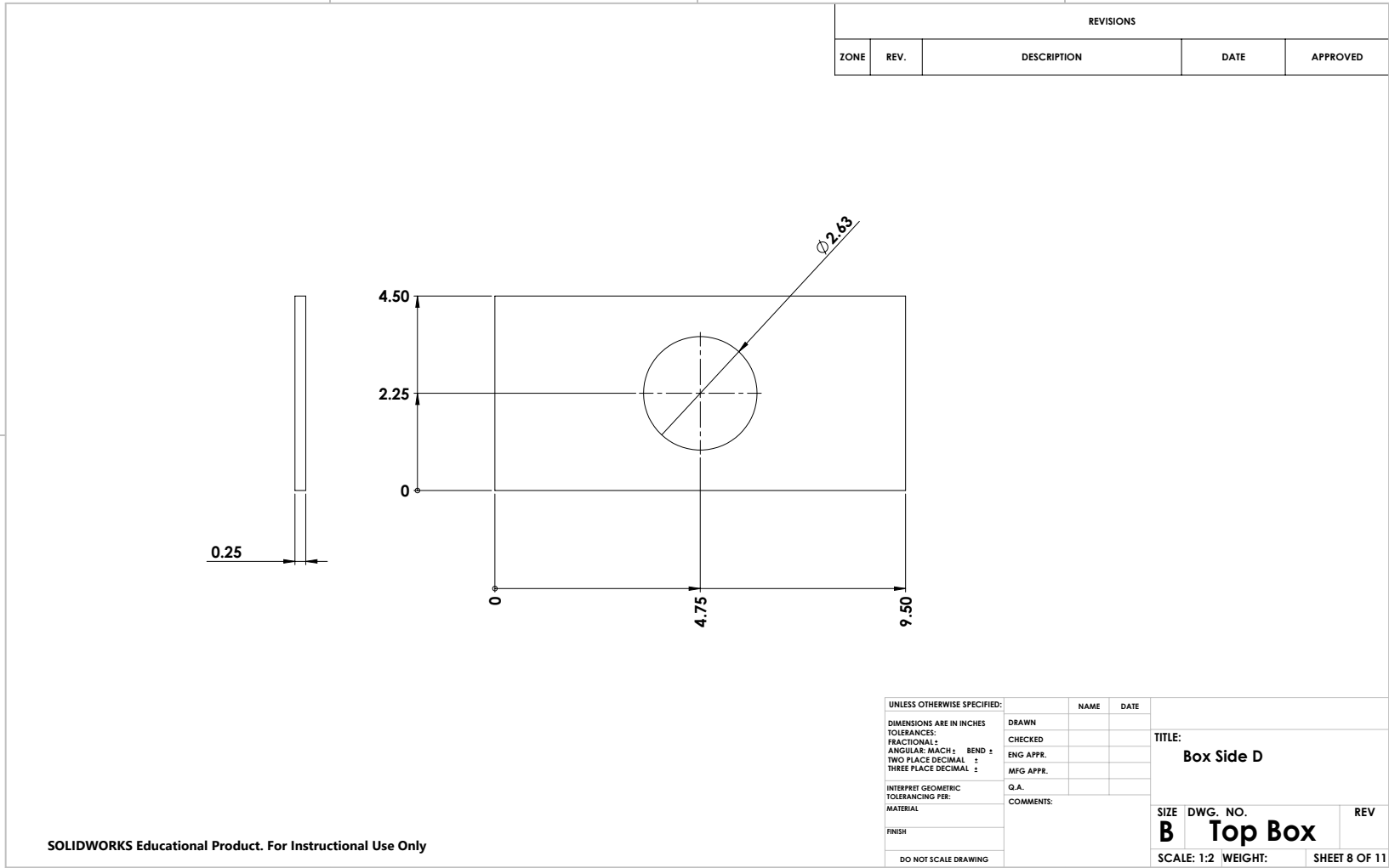
A

4

3

2

1



REVISIONS				
ZONE	REV.	DESCRIPTION	DATE	APPROVED

B

A

SOLIDWORKS Educational Product. For Instructional Use Only

4

3

2

1

UNLESS OTHERWISE SPECIFIED:	NAME	DATE	
DIMENSIONS ARE IN INCHES	DRAWN		
TOLERANCES:	CHECKED		
FRACTIONAL: ±	ENG APPR.		
ANGULAR: MACH ± BEND ±	MFG APPR.		
TWO PLACE DECIMAL ±			
THREE PLACE DECIMAL ±			
INTERPRET GEOMETRIC TOLERANCING PER:	Q.A.		
MATERIAL	COMMENTS:		
FINISH			
DO NOT SCALE DRAWING			

TITLE: Box Side D		
SIZE	DWG. NO.	REV
B	Top Box	
SCALE: 1:2	WEIGHT:	SHEET 8 OF 11

105

B

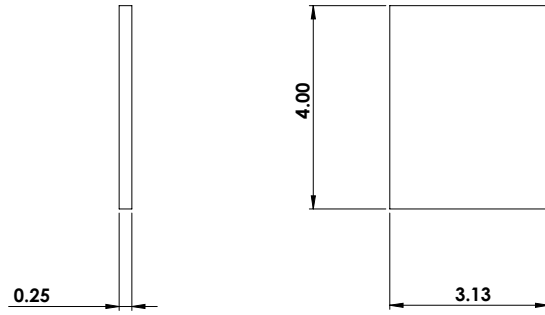
A

4

3

2

1



SOLIDWORKS Educational Product. For Instructional Use Only

4

3

2

1

REVISIONS				
ZONE	REV.	DESCRIPTION	DATE	APPROVED

B

A

UNLESS OTHERWISE SPECIFIED:	NAME	DATE	
DIMENSIONS ARE IN INCHES	DRAWN		
TOLERANCES:	CHECKED		
FRACTIONAL: ±	ENG APPR.		
ANGULAR: MACH ±	MFG APPR.		
TWO PLACE DECIMAL ±			
THREE PLACE DECIMAL ±			
INTERPRET GEOMETRIC TOLERANCING PER:	Q.A.		
MATERIAL	COMMENTS:		
FINISH			
DO NOT SCALE DRAWING			

TITLE: Column Side A (Top)

SIZE DWG. NO. REV
B Top Box
 SCALE: 1:2 WEIGHT: SHEET 9 OF 11

106

B

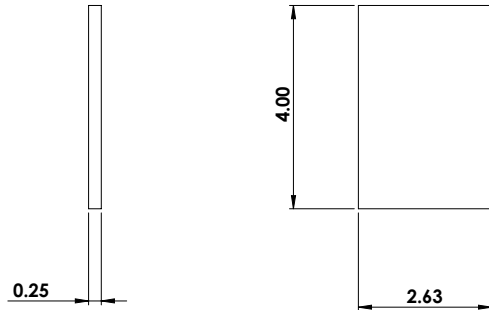
A

4

3

2

1



REVISIONS				
ZONE	REV.	DESCRIPTION	DATE	APPROVED

B

A

SOLIDWORKS Educational Product. For Instructional Use Only

4

3

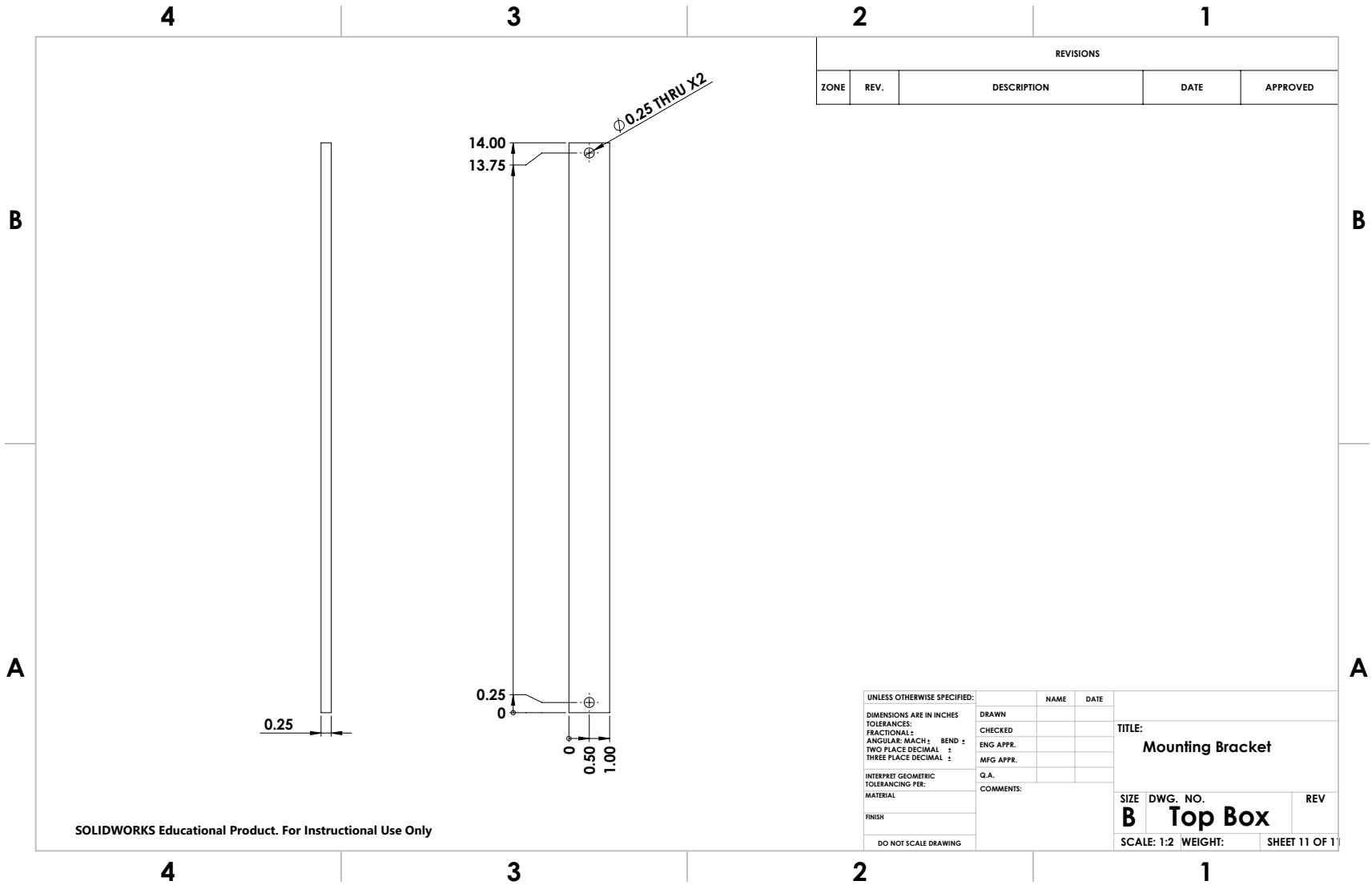
2

1

UNLESS OTHERWISE SPECIFIED:	NAME	DATE	
DIMENSIONS ARE IN INCHES	DRAWN		
TOLERANCES:	CHECKED		
FRACTIONAL: ±	ENG APPR.		
ANGULAR: MACH ±	MFG APPR.		
TWO PLACE DECIMAL ±			
THREE PLACE DECIMAL ±			
INTERPRET GEOMETRIC TOLERANCING PER:	Q.A.		
MATERIAL	COMMENTS:		
FINISH			
DO NOT SCALE DRAWING			

TITLE:		
Column Side B (Top)		
SIZE	DWG. NO.	REV
B	Top Box	
SCALE: 1:2	WEIGHT:	SHEET 10 OF 11

107



SOLIDWORKS Educational Product. For Instructional Use Only

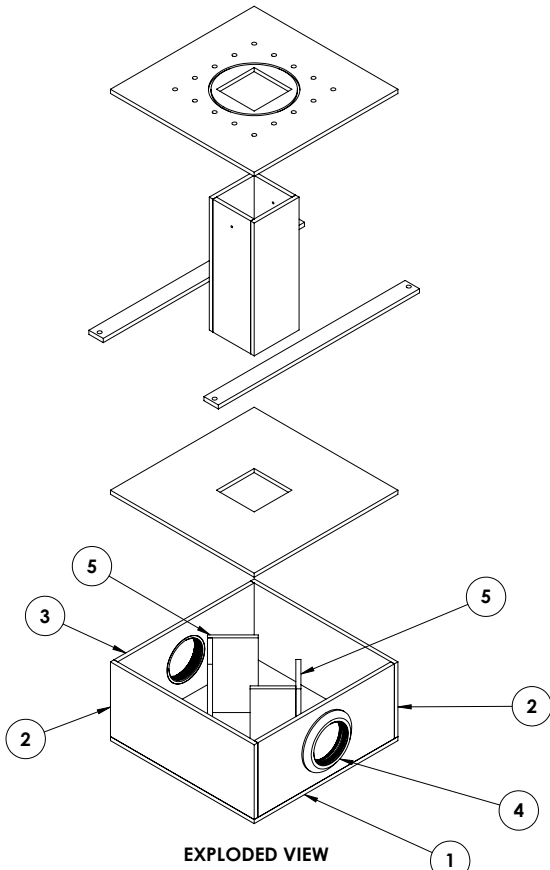
4 3 2 1

B

B

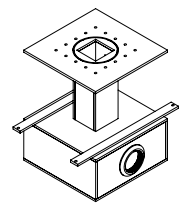
A

A



EXPLODED VIEW

REVISIONS				
ZONE	REV.	DESCRIPTION	DATE	APPROVED



ASSEMBLED VIEW

ITEM NO.	PART NUMBER	DESCRIPTION	QTY.
1	Box Side B		1
2	Box Side C		2
3	Box Side D		2
4	8694T49		2
5	Flow Diverter		2
6	Box Side A		1
7	Column Side A		2
8	Column Side B		2
9	Flange		1
10	Mounting Bracket		2

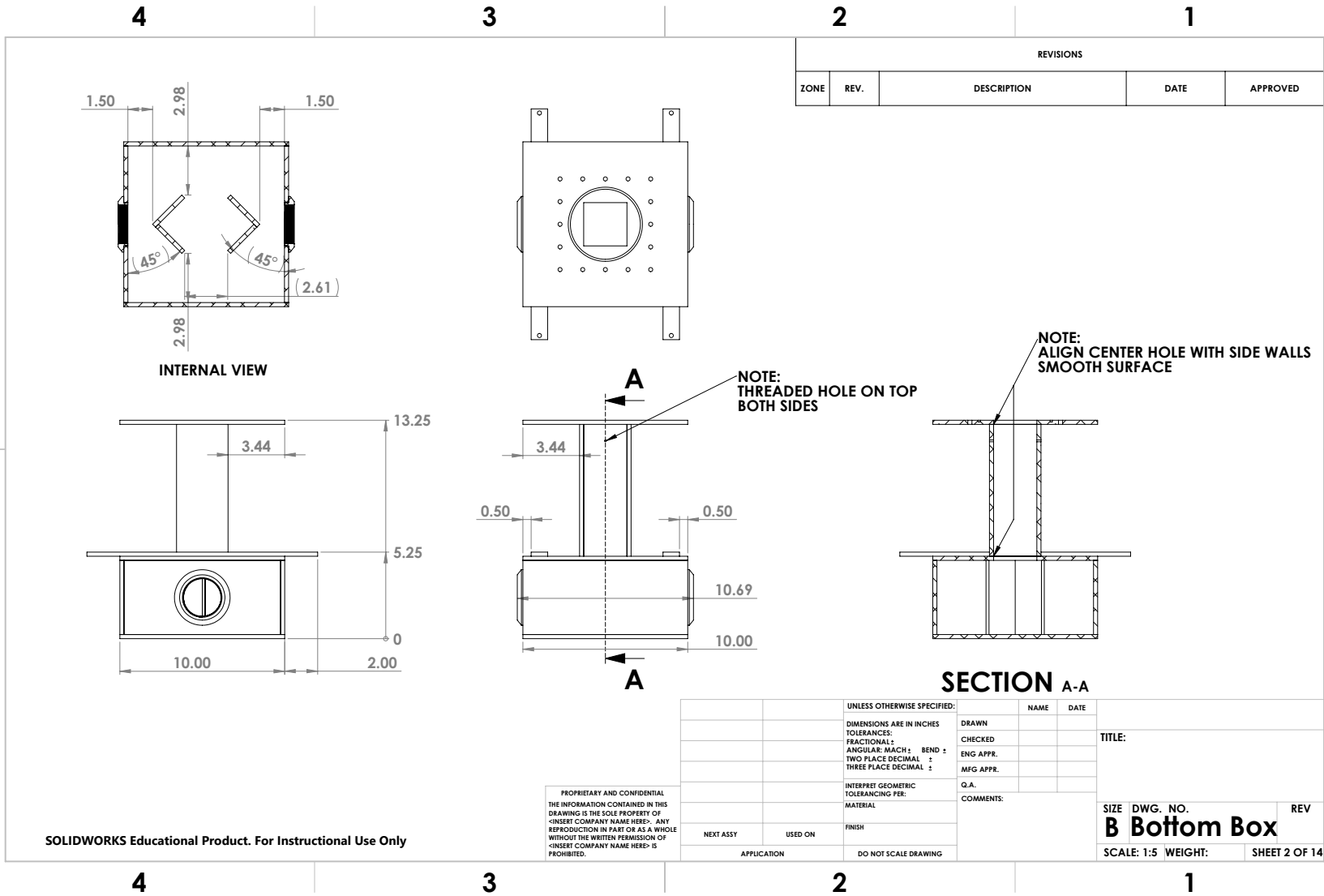
UNLESS OTHERWISE SPECIFIED:		NAME	DATE	TITLE:
DIMENSIONS ARE IN INCHES		DRAWN		
TOLERANCES:		CHECKED		
FRACTIONAL: ±		ENG APPR.		
ANGULAR: MACH ± BEND ±		MFG APPR.		SIZE DWG. NO. REV
TWO PLACE DECIMAL ±				
THREE PLACE DECIMAL ±		Q.A.		SCALE: 1:5 WEIGHT: SHEET 1 OF 14
INTERPRET GEOMETRIC TOLERANCING PER:		COMMENTS:		
NEXT ASSY	USED ON	FINISH		
APPLICATION		DO NOT SCALE DRAWING		

PROPRIETARY AND CONFIDENTIAL
 THE INFORMATION CONTAINED IN THIS DRAWING IS THE SOLE PROPERTY OF <INSERT COMPANY NAME HERE>. ANY REPRODUCTION IN PART OR AS A WHOLE WITHOUT THE WRITTEN PERMISSION OF <INSERT COMPANY NAME HERE> IS PROHIBITED.

SOLIDWORKS Educational Product. For Instructional Use Only

4 3 2 1

109



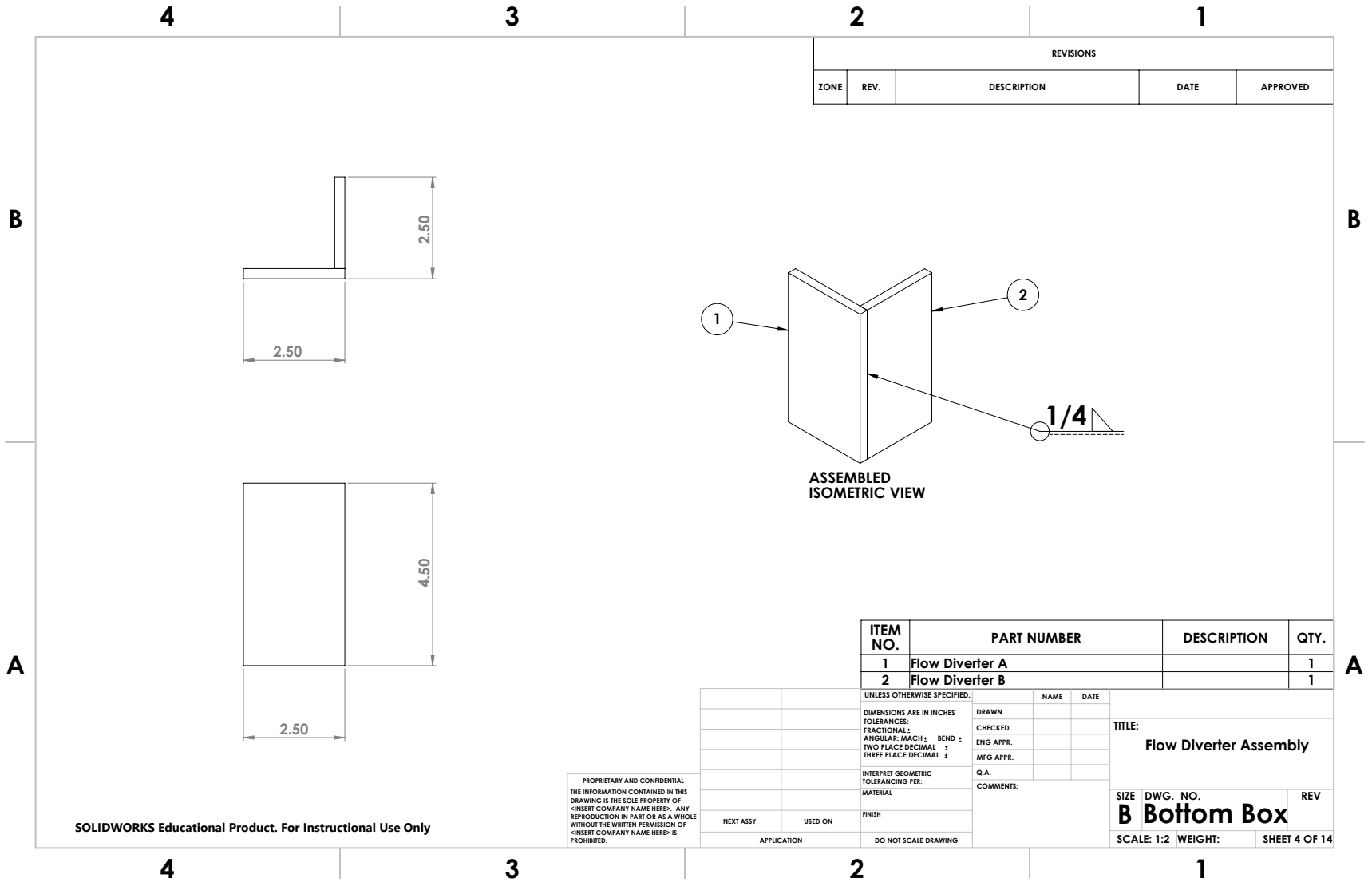
REVISIONS				
ZONE	REV.	DESCRIPTION	DATE	APPROVED

SOLIDWORKS Educational Product. For Instructional Use Only

PROPRIETARY AND CONFIDENTIAL
 THE INFORMATION CONTAINED IN THIS
 DRAWING IS THE SOLE PROPERTY OF
 <INSERT COMPANY NAME HERE>. ANY
 REPRODUCTION IN PART OR AS A WHOLE
 WITHOUT THE WRITTEN PERMISSION OF
 <INSERT COMPANY NAME HERE> IS
 PROHIBITED.

UNLESS OTHERWISE SPECIFIED:		NAME	DATE	TITLE:
DIMENSIONS ARE IN INCHES TOLERANCES:				
FRACTIONAL ±		DRAWN		
ANGULAR: MACH ± BEND ±		CHECKED		
TWO PLACE DECIMAL ±		ENG APPR.		
THREE PLACE DECIMAL ±		MFG APPR.		
INTERPRET GEOMETRIC TOLERANCING PER:		Q.A.		
MATERIAL		COMMENTS:		
FINISH				SIZE DWG. NO. REV
NEXT ASSY	USED ON			B Bottom Box
APPLICATION	DO NOT SCALE DRAWING			SCALE: 1:5 WEIGHT: SHEET 2 OF 14

111



REVISIONS				
ZONE	REV.	DESCRIPTION	DATE	APPROVED

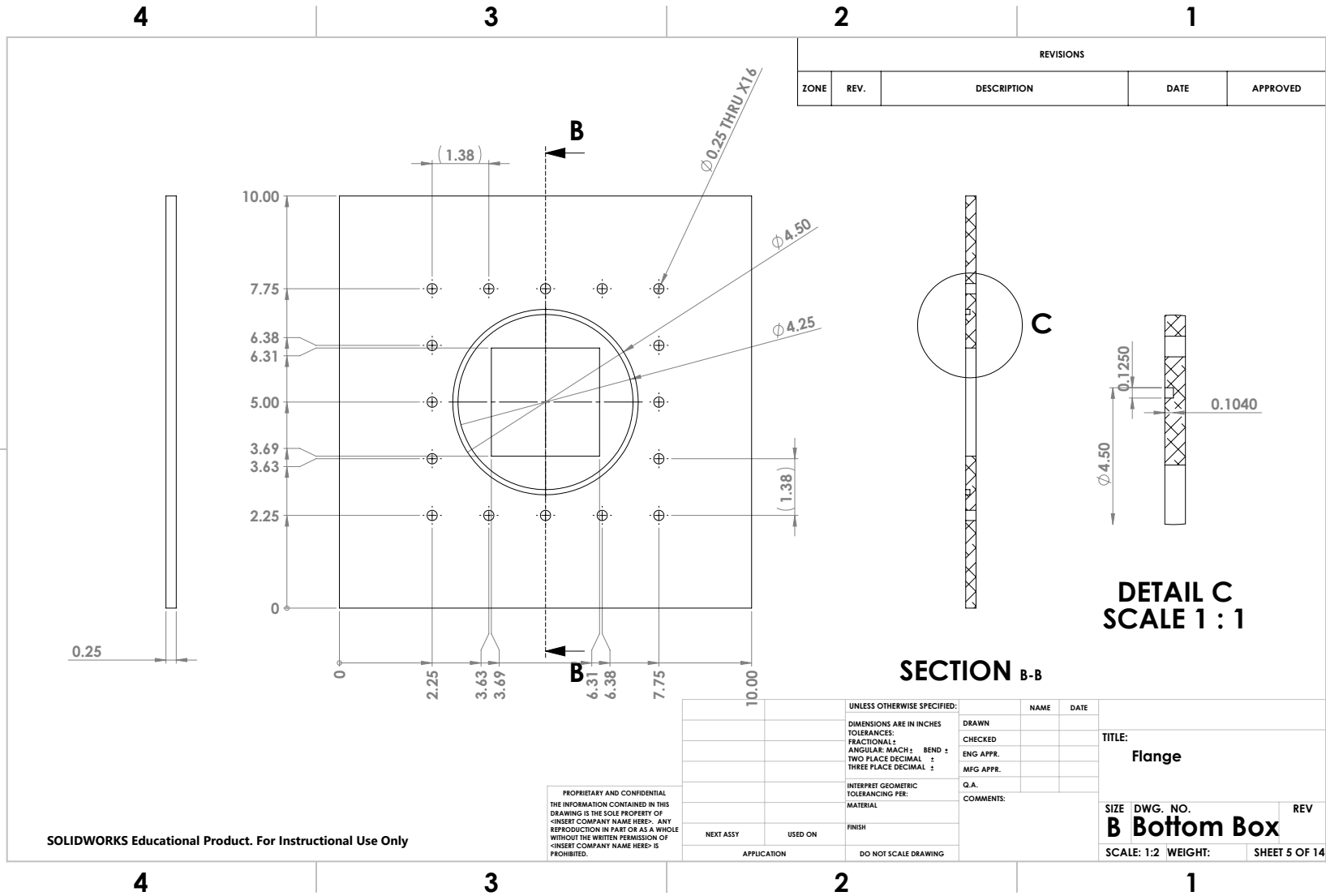
ITEM NO.	PART NUMBER	DESCRIPTION	QTY.
1	Flow Diverter A		1
2	Flow Diverter B		1

UNLESS OTHERWISE SPECIFIED:		NAME	DATE
DIMENSIONS ARE IN INCHES		DRAWN	
TOLERANCES:		CHECKED	
FRACTIONAL ±		ENG APPR.	
ANGULAR: MACH ±	BEND ±	MFG APPR.	
TWO PLACE DECIMAL ±			
THREE PLACE DECIMAL ±			
INTERPRET GEOMETRIC	Q.A.		
TOLERANCING PER:	COMMENTS:		
MATERIAL			
FINISH			
NEXT ASSY	USED ON		
APPLICATION	DO NOT SCALE DRAWING		

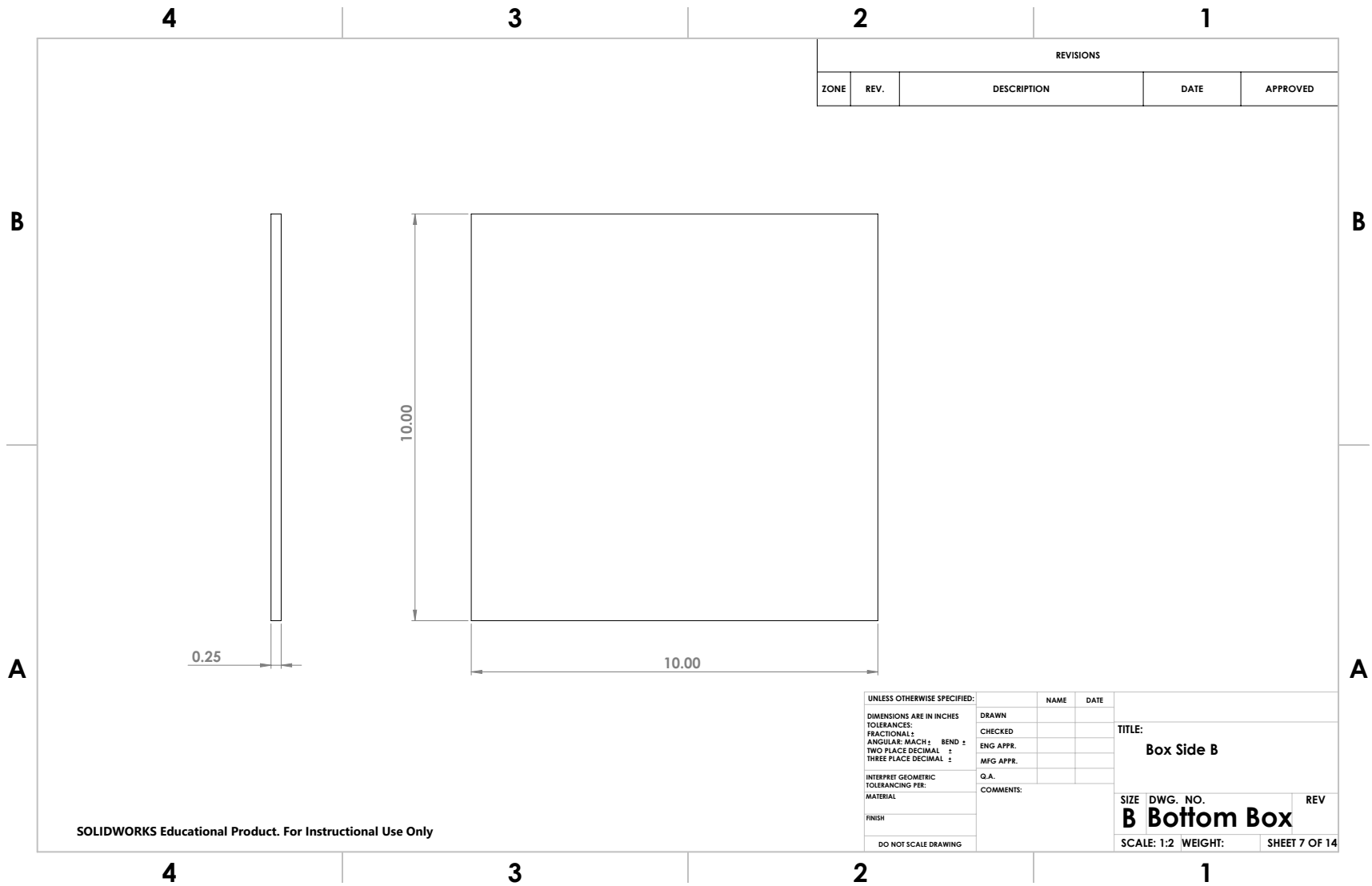
TITLE:		
Flow Diverter Assembly		
SIZE	DWG. NO.	REV
B	Bottom Box	
SCALE: 1:2	WEIGHT:	SHEET 4 OF 14

PROPRIETARY AND CONFIDENTIAL
 THE INFORMATION CONTAINED IN THIS DRAWING IS THE SOLE PROPERTY OF <INSERT COMPANY NAME HERE>. ANY REPRODUCTION IN PART OR AS A WHOLE WITHOUT THE WRITTEN PERMISSION OF <INSERT COMPANY NAME HERE> IS PROHIBITED.

SOLIDWORKS Educational Product. For Instructional Use Only



114



REVISIONS				
ZONE	REV.	DESCRIPTION	DATE	APPROVED

UNLESS OTHERWISE SPECIFIED:	NAME	DATE	
DIMENSIONS ARE IN INCHES	DRAWN		
TOLERANCES:	CHECKED		
FRACTIONAL: ±	ENG APPR.		
ANGULAR: MACH ± BEND ±	MFG APPR.		
TWO PLACE DECIMAL ±			
THREE PLACE DECIMAL ±			
INTERPRET GEOMETRIC TOLERANCING PER:	Q.A.		
MATERIAL	COMMENTS:		
FINISH			
DO NOT SCALE DRAWING			

TITLE:		
Box Side B		
SIZE	DWG. NO.	REV
B	Bottom Box	
SCALE: 1:2	WEIGHT:	SHEET 7 OF 14

SOLIDWORKS Educational Product. For Instructional Use Only

115

B

B

A

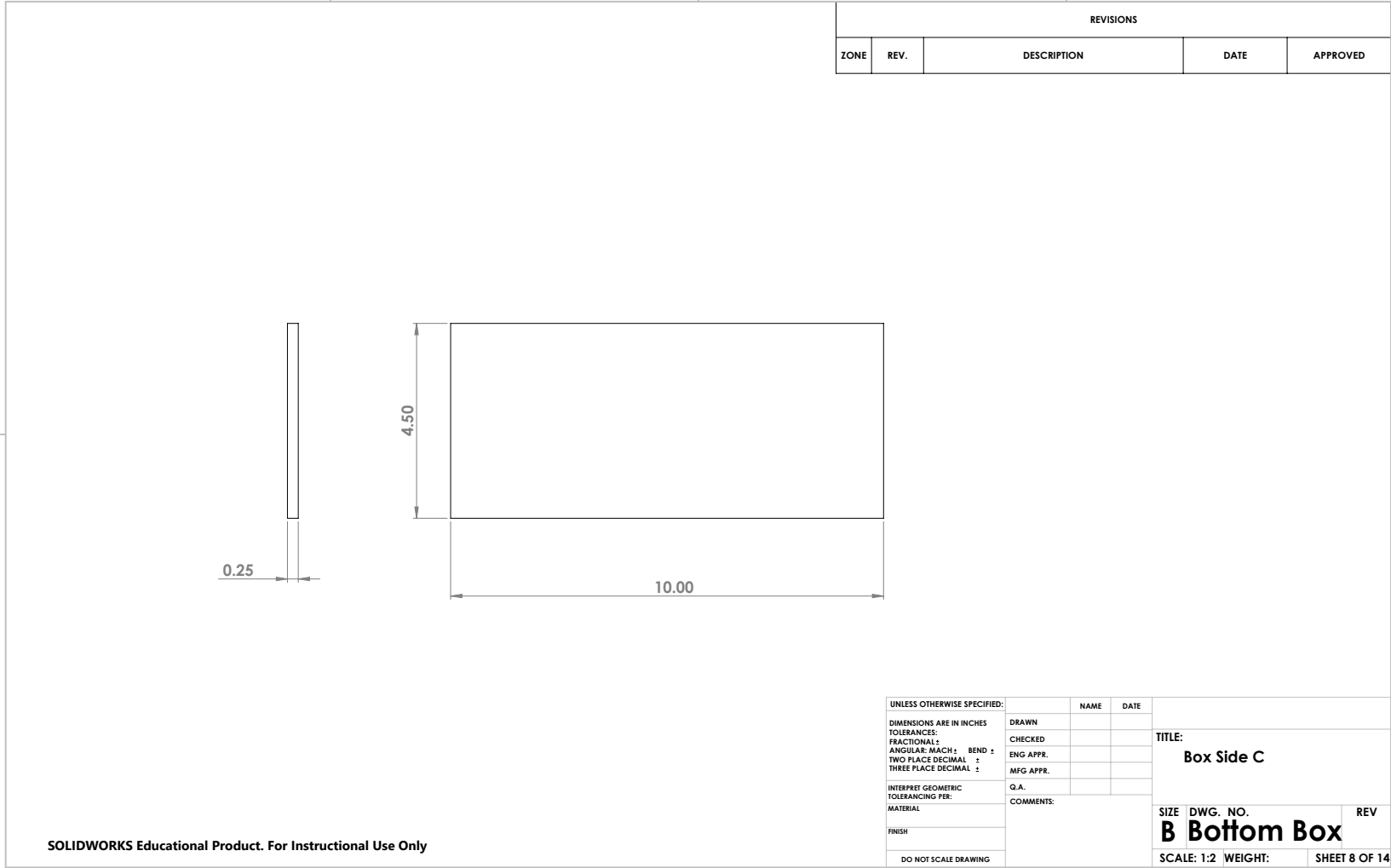
A

4

3

2

1



SOLIDWORKS Educational Product. For Instructional Use Only

4

3

2

1

4 3 2 1

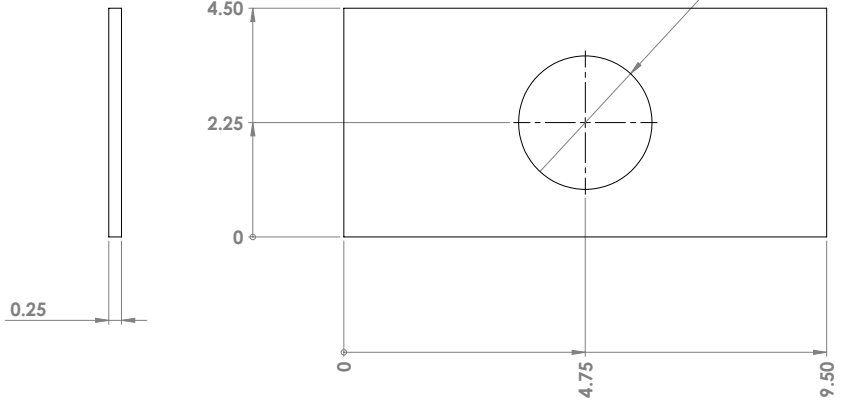
B

B

A

A

REVISIONS				
ZONE	REV.	DESCRIPTION	DATE	APPROVED

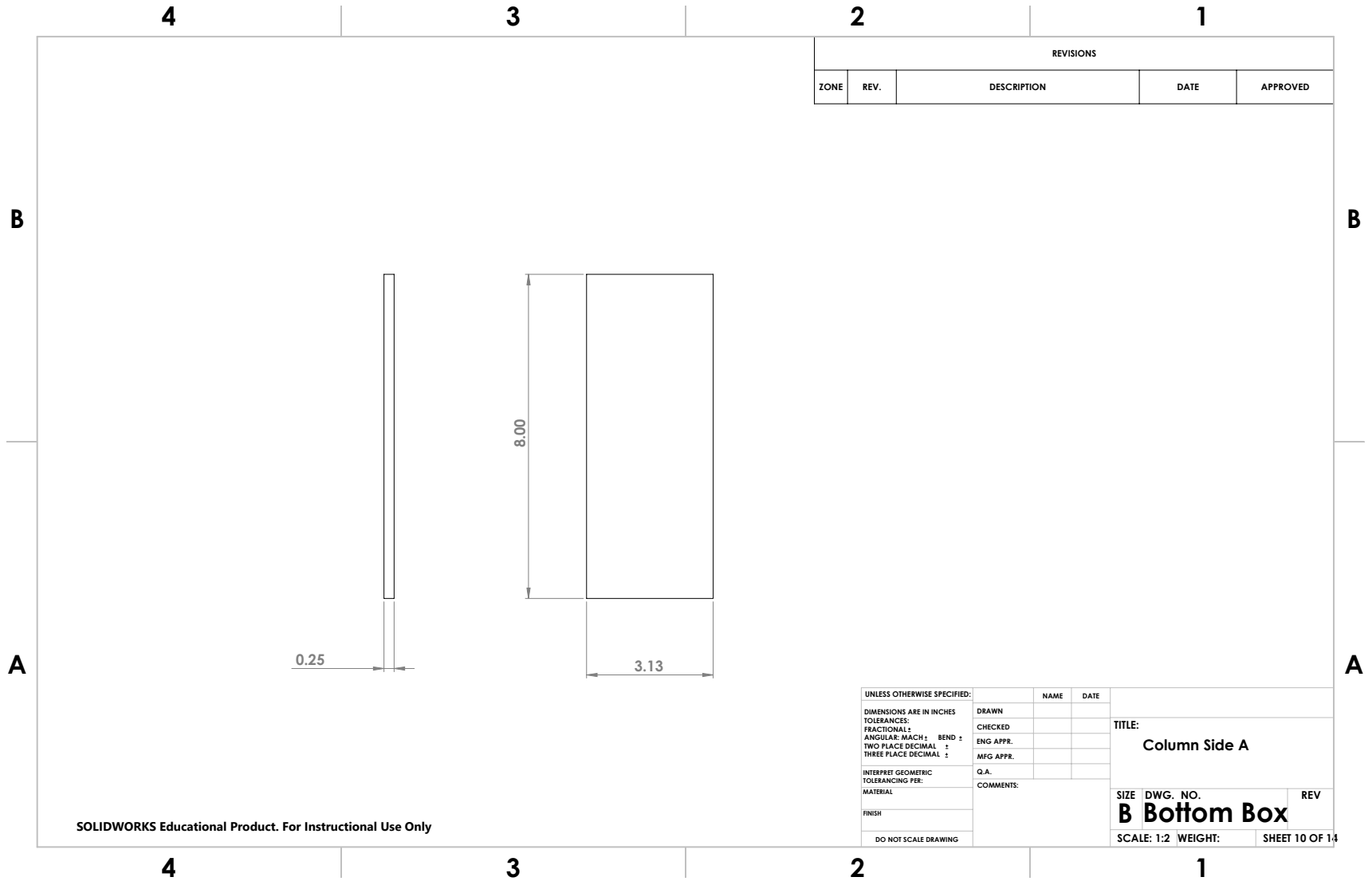


UNLESS OTHERWISE SPECIFIED:	NAME	DATE	
DIMENSIONS ARE IN INCHES	DRAWN		
TOLERANCES:	CHECKED		
FRACTIONAL: ±	ENG APPR.		
ANGULAR: MACH ± BEND ±	MFG APPR.		
TWO PLACE DECIMAL ±			
THREE PLACE DECIMAL ±			
INTERPRET GEOMETRIC TOLERANCING PER:	Q.A.		
MATERIAL	COMMENTS:		
FINISH			
DO NOT SCALE DRAWING			

TITLE:		
Box Side D		
SIZE	DWG. NO.	REV
B	Bottom Box	
SCALE: 1:2	WEIGHT:	SHEET 9 OF 14

4 3 2 1

117



SOLIDWORKS Educational Product. For Instructional Use Only

REVISIONS				
ZONE	REV.	DESCRIPTION	DATE	APPROVED

UNLESS OTHERWISE SPECIFIED:	NAME	DATE	
DIMENSIONS ARE IN INCHES	DRAWN		
TOLERANCES:	CHECKED		
FRACTIONAL: ±	ENG APPR.		
ANGULAR: MACH ± BEND ±	MFG APPR.		
TWO PLACE DECIMAL ±			
THREE PLACE DECIMAL ±			
INTERPRET GEOMETRIC TOLERANCING PER:	Q.A.		
MATERIAL	COMMENTS:		
FINISH			
DO NOT SCALE DRAWING			

TITLE:		
Column Side A		
SIZE	DWG. NO.	REV
B	Bottom Box	
SCALE: 1:2	WEIGHT:	SHEET 10 OF 14

118

B

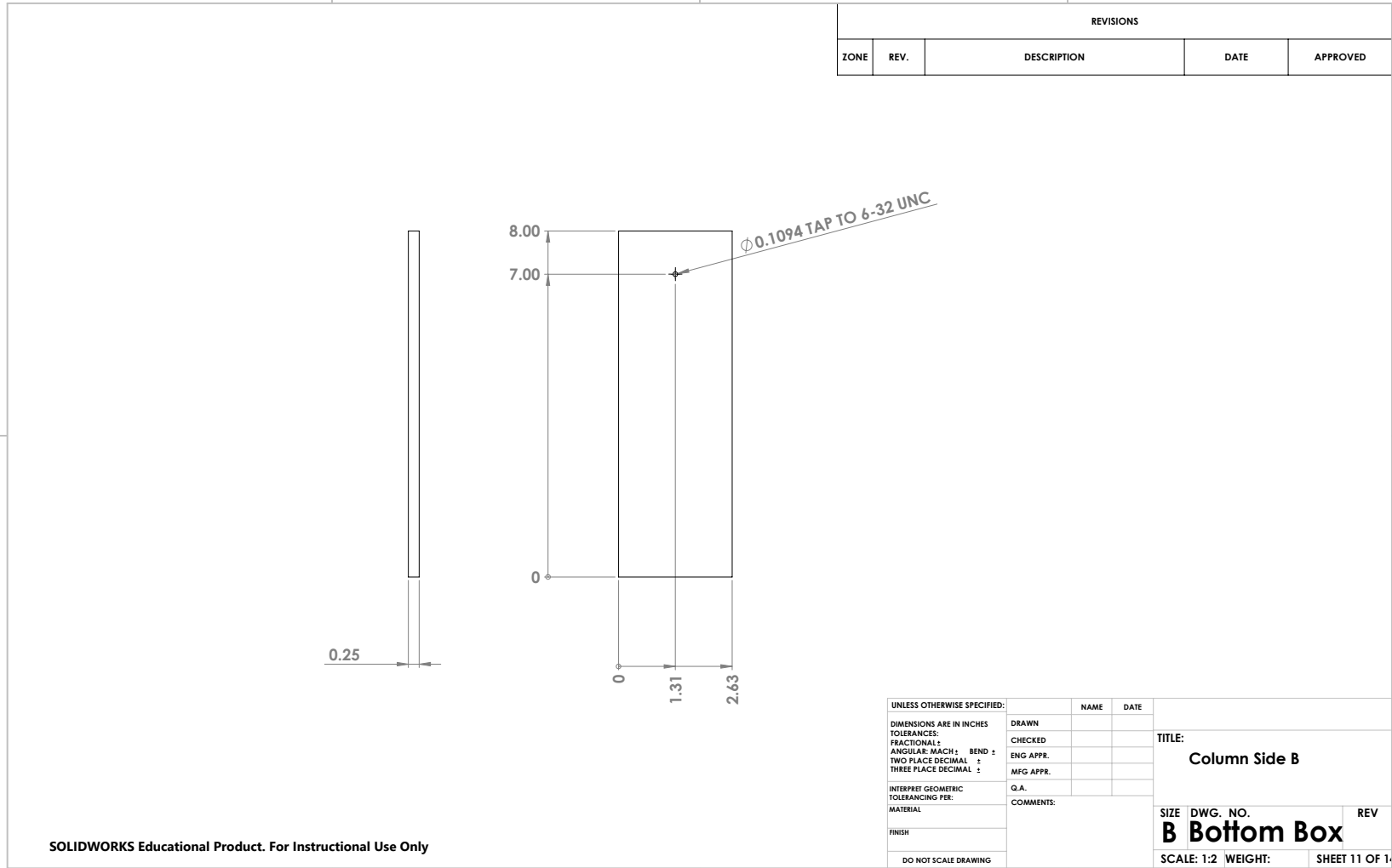
A

4

3

2

1



SOLIDWORKS Educational Product. For Instructional Use Only

4

3

2

1

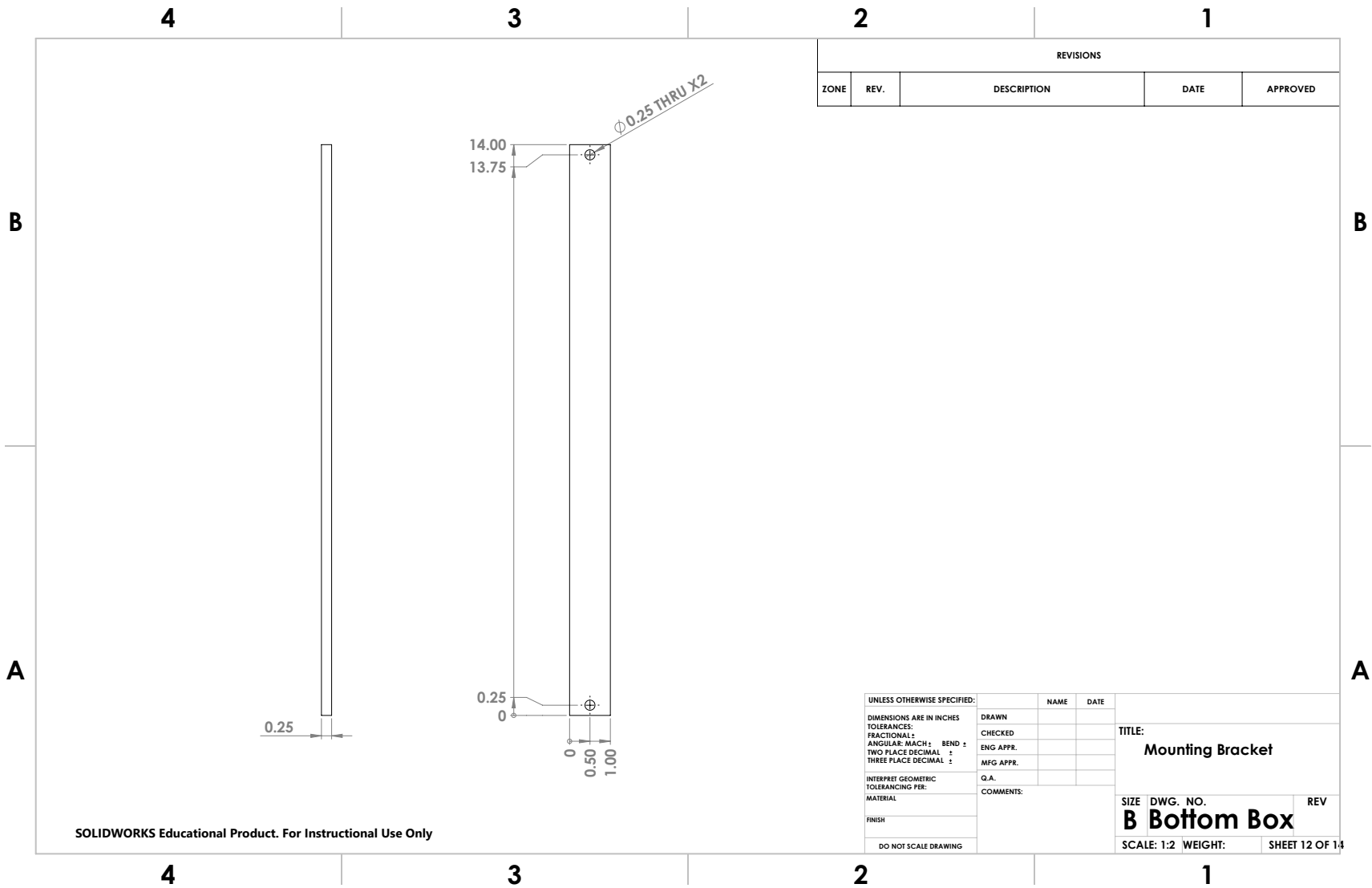
REVISIONS				
ZONE	REV.	DESCRIPTION	DATE	APPROVED

B

A

UNLESS OTHERWISE SPECIFIED:	NAME	DATE		
DIMENSIONS ARE IN INCHES	DRAWN			
TOLERANCES:	CHECKED			
FRACTIONAL: ±	ENG APPR.			
ANGULAR: MACH ± BEND ±	MFG APPR.			
TWO PLACE DECIMAL ±				
THREE PLACE DECIMAL ±				
INTERPRET GEOMETRIC TOLERANCING PER:	Q.A.			
MATERIAL	COMMENTS:			
FINISH				
DO NOT SCALE DRAWING				
TITLE:			Column Side B	
SIZE	DWG. NO.	REV		
B Bottom Box				
SCALE: 1:2		WEIGHT:	SHEET 11 OF 14	

119



SOLIDWORKS Educational Product. For Instructional Use Only

120

B

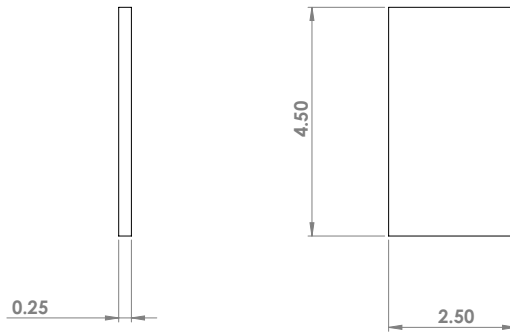
A

4

3

2

1



REVISIONS				
ZONE	REV.	DESCRIPTION	DATE	APPROVED

B

A

SOLIDWORKS Educational Product. For Instructional Use Only

4

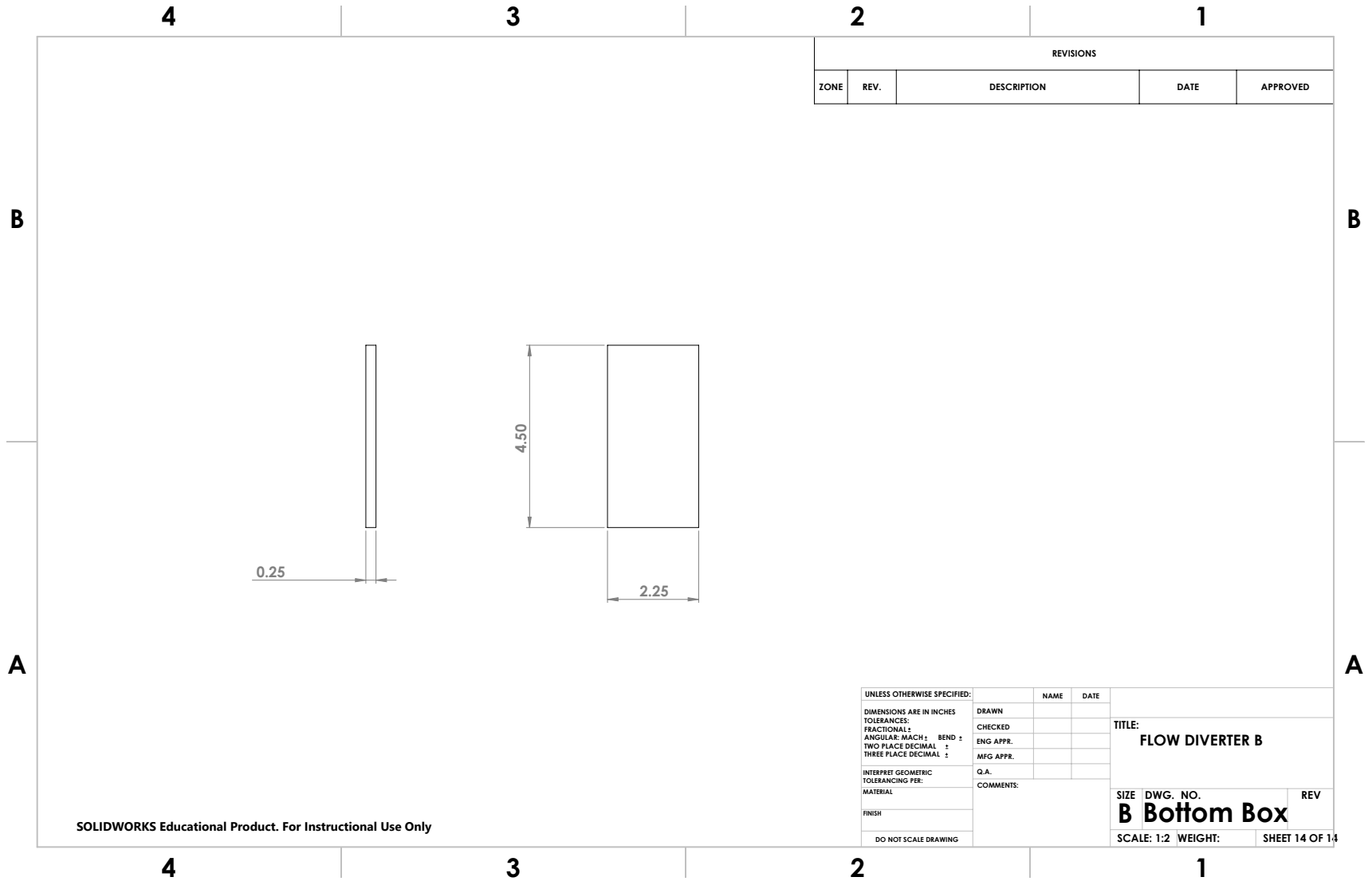
3

2

1

UNLESS OTHERWISE SPECIFIED:	NAME	DATE	
DIMENSIONS ARE IN INCHES	DRAWN		
TOLERANCES:	CHECKED		
FRACTIONAL: ±	ENG APPR.		
ANGULAR: MACH ±	MFG APPR.		
TWO PLACE DECIMAL ±			
THREE PLACE DECIMAL ±			
INTERPRET GEOMETRIC TOLERANCING PER:	Q.A.		
MATERIAL	COMMENTS:		
FINISH			
DO NOT SCALE DRAWING			
TITLE:			
Flow Diverter A			
SIZE	DWG. NO.	REV	
B	Bottom Box		
SCALE: 1:2	WEIGHT:	SHEET 13 OF 14	

121



SOLIDWORKS Educational Product. For Instructional Use Only

REVISIONS				
ZONE	REV.	DESCRIPTION	DATE	APPROVED

UNLESS OTHERWISE SPECIFIED:	NAME	DATE		
DIMENSIONS ARE IN INCHES	DRAWN			
TOLERANCES:	CHECKED			
FRACTIONAL: ±	ENG APPR.			
ANGULAR: MACH ±	MFG APPR.			
TWO PLACE DECIMAL ±				
THREE PLACE DECIMAL ±				
INTERPRET GEOMETRIC TOLERANCING PER:	Q.A.			
MATERIAL	COMMENTS:			
FINISH			SIZE	DWG. NO.
DO NOT SCALE DRAWING			B Bottom Box	REV
			SCALE: 1:2	WEIGHT:
				SHEET 14 OF 14

TITLE: FLOW DIVERTER B

SCALE: 1:2 WEIGHT: SHEET 14 OF 14

APPENDIX C

CALIBRATION DATA

The following data was collected from images of the LaVision 058-5-DSDP calibration plate. The number of planes used in the determination of M was constrained by the depth of the calibration box and the thickness of the plate.

Table C.1: Magnification factor calculations for measurements of u and w_1 . Depth of planes, y , indicates nominal center position of the 1.5 mm thick sheet.

Plane label	y (mm)	M (mm/pixel)	U_M (mm/pixel)
A	0.75	0.028468	0.00020271
B	2.25	0.028444	0.00020758
C	3.75	0.028446	0.00021149
D	5.25	0.028445	0.00021327
E	6.75	0.028440	0.00021327
F	8.25	0.028528	0.00021210
G	9.75	0.028438	0.00021101
L	17.25	0.028434	0.00022474
M	18.75	0.028435	0.00021848
N	20.25	0.028439	0.00020447
O	21.75	0.028433	0.00020413
P	23.25	0.028434	0.00020448
U	30.75	0.028440	0.00020161
V	32.25	0.028438	0.00020417
W	33.75	0.028431	0.00020843
X	35.25	0.028441	0.00020627
mean	N/A	0.028446	0.00020926

Table C.2: Magnification factor calculations for measurements of v and w_2 . Depth of planes, x , indicates nominal center position of the 1.5 mm thick sheet.

Plane label	x (mm)	M (mm/pixel)	U_M (mm/pixel)
AAA	65.75	0.028484	0.00029787
BBB	64.25	0.028485	0.00024864
CCC	62.75	0.028486	0.00024597
DDD	61.25	0.028485	0.00026202
EEE	59.75	0.028483	0.00026236
JJJ	52.25	0.028483	0.00026205
KKK	50.75	0.028486	0.00026453
LLL	49.25	0.028485	0.00025834
MMM	47.75	0.028484	0.00024522
NNN	46.25	0.028483	0.00024291
OOO	44.75	0.028485	0.00024766
PPP	43.25	0.028487	0.00024592
QQQ	41.75	0.028482	0.00031352
VVV	34.25	0.028487	0.00036713
WWW	32.75	0.028478	0.00023582
mean	N/A	0.028484	0.00026666

APPENDIX D

TWO DIMENSION TWO COMPONENT RESULTS

The following section contains results for mean velocity components, fluctuating RMS, Reynolds shear stress, and vorticity for a selection of planes in the bundle. Results presented represent the last set means for convergence analysis, $N=2000$. Planes selected correspond to positions in the near-center of subchannels as indicated in Table D.1.

Additional planes which intersect rods have been omitted for brevity. Data collected from all planes is available upon request.

Table D.1: Plane positions for select full subchannel planes.

Test No.	Span Coordinates	Position Coordiante	Plane Label	Position (mm)
1	xz	y	B	2.25
			J	14.25
			R	26.25
			AA	39.75
			II	51.75
			QQ	63.75
2	yz	x	QQQQ	2.75
			III	14.75
			AAAA	26.75
			RRR	40.25
			JJJ	52.25
			BBB	64.25

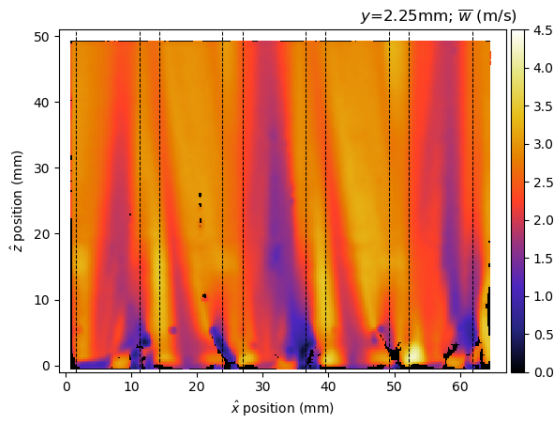


Figure D.1: \bar{w} , $y = 2.25\text{mm}$.

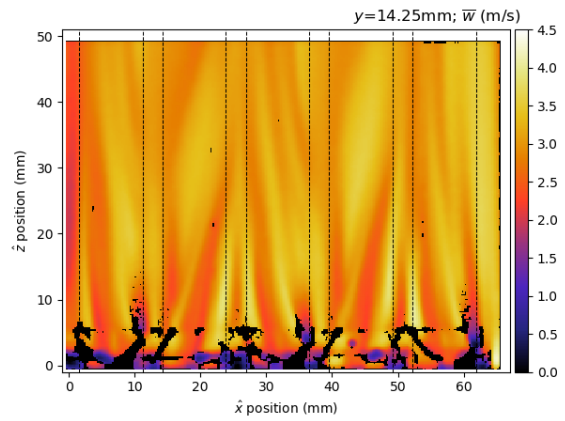


Figure D.2: \bar{w} , $y = 14.25\text{mm}$.

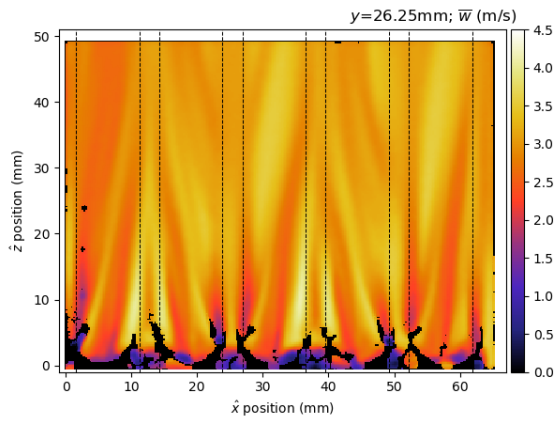


Figure D.3: \bar{w} , $y = 26.25\text{mm}$.

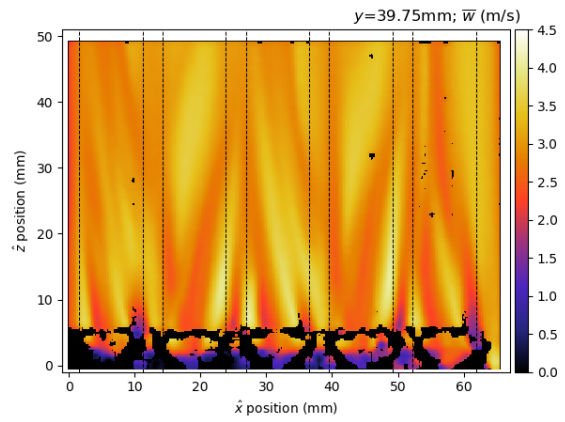


Figure D.4: \bar{w} , $y = 39.75\text{mm}$.

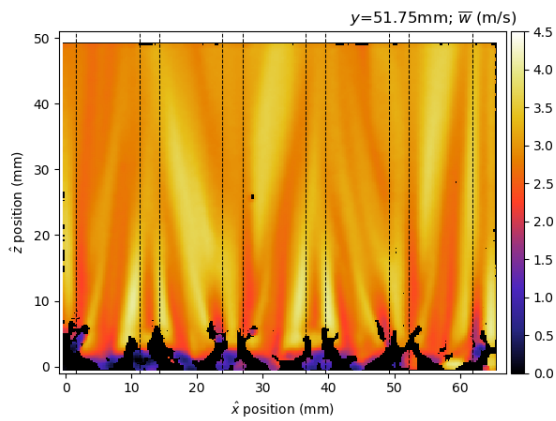


Figure D.5: \bar{w} , $y = 51.75\text{mm}$.

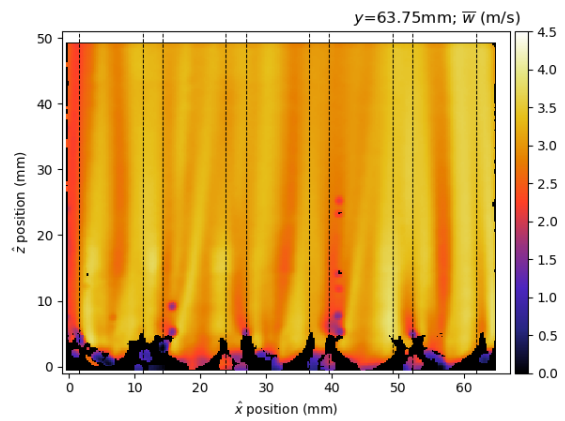


Figure D.6: \bar{w} , $y = 63.75\text{mm}$.

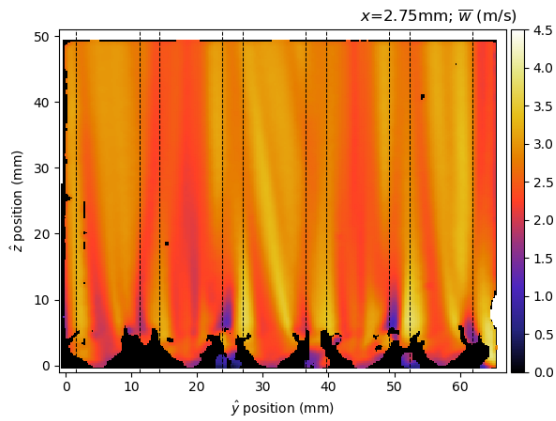


Figure D.7: \bar{w} , $x = 2.75\text{mm}$.

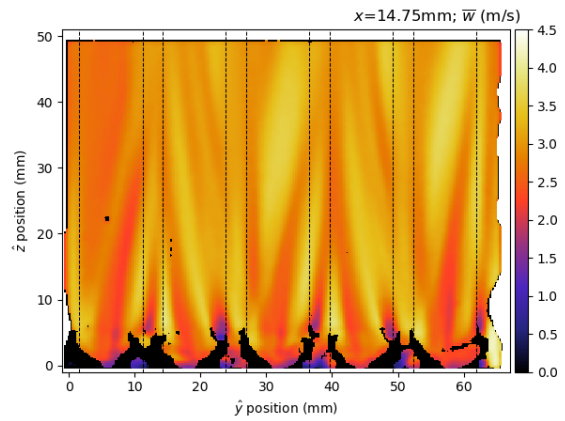


Figure D.8: \bar{w} , $x = 14.75\text{mm}$.

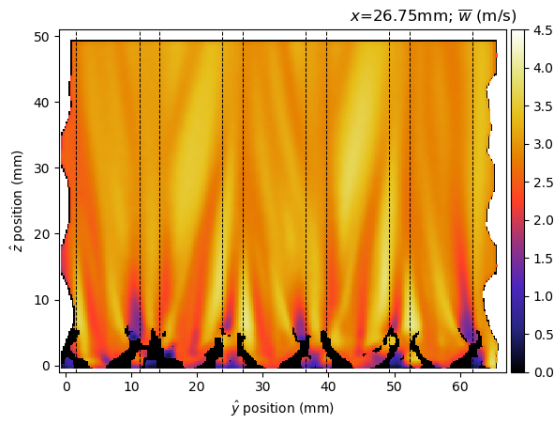


Figure D.9: \bar{w} , $x = 26.75\text{mm}$.

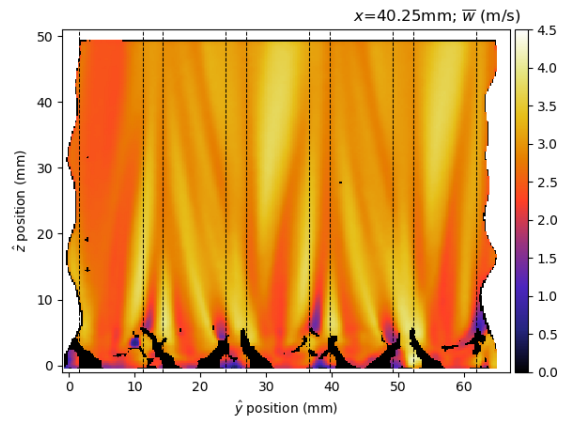


Figure D.10: \bar{w} , $x = 40.25\text{mm}$.

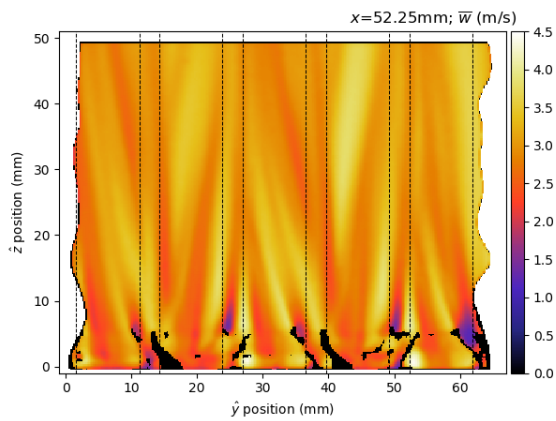


Figure D.11: \bar{w} , $x = 52.25\text{mm}$.

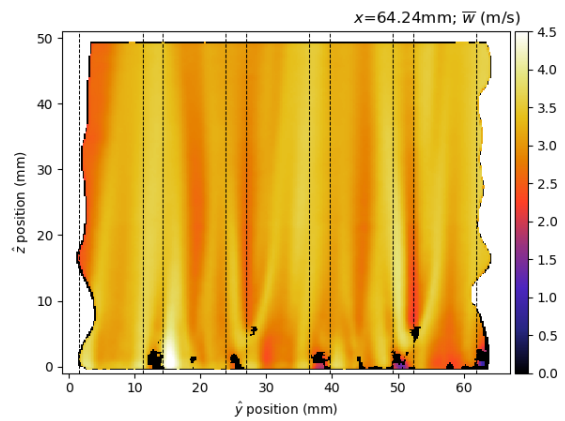


Figure D.12: \bar{w} , $x = 64.25\text{mm}$.

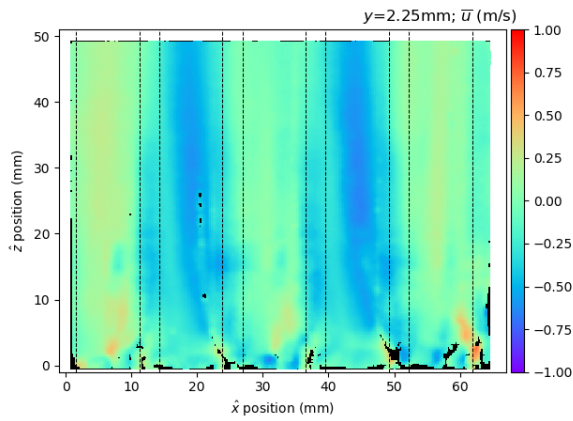


Figure D.13: \bar{u} , $y = 2.25\text{mm}$.

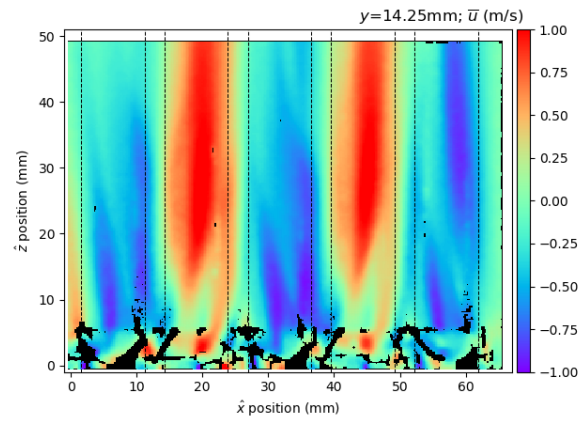


Figure D.14: \bar{u} , $y = 14.25\text{mm}$.

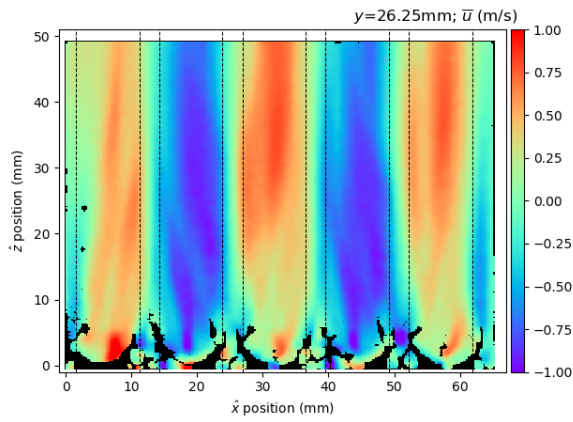


Figure D.15: \bar{u} , $y = 26.25\text{mm}$.

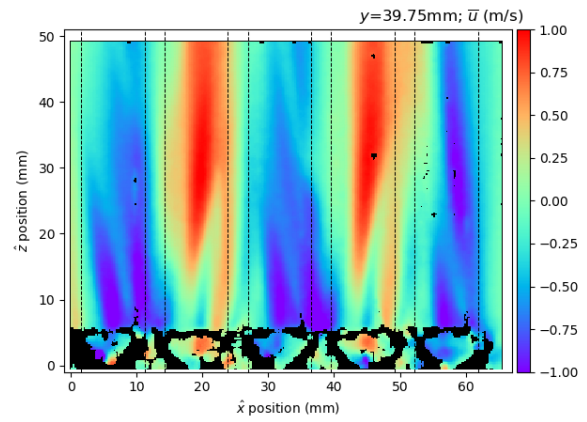


Figure D.16: \bar{u} , $y = 39.75\text{mm}$.

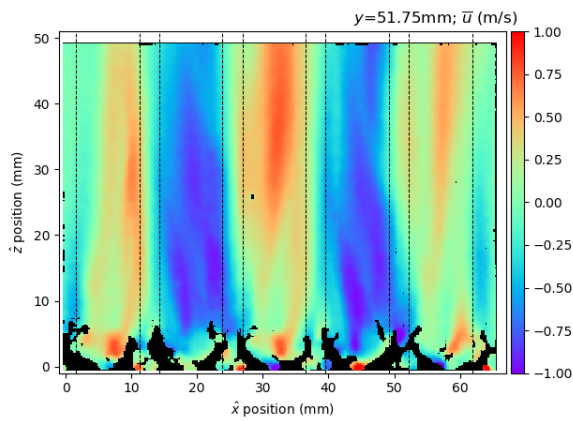


Figure D.17: \bar{u} , $y = 51.75\text{mm}$.

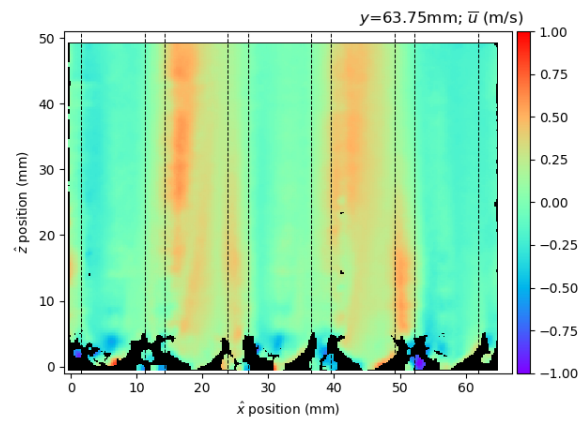


Figure D.18: \bar{u} , $y = 63.75\text{mm}$.

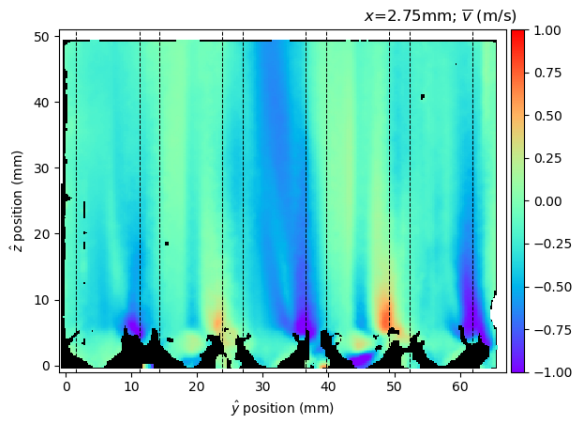


Figure D.19: \bar{v} , $x = 2.75\text{mm}$.

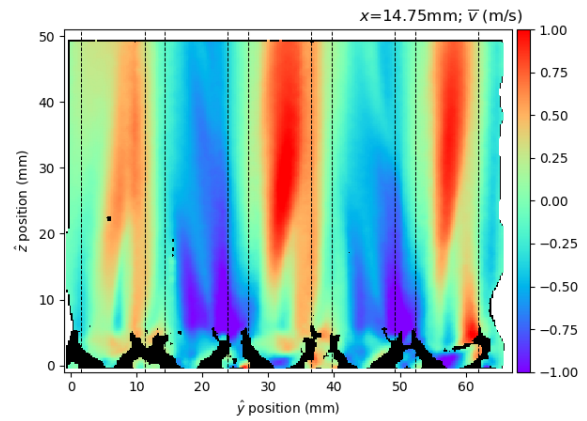


Figure D.20: \bar{v} , $x = 14.75\text{mm}$.

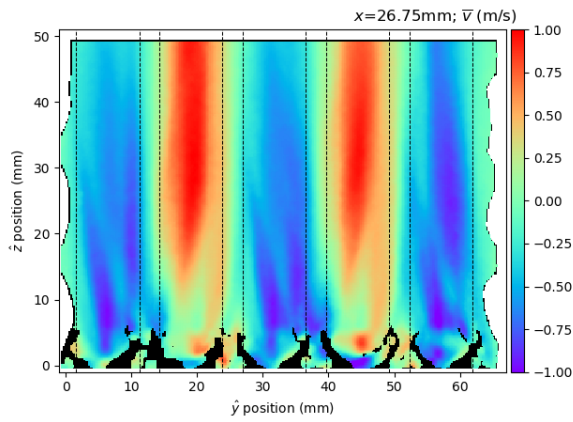


Figure D.21: \bar{v} , $x = 26.75\text{mm}$.

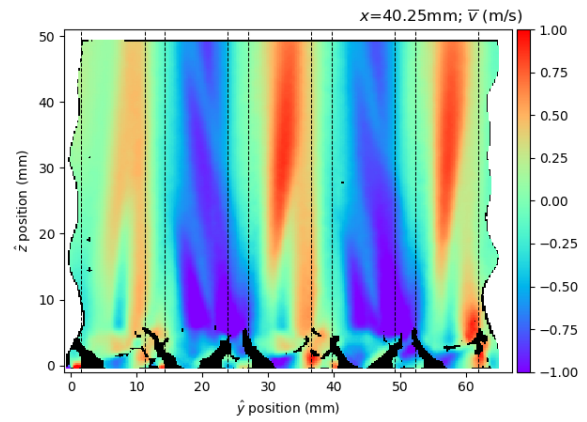


Figure D.22: \bar{v} , $x = 40.25\text{mm}$.

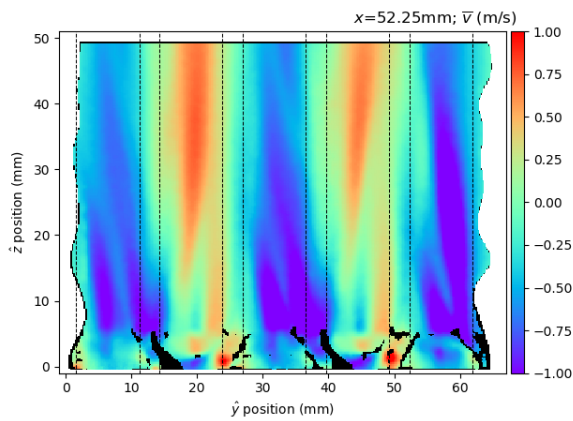


Figure D.23: \bar{v} , $x = 52.25\text{mm}$.

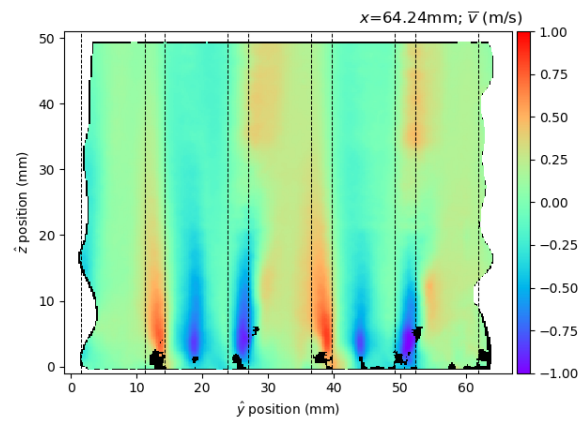


Figure D.24: \bar{v} , $x = 64.25\text{mm}$.

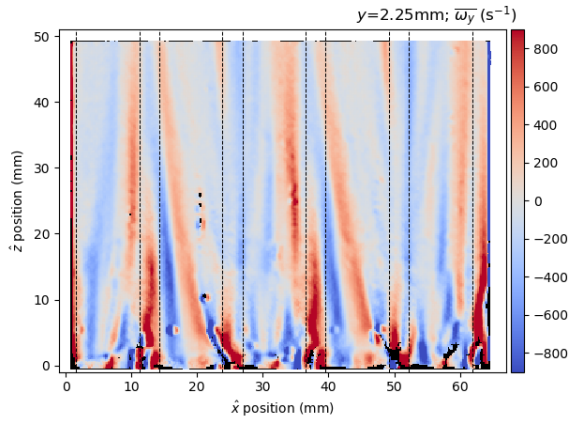


Figure D.25: $\bar{\omega}_y$, $y = 2.25\text{mm}$.

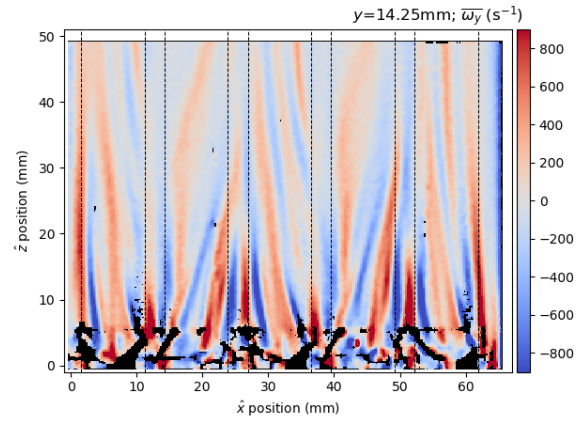


Figure D.26: $\bar{\omega}_y$, $y = 14.25\text{mm}$.

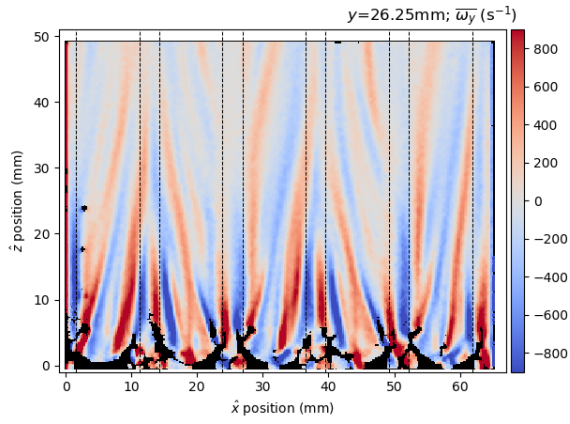


Figure D.27: $\bar{\omega}_y$, $y = 26.25\text{mm}$.

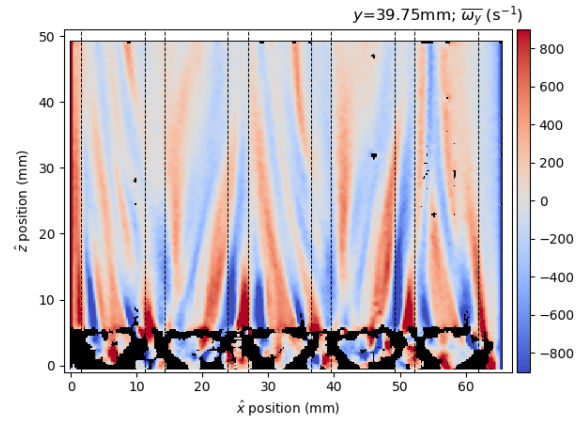


Figure D.28: $\bar{\omega}_y$, $y = 39.75\text{mm}$.

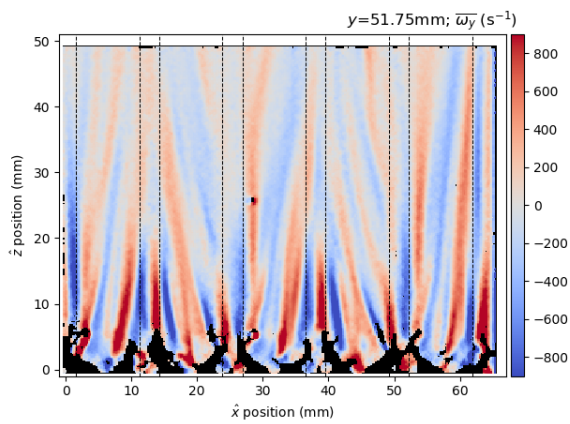


Figure D.29: $\bar{\omega}_y$, $y = 51.75\text{mm}$.

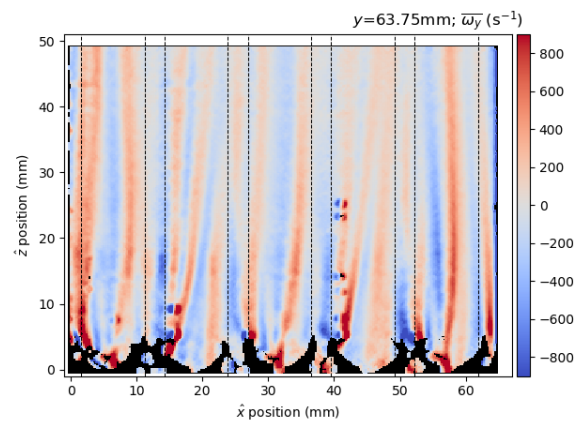


Figure D.30: $\bar{\omega}_y$, $y = 63.75\text{mm}$.

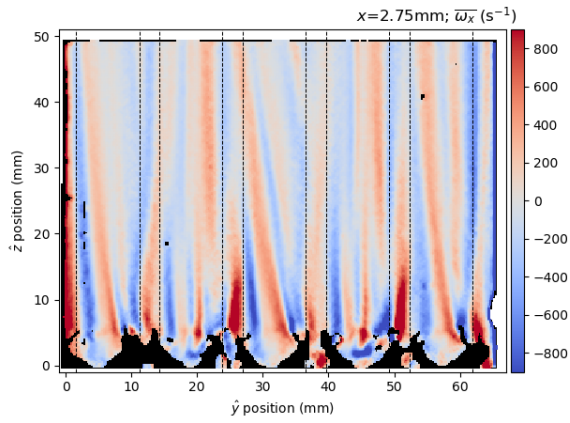


Figure D.31: $\bar{\omega}_x$, $x = 2.75$ mm.

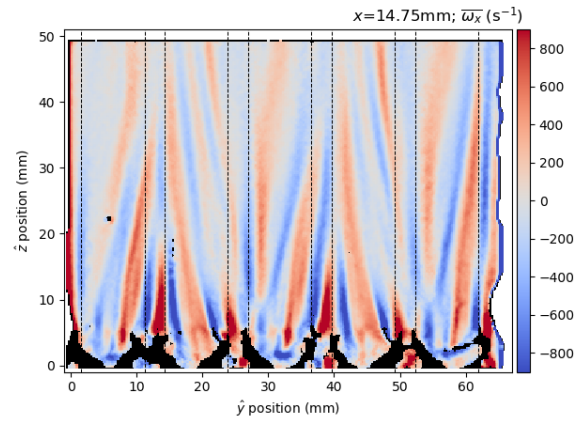


Figure D.32: $\bar{\omega}_x$, $x = 14.75$ mm.

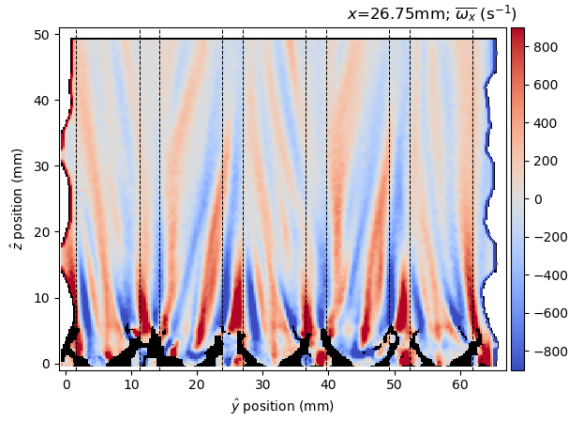


Figure D.33: $\bar{\omega}_x$, $x = 26.75$ mm.

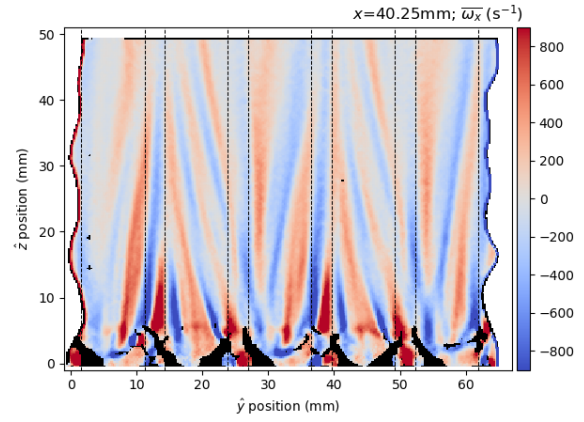


Figure D.34: $\bar{\omega}_x$, $x = 40.25$ mm.

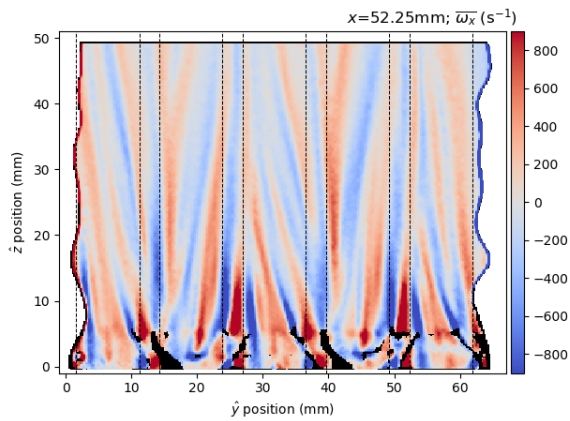


Figure D.35: $\bar{\omega}_x$, $x = 52.25$ mm.

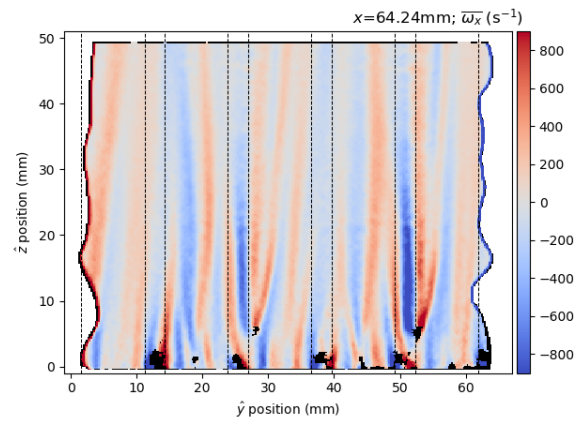


Figure D.36: $\bar{\omega}_x$, $x = 64.25$ mm.

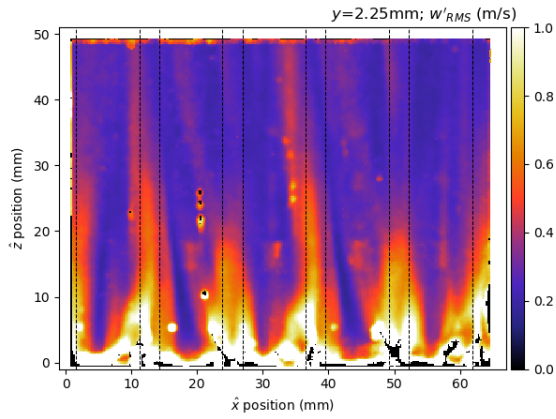


Figure D.37: $\sqrt{w'w'}$, $y = 2.25\text{mm}$.

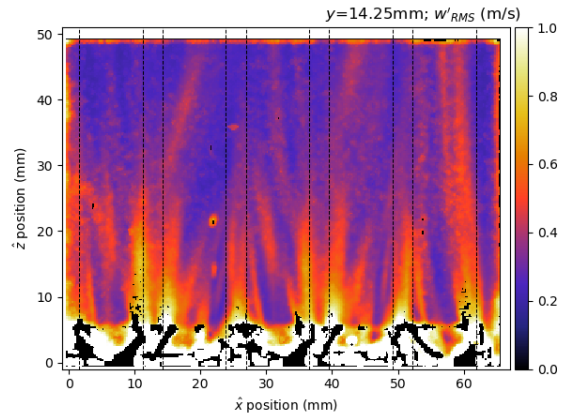


Figure D.38: $\sqrt{w'w'}$, $y = 14.25\text{mm}$.

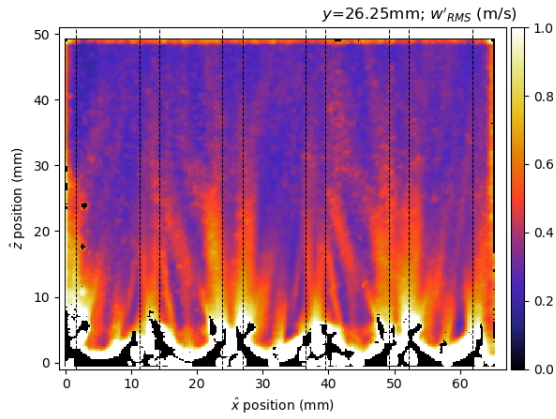


Figure D.39: $\sqrt{w'w'}$, $y = 26.25\text{mm}$.

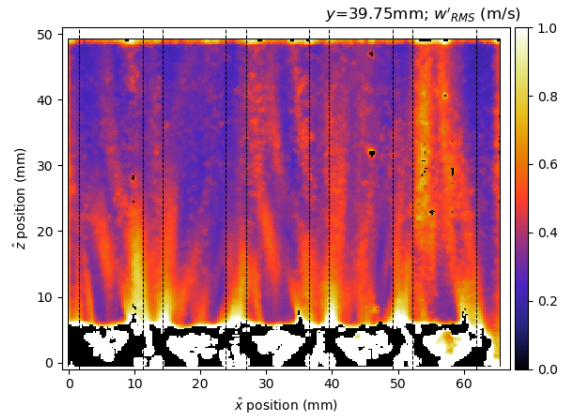


Figure D.40: $\sqrt{w'w'}$, $y = 39.75\text{mm}$.

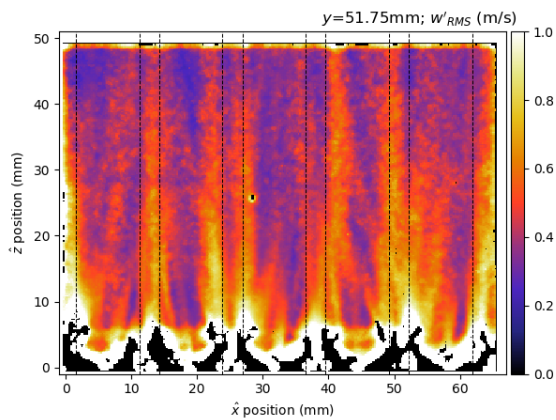


Figure D.41: $\sqrt{w'w'}$, $y = 51.75\text{mm}$.

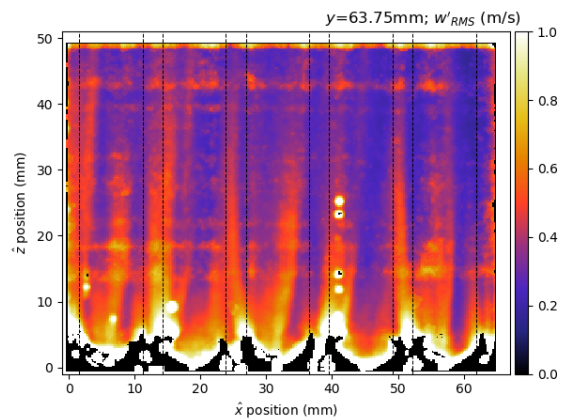


Figure D.42: $\sqrt{w'w'}$, $y = 63.75\text{mm}$.

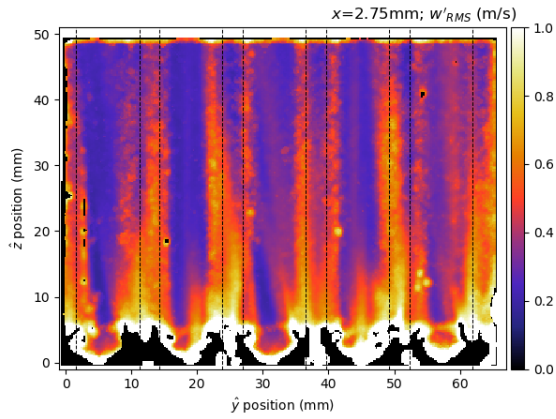


Figure D.43: $\sqrt{w'w'}$, $x = 2.75\text{mm}$.

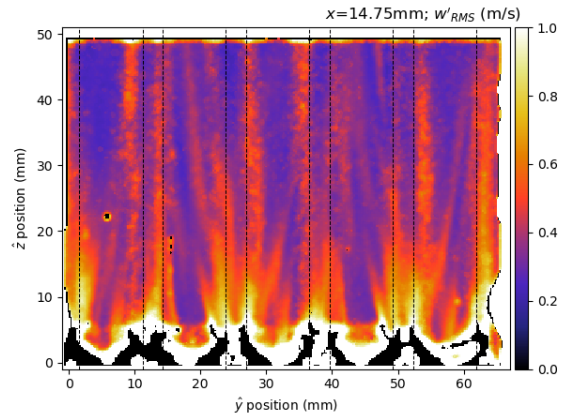


Figure D.44: $\sqrt{w'w'}$, $x = 14.75\text{mm}$.

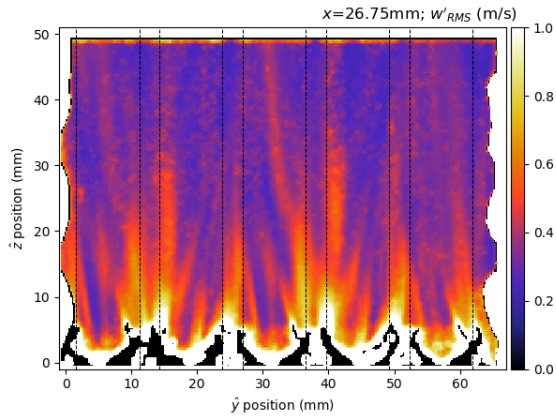


Figure D.45: $\sqrt{w'w'}$, $x = 26.75\text{mm}$.

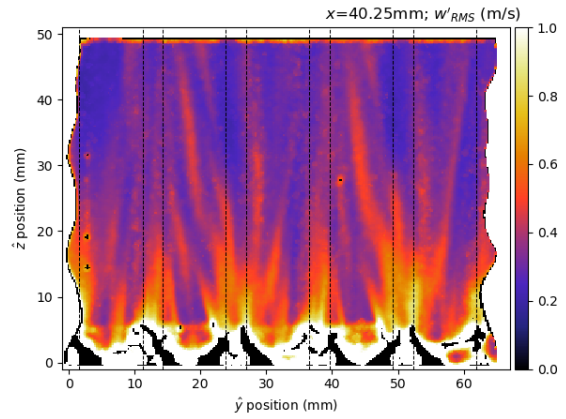


Figure D.46: $\sqrt{w'w'}$, $x = 40.25\text{mm}$.

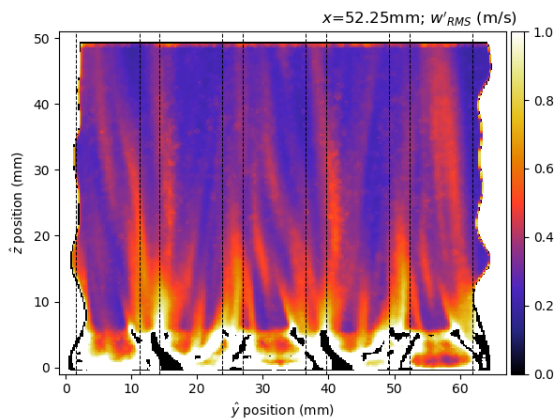


Figure D.47: $\sqrt{w'w'}$, $x = 52.25\text{mm}$.

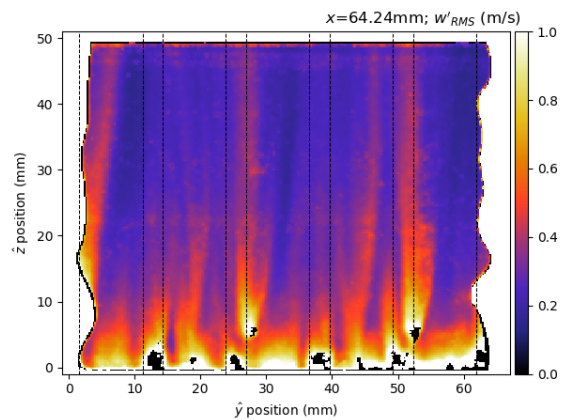


Figure D.48: $\sqrt{w'w'}$, $x = 64.25\text{mm}$.

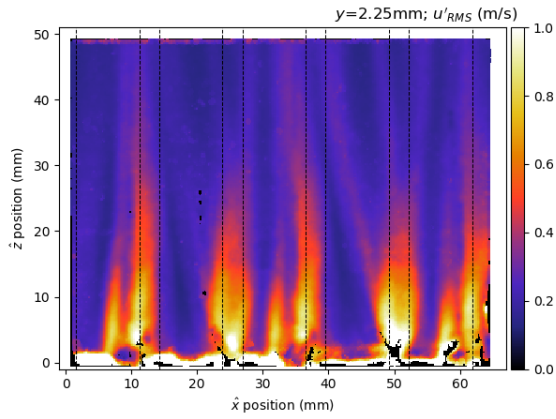


Figure D.49: $\sqrt{u'u'}$, $y = 2.25\text{mm}$.

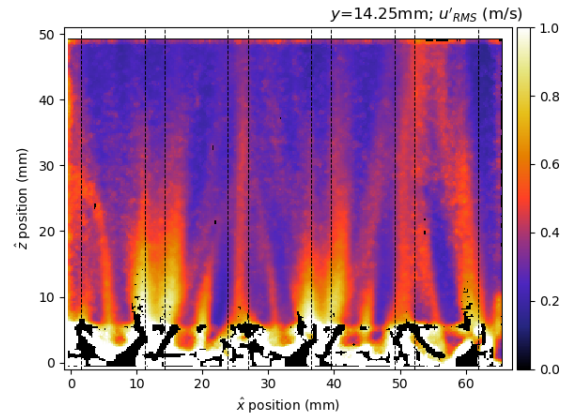


Figure D.50: $\sqrt{u'u'}$, $y = 14.25\text{mm}$.

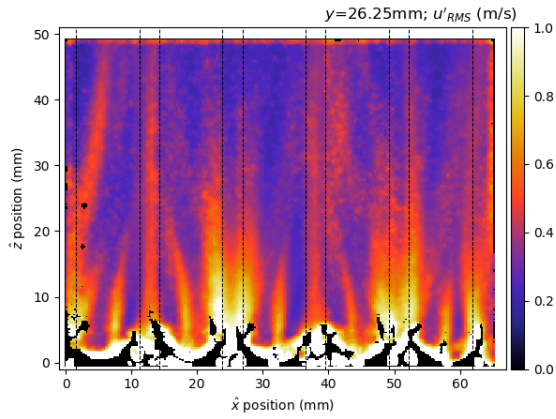


Figure D.51: $\sqrt{u'u'}$, $y = 26.25\text{mm}$.

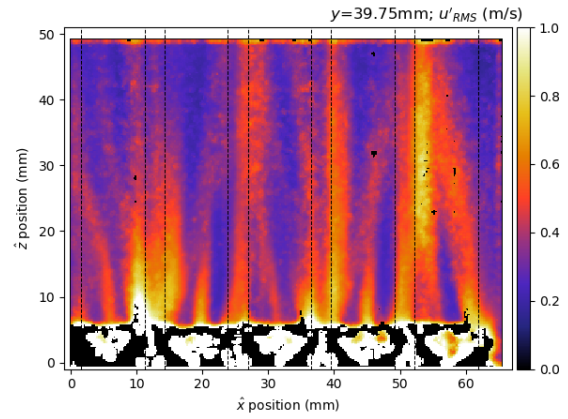


Figure D.52: $\sqrt{u'u'}$, $y = 39.75\text{mm}$.

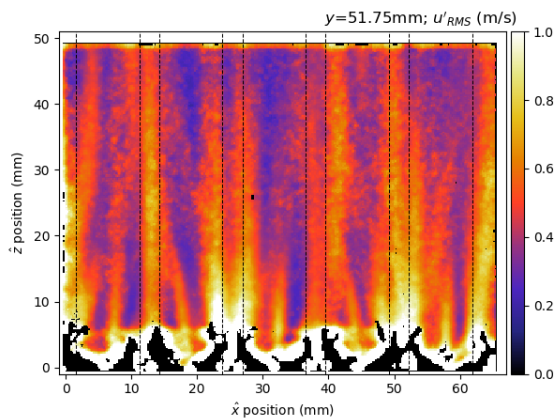


Figure D.53: $\sqrt{u'u'}$, $y = 51.75\text{mm}$.

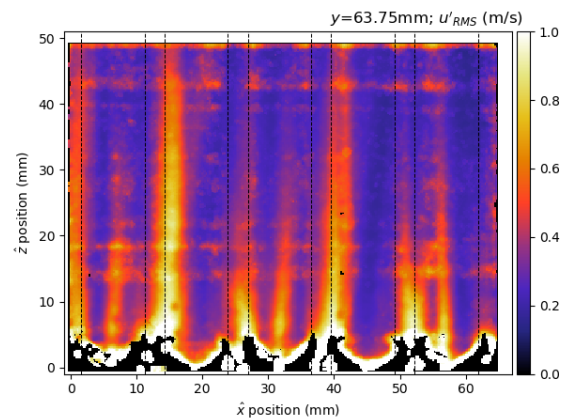


Figure D.54: $\sqrt{u'u'}$, $y = 63.75\text{mm}$.

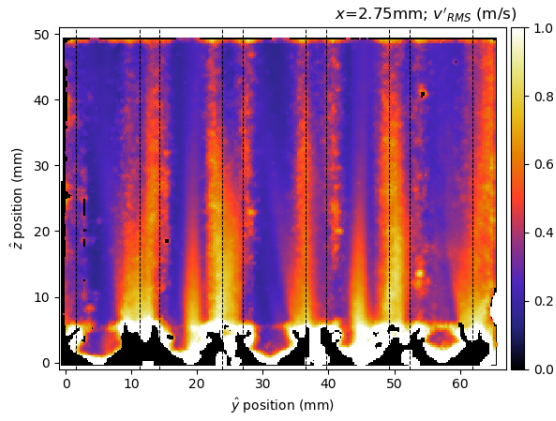


Figure D.55: $\sqrt{v'v'}$, $x = 2.75\text{mm}$.

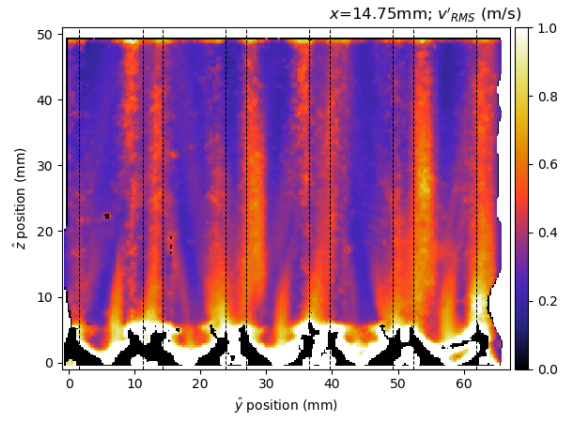


Figure D.56: $\sqrt{v'v'}$, $x = 14.75\text{mm}$.

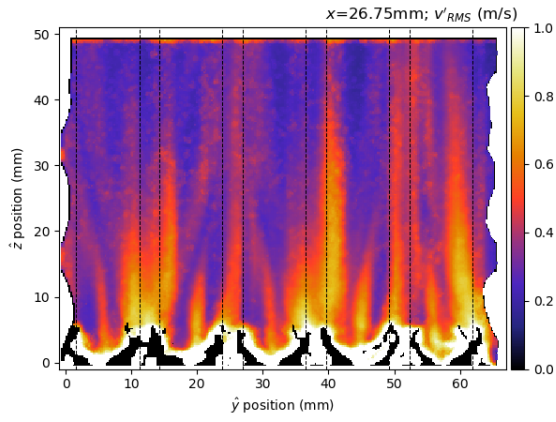


Figure D.57: $\sqrt{v'v'}$, $x = 26.75\text{mm}$.

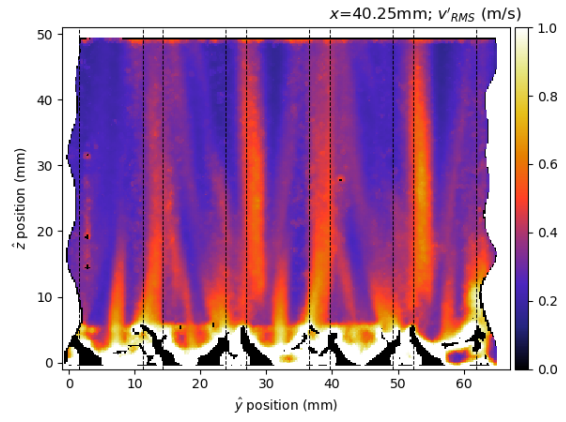


Figure D.58: $\sqrt{v'v'}$, $x = 40.25\text{mm}$.

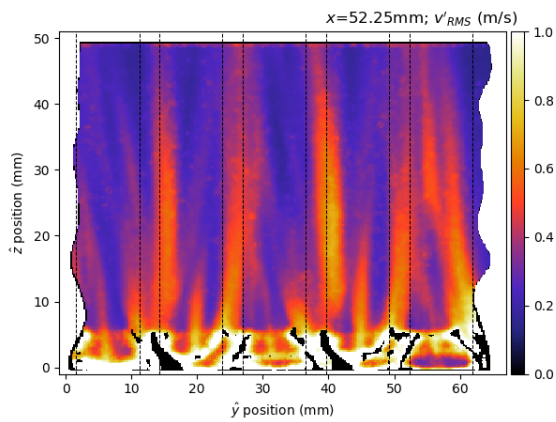


Figure D.59: $\sqrt{v'v'}$, $x = 52.25\text{mm}$.

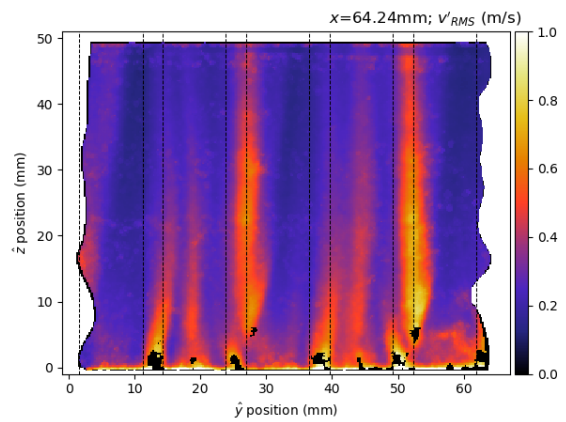


Figure D.60: $\sqrt{v'v'}$, $x = 64.25\text{mm}$.

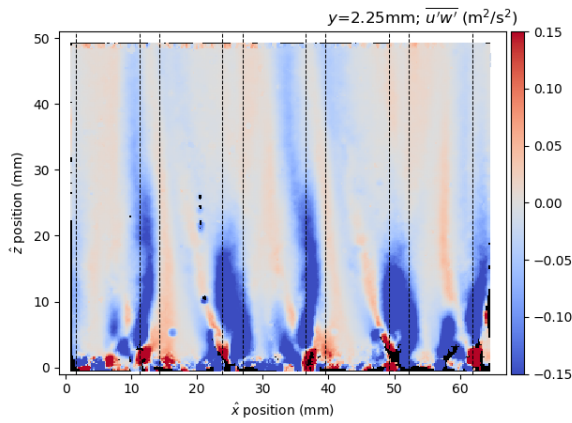


Figure D.61: $\overline{u'w'}$, $y = 2.25\text{mm}$.

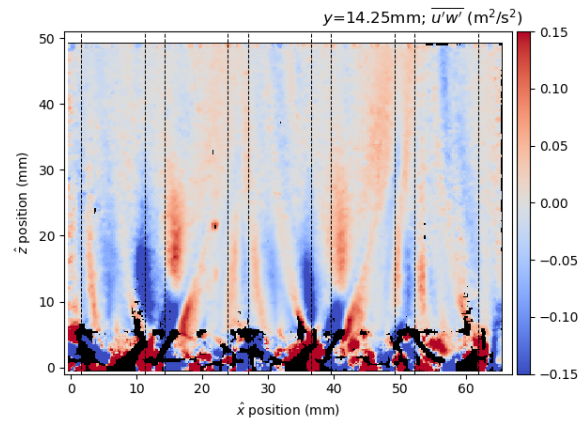


Figure D.62: $\overline{u'w'}$, $y = 14.25\text{mm}$.

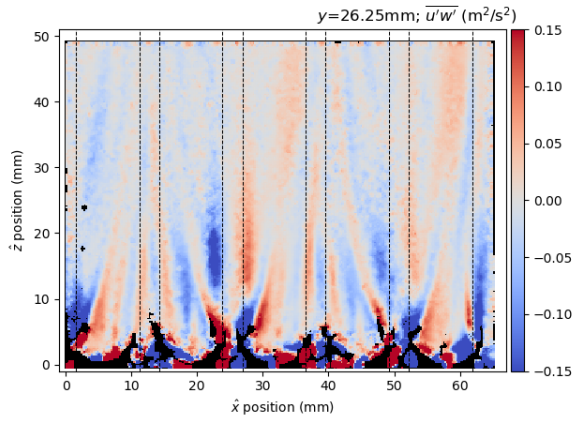


Figure D.63: $\overline{u'w'}$, $y = 26.25\text{mm}$.

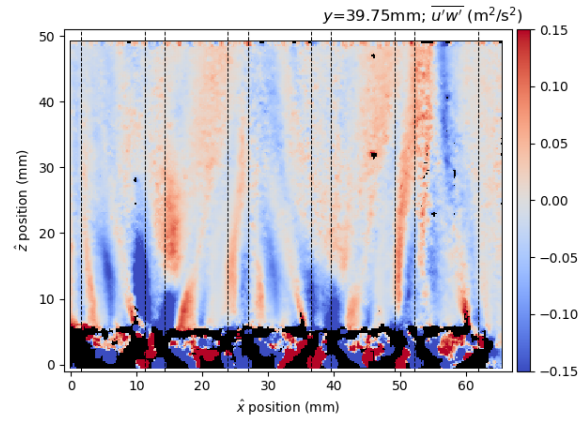


Figure D.64: $\overline{u'w'}$, $y = 39.75\text{mm}$.

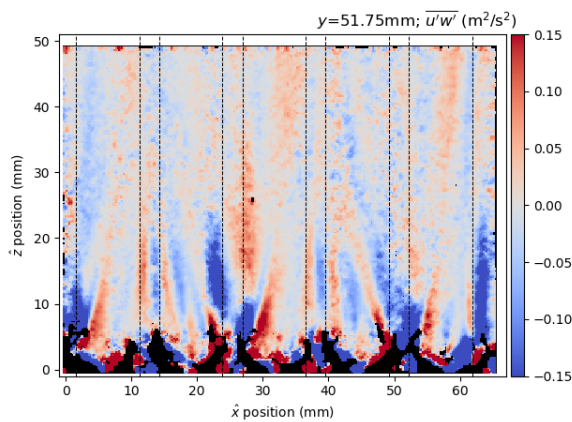


Figure D.65: $\overline{u'w'}$, $y = 51.75\text{mm}$.

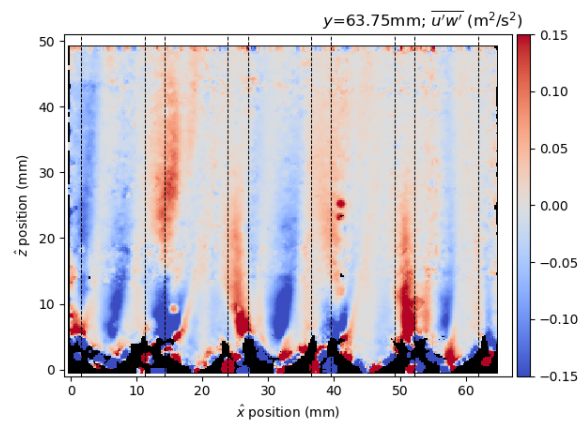


Figure D.66: $\overline{u'w'}$, $y = 63.75\text{mm}$.

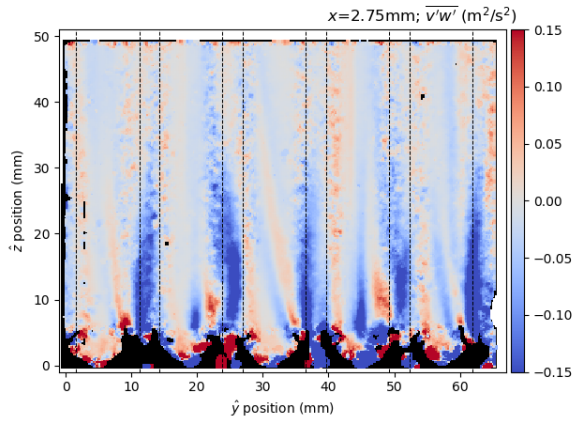


Figure D.67: $\overline{v'w'}$, $x = 2.75$ mm.

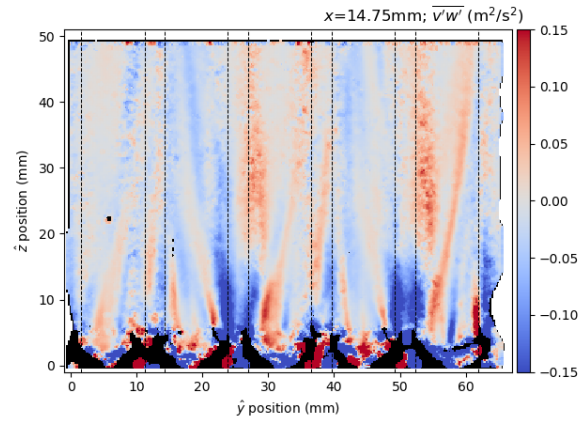


Figure D.68: $\overline{v'w'}$, $x = 14.75$ mm.

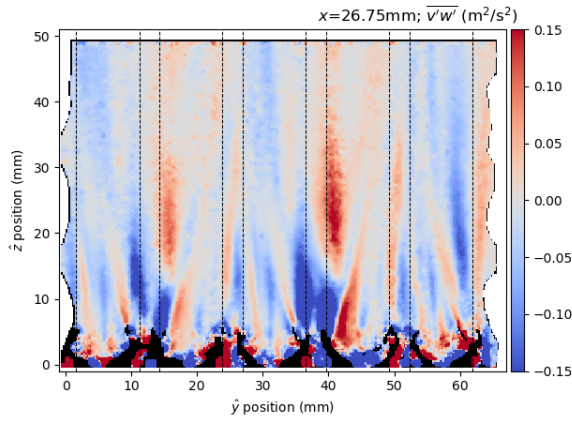


Figure D.69: $\overline{v'w'}$, $x = 26.75$ mm.

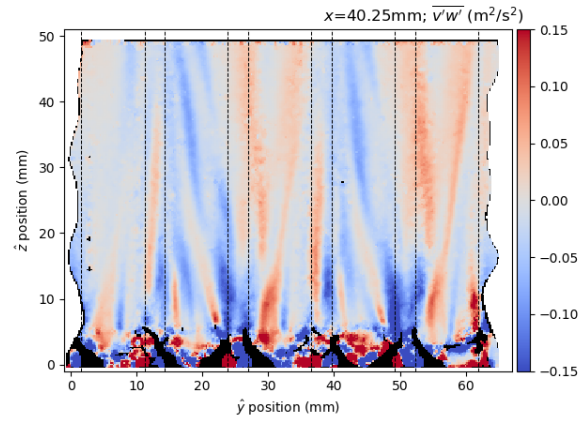


Figure D.70: $\overline{v'w'}$, $x = 40.25$ mm.

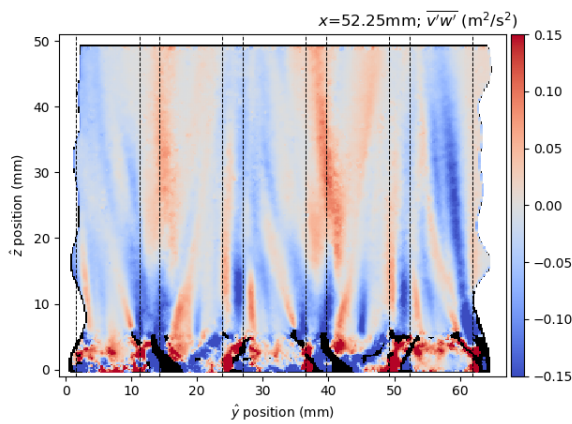


Figure D.71: $\overline{v'w'}$, $x = 52.25$ mm.

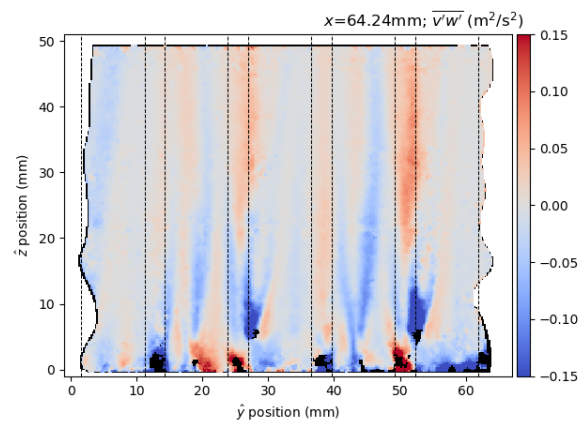


Figure D.72: $\overline{v'w'}$, $x = 64.25$ mm.

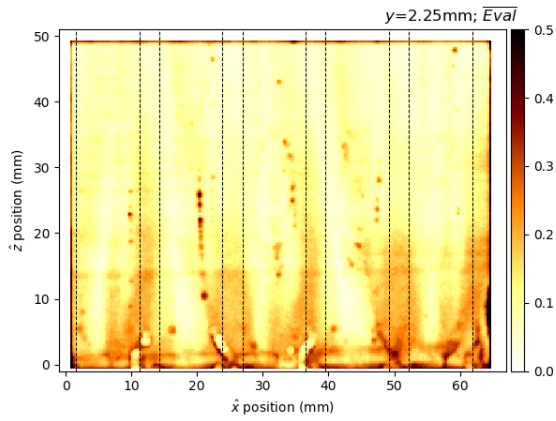


Figure D.73: \overline{Eval} , $y = 2.25\text{mm}$.

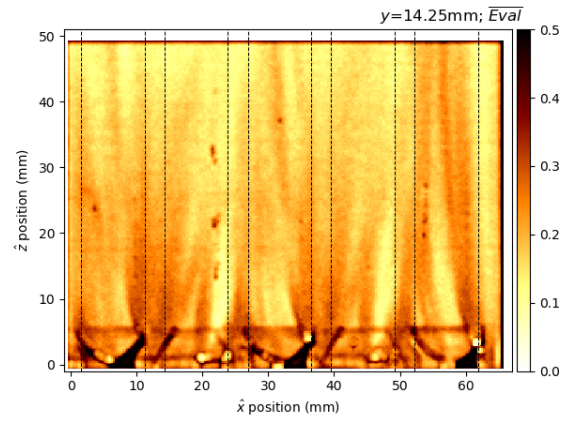


Figure D.74: \overline{Eval} , $y = 14.25\text{mm}$.

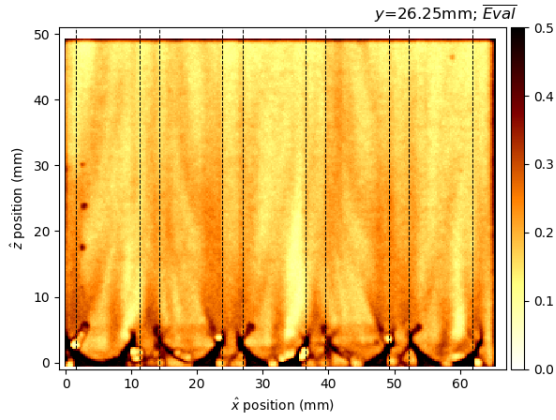


Figure D.75: \overline{Eval} , $y = 26.25\text{mm}$.

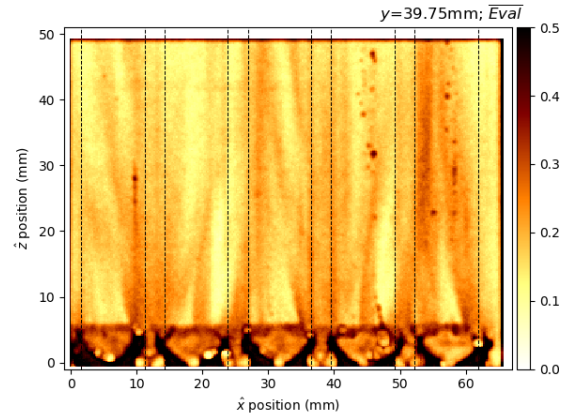


Figure D.76: \overline{Eval} , $y = 39.75\text{mm}$.

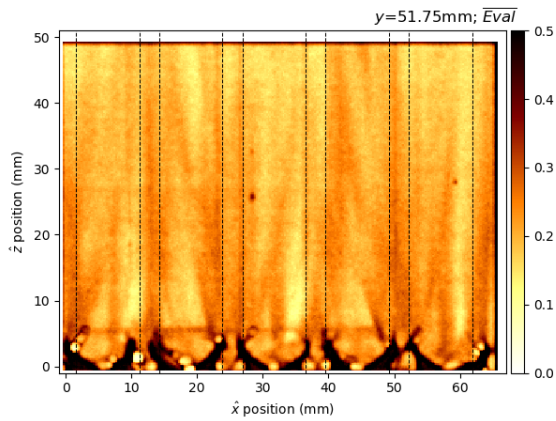


Figure D.77: \overline{Eval} , $y = 51.75\text{mm}$.

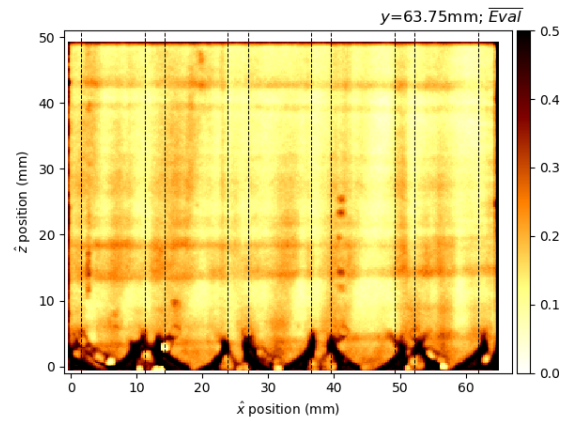


Figure D.78: \overline{Eval} , $y = 63.75\text{mm}$.

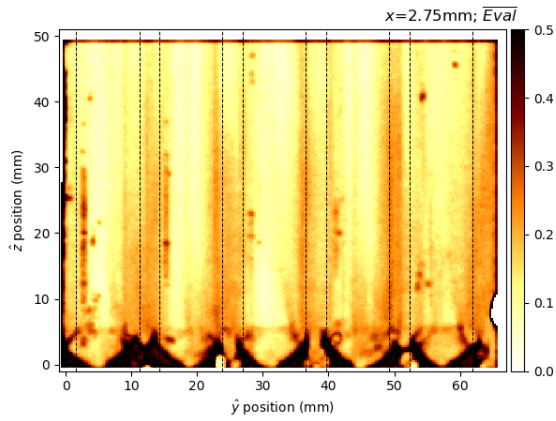


Figure D.79: \overline{Eval} , $x = 2.75\text{mm}$.

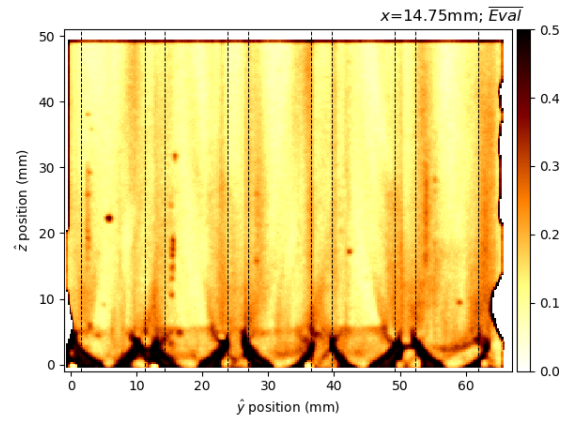


Figure D.80: \overline{Eval} , $x = 14.75\text{mm}$.

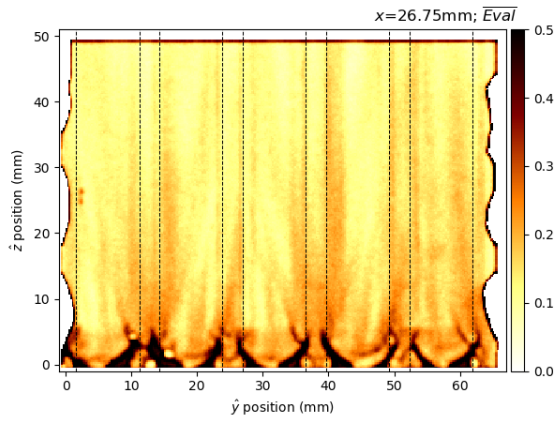


Figure D.81: \overline{Eval} , $x = 26.75\text{mm}$.

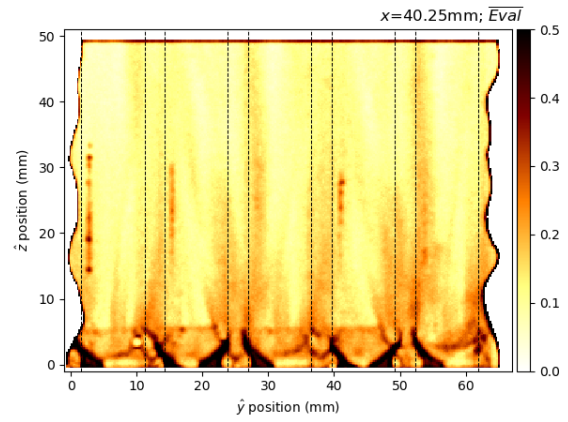


Figure D.82: \overline{Eval} , $x = 40.25\text{mm}$.

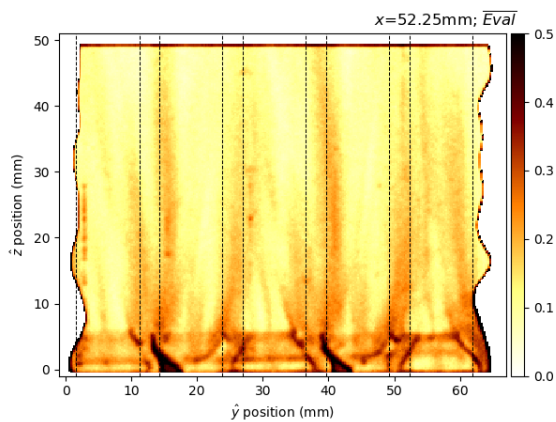


Figure D.83: \overline{Eval} , $x = 52.25\text{mm}$.

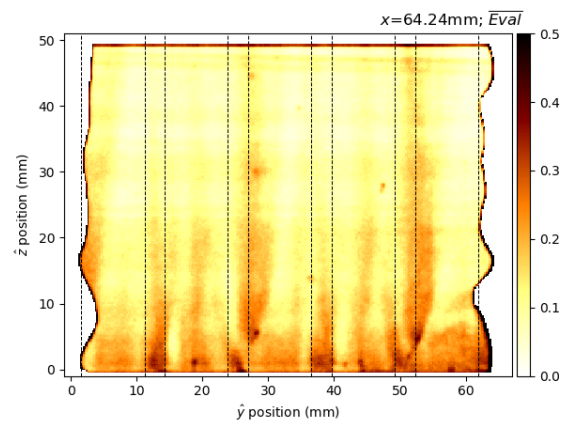


Figure D.84: \overline{Eval} , $x = 64.25\text{mm}$.